

НАУЧНОМ ВЕЋУ ИНСТИТУТА ЗА ФИЗИКУ БЕОГРАД
УНИВЕРЗИТЕТ У БЕОГРАДУ

ИНСТИТУТ ЗА ФИЗИКУ

ПРИМЉЕНО:		28. 09. 2023	
Рад.јед.	б р о ј	Арх.шифра	Прилог
0801	140311		

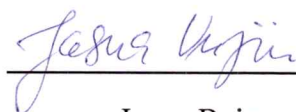
Предмет: Молба за покретање поступка за избор у звање научни сарадник

Молим Научно веће Института за физику Београд, Универзитет у Београду, да у складу са Правилником о поступку и начину вредновања и квантитативном исказивању научно-истраживачких резултата покрене поступак за мој избор у звање **научни сарадник**.

У прилогу достављам:

1. Мишљење руководиоца центра са предлогом чланова комисије за избор у звање.
2. Стручну биографију.
3. Преглед научне активности кандидаткиње
4. Елементе за квалитативну анализу рада кандидаткиње разврстане по ставкама у складу са Прилогом 1 Правилника, уз обавезне доказе за сваку ставку од наведених ставки.
5. Елементе за квантитативну анализу рада кандидаткиње приказане у виду табеле из Прилога 4 Правилника, разврстане у складу са Прилозима 2 и 3 Правилника.
6. Списак објављених радова и других публикација разврстаних по важећим категоријама прописаних Правилником.
7. Податке о цитираности кандидаткиње
8. Уверење о одбрањеној докторској дисертацији.
9. Копије објављених радова и других публикација.

У Београду, 28.9.2023.



Јасна Вујин

ПРИМЉЕНО:		28. 09. 2023	
Рад.јед.	б р о ј	Арх.шифра	Прилог
0801	К03/2		

**НАУЧНОМ ВЕЋУ ИНСТИТУТА ЗА ФИЗИКУ БЕОГРАД
УНИВЕРЗИТЕТ У БЕОГРАДУ**

Предмет: Мишљење руководиоца Центра за физику чврстог стања и нове материјале о избору у звање научни сарадник кандидаткиње др Јасне Вујин са предлогом чланова комисије

Јасна Вујин је од 9.3.2015. године запослена у Лабораторији за 2Д материјале у оквиру Центра за физику чврстог стања и нове материјале на Институту за физику Београд, Универзитета у Београду, где је првобитно била ангажована на националном пројекту “Физика уређених наноструктура и нових материјала у нанофотоници” ОИ171005, који је финансирало Министарство за просвету, науку и технолошки развој Републике Србије. У истраживачком раду бави се испитивањем могућности употребе 2Д-материјала, добијених ексфолијацијом из течне фазе, као претварача код биосензора, за детекцију/идентификацију биолошки молекули који би имали улогу биорецептора и/или анализата. Кандидаткиња је одбранила докторску дисертацију под називом „Физичкохемијска карактеризација хетероструктура дводимензионалних материјала (графен, волфрам дисулфид) и биолошких молекула (цистеин, 1,2 дипалмитоли-сн-глицеро-3-фосфохолин)” 26.9.2023. године на Факултету за физичку хемију, Универзитета у Београду. Ауторка/коауторка је 7 научних радова са SCI-листе и 11 саопштења са међународних конференција.

С обзиром да кандидаткиња испуњава све услове предвиђене Законом о научно-истраживачкој делатности и Правилником о стицању истраживачких и научних звања Министарства науке, технолошког развоја и иновација Републике Србије, сагласан сам са покретањем поступка за избор у звање др Јасне Вујин у звање научни сарадник.

За чланове комисије за избор др Јасне Вујин у звање научни сарадник предлажем:

1. Др Ивану Милошевић, научног сарадника, Института за физику Београд, Универзитета у Београду
2. Др Радмилу Панајотовић, научног сарадника, Института за физику Београд, Универзитета у Београду
3. Др Игор Паштија, редовног професора на Факултету за физичку хемију, Универзитета у Београду

28.9.2023, Београд

Руководилац Центра за физику чврстог
стања и нове материјале



др Ненад Лазаревић

1. СТРУЧНА БИОГРАФИЈА

Јасна (Миодраг) Вујин рођена је 7.8.1984. године у Београду. Академске 2003/2004. године уписала је Факултет за физичку хемију Универзитета у Београду, на којем је 2011. године дипломирала са темом „Теоријско изучавање вибрационих прелаза код П–Σ стања троатомских линеарних молекула“ код др Миљенка Перића, редовног професора Факултета за физичку хемију. Мастер студије завршила је на истом факултету 2013. године са темом „Електрохемијска активност поликристалне Pt за реакцију редукције кисеоника-теоријски и практични аспект“ код др Игора Паштија, редовног професора на Факултету за физичку хемију. Од академске 2014/2015. године студенткиња је докторских студија Факултет за физичку хемију.

На Институту за физику Београд запослена је 2015. године, као истраживач приправник у Лабораторији за 2Д-материјале у оквиру Центра за физику чврстог стања и нове материјале, где је првобитно била аганжована на националном пројекту “Физика уређених наноструктура и нових материјала у нанофотоници” ОИ171005, који је финансирало Министарство за просвету, науку и технолошки развој Републике Србије. У истраживачком раду бави се испитивањем могућности употребе 2Д-материјала, добијених ексфолијацијом из течне фазе, као претварача код биосензора, за детекцију/идентификацију биолошки молекули који би имали улогу биорецептора и/или анализита. Након прихваћеног предлога теме докторске дисертације, одлуком Научног већа Института за физику Београд, Јасна Вујин изабрана је 2019. године у звање истраживач сарадник. У априлу 2023. године изабрана је у звање стручни саветник.

Докторску дисертацију под називом *„Физичкохемијска карактеризација хетероструктура дводимензионалних материјала (графен, волфрам дисулфид) и биолошких молекула (цистеин, 1,2 дипалмитоли-sn-глицеро-3-фосфохолин)“* одбрањена је 26.9.2023. године на Факултету за физичку хемију, Универзитета у Београду.

Ангажована је на три билатерална пројекта између Србије и Аустрије. Јасна Вујин је ауторка/коауторка 7 научних радова са SCI-листе и 11 саопштења са међународних конференција штампаних у изводу.

2. ПРЕГЛЕД НАУЧНЕ АКТИВНОСТИ

Истраживачки рад у оквиру докторске дисертације представља експериментално проучавање интеракције танких филмова течне ексфолираних 2D материјала (графена и WS₂) и биолошких молекула (цистеина и DPPC) са којима чине хетероструктурни танки филм. С обзиром на то да се припрема хетероструктура изводила у амбијенталним условима и да су коришћени водени раствори биолошких молекула, испитивање утицаја молекула воде на структуру графенских и WS₂ филмова представља неизоставни део овог истраживања.

У првом делу рада приказана је ексфолијација 2D материјала (графен, WS₂), поступак формирања и депозиције филмова као и њихова физичка и хемијска карактеризација. Метода течне ексфолијације представља сонохемијску синтезу почетног материјала у растварачу (у овом случају коришћен је NMP (енгл. *N-methyl-2-Pyrrolidone*), омогућавајући добијање дисперзије монослојних и вишеслојних љуспица наноматеријала (графена и WS₂). Дисперзије су коришћене за припрему графенских филмова на граници фаза ваздух/вода и WS₂ филмова на граници фаза толуен/вода, док су се за њихову депозицију на одабране супстрате користиле Лангмир-Блоџет (енгл. *Langmuir-Blodgett*, LB) и Лангмир-Шефер (енгл. *Langmuir-Schaefer*, LS) технике. На основу резултата добијених испитивањем оптичких, морфолошких, структурних и хемијских својстава графенских и WS₂ филмова, применом UV/VIS (енгл. *Ultraviolet-Visible*) спектроскопије, скенирајуће електронске микроскопије (енгл. *Scanning Electron Microscopy*, SEM), микроскопије атомских сила (енгл. *Atomic Force Microscopy*, AFM) и Раманске спектроскопије, закључује се да су добијени компактни, хомогени, танки и транспарентни графенски и WS₂ филмови релативно великих димензија (величина филма одређена је величином површине међуфазне границе).

Такође, у овом делу истраживања испитиван је ефекат присуства молекула воде на хемијску структуру LPE-LB графенских и LPE-LS WS₂ филмова. За те потребе коришћена је фотоелектронска спектроскопија X зрачења (енгл. *X-ray Photoelectron Spectroscopy*, XPS), при чему су филмови излагани притиску водене паре од 1 mbar и 5 mbar, што одговара релативној влажности ваздуха околине од 4 и 22%, редом. На основу анализе XPS резултата, могуће је закључити да дефекти графенских и WS₂ филмова представљају активна места за адсорпцију молекула воде (било да је вода пореклом из атмосфере и/или да је компонента међуфазне границе) и њених дисосованих компоненти (H⁺ и OH⁻ јона). При минималном притиску водене паре (1 mbar) интеракција молекула воде и графена је елекстростатичке природе у којој графен има улогу донора електрона. Због своје поларне природе, молекули воде привлаче π делокализоване електроне графена што је праћено повећањем енергије везе електрона код C атома и смањењем енергије везе електрона код O атома. Такође, хемијски помераји сугеришу да кисеоничне функционалне групе на графенском филму активно учествују у интеракцији са молекулима H₂O, која се остварује кроз формирање водоничних веза. Повећањем притиска водене паре (на 5 mbar), молекули воде немају могућност директне адсорпције на површини графенског филма припремљеног Лангмир-Блоџет методом, већ се физисорбују на постојећи слој, формирајући тако додатне слојеве путем водоничних веза. У случају филма WS₂ припремљеног Лангмир-Шефер техником, услед излагања притисцима водене паре на 1 и 5 mbar, поред оксидације W⁵⁺ и физисорпције молекула воде као доминантног процеса, оксиди волфрама (WO₃, WO_{3-x}) имају улогу дефеката тј. постају потенцијална места за адсорпцију воде било у дисосованом или молекулском облику, услед чега долази до настајања додатних WO₃·nH₂O врста.

У другом и трећем делу докторске тезе приказана је припрема хетероструктура биолошки молекул/2D материјал методом накапавања (енгл. *drop casting*) и испитивање њихових физикохемијских својстава. Оптичка и скенирајућа електронска микроскопија примењена је како би се анализирале морфолошке и структурне карактеристике

хетероструктура: цистеин/графенски филм, цистеин/WS₂ филм, DPPC/графенски филм и DPPC/WS₂ филм. На основу добијених резултата утврђено је да биолошки молекули формирају танак филм који у потпуности прекрива површину танких филмова 2D-материјала. Агломерација цистеина и DPPC липида на ободу капи (енгл. *coffee ring effect*) и по површини графенских и WS₂ филмова је такође присутна.

За испитивање интеракције биолошких молекула са површином филмова 2D материјала коришћена је Раманска спектроскопија. Код хетероструктура са цистеином, интензивна интеракција тиолне групе са графенским и WS₂ филмом директно утиче на конформационе промене биолошког молекула. Односно, *trans* ротамери се јављају као доминантна конформација на површини графенских филмова, док је у случају WS₂ филмова то *gauche* конформација. Раскидање SH···O водоничних веза, чиме је омогућена интеракција графена са карбоксилном групом и формирање SH···C водоничних веза, настаје као последица физисорпције цистеина. С друге стране, код WS₂ филмова интеракција са аминок групом постаје знатно израженија.

Приликом формирања хетероструктура са DPPC молекулима долази до фаворизовања интеракција графенских односно WS₂ филмова са одређеним делом липида. Интеракција графена са хидрофобним делом молекула DPPC остварује се путем *van der Waals*-ових сила, при чему липиди на површини филма заузимају *trans* конформацију као доминантну. Ова интеракција доводи до преноса неелектрисања са графенског филма на липидне молекуле, с тим што је допринос молекула H₂O овом ефекту неопходно узети у обзир. Код хетероструктуре DPPC/LPE-LS WS₂, интеракција WS₂ филма се остварује са хидрофилним делом DPPC молекула успостављањем хемијске везе W–O–W, која се остварује између кисеоника фосфатне групе липидног молекула са атомом волфрама, било да је он дефинисан као ивични дефект или се налази у склопу WO_{3-x}. Наведене интеракције имају за последицу промене у хемијској и електронској структури филмова, омогућавајући тиме њихову употребу за детекцију одабраног фосфолипида. Такође, хетероструктуре DPPC/графенски филм и DPPC/WS₂ филм могу послужити као активне компоненте за селективну детекцију других биолошких молекула, зависно од њиховог афинитета везивања према хидрофилном или хидрофобном делу липида који остаје изузет у реакцији са графенским, односно WS₂ филмом.

Резултати овог истраживања су приказани у оквиру два рада са СЦИ листе и презентовани на шест конференције, при чему је више радова у припреми:

1. **J. Vujin**, W. Huang, J. Ciganović, S. Ptasinska, R. Panajotović, *Direct Probing of Water Adsorption on Liquid-Phase Exfoliated WS₂ Films Formed by the Langmuir–Schaefer Technique*, Langmuir 39, 8055–8064 (2023) DOI: 10.1021/acs.langmuir.3c00107
2. J. Pešić, **J. Vujin**, T. T. Ilić, M. Spasenović, R. Gajić, *DFT study of optical properties of MoS₂ and WS₂ compared to spectroscopic results on liquid phase exfoliated nanoflakes*, Optical and Quantum Electronics, 50:291 (2018) DOI: 0.1007/s11082-018-1553-6
3. **J. Vujin**, W. Huang, S. Ptasinska, R. Panajotovic, *Effects of water on thin films consisting of biomolecules and 2D-materials*, Seventh International Conference on Radiation and Applications in Various Fields of Research, RAD7, 10–14.06.2019, Herceg Novi, Montenegro,

(2019)p. 24

4. **J. Vujin**, M. Gilić, R. Panajotović,, „*Application of 2D-materials in building biomolecular heterostructures*”, Seventh International Conference on Radiation and Applications in Various Fields of Research, RAD7, 10–14.06.2019, Herceg Novi, Montenegro, (2019) p. 25
5. J. Pešić, **J. Vujin**, T.T Ilić, M. Spasenović, R. Gajić, *Ab-initio study of optical properties of MoS₂ and WS₂ compared to spectroscopic results of liquid phase exfoliated nanoflakes*, Photonica 2017, 28.8 - 1.9.2017., Belgrade, Serbia, (2017), p. 94
6. **J. Vujin**, R. Panajotović, *Modifications of lipid/2D-material heterostructures by SEM*, 28th Summer School and International Symposium on the Physics of Ionized Gases (SPIG 2016), 29. Aug - 2. Sep 2016, Belgrade, Serbia,(2016), p. 182
7. **J. Vujin**, Đ. Jovanović, R. Panajotović, *Physico-chemical characterization of lipid-2D materials self- assembly for biosensors*, The Fourth International Conference on Radiation and Applications in Various Fields of Research (RAD 2016), 23. - 27. May 2016, Niš, Serbia, (2016), p. 58
8. **J. Vujin**, Đ. Jovanović, R. Panajotović, *Electron-beam damage from SEM to lipid-(graphene, MoS₂, WS₂) heterostructures*, Fourth International Conference on Radiation and Applications in Various Fields of Research, RAD4, 23. – 27. May, 2016, Niš, Serbia (2016), p. 305

Поред истраживања која се односе на израду докторске тезе, кандидаткиња се бави истраживањима усмереним ка формирању и физичкохемијској карактеризацији са акцентом на испитивање електричних особина van der Waals органско/неорганских хетероструктура. Резултати овог истраживања публиковани су у раду и на конференцији:

1. A. Matković, M. Kratzer, B. Kaufmann, **J. Vujin**, R. Gajić, C. Teichert, *Probing charge transfer between molecular semiconductors and graphene*, Scientific Reports 7:9544,(2017) DOI: 10.1038/s41598-017-09419-3
2. A. Matković, M. Kratzer, J. Genser, B. Kaufmann, **J. Vujin**, R. Gajić, and C. Teichert, *Thin Film Growth of Organic Rod-Like Conjugated Molecules on 2D Materials*, NanoFIS2016 - 2nd international conference on functional integrated nano systems, 27-29.06.2016. Graz, Österreich (2016), p. 154

Експериментално научно истраживања кандидаткиње посвећено је и унапређивању постојећих особина графенских филмова са акцентом на побољшања електричних особина како би се испитала могућа примена LPE-LB графена као катодног односно анодног материјала. У ту сврху вршена је површинска модификације тј. хемијско допирање солима метала (литијумом и златом). Приликом формирања графенских филмова извршен је утицај на њихову радну

функцију. Приказано је да се коришћењем соли литијума врши п-допирање графена, док се р-допирање врши солима злата. Таквим једноставним начином хемијског допирања врши се утицај на радну функцију графена и омогућава да графенски филмови имају двојаку улогу и као катода и као анода. Опсег укупне промене радне функције износи 0.7 eV. Значај оваквог поступка допирања огледа се у побољшању ефикасности транспорта носиоца наелектрисања и смањења контактне отпорности, чиме се могу унапредити перформансе уређаја.

Резултати истраживања су публиковани у два рада и конференцијама:

1. Т. Tomašević, Ј. Pešić, I.R. Milošević, **J. Vujin**, А. Matković, М. Spasenović, R. Gajić, *Transparent and conductive films from liquid phase exfoliated graphene*, Optical and Quantum Electronics 48:319 (2016) DOI: 10.1007/s11082-016-0591-1
3. I.R. Milošević, В. Vasić, А. Matković, **J. Vujin**, S. Aškračić, М. Kratzer, Thomas Griesser, Christian Teichert, Radoš Gajić, *Single-step fabrication and work function engineering of Langmuir-Blodgett assembled few-layer graphene films with Li and Au salts*, Scientific Reports 10, 10:8476(2020) DOI: 10.1038/s41598-020-65379-1
4. T.T Ilić, Ј. Pešić, I. Milošević, **J. Vujin**, А. Matković М. Spasenović, R. Gajić, *Transparent and conductive films from liquid phase exfoliated graphene*, Photonica 2015, 24. - 28. August, Belgrade, Serbia, (2015), p. 191
5. I. R. Milošević, В. Vasić, А. Matković, **J.Vujin**, R. Gajić, *Liquid-phase Exfoliation of graphene and chemical doping of Langmuir-Blodgett assembled graphene films*, The 20th Symposium on Condensed Matter Physics-SFKM 2019, 7-11.10.2019., Belgrade, Serbia, (2019) p. 55;
6. I. R. Milošević, В. Vasić, А. Matković, **J. Vujin**, S. Aškračić, C. Teichert and R. Gajić, *Chemical doping of Langmuir-Blodgett assembled few-layer graphene films with Au and Li salts aimed for optoelectronic applications*, Photonica 2019, 26-30.08.2019., Belgrade, Serbia, (2019) p. 101;

Такође, кандидаткиња се бави истраживањима која обухватају примену танких LPE-LB графенских филмова за пречишћавање воде од тешких метала, конкретно Pb^{2+} . Поступак функционализације површине графенских филмова вршено је наночестицама Fe са циљем да се индукују локални магнетни домени. Резултати истраживања су потврдили да у поређењу са немодификованим графенским филмом, који нема детектабилног магнетног одговора, МФМ фазне слике модификованог показују јаку разлику фазног помака у поређењу са супстратом ($\sim 0,2^\circ$), што указује на присуство локалног магнетног момента. Резултати XPS мерења указују да модификовани LPE-LB графенских филмови имају могућност детекције и адсорпције јона Pb^{2+} из водених раствора, што је приказано на конференцији:

1. I.R. Milošević, **J. Vujin**, M.Z. Khan, T. Griesser, C. Teichert, T.T Ilić, *Fe-nanoparticle-modified Langmuir-Blodgett Graphene Films for Pb(II) Water Purification*, The 21th Symposium on Condensed Matter Physics-SFKM 2023, 26-30.06.2023., Belgrade, Serbia, (2023) p. 87

У сарадњи са Стоматолошким факултетом, кандидаткиња учествује у истраживањима везаним за испитивање утицаја механичких особина и морфологије површине супстрата-танки филмови 2Д-материјала као имплантибилне композитне структуре, на процесе пролиферације и диференцијације депонованих матичних ћелија из зуба.

Резултати ових истраживања публиковани су у радовима:

1. J. Simonovic, B. Toljic, M. Lazarevic, M. M. Markovic, M. Peric, **J. Vujin**, R. Panajotovic and J. Milasin, *The Effect of Liquid-Phase Exfoliated Graphene Film on Neurodifferentiation of Stem Cells from Apical Papilla*, Nanomaterials 12:3116 (2022) DOI: [10.3390/nano12183116](https://doi.org/10.3390/nano12183116)
2. J. Simonovic, B. Toljic, N. Nikolic, M. Peric, **J. Vujin**, RadmilaPanajotovic, Rados Gajic, Elena Bekyarova, Amelia Cataldi, Vladimir Parpura, Jelena Milasin, *Differentiation of stem cells from apical papilla into neural lineage using graphene dispersion and single walled carbon nanotubes*, Journal of Biomedical Materials Research Part A, 106, 2653-2661 (2018) DOI: [10.1002/jbm.a.36461](https://doi.org/10.1002/jbm.a.36461)

3. ЕЛЕМЕНТИ ЗА КВАЛИТАТИВНУ ОЦЕНУ НАУЧНОГ ДОПРИНОСА

3.1. Квалитет научних резултата

а. 3.1.1. Значај научних резултата

У свом досадашњем раду, др Јасна Вујин је објавила укупно седам радова: три рада категорије M21, три рада категорије M22 и један рад категорије M23.

Најзначајнији рад кандидаткиње је:

J. Vujin, W. Huang, J. Ciganović, S. Ptasinska, R. Panajotović, *Direct Probing of Water Adsorption on Liquid-Phase Exfoliated WS₂ Films Formed by the Langmuir–Schaefer Technique*, Langmuir 39, 8055–8064 (2023) DOI: [10.1021/acs.langmuir.3c00107](https://doi.org/10.1021/acs.langmuir.3c00107)

Истраживачки рад представља експериментално проучавање утицаја молекула воде на структуру танких филмова течно екслоираног WS₂. Филмови WS₂, формиран на међуфазној граници толуен/вода и депоновани на одабране супстрате применом Лангмир –Блоџет методе излагани су воденој пари при притиску од 1 и 5 mbar. Резултати указују да осим физисорпције молекула воде, као доминантног процеса, долази и до процеса оксидације W⁵⁺ у W⁶⁺ праћеног формирањем додатних WO₃·nH₂O врста. Осетљивост LPE-LS WS₂ филмова на присуство молекула воде указује на њихову потенцијану могућност примене као активне компоненте код сензора за мерење влажности. Такође, добија се увид о доприносу молекула H₂O, када се испитује интеракција водених раствора биолошких молекула и LPE-LS WS₂ филмова.

б. 3.1.2. Цитираност научних радова кандидата

Према бази Web of Science на дан 02.10.2023. године, радови кандидаткиње су цитирани укупно 86 пута, без самоцитата 80 пута. Према истој бази, Хиршов индекс кандидаткиње је 5.

с. 3.1.3. Параметри квалитета радова и часописа

Кандидаткиња др Јасна Вујин је објавила укупно седам радова у међународним часописима и то:

- **Три рада М21:**
 1. Scientific Reports (ИФ2017=4.12, СНИП2017=1.27)
 2. Journal of Biomedical Materials Research Part A, (ИФ2018=3.22, СНИП2018=0.96)
 3. Scientific Reports (ИФ2020=4.38, СНИП2020=1.37)

- **Три рада М22:**
 1. Optical and Quantum Electronics (ИФ2016=1.06, СНИП2016=0.62)
 2. Nanomaterials (ИФ2022=5.23, СНИП2022=1.06)
 3. Langmuir (ИФ2022=3.90, СНИП2022=0.93)

- **Један рад М23**
 1. Optical and Quantum Electronics, (ИФ2018=1.55, СНИП2018=0.66)

Библиометарски показатељи су сумирани у наредној табели

	ИФ	М	СНИП
Укупно	19.29	42	6.87
Усредњено по чланку	2.76	6	0.98
Усредњено по аутору	3.36	5.9	0.99

3.1.4. Елементи применљивости научних резултата

Експериментална истраживања др Јасне Вујин, која обухватају синтезу 2Д материјала, формирање и физичко хемијску карактеризацију филмова 2Д материјал насталих методом течне ексфолијације имају за циљ испитивање њихове примене као потенцијаних активних платформи- саставних делова биосензорских уређаја.

3.2. Нормирање броја коауторских радова, патената и техничких решења

Кандидаткиња је публиковала три рада у М21 категорији (први има 9 аутора, други 11 и трећи 6), три рада у М22 категорији (први има 5 аутора, други 8 и трећи 7 аутора) и један рад у М23 (5 аутора).

3.3 Учешће у пројектима, потпројектима и пројектним задацима

Др Јасна Вујин учествовала је на два билатерална пројекта између Србије и Аустрије: „Физика уређених наноструктура и нових материјала у нанофотоници“ (2018-2021) и „Моделирање и мерење фазних прелаза и оптичких особина перовскита“ (2018-2021).

Тренутно је ангажована на билатералном пројекту између Србије и Аустрије: „Модулација магнетних особина самоорганизујућих графенских филмова за пречишћавање отпадних вода“ (2022-2024)

3.4 Утицај научних резултата

Утицај научних резултата кандидаткиње се огледа у броју цитата који су наведени у тачки 3.1.2 овог прилога, као и у прилогу о цитираности. Значај резултата кандидаткиње је такође описан у тачки 3.1.1.

3.5 Конкретан допринос кандидаткиње у реализацији радова у научним центрима у земљи и иностранству

Кандидаткиња је све своје истраживачке активности реализовала у Лабораторији за 2Д материјала у оквиру Центра за физику чврстог стања и нове материјале на Институту за физику Београд. Свој допринос током истраживања дала је у припреми 2Д материјала, усавршавању технике формирања и депозиције филмова течно екслолираних 2Д материјала као и у њиховој физичко хемијској карактеризацији, анализи и интерпретацији добијених резултата, као и писању радова.

4. ЕЛЕМЕНТИ ЗА КВАНТИТАТИВНУ ОЦЕНУ НАУЧНОГ ДОПРИНОСА

Остварен број М бодова по категоријама публикација

Категорија	М-бодова по публикацији	Број публикација	Укупно М бодова (нормирано)
M21	8.0	3	24 (18.14)
M22	5	3	15 (14.12)
M23	3.0	1	3
M33	1.0	1	1
M34	0.5	9	4.5
M64	0.2	1	0.2
M70	6	1	6

Поређење са минималним квантитативним условима за избор у звање научни сарадник

	Потребно	Остварено (нормирано)
Укупно	16	85(71.52)
M10+M20+M31+M32+M33+M41+M42	10	43(36.26)
M11+M12+M21+M22+M23	6	42(35.26)

5. СПИСАК ПУБЛИКАЦИЈА

Радови у врхунским међународним часописима (M21)

1. A. Matković, M. Kratzer, B. Kaufmann, **J. Vujin**, R. Gajić, C. Teichert, *Probing charge transfer between molecular semiconductors and graphene*, Scientific Reports 7:9544, (2017) DOI: 10.1038/s41598-017-09419-3
2. J. Simonovic, B. Toljic, N. Nikolic, M. Peric, **J. Vujin**, Radmila Panajotovic, Rados Gajic, Elena Bekyarova, Amelia Cataldi, Vladimir Parpura, Jelena Milasin, *Differentiation of stem cells from apical papilla into neural lineage using graphene dispersion and single walled carbon nanotubes*, Journal of Biomedical Materials Research Part A, 106, 2653-2661 (2018) DOI: 10.1002/jbm.a.36461
3. I.R. Milošević, B. Vasić, A. Matković, **J. Vujin**, S. Aškračić, M. Kratzer, Thomas Griesser, Christian Teichert, Radoš Gajić, *Single-step fabrication and work function engineering of Langmuir-Blodgett assembled few-layer graphene films with Li and Au salts*, Scientific Reports 10, 10:8476 (2020) DOI: 10.1038/s41598-020-65379-1

Радови у истакнутим међународним часописима (M22)

1. T. Tomašević, J. Pešić, I.R. Milošević, **J. Vujin**, A. Matković, M. Spasenović, R. Gajić, *Transparent and conductive films from liquid phase exfoliated graphene*, Optical and Quantum Electronics 48:319 (2016) DOI: 10.1007/s11082-016-0591-1
2. J. Simonovic, B. Toljic, M. Lazarevic, M. M. Markovic, M. Peric, **J. Vujin**, R. Panajotovic and J. Milasin, *The Effect of Liquid-Phase Exfoliated Graphene Film on Neurodifferentiation of Stem Cells from Apical Papilla*, Nanomaterials 12:3116 (2022) DOI: 10.3390/nano12183116
3. **J. Vujin**, W. Huang, J. Ciganović, S. Ptasinska, R. Panajotović, *Direct Probing of Water Adsorption on Liquid-Phase Exfoliated WS₂ Films Formed by the Langmuir–Schaefer Technique*, Langmuir 39, 8055–8064 (2023) DOI: 10.1021/acs.langmuir.3c00107

Радови у међународним часописима (M23)

1. J. Pešić, **J. Vujin**, T. T. Ilić, M. Spasenović, R. Gajić, *DFT study of optical properties of MoS₂ and WS₂ compared to spectroscopic results on liquid phase exfoliated nanoflakes*, Optical and Quantum Electronics, 50:291 (2018) DOI: 10.1007/s11082-018-1553-6

Саопштење са скупова међународног значаја штампаног у целости (M33)

1. **J. Vujin**, Đ. Jovanović, R. Panajotović, *Electron-beam damage from SEM to lipid-(graphene, MoS₂, WS₂) heterostructures*, Fourth International Conference on Radiation and Applications in Various Fields of Research, RAD4, 23. – 27. May, 2016, Niš, Serbia (2016), p. 305

Саопштење са скупова међународног значаја штампаног у изводу (M34)

1. T. Tomašević-Ilić, J. Pešić, I. Milošević, **J. Vujin**, A. Matković, M. Spasenović, R. Gajić, *Transparent and conductive films from liquid phase exfoliated graphene*, Photonica 2015, 24. -

28. August, Belgrade, Serbia, (2015), p. 191
2. **J. Vujin**, R. Panajotović, *Modifications of lipid/2D-material heterostructures by SEM*, 28th Summer School and International Symposium on the Physics of Ionized Gases (SPIG 2016), 29. Aug - 2. Sep 2016, Belgrade, Serbia,(2016), p. 182
 3. **J. Vujin**, Đ. Jovanović, R. Panajotović, *Physico-chemical characterization of lipid-2D materials self- assembly for biosensors*, The Fourth International Conference on Radiation and Applications in Various Fields of Research (RAD 2016), 23. - 27. May 2016, Niš, Serbia, (2016), p. 58
 4. A. Matković, J. Genser, B. Kaufmann, **J. Vujin**, B. Vasić, R. Gajić, and C. Teichert, *Epitaxy of highly ordered conjugated organic semiconductor crystallite networks on graphene based devices*, ICSFS18 - 18th International Conference on Solid Films and Surfaces, 27.08.-03.09.2016. Chemnitz, Germany, (2016), p154.
 5. J. Pešić, **J. Vujin**, T.Tomašević-Ilić, M. Spasenović, R. Gajić, *Ab-initio study of optical properties of MoS₂ and WS₂ compared to spectroscopic results of liquid phase exfoliated nanoflakes*, Photonica 2017, 28.8 - 1.9.2017., Belgrade, Serbia, (2017), p. 94
 6. **J. Vujin**, W. Huang, S. Ptasinska, R. Panajotovic, *Effects of water on thin films consisting of biomolecules and 2D-materials*, Seventh International Conference on Radiation and Applications in Various Fields of Research, RAD7, 10–14.06.2019, Herceg Novi, Montenegro, (2019)p. 24
 7. **J. Vujin**, M. Gilić, R. Panajotović,,*Application of 2D-materials in building biomolecular heterostr-uctures*”, Seventh International Conference on Radiation and Applications in Various Fields of Research, RAD7, 10–14.06.2019, Herceg Novi, Montenegro, (2019) p. 25
 8. I. R. Milošević, B. Vasić, A. Matković, **J. Vujin**, S. Aškračić, C. Teichert and R. Gajić, *Chemical doping of Langmuir-Blodgett assembled few-layer graphene films with Au and Li salts aimed for optoelectronic applications*, Photonica 2019, 26-30.08.2019., Belgrade, Serbia, (2019) p. 101;
 9. I.R. Milošević, **J. Vujin**, M.Z. Khan, T. Griesser, C. Teichert, T. Tomašević-Ilić, *Fe-nanoparticle-modified Langmuir-Blodgett Graphene Films forPb(II) Water Purification*, The 21th Symposium on Condensed Matter Physics-SFKM 2023, 26-30.06.2023., Belgrade, Serbia, (2023) p. 87

Саопштење са скупова националног значаја штампаног у изводу (M64)

1. I. R. Milošević, B. Vasić, A. Matković, **J.Vujin**, R. Gajić, *Liquid-phase Exfoliation of graphene and chemical doping of Langmuir-Blodgett assembled graphene films*, The 20th Symposium on Condensed Matter Physics-SFKM 2019, 7-11.10.2019., Belgrade, Serbia, (2019) p. 55;

Одбрањена докторска дисертација (M70)

1. Јасна Вујин, „Физичкохемијска карактеризација хетероструктура дводимензионалних материјала (графен, волфрам дисулфид) и биолошких молекула (цистеин, 1,2 дипалмитоли-sn-глицеро-3-фосфохолин)”, Факултет за физичку хемију, Универзитет у Београду.



OPEN

Single-step fabrication and work function engineering of Langmuir-Blodgett assembled few-layer graphene films with Li and Au salts

Ivana R. Milošević¹✉, Borislav Vasić¹, Aleksandar Matković²✉, Jasna Vujin¹, Sonja Aškrić³, Markus Kratzer², Thomas Griesser⁴, Christian Teichert² & Radoš Gajić¹

To implement large-area solution-processed graphene films in low-cost transparent conductor applications, it is necessary to have the control over the work function (WF) of the film. In this study we demonstrate a straightforward single-step chemical approach for modulating the work function of graphene films. In our approach, chemical doping of the film is introduced at the moment of its formation. The films are self-assembled from liquid-phase exfoliated few-layer graphene sheet dispersions by Langmuir-Blodgett technique at the water-air interfaces. To achieve a single-step chemical doping, metal standard solutions are introduced instead of water. Li standard solutions (LiCl, LiNO₃, Li₂CO₃) were used as n-dopant, and gold standard solution, H(AuCl₄), as p-dopant. Li based salts decrease the work function, while Au based salts increase the work function of the entire film. The maximal doping in both directions yields a significant range of around 0.7 eV for the work function modulation. In all cases when Li-based salts are introduced, electrical properties of the film deteriorate. Further, lithium nitrate (LiNO₃) was selected as the best choice for n-type doping since it provides the largest work function modulation (by 400 meV), and the least influence on the electrical properties of the film.

Graphene, consisting of a single layer carbon arranged in a hexagonal lattice, has attracted extensive interest because of the excellent mechanical and electrical properties associated with its two dimensional structure¹⁻⁴. Chemical vapor deposition (CVD) method has become the most common method for production of large-area graphene films⁵. Still, simple and low-cost methods are needed for mass production especially when considering the cases where high-quality films are not needed for the desired functionality, as in low-power lighting, sensors, transparent heating, and de-icing applications⁶. In that context, liquid-phase exfoliation (LPE) is a perspective way of obtaining large quantities of exfoliated graphite in solution. LPE of graphite results in a dispersion of few-layer graphene sheets (GSs) in the solvent. However, in order to access the full potential of LPE-processed graphene, thin-films needs to be controllably fabricated utilizing techniques capable to introduce self-ordering of GSs⁷. One such example is Langmuir-Blodgett assembly (LBA). Based on surface-tension induced self-assembly of nanoplatelets at the liquid-air interface or the interface of two liquids, LBA is a good method for production of large-scale, highly transparent, thin solution-processed graphene films⁸⁻¹¹.

Excellent electrical conductivity, flexibility and transparency in the visible domain make graphene a natural choice for ultrathin, flexible and transparent electrodes in electronic devices^{10,12-19}. Still, a significant work function difference between graphene and frequently employed active layers of photovoltaic and light-emitting diode (LED) devices gives rise to a high contact resistance. Contact resistance can have a significant impact on overall efficiency and performance of the devices²⁰. This is of a particular technological relevance considering that any realistic application of graphene based transparent electrode must compete against those based on indium tin

¹Laboratory for Graphene, other 2D Materials and Ordered Nanostructures of Center for Solid State Physics and New Materials, Institute of Physics, University of Belgrade, Pregrevica 118, 11080, Belgrade, Serbia. ²Institute of Physics, Montanuniversität Leoben, Franz Josef Str. 18, 8700, Leoben, Austria. ³Nanostructured Matter Laboratory of Center for Solid State Physics and New Materials, Institute of Physics, University of Belgrade, Pregrevica 118, 11080, Belgrade, Serbia. ⁴Institute of Chemistry of Polymeric Materials, Montanuniversität Leoben, Otto-Gloeckel-Strasse 2, 8700, Leoben, Austria. ✉e-mail: novovic@ipb.ac.rs; aleksandar.matkovic@unileoben.ac.at

oxide (ITO) or fluorine-doped tin oxide (FTO), which have already gone through decades of interfacial optimization in order to deliver today's performance^{21–23}. Therefore, the understanding of the efficient ways for modulation of the graphene work function is crucial for improving device performances^{21,22,24}. In order to enhance the charge injection, the work function of the graphene electrode should be optimized to better match WF of the adjacent layer in order to form an ohmic contact²⁴.

Recently, the chemical doping has been reported to be an effective method for doping of CVD graphene and tuning its work function by charge transfer between the graphene sheet and metal salts, organic dopants, or metal oxide layers^{12,14,21–28}. Such surface charge transfer induced by chemical doping is expected to efficiently control the Fermi level of graphene sheets without introducing substitutional impurities or basal plane reactions, thus, preventing any damage to the carbon networks and not introducing scattering centres that would lower carrier mobility²¹. Kwon *et al.* reported n-type chemical doping of CVD graphene with alkali metal carbonates by soaking in appropriate solutions²³ and alkali metal chlorides by spin-coating of appropriate solutions on the transferred graphene substrates²⁵. So far, doping of Langmuir-Blodgett graphene films prepared from LPE dispersions has been done with nitric acid and ozone after the film was formed using the drop-casting method and UV/ozone treatment^{9,29}. Chemical doping is especially attractive for LPE-based graphene films since many exposed edges of GSs are expected to enable very efficient functionalization through charge transfer doping. However, the chemical doping with metal salt solutions has not been used to control the work function of LBA graphene films so far. In this work LBA graphene films obtained from LPE dispersion were doped during the process of film formation. Therefore, the formation and doping of the LBA graphene films in our work represent a single-step process. This is a significant improvement compared to previous works where the chemical doping was applied only after the graphene fabrication.

In the present work, we systematically investigated single-step work function modulation (increase and decrease) of the LPE GS films achieved by chemical doping. In particular, using Li standard solutions (LiCl, LiNO₃ and Li₂CO₃) as n-dopant, and gold standard solution H(AuCl₄) as p-dopant was investigated. In contrast to previous methods for chemical doping of CVD graphene which can be applied only after the graphene films fabrication, here we described the method for the production and doping of LPE graphene films in a single-step. Single-step work function modulation means doping of the film at the moment of its formation from the LPE graphene dispersion by LBA technique at the air-metal standard solution interface. We have demonstrated tunability of the WF in the range of almost 1 eV, making these metal-salt treated LPE-based graphene electrodes suitable candidates for both electron and hole injection interfaces.

Results and discussion

Morphology of LPE GS films. Fabrication and doping of the GS films is schematically represented in Fig. 1(a): air-metal standard solution interface, introduction of LPE dispersion and formation of the LPE GS film at the interface, scooping of the doped film on the target substrate and finally, obtained doped LPE GS film which is further investigated with different techniques.

Morphology of LPE GS films is depicted in Fig. 1 consisting of both optical (Fig. 1(b1–f1)) and Atomic Force Microscopy (AFM) topographic images (Fig. 1(b2–f2)) for both undoped and metal doped LPE GS films. As can be seen from AFM images, the doping process does not change morphology of LPE films, except that the doped films contain more agglomerates (visible as bright particle-like domains). The following values for the surface roughness were obtained by AFM measurements averaged on ten 50 × 50 μm² areas: (a) 11.9 ± 1.5 nm for undoped LPE GS film, (b) 11.5 ± 3.5 nm for Li₂CO₃ doped, (c) 13.3 ± 2 nm for H(AuCl₄) doped, (d) 13.7 ± 1.6 nm for LiCl doped, and (e) 13.8 ± 1.2 nm for LiNO₃ doped LPE GS films. Therefore, the surface roughness slightly increases by around 2 nm after the doping, while for Li₂CO₃ doped LPE GS film is practically the same as for the undoped film. Still, optical images recorded on larger scale depict formation of agglomerates in doped films which could degraded their optical (leading to an increased scattering and/or absorption of incoming lights on these clusters) and electrical properties (due to enhanced scattering of charge carriers).

The observed formation of the agglomerates is most likely not an inherent property of the particular metal-salt doping. Overcoming this would likely require further optimization of the LBA process. However, as a benchmark the LBA process in this study was optimized for an undoped film and was left unchanged for all of the metal-salt doped films.

Transmittance measurements. Using the different doping metal standard solution during LBA of graphene films was found to result in different transparency. In the UV region, the transmittance of graphene is dominated by an exciton-shifted van Hove peak in absorption^{9,30}. Transmittance at 550 nm was 82% for undoped and 80%, 76%, 74%, 68% for H(AuCl₄), LiCl, LiNO₃, Li₂CO₃ doped LPE GS films, respectively (Fig. 2). It can be seen that transmittance decreases for doped LPE GS films. Metal salts decrease the transmittance of the graphene films regardless the type of the present metal (gold or lithium). The degree of the transmittance decrease was related to not only the metal cations but also the anions. Different lithium salts decrease transmittance in different amounts. Transmittance decrease of 14% was the highest for the LPE GS film doped with lithium carbonate (Li₂CO₃). Similar results of the transmittance decrease for metal doped CVD graphene films were obtained in studies of Kwon *et al.*^{22,23,25}. Transmittance decrease could be a consequence of the metal particles adsorption and agglomeration on doped films after the solvent evaporation process. Changes in the thickness of LPE GS films with doping could not be excluded because LBA process in this study was optimized for an undoped film and was left unchanged for all of the metal-salt doped films.

Raman measurements. Raman spectra for undoped and H(AuCl₄), LiCl, LiNO₃, Li₂CO₃ doped LPE GS films are given in Fig. 3(a). The four basic graphene/graphite peaks D (~1348 cm⁻¹), G (~1579 cm⁻¹), D' (1614

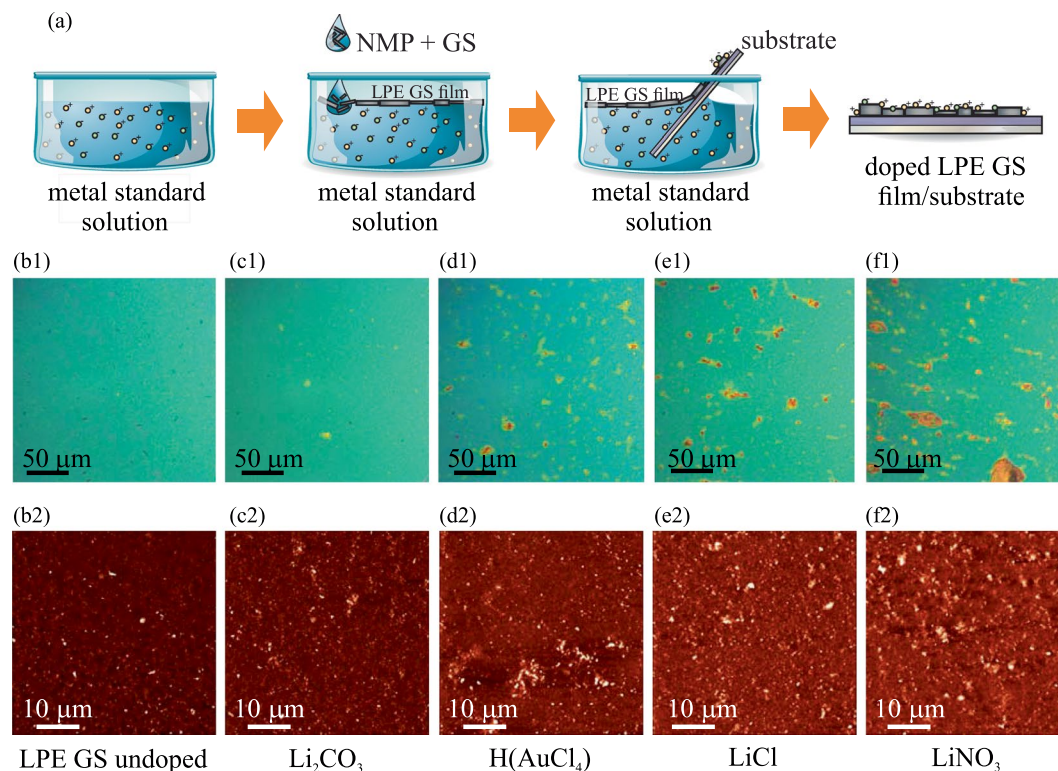


Figure 1. (a) Schematic representation of the LPE GS film formation and its doping in the single-step process. (b1–f1) Optical images are shown in the top row, whereas (b2–f2) AFM topographic images are shown in the bottom row for the following cases: (b) undoped LPE GS film, and (c) Li₂CO₃, (d) H(AuCl₄), (e) LiCl, (f) LiNO₃ doped LPE GS films. z-scale in all AFM images is 100 nm.

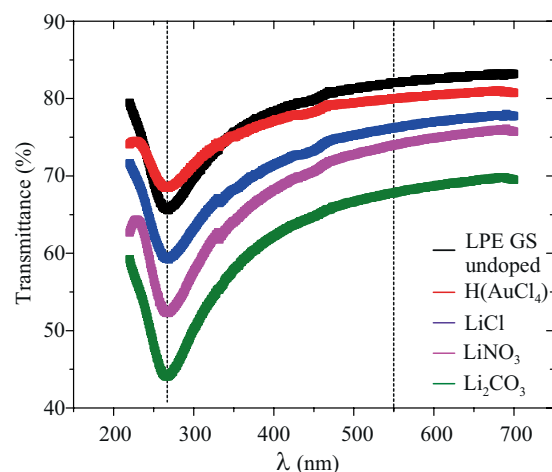


Figure 2. Transmittance spectra of undoped and H(AuCl₄), LiCl, LiNO₃, Li₂CO₃ doped LPE GS films.

cm⁻¹) and 2D (2700 cm⁻¹) are observed for all the samples. No significant shifts of any characteristic Raman peaks of graphene were detected after chemical doping (Fig. 3(a)).

The change of the full width at half-maximum (FWHM) of the Raman spectra after doping with metal standard solutions was negligible Fig. 3(b). The only notable change of the Raman spectra was the increase of the intensity ratio of D to G peaks, I(D)/I(G) (Fig. 3(c)). The quantity of defects has been shown to be related to the ratio between the D and G peaks, I(D)/I(G); the larger the ratio, the larger the defect density³¹. We observe increase of the defect density with H(AuCl₄), LiCl, LiNO₃, Li₂CO₃ doping in relation to the undoped film and the amount of the increase expressed in percent was 37%, 24%, 29% and 21%, respectively.

All self-assembled films suffer from a large defect density that often leads to a high sheet resistance of deposited film. Therefore, the nature and density of defects in any thin film transparent conductor is important, especially when chemical treatment was used to enhance films' performance. The intensity ratio between the D and

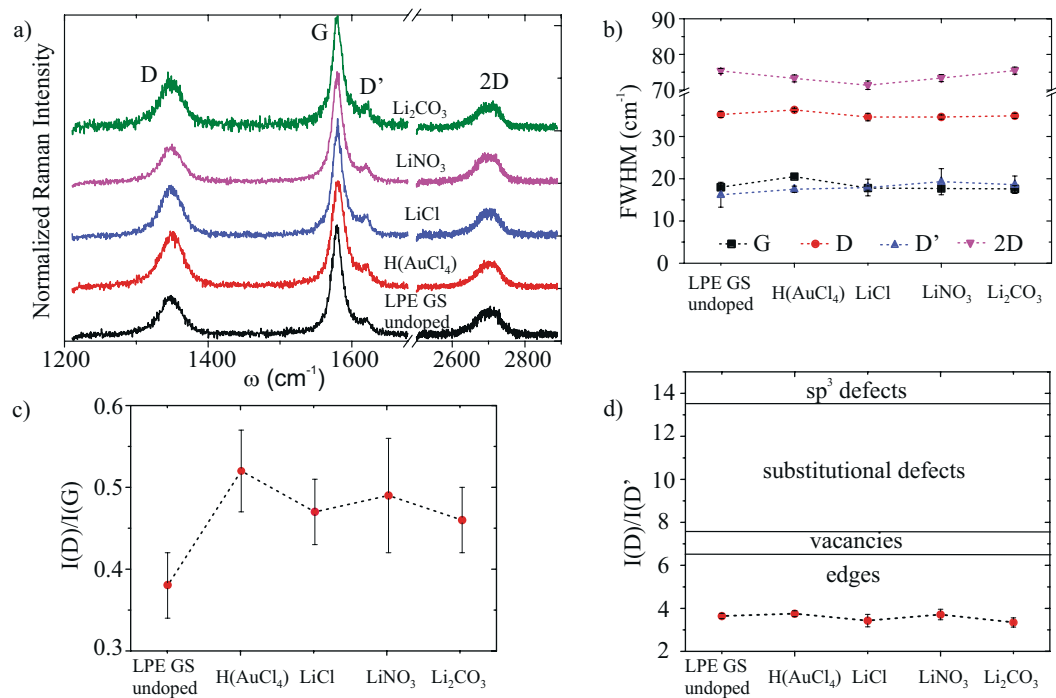


Figure 3. (a) Raman spectra of the undoped LPE GS film and films doped with Li and Au salts, (b) FWHM of the four basic Raman peaks (c) The intensity ratio of D to G peak for different doping metal salts, $I(D)/I(G)$, (d) The intensity ratio of D to D' peak, $I(D)/I(D')$, for different doping metal salts. We refer to peak intensity as the height of the peaks as proposed by Eckmann *et al.*³²

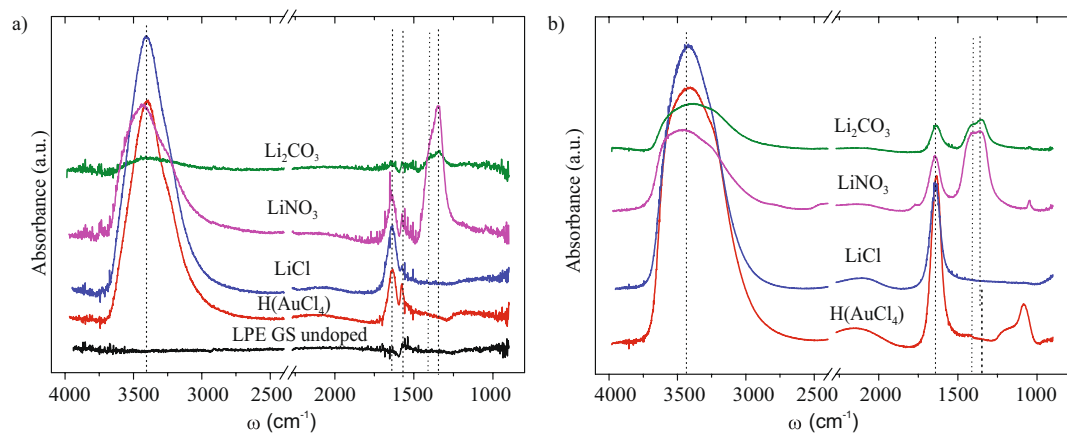


Figure 4. FT-IR spectra of (a) undoped and H(AuCl₄), LiCl, LiNO₃, Li₂CO₃ LPE GS doped films, (b) metal standard solutions (0.1 mg/mL) used for doping processes.

D' peak can be used to get information on the nature of defects in graphene^{32,33}. $I(D)/I(D')$ was calculated, and the obtained results were presented in Fig. 3(d). Topological defects (like pentagon-heptagon pairs), boundaries, vacancies, substitutional impurities and sp^3 defects are possible defects in graphene³¹. Studies reporting a ratio of 3.5 for boundaries, 7 for vacancies, 13 for sp^3 and values in-between those for vacancies and sp^3 for substitutional impurities can be found in the literature^{31,32,34}. From Fig. 3(d) it can be observed that the D to D' intensity peak ratio is nearly constant in our samples regardless of the doping solution, and the value of the ratio indicates that the edges are the dominant type of defects in our LPE GS films.

Fourier transform infrared absorbance (FT-IR) measurements. FT-IR spectra of undoped and LiCl, LiNO₃, Li₂CO₃, H(AuCl₄) doped LPE GS films, as well as FT-IR spectra of corresponding metal standard solutions are shown in Fig. 4.

For the undoped LPE GS film FT-IR spectra is simple. It can be seen only a small peak assignable to C=C skeletal vibration^{35–37} of the graphene basal planes at $\sim 1560\text{ cm}^{-1}$. This peak can also be seen in FT-IR spectra for

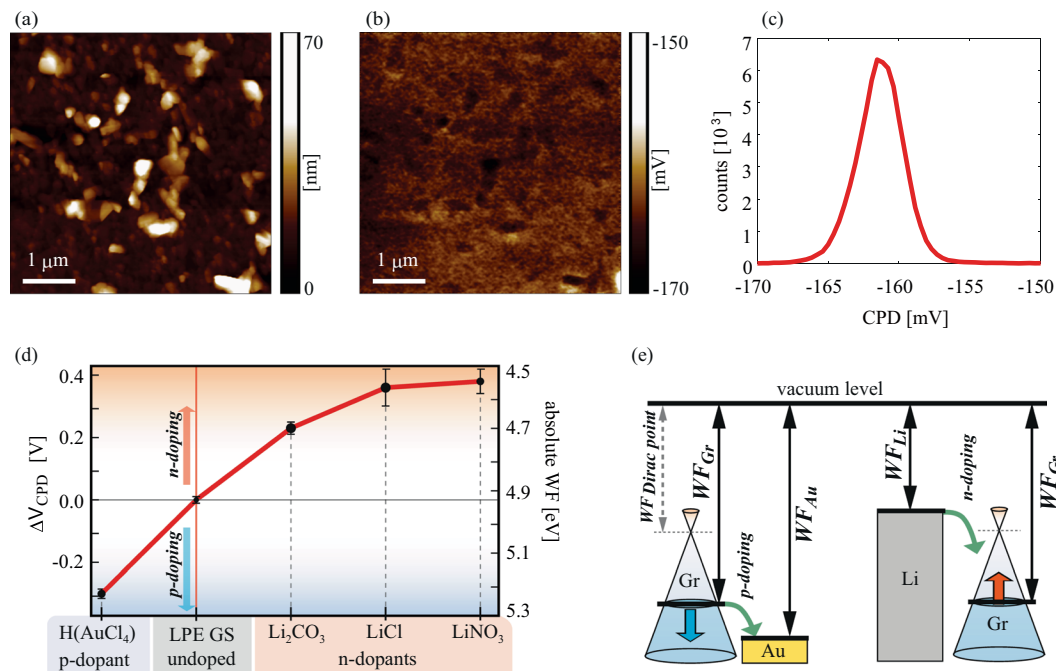


Figure 5. (a) AFM topography, (b) CPD map measured by KPFM, and (c) histogram of (b) shown for H(AuCl₄) doped LPE GS film as an example. (d) Change in WF for doped LPE GS films for different dopants, in comparison to the undoped LPE GS film. Solid red line in (d) is only a guide for the eye. (e) Schematic representation of the work functions prior to the interaction (equal vacuum levels) for Au-based salt/graphene and Li-based salt/graphene. The green arrows indicate direction of electron flow showing that in the case of Li (Au) based salts, electrons are transferred to (from) graphene.

all investigated doped films at the same wavenumber indicating that graphene basal planes were not interrupted by doping. The strong peak at around $\sim 3400\text{ cm}^{-1}$ and another, smaller one, near $\sim 1630\text{ cm}^{-1}$ can be seen in all doped LPE GS films (Fig. 4(a)) and corresponding metal standard solutions (Fig. 4(b)). They are attributed to the water molecules and are assignable to the O-H stretching vibrations ($\sim 3400\text{ cm}^{-1}$) and H-O-H bending mode ($\sim 1630\text{ cm}^{-1}$)^{38,39}. In the case of FT-IR spectra for LPE GS film doped with LiNO₃ the peak at $\sim 1340\text{ cm}^{-1}$ and $\sim 1390\text{ cm}^{-1}$ are assignable to the vibration mode of the NO₃⁻ ions and asymmetric stretch of O-NO₂, respectively^{38,40}. Similar vibration modes can be observed in the case of FT-IR spectra for LPE GS film doped with Li₂CO₃ and can be assigned to the vibration mode of the CO₃⁻ ions (1340 cm^{-1}) and asymmetric stretch of O-CO₂ ($\sim 1390\text{ cm}^{-1}$)⁴¹. The same vibrational modes could be seen for LiNO₃ and Li₂CO₃ standard solutions (Fig. 4(b)).

From the observed FT-IR results (Fig. 4(a)) it is clear that additional peaks appear with LPE GS film chemical doping. These additional peaks match with vibrational modes of the anions in solution (Fig. 4(b)). Considering that no new peaks are visible in the given spectra (which would indicate the formation of chemical bonds) the present peaks could be a consequence of the metal salts adsorption to the graphene lattice during the doping. In order to understand Li and Au doping mechanisms XPS measurements were performed and they are presented in separate section.

Work function modulation. Results for the work function dependent on the different metal standard solution used in the LBA process are summarized in Fig. 5. The top row depicts an example with the topography (Fig. 5(a)), corresponding contact potential difference (CPD) map measured by Kelvin probe force Microscopy-KPFM (Fig. 5(b)), and the histogram of the CPD distribution measured on H(AuCl₄) doped graphene film (Fig. 5(c)). The histogram is characterized with a single peak, which is used for the averaging and calculation of the absolute value of work function. The same procedure was done for all considered films. More details about the measurements of CPD and WF calculations are given in Supplementary information in Supplementary Figs. S3-S5. As a result, the values of the absolute work function are presented in Fig. 5(d) for both, doped and undoped LPE GS films. As can be seen, n-doping of graphene films is achieved by Li-based salts, whereas Au-based salt leads to p-doping.

The change of the WF due to the doping can be explained according to the schematic presentation in Fig. 5(e), illustrating that Li (Au) as a lower (higher) work function material compared to GS films. Therefore, presence of Li-based salts into the graphene film results in a reduction of the work function of the entire film. This behavior can be interpreted as an increase in the Fermi level of GSs – compared to the value for the undoped films – indicating predominantly a charge transfer from Li-based salts to graphene (n-doping), as expected when considering that Li has lower WF than graphene (graphite). In contrast to Li-based salts, the Au-based salt shows an opposite trend for the relative change of the work function. This indicates charge transfer from graphene to

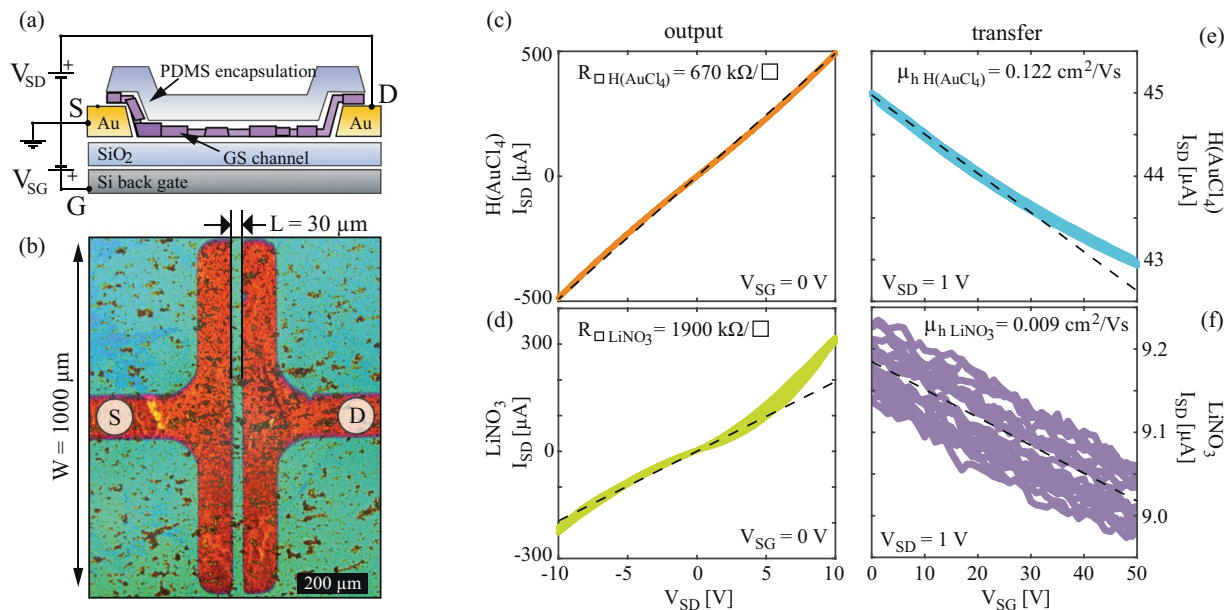


Figure 6. (a) Schematic cross-section of the bottom-contacted back-gated FET devices, also indicating electrical connections. (b) Optical microscopy image of one of the devices, without PDMS capping (for clarity). LBA GS film covers the entire sample surface. (c,d) Output curves of H(AuCl₄) and LiNO₃ doped samples, and (e,f) transfer curves of H(AuCl₄) and LiNO₃ doped samples, respectively. Dashed lines represent least squares linear fits (to selected regions) that were used to extract sheet resistance and linear mobility.

Au-based salt and a relative reduction of the Fermi level in GSs (p-doping). It is also worth mentioning that poly-crystalline nature of LPE based GS films, large amount of sheet edges and presence of the residual solvent (NMP) results in p-doped films⁹, as was also observed in the electrical measurements presented in the following subsection. Therefore, WF values are lower for the LPE-based films by at least 200 meV, than for the pristine exfoliated single-crystals⁴². p-type doping is also reflected on the WF of the reference samples (undoped LPE GS), and therefore on the whole accessible range for the WF modulation by this method. This was also highlighted in Fig. 5(e), where the $WF_{Dirac\ point}$ depicts the case of undoped graphene⁴².

According to Fig. 5(d), the maximal doping in both directions is similar, around 0.3–0.4 eV, finally providing a significant range of around 0.7 eV for the work function modulation of LPE GS films. The achieved range was obtained for 0.1 mg/mL concentration of dopants. For smaller concentrations (one order of magnitude lower, 0.01 mg/mL), the observed changes in CPD were in the order of 10 mV. On the other hand, for higher concentrations (for one order of magnitude higher, 1 mg/mL) gave rise to the problems related to the formation of continuous, large-area LPE GS films, and were therefore excluded from this study. The reported shift of the Fermi level is very similar to the other (comparable) systems in the literature. WF values change of 0.3 eV in our experiment (chemical doping by Au ions) are the same order of magnitude as in Kwon *et al.* manuscripts for gold-chloride (WF change of 0.6 eV²¹, 0.6 eV²², 0.4 eV²⁵). Compared with Kwon *et al.* alkali carbonate²³ and chloride²⁵ graphene chemical doping data (0.4 eV and 0.3–0.4 eV, respectively) WF values change for Li in our manuscript (0.2 eV and 0.4 eV) are in the same order of magnitude. Compared with literature data the same effect can be achieved but advantages of our approach is fast and simple solution-based method for one-step fabrication and WF control of large-area graphene films.

Sheet resistance. The schematic cross-section of the devices used for the electrical characterization is shown in Fig. 6(a), also indicating electrical connections. An optical microscopy image for one of the devices without PDMS encapsulation (for clarity) is shown in Fig. 6(b) illustrating source (S) and drain (D) contact geometries. One characteristic set of transport and output curves for H(AuCl₄) and LiNO₃ doped film is presented in Fig. 6(c–f). Here linear fits were used to extract sheet resistances and apparent linear hole mobilities. Transfer curves for all four salt-treatments and for the reference LPE GS film are presented in the Supplementary information (Supplementary Fig. S1).

In the cases of a reference (undoped) and H(AuCl₄) doped LPE GS samples, output curves barely deviate from a perfect linear behavior in a rather large bias range, indicating that the contact resistance is negligible in comparison to the channel. This is in contrast to all samples doped with Li-based salts, where a significant deviation from the linear output curves were observed at higher bias, indicating non-negligible contact resistance. This can be attributed to large WF differences with Au bottom contacts in the case of Li-based salt doping of the films. Furthermore, while H(AuCl₄) doping enhances electrical performance of the films, a significant increase of the resistivity and reduction of the mobility was observed in the case of all Li-based salt dopings.

The slope of the transfer curves indicates that holes are the majority carriers for all samples, including both the undoped (reference) and all metal salt doped films. Linear fits to the transfer curves were used to estimate

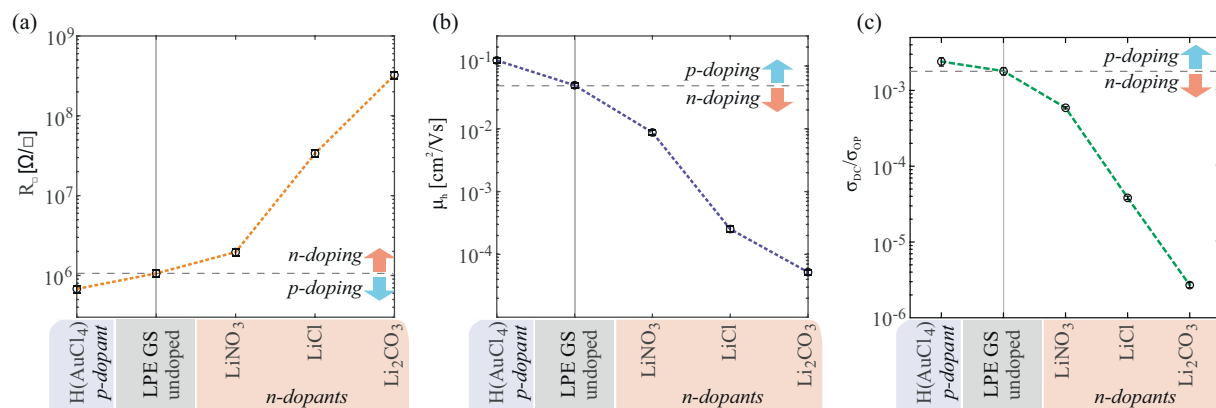


Figure 7. The dependence of the electrical properties of LBA graphene films on the type of metal standard solution based doping; (a) sheet resistance, and (b) apparent linear hole mobility, and (c) direct current conductivity to optical conductivity ratio (σ_{DC}/σ_{OP}). Dashed lines in (a–c) serve only as a guide for the eye.

apparent hole mobility of the devices. While the type of majority carriers was not affected by the doping, a significant (over one order of magnitude) suppression of the field-effect was observed for Li salt dopings of the films.

Figure 7 summarizes electrical properties obtained for all of the measured devices as a function of the different metal based doping.

The results indicate that anions also play a significant role. In the case of Li-based salts, a large variation of the electrical properties was obtained by the different choice of the anion species. Nonetheless, the experiments point out that metal cations dictate the direction of the WF shift (see Fig. 5), as is apparent in the case of H(AuCl₄) and LiCl where only cation species is varied. Our results of metal based doping of LPE graphene films demonstrate a tradeoff between enhancement of the electrical performance and modulation of the WF. Similar results were obtained for CVD doping with Li and Au salts^{23,25}. Of a particular technological relevance is large reduction of the WF of graphene. While many methods for chemical modulation of graphene result in p-type doping^{43–46}, stable and simple n-type doping is much harder to achieve^{47–49}. For an efficient electron injection, a significant reduction of graphene's WF is required. As pointed out by WF measurements and electrical characterization, LiNO₃ is the best choice from the tested Li-based salts with respect to both the largest WF reduction (by 400 meV) and least deterioration of the electrical properties of the films with ~2–3 times increase in sheet resistance compared to the reference (undoped LPE GS).

In contrast, doping of LPE GS films by HNO₃ vapor results in an increase of the apparent mobility⁹. However, using a LiNO₃ solution reduces the mobility by one order of magnitude. Therefore, Li⁺ cations – and not anions – are likely responsible for the deterioration of the electrical properties upon n-doping. An increase of sheet resistance was observed in doping of CVD graphene with alkali metal carbonates and chlorides^{23,25}. There, a significant increase in the sheet resistance was related to the combination of carbon atoms and dopant metals because electron donation occurred^{23,25}. Also, Chen *et al.* observed that the mobility of the charge carriers decreases with the increase of the potassium doping concentration which they attributed to additional scattering caused by ionized potassium atoms^{49,50}. It is most likely that Li⁺ cations are acting as scattering centers for the carriers, or provide traps at the boundaries between neighbouring GSs and effectively increase contact resistance between the overlapping GSs.

Finally, considering that the main potential application of these LPE GS films lies in transparent electrodes, direct current conductivity to optical conductivity ratio (σ_{DC}/σ_{OP}) is presented in Fig. 7(c) for all metal standard solution doping cases and for the reference (undoped). σ_{DC}/σ_{OP} is a parameter frequently reported in order to characterize the relative performance of the films in terms of transparency and sheet resistance^{11,33,51}. The higher the ratio the better the quality of transparent electrodes³³. Compared to the changes in the electrical properties (Fig. 7(a)) the changes in the optical properties (Fig. 2) are minor. Therefore, the dependence of the σ_{DC}/σ_{OP} on the type of the metal-ion doping clearly follows the trend set by $1/R_{\square}$.

X-ray Photoemission Spectroscopy (XPS) measurements. In order to understand Au and Li ion doping mechanisms XPS measurements were performed. C 1s, Au 4f and Li 1s core-level XPS spectra are shown in Fig. 8. N 1s, Cl 2p and O 1s spectra are presented as Supplementary Fig. S2. The C 1s peak of undoped and LiCl, LiNO₃, Li₂CO₃, H(AuCl₄) doped LPE GS films is shown on Fig. 8(a). The C 1s peak is deconvoluted using Gaussian profile into 4 components for undoped and doped films: C=C/C–C in aromatic rings (284.5 eV); C–C sp³ (285.4 eV); C–O (286.6 eV) and C=O (289 eV)^{23,52}. In the case of Li₂CO₃ we can see a small additional peak at 289.2–291.0 eV⁵³ which can be assigned to carbonate. Detected oxygen peak (C=O) is likely due to the residual of NMP and oxygen functionalized edges (C–O) on graphene^{54,55}. The C=C/C–C peak was shifted to a lower binding energy by about 0.16, 0.48, 0.10 and 0.83 eV for H(AuCl₄), LiCl, LiNO₃ and Li₂CO₃ doping process, respectively. The C=C/C–C peak shifts in present work are a consequence of doping by different metal standard solutions. Kwon *et al.* have shown that degree of doping was related to the electronegativity of the anion in the Au complex where anions with a high electronegativity and high bond strength are adequate for use as a p-type

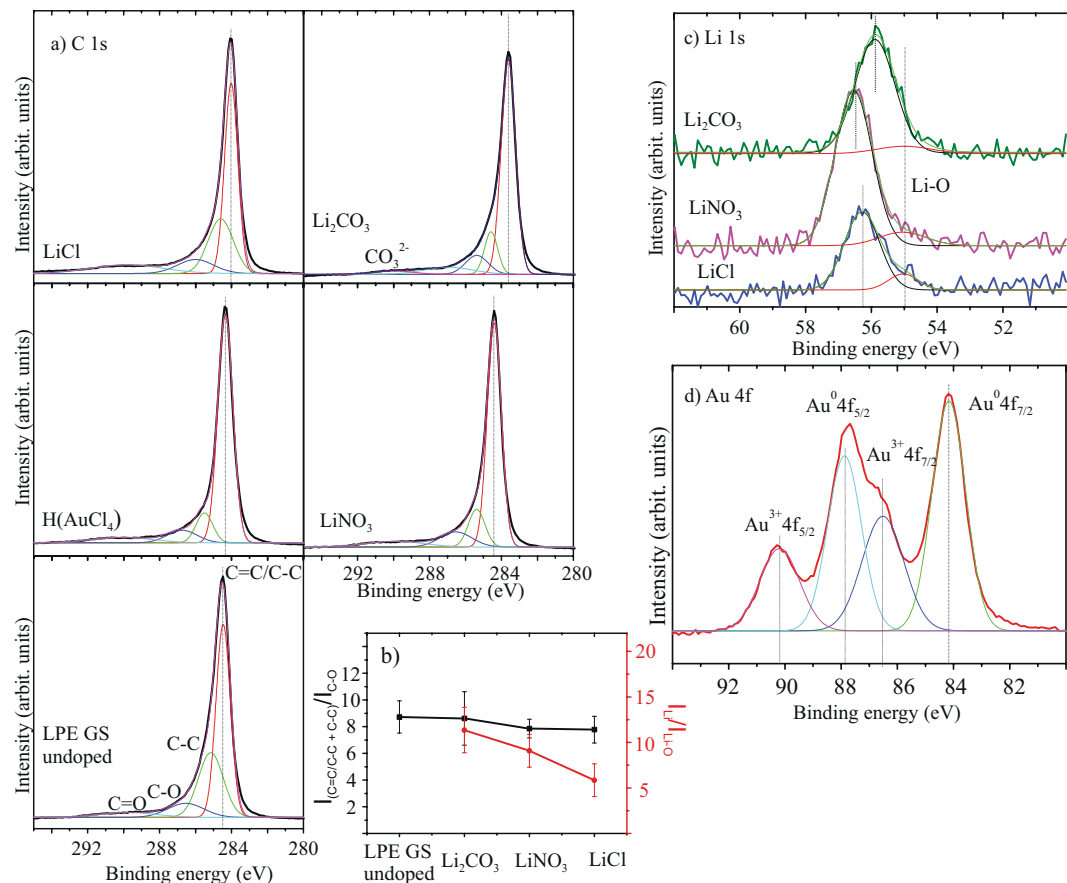


Figure 8. (a) XPS C 1s spectra of undoped and H(AuCl₄), LiCl, LiNO₃, Li₂CO₃ doped LPE GS films. C=C/C-C in aromatic rings (284.5 eV); C-C sp³ (285.4 eV); C-O (286.6 eV) and C=O (289 eV) were considered. For Li₂CO₃ a small additional peak at 289.2–291.0 eV can be assigned to carbonate. (b) Peak intensity ratio for the sum of C=C/C-C and C-C peaks intensities, and the intensity of C-O, $I_{(C=C/C-C+C-C)}/I_{(C-O)}$ (black line) and the ratio of Li 1s intensity from Li salts to Li-O intensity, I_{Li}/I_{Li-O} (red line). (c) XPS Li 1s spectra for different Li compounds and for Li-O. (d) The Au 4f peak in the XPS data of H(AuCl₄).

dopant in graphene²¹. Thus, different shifts of C=C/C-C peak for different metal-salt doping materials could be also a consequence of anions influence on graphene films.

Figure 8(c) show the Li 1s core-level XPS spectra. Literature values for Li 1s core-level for different Li compounds are: LiCl (56.2 eV), Li₂CO₃ (55.5 eV) and LiNO₃ (55.8 eV)⁵⁶ and they correspond well to the values obtained in this work. Li 1s peak at 55.0 eV is assigned to Li-O bond⁵⁷. Vijayakumar and Jianzhi have shown that lithium ion tends to bind with the oxygen rather than the carbon on graphene surface, and interacts by forming Li-O ionic bond⁵⁸. Also Kwon *et al.* have proposed that C-O-X complexes can be formed during doping treatment and can act as an additional dipole to further reduce the value of WF^{23–25,59}. The intensity ratio between sum of the intensities of C=C/C-C and C-C peaks, and the intensity of C-O ($I_{(C=C/C-C+C-C)}/I_{(C-O)}$) is shown in Fig. 8(b). Also, the ratio of Li 1s intensity from Li salts to Li-O intensity (I_{Li}/I_{Li-O}) can be seen in Fig. 8(b). In both cases, intensity ratios decrease for Li₂CO₃, LiNO₃, LiCl, respectively and this implies increased formation of C-O and Li-O bonds. Increased number of Li-O bonds follow the increasing trend of C-O bonds, which is in correlation with the WF change (Fig. 5(d)). The above mentioned results strongly suggest that the mechanism of n-type doped LPE GS films with lithium-salts could be explained with formation of Li complexes (C-O-Li).

Figure 8(d) show the Au 4f peak of gold-chloride doped LPE GS film. The peak is composed of metal (Au⁰) and metal ion (Au³⁺). The peaks at 84.2 eV and 87.9 eV are assigned to neutral Au (Au⁰ 4f_{7/2} and Au⁰ 4f_{5/2}, respectively), and the peaks at 86.5 eV and 90.2 eV are assigned to Au ion (Au³⁺ 4f_{7/2} and Au³⁺ 4f_{5/2}, respectively). Au ions (Au³⁺) have positive reduction potential and have tendency to spontaneously accept charges from other materials (graphene) and reduce to Au⁰^{21,22,25,60}. Therefore, the mechanism of p-doped LPE GS film can be explained as spontaneous electron transfer from graphene film to Au³⁺, resulting in depletion of electrons in the graphene networks, thus increasing the WF of doped graphene.

Conclusion

We demonstrate a straightforward single-step method for forming and doping of LPE GS films by metal standard solutions through charge transfer processes. Chemical doping of graphene allows to modulate its WF in a very large range, and therefore potentially enables to use the same electrode material for both, the injection and for the extraction of the electrons. n-doping of graphene films is achieved by Li-based salts, whereas Au-based salt leads

to p-doping. Furthermore, solution-processed graphene films are in particular suited for the chemical modulations, since a large number of the sheet edges opens up many adsorption sites and enhances the doping effects when compared to many other types of graphene.

The morphology of the LPE GS films does not change with the doping process, except that doped films contain agglomerates. FT-IR measurements point out that graphene basal planes stay chemically unchanged with metal doping and the charge transfer process is enabled with adsorption of the metal salts. Li-based salts decrease the WF, while Au-based salts increase the WF of the entire film. The maximal doping in both directions gives a significant range of around 0.7 eV for the work function modulation. Changing the dopant (Au or Li based salts) significantly affects the electrical properties of the films. In the case of the Li-based salts doping of the film, a significant suppression of the field-effect mobility and the increase of the sheet resistance was observed. This indicates that adsorbed Li-anions act as scattering centers for the charges. XPS data indicated that different mechanisms exist in the case of Au and Li doping. For Au ions spontaneous charge transfer occurred from graphene, thus increasing WF. In the case of Li doping, potential adsorption sites are a large number of the sheet edges where C-O bonds are preferential sites for lithium ions and for forming of C-O-Li complexes. In all cases graphene films are p-type, which is in accordance with KPFM measurements. Also, tradeoff between Li complex which reduce the value of WF and anion which increase the value of WF could be a reason of such a doping.

Metal salts charge transfer doping – which happens with this single-step method – provides a facile and effective method to tune the WF of LPE graphene therefore extending the potential use of these materials in low-cost transparent electrode applications.

Methods

Preparation of GS dispersion and doping solutions. A dispersion of GS in N-methyl-2-pyrrolidone (NMP, Sigma Aldrich, product no. 328634) has been used. GS dispersion was prepared from graphite powder (Sigma Aldrich, product no. 332461) of initial concentration 18 mg/mL. The solution was sonicated in a low-power ultrasonic bath for 14 h. The resulting dispersion was centrifuged for 60 min at 3000 rpm immediately after the sonication.

Stock standard solutions used in our work for n-doping are 1 mg/mL LiCl, LiNO₃ and Li₂CO₃ and for p-doping is 1 mg/mL gold standard solution (Merck, H(AuCl₄), product no. 170216). Lithium standard solutions were prepared from originated Li salts (LiCl, LiNO₃ and Li₂CO₃, Merck, product no. 105679, 105653 and 105680, respectively). By appropriate dilution of the stock solution with deionized water we obtained 0.1 mg/mL metal water solution which is then used in doping process.

Deposition on a substrate and doping of LPE GS films. GS dispersion in NMP was used to fabricate transparent and conductive films by LBA technique at a water-air interface, like in our previous work^{9,29,61}. A small amount of GS dispersion was added to the water-air interface and after the film was formed it was slowly scooped onto the target substrate. Applying the same process of fabricating the GS films and using the appropriate metal standard solution instead of water, chemical doping was achieved. As substrates SiO₂/Si wafer were used for electrical and WF measurements, while quartz and CaF₂ substrates were chosen for optical and FT-IR spectroscopy, respectively.

Characterization of undoped and doped LPE GS films. The Morphology of LPE GS films was studied by optical and atomic force microscopy (AFM). Topographic AFM measurements were done by NTEGRA Prima AFM system and NSG01 probes with a typical tip radius of around 10 nm. The surface roughness of LPE GS films was calculated as a root-mean square of the height distribution and averaged on ten 50 × 50 μm² areas.

Kelvin probe force microscopy (KPFM) – established almost three decades ago⁶² and in the meantime frequently applied to graphene^{42,63–65} – was employed in order to characterize changes in the electrical surface potential and corresponding Fermi level shifts due to doping. For this purpose, we measured the contact potential difference (CPD) between AFM tip and the sample surface⁶⁶ by using Pt covered NSG01/Pt probes with a typical tip curvature radius of 35 nm. In the first pass of KPFM, the sample topography was measured in tapping AFM mode. In the second pass, the probe was lifted by 20 nm, and moved along the trajectory measured in the first pass. Simultaneously, the sum of AC and DC voltage was applied between the sample and the probe. The AC voltage excites AFM probe oscillations during its movement, while the CPD between AFM tip and the sample surface in every point is then equal to the value of variable DC voltage which cancels the AFM probe oscillations. For all samples, the CPD was measured on five 5 × 5 μm² areas, and then averaged. In order to obtain the absolute value of the work function, the following procedure was applied⁴². The CPD is equal to the work function difference between AFM tip (WF_t) and sample (WF_s), CPD = WF_t - WF_s. The calibration of the WF_t was done by a standard procedure consisting of KPFM measurements on a freshly cleaved HOPG with a well known work function of 4.6 eV⁴². Finally, the sample work function was calculated as WF_s = WF_t - CPD, where CPD is measured by KPFM for all, undoped and doped LPE GS films.

The effect of chemical doping on optical properties of LBA GS films was investigated with measurements of optical transmittance, using UV-VIS spectrophotometer (Beckman Coulter DU 720 UV-VIS Spectrophotometer).

Electrical measurements were performed under ambient conditions in a standard field-effect device configuration with Si substrate acting as a back gate electrode, using Keithley 2636 A SYSTEM SourceMeter. Devices were based on bottom-contact gold pads defined by a shadow mask with L/W = 30 μm/1000 μm, and SiO₂ as a gate dielectric with thickness of 285 nm. Graphene films were deposited using the same LBA method as described above. The top surface of the devices was encapsulated by polydimethylsiloxane (PDMS) films (GelPak X4) to ensure stable performance and minimize any adsorption/desorption during electrical measurements that could occur from the surroundings (e.g. water vapor). Electrical characterization was performed on several devices of each doping with metal standard solution, and for undoped films as a reference. For each device ten subsequent forward and

backward transfer and output curves were measured, using low sweeping rate ($\sim 0.005\text{--}1$ Hz per point in a voltage sweep) to minimize parasitic capacitance. Sheet resistance and apparent linear field-effect mobility were extracted using fits to output and transfer curves, respectively. For the output measurements source-drain bias was varied in a range between -10 V and $+10$ V, with the gate electrode grounded. For transfer measurements, the gate voltage was varied between 0 V and 50 V, with source-drain bias at 1 V in all cases except for Li_2CO_3 where due to a very weak field-effect (very low mobility) 10 V bias was used.

The room-temperature micro-Raman spectra of undoped and metal salt doped LPE GS films were collected using Tri Vista 557 triple spectrometer coupled to the liquid nitrogen-cooled CCD detector. Nd:YAG laser line of 532 nm was used for the excitation and 50 magnification objective was used for focusing the beam onto the sample. Low laser power (less than 1 mW) was applied to prevent the thermal degradation of the sample. Each LPE GS film sample was measured at eight different positions.

Fourier transform infrared absorbance spectra (FT-IR spectra) of undoped and metal salt doped LPE GS films were measured over a range of $400\text{--}4000$ cm^{-1} with Nicolet Nexus 470 FT-IR spectrometer. Standard solutions which were used for the preparation of doped films were measured too and they were prepared by drop casting method on the CaF_2 substrate.

XPS spectra were recorded using a Thermo Scientific instrument (K-Alpha spectrometer, Thermo Fisher Scientific, Waltham, USA) equipped with a monochromatic Al $K\alpha$ X-ray source (1486.6 eV). High-resolution scans were performed with a pass energy of 50 eV and a step size of 0.1 eV. All analyses were performed at room temperature.

Data availability

The datasets obtained and analysed during the current study that are not included in this article are available from the corresponding authors on reasonable request.

Received: 17 June 2019; Accepted: 28 April 2020;

Published online: 21 May 2020

References

- Geim, A. K. Graphene: Status and prospects. *Science* **324**, 1530–1534 (2009).
- Geim, A. K. & Novoselov, K. S. The rise of graphene. *Nat. Mater.* **6**, 183–191 (2007).
- Novoselov, K. S. *et al.* Room-temperature quantum hall effect in graphene. *Science* **315**, 1379–1379 (2007).
- Bonaccorso, F., Sun, Z., Hasan, T. & Ferrari, A. C. Graphene photonics and optoelectronics. *Nat. Photonics* **4**, 611–622 (2010).
- Kwon, K. C., Kim, B. J., Lee, J. L. & Kim, S. Y. Role of ionic chlorine in the thermal degradation of metal chloride-doped graphene sheets. *J. Mater. Chem. C* **1**, 253–259 (2013).
- Ferrari, A. C. *et al.* Science and technology roadmap for graphene, related two-dimensional crystals, and hybrid systems. *Nanoscale* **7**, 4598–4810 (2015).
- Backes, C. *et al.* Guidelines for exfoliation, characterization and processing of layered materials produced by liquid exfoliation. *Chem. Mater.* **29**, 243–255 (2017).
- Li, X. *et al.* Highly conducting graphene sheets and Langmuir-Blodgett films. *Nat. Nanotechnol.* **3**, 538–542 (2008).
- Matković, A. *et al.* Enhanced sheet conductivity of Langmuir-Blodgett assembled graphene thin films by chemical doping. *2D Mater.* **3**, 015002 (2016).
- Lee, S. K. *et al.* All graphene-based thin film transistors on flexible plastic substrates. *Nano Lett.* **12**, 3472–3476 (2012).
- Zheng, Q. *et al.* Transparent conductive films consisting of ultralarge graphene sheets produced by Langmuir-Blodgett assembly. *ACS Nano* **5**, 6039–6051 (2011).
- Park, J. *et al.* Work-function engineering of graphene electrodes by self-assembled monolayers for high-performance organic field-effect transistors. *J. Phys. Chem. Lett.* **2**, 841–845 (2011).
- Tong, S. W., Wang, Y., Zheng, Y., Ng, M. F. & Loh, K. P. Graphene intermediate layer in tandem organic photovoltaic cells. *Adv. Funct. Mater.* **21**, 4430–4435 (2011).
- Wang, Y., Tong, S. W., Xu, X. F., Özyilmaz, B. & Loh, K. P. Interface engineering of layer-by-layer stacked graphene anodes for high-performance organic solar cells. *Adv. Mater.* **23**, 1514–1518 (2011).
- Wu, J. *et al.* Organic light-emitting diodes on solution-processed graphene transparent electrodes. *ACS Nano* **4**, 43–48 (2010).
- Wang, X., Zhi, L. & Mullen, K. Transparent, conductive graphene electrodes for dye-sensitized solar cells. *Nano Lett.* **8**, 323–327 (2008).
- Alfano, B. *et al.* Modulating the sensing properties of graphene through an eco-friendly metal-decoration process. *Sensors Actuators, B Chem.* **222**, 1032–1042 (2016).
- Lynch, P., Khan, U., Harvey, A., Ahmed, I. & Coleman, J. N. Graphene-MoS₂ nanosheet composites as electrodes for dye sensitised solar cells. *Mater. Res. Express* **3**, 035007 (2016).
- Mosciatti, T. *et al.* A multifunctional polymer-graphene thin-film transistor with tunable transport regimes. *ACS Nano* **9**, 2357–2367 (2015).
- Giubileo, F. & Di Bartolomeo, A. The role of contact resistance in graphene field-effect devices. *Prog. Surf. Sci.* **92**, 143–175 (2017).
- Kwon, K. C., Kim, B. J., Lee, J. L. & Kim, S. Y. Effect of anions in Au complexes on doping and degradation of graphene. *J. Mater. Chem. C* **1**, 2463–2469 (2013).
- Kwon, K. C., Choi, K. S. & Kim, S. Y. Increased work function in few-layer graphene sheets via metal chloride doping. *Adv. Funct. Mater.* **22**, 4724–4731 (2012).
- Kwon, K. C., Choi, K. S., Kim, B. J., Lee, J. L. & Kim, S. Y. Work-function decrease of graphene sheet using alkali metal carbonates. *J. Phys. Chem. C* **116**, 26586–26591 (2012).
- Huang, J. H., Fang, J. H., Liu, C. C. & Chu, C. W. Effective work function modulation of graphene/carbon nanotube composite films as transparent cathodes for organic optoelectronics. *ACS Nano* **5**, 6262–6271 (2011).
- Kwon, K. C., Choi, K. S., Kim, C. & Kim, S. Y. Role of metal cations in alkali metal chloride doped graphene. *J. Phys. Chem. C* **118**, 8187–8193 (2014).
- Wang, X., Xu, J. B., Xie, W. & Du, J. Quantitative analysis of graphene doping by organic molecular charge transfer. *J. Phys. Chem. C* **115**, 7596–7602 (2011).
- Shin, H. J. *et al.* Control of electronic structure of graphene by various dopants and their effects on a nanogenerator. *J. Am. Chem. Soc.* **132**, 15603–15609 (2010).
- Shi, Y. *et al.* Work function engineering of graphene electrode via chemical doping. *ACS Nano* **4**, 2689–2694 (2010).

29. Tomašević-Ilić, T. *et al.* Reducing sheet resistance of self-assembled transparent graphene films by defect patching and doping with UV/ozone treatment. *Appl. Surf. Sci.* **458**, 446–453 (2018).
30. Matković, A. *et al.* Spectroscopic imaging ellipsometry and Fano resonance modeling of graphene. *J. Appl. Phys.* **112**, 123523 (2012).
31. Bracamonte, M. V., Lacconi, G. I., Urreta, S. E. & Foa Torres, L. E. F. F. On the nature of defects in liquid-phase exfoliated graphene. *J. Phys. Chem. C* **118**, 15455–15459 (2014).
32. Eckmann, A. *et al.* Probing the nature of defects in graphene by Raman spectroscopy. *Nano Lett.* **12**, 3925–3930 (2012).
33. Rytel, K. *et al.* Ultrasonication-induced sp³ hybridization defects in Langmuir-Schaefer layers of turbostratic graphene. *Phys. Chem. Chem. Phys.* **20**, 12777–12784 (2018).
34. Eckmann, A., Felten, A., Verzhbitskiy, I., Davey, R. & Casiraghi, C. Raman study on defective graphene: Effect of the excitation energy, type, and amount of defects. *Phys. Rev. B - Condens. Matter Mater. Phys.* **88**, 035426 (2013).
35. Drewniak, S. *et al.* Studies of reduced graphene oxide and graphite oxide in the aspect of their possible application in gas sensors. *Sensors* **16**, 103 (2016).
36. Kim, W. J., Basavaraja, C., Thinh, P. X. & Huh, D. S. Structural characterization and DC conductivity of honeycomb-patterned poly(ϵ -caprolactone)/gold nanoparticle-reduced graphite oxide composite films. *Mater. Lett.* **90**, 14–18 (2013).
37. Țucureanu, V., Matei, A. & Avram, A. M. FTIR spectroscopy for carbon family study. *Crit. Rev. Anal. Chem.* **46**, 502–520 (2016).
38. Wu, X. *et al.* One-step freezing temperature crystallization of layered rare-earth hydroxide (Ln₂(OH)₅NO₃·nH₂O) nanosheets for a wide spectrum of Ln (Ln = Pr-Er, and Y), anion exchange with fluorine and sulfate, and microscopic coordination probed via photoluminescence. *J. Mater. Chem. C* **3**, 3428–3437 (2015).
39. Nakamoto, K. *Infrared and Raman Spectra of Inorganic and Coordination Compounds. Part A: Theory and Applications in Inorganic Chemistry; Part B: Application in Coordination, Organometallic, and Bioinorganic Chemistry*, 5th Edition (Nakamoto, Kazuo). *John Wiley and Sons* (John Wiley and Sons, 2009).
40. Geng, F. *et al.* New layered rare-earth hydroxides with anion-exchange properties. *Chem. Eur. J.* **14**, 9255–9260 (2008).
41. Lefèvre, G. *In situ* Fourier-transform infrared spectroscopy studies of inorganic ions adsorption on metal oxides and hydroxides. *Adv. Colloid Interface Sci.* **107**, 109–123 (2004).
42. Yu, Y. *et al.* Tuning the graphene work function by electric field effect. *Nano Lett.* **9**, 3430–3434 (2009).
43. Levesque, P. L. *et al.* Probing charge transfer at surfaces using graphene transistors. *Nano Lett.* **11**, 132–137 (2011).
44. Kuruvila, A. *et al.* Organic light emitting diodes with environmentally and thermally stable doped graphene electrodes. *J. Mater. Chem. C* **2**, 6940–6945 (2014).
45. Meyer, J. *et al.* Metal oxide induced charge transfer doping and band alignment of graphene electrodes for efficient organic light emitting diodes. *Sci. Rep.* **4**, 5380 (2014).
46. Matković, A. *et al.* Probing charge transfer between molecular semiconductors and graphene. *Sci. Rep.* **7**, 9544 (2017).
47. Sanders, S. *et al.* Engineering high charge transfer n-doping of graphene electrodes and its application to organic electronics. *Nanoscale* **7**, 13135–13142 (2015).
48. Han, K. S. *et al.* A non-destructive n-doping method for graphene with precise control of electronic properties via atomic layer deposition. *Nanoscale* **8**, 5000–5005 (2016).
49. Chen, J. H. *et al.* Charged-impurity scattering in graphene. *Nat. Phys.* **4**, 377–381 (2008).
50. Pinto, H. & Markevich, A. Electronic and electrochemical doping of graphene by surface adsorbates. *Beilstein J. Nanotechnol.* **5**, 1842–1848 (2014).
51. De, S. & Coleman, J. N. Are there fundamental limitations on the sheet resistance and transmittance of thin graphene films? *ACS Nano* **4**, 2713–2720 (2010).
52. Benayad, A. *et al.* Controlling work function of reduced graphite oxide with Au-ion concentration. *Chem. Phys. Lett.* **475**, 91–95 (2009).
53. López, G. P., Castner, D. G. & Ratner, B. D. XPS O 1s binding energies for polymers containing hydroxyl, ether, ketone and ester groups. *Surf. Interface Anal.* **17**, 267–272 (1991).
54. Hernandez, Y. *et al.* High-yield production of graphene by liquid-phase exfoliation of graphite. *Nat. Nanotechnol.* **3**, 563–568 (2008).
55. Kim, H. *et al.* Optoelectronic properties of graphene thin films deposited by a Langmuir-Blodgett assembly. *Nanoscale* **5**, 12365–12374 (2013).
56. Naumkin, A. V., Kraut-Vass, A., Gaarenstroom, S. W. & Powell, C. J. NIST X-ray photoelectron spectroscopy database. Available at: https://srdata.nist.gov/xps/EngElmSrChQuery.aspx?EType=PE&CSOpt=Retri_ex_dat&Elm=Li. (2019).
57. Moulder, J. F., Stickle, W. F., Sobol, P. E. & Bomben, K. D. *Handbook of X-ray photoelectron spectroscopy. Reference book of standard spectra for identification and interpretation of XPS data* (Perkin-Elmer Corporation, Physical Electronic division, 1992).
58. Vijayakumar, M. & Jianzhi, H. Exploring the interaction between lithium ion and defective graphene surface using dispersion corrected DFT studies. *ECS Trans* **53**, 23–32 (2013).
59. Pickett, W. E. Negative electron affinity and low work function surface: Cesium on oxygenated diamond (100). *Phys. Rev. Lett.* **73**, 1664–1667 (1994).
60. Syu, J. Y. *et al.* Wide-range work-function tuning of active graphene transparent electrodes via hole doping. *RSC Adv.* **6**, 32746–32756 (2016).
61. Tomašević-Ilić, T. *et al.* Transparent and conductive films from liquid phase exfoliated graphene. *Opt. Quantum Electron.* **48**, 319 (2016).
62. Nonnenmacher, M., O'Boyle, M. P. & Wickramasinghe, H. K. Kelvin probe force microscopy. *Appl. Phys. Lett.* **58**, 2921–2923 (1991).
63. Vasić, B. *et al.* Atomic force microscopy based manipulation of graphene using dynamic plowing lithography. *Nanotechnology* **24**, 015303 (2013).
64. Vasić, B. *et al.* Low-friction, wear-resistant, and electrically homogeneous multilayer graphene grown by chemical vapor deposition on molybdenum. *Appl. Surf. Sci.* **509**, 144792 (2020).
65. Panchal, V., Pearce, R., Yakimova, R., Tzalenchuk, A. & Kazakova, O. Standardization of surface potential measurements of graphene domains. *Sci. Rep.* **3**, 2597 (2013).
66. Udum, Y. *et al.* Inverted bulk-heterojunction solar cell with cross-linked hole-blocking layer. *Org. Electron.* **15**, 997–1001 (2014).

Acknowledgements

This work has been supported from the Serbian MPNTR through projects OI 171005, OI 171032, 451-03-02141/2017-09/32 and with support from the Lise Meitner fellowship by Austrian Science Fund (FWF): M 2323-N36. We further acknowledge support by the Austrian Academic Exchange Service (OeAD) via the project SRB 13/2018.

Author contributions

I.M. devised the concept of LPE GS films doping with metal standard solutions in the single-step method. I.M. and J.V. prepared LPE dispersions and fabricated undoped and doped LPE GS films on different substrates. B.V. did AFM and KPFM measurements, A.M. performed electrical measurements, I.M. and J.V. did FTIR measurements, S.A. and I.M. performed Raman measurements and I.M., T.G., M.K., S.A. and J.V. performed and

processed XPS measurements. C.T. and R.G. oversaw the study. I.M., A.M. and B.V. wrote the manuscript. All authors discussed and analysed the results and reviewed the manuscript.

Competing interests

The authors declare no competing interests.

Additional information

Supplementary information is available for this paper at <https://doi.org/10.1038/s41598-020-65379-1>.

Correspondence and requests for materials should be addressed to I.R.M. or A.M.

Reprints and permissions information is available at www.nature.com/reprints.

Publisher's note Springer Nature remains neutral with regard to jurisdictional claims in published maps and institutional affiliations.



Open Access This article is licensed under a Creative Commons Attribution 4.0 International License, which permits use, sharing, adaptation, distribution and reproduction in any medium or format, as long as you give appropriate credit to the original author(s) and the source, provide a link to the Creative Commons license, and indicate if changes were made. The images or other third party material in this article are included in the article's Creative Commons license, unless indicated otherwise in a credit line to the material. If material is not included in the article's Creative Commons license and your intended use is not permitted by statutory regulation or exceeds the permitted use, you will need to obtain permission directly from the copyright holder. To view a copy of this license, visit <http://creativecommons.org/licenses/by/4.0/>.

© The Author(s) 2020



DFT study of optical properties of MoS₂ and WS₂ compared to spectroscopic results on liquid phase exfoliated nanoflakes

Jelena Pešić¹ · Jasna Vujin¹ · Tijana Tomašević-Ilić¹ · Marko Spasenović¹ · Radoš Gajić¹

Received: 1 November 2017 / Accepted: 23 June 2018
© Springer Science+Business Media, LLC, part of Springer Nature 2018

Abstract

We calculate the dielectric function within the framework of the random-phase approximation (RPA) based on DFT ground-state calculations, starting from eigenvectors and eigenvalues. The final goal of our theoretical work is a comparison to corresponding experimental data. We compare our computational results with optical measurements on MoS₂ and WS₂ nanoflakes. MoS₂ and WS₂ were exfoliated by ultrasonic treatment in high-boiling point organic solvent and characterized using UV–VIS spectrophotometry. We find that DFT-RPA yields a good, computationally inexpensive first approximation of the imaginary part of the dielectric function, although excitonic effects require more complex code and extra computing power.

Keywords DFT optical properties · MoS₂ and WS₂ · 2D materials

1 Introduction

Even though graphene is being the most promising two-dimensional material, absence of the gap has imposed limitations of its applications in nanoelectronics and nanophotonics. Transition metal dichalcogenide crystals (TMDCs) emerged as important alternative as a layered 2D materials family with the finite gap and received considerable attention owing to their extraordinary potential for applications in electronics and optics (Pospischil et al. 2014; Baugher et al. 2014; Britnell et al. 2013; Koppens et al. 2014; Ross et al. 2014; Shi 2013; Zhang 2016; Huang 2016; He 2016; Szczesniak 2017). MoS₂ and WS₂ are part of the family of transition

Topical Collection on Focus on Optics and Bio-photonics, Photonica 2017.

Guest Edited by Jelena Radovanovic, Aleksandar Krmpot, Marina Lekic, Trevor Benson, Mauro Pereira, Marian Marciniak.

✉ Jelena Pešić
yelena@ipb.ac.rs

¹ Graphene Laboratory (GLAB) of Center for Solid State Physics and New Materials, Institute of Physics Belgrade, University of Belgrade, Pregrevica 118, 11080 Belgrade, Serbia

metal dichalcogenide crystals. They display distinctive properties at a thickness of one and few layers (Butler et al. 2013; Wang et al. 2012; Xu et al. 2014) and very peculiar physics, ranging from trions (Mak et al. 2013) to superconductivity (Szczesniak et al. 2018). They have also attracted much interest for applications in optoelectronics as detectors, photovoltaic devices and light emitters (Pospischil et al. 2014; Baugher et al. 2014; Britnell et al. 2013; Koppens et al. 2014; Ross et al. 2014). MoS₂ and WS₂ are layered crystals in hexagonal structure, consisting of metal atoms sandwiched between two chalcogenide atoms, with covalent interaction within layer and van der Waals interaction between layers. For many applications knowledge of the optical properties is of fundamental importance. Spectroscopic techniques are among the most important methods for research in the field of nanoscience and nanotechnologies. Parallel with the development of experimental methods, computational science becomes a very valuable tool in pursuit for new low-dimensional materials and their characterization. Employing high-end modeling codes, it is possible to simulate from first principles more than a few spectroscopic techniques. The most basic description of light-matter interactions in TMDC thin layers is given by the materials complex dielectric function. Importance of the dielectric function is not only in understanding theoretical concepts underlying interesting properties of TMDCs but it is crucial for the characterization of these materials i.e. the imaginary part of dielectric function is directly related to the absorption. The observed double-peak structure in the optical absorption spectra of monolayer TMDCs is connected to excitonic excitations. These excitons are due to the vertical transition at the K point of the Brillouin zone from a spin-orbit-split valence band to doubly degenerate conduction band (Zhu et al. 2011). For experimental approach, spectroscopic ellipsometry allows determination of material's optical properties in nondestructive manner (Tompkins and McGahan 1999; Liu et al. 2014). The liquid-phase exfoliation is a simple and effective method to exfoliate bulk layered materials into mono- and/or few-layer 2D nanosheets. In this work, high quality TMDC, MoS₂ and WS₂ were prepared in NMP with the similar procedure as our previous works (Matković et al. 2016; Tomašević-Ilić et al. 2016). UV–VIS spectroscopic measurements effectively characterize dispersions by their absorption spectra. Using approaches based on density functional theory (DFT), implemented in the Quantum Espresso software package (Giannozzi et al. 2009), we study optical properties of low-dimensional materials, MoS₂ and WS₂. We calculate the dielectric function within the framework of the random-phase approximation (RPA) (Brener 1975) based on DFT ground-state calculations, starting from eigenvectors and eigenvalues. Although the tight-binding approximation prove their efficiency and accuracy in describing low-dimensional bands and energy gaps in TDMC materials (Liu et al. 2013; Shanavas et al. 2015; Szczesniak et al. 2016), even for study of the optical properties (Ghader et al. 2015) we rely on DFT based methods due to their applicability on large spectra of systems joint with simplicity of use. The final goal of this study is a comparison to corresponding experimental data provided by spectroscopic measurements of liquid exfoliated nanoflakes of MoS₂ and WS₂. We use our results for analysis of optical properties of liquid phase exfoliated MoS₂ and WS₂ nanoflakes, as a proven method for analysis of basic optical properties of 2D materials (Pešić et al. 2016).

2 Computational details

For presented analysis, Quantum Espresso (QE) code (Giannozzi et al. 2009), based on DFT, was used. The approach is established on an iterative solution of the Kohn–Sham equations of the DFT in a plane-wave basis set. The ionic positions in the

cell are fully relaxed, in all calculations, to their minimum energy configuration using the Broyden–Fletcher–Goldfarb–Shanno (BFGS) algorithm. We modeled monolayer MoS₂ and WS₂ with hexagonal unit cell with 3 atoms per unit cell (Fig. 1). For presented analysis, GGA exchange–correlation functional, Perdew–Burke–Ernzerhof (PBE) (Krack 2005) was used. This parameter-free GGA functional, PBE, is known for its general applicability and gives rather accurate results for a wide range of systems. Compared to hybrid, PBE potential is significantly faster, hence more convenient for qualitative description we aim in this discussion. Although LDA is computationally even more affordable, GGA (i.e. PBE) has proven to be closer to experimental results for spectra of properties in low-dimensional materials (Rasmussen 2015; Molina-Sanchez et al. 2015). Additional accuracy that would be obtained with addition of spin orbit correction, however it would lead to significant increase in computational costs (Rasmussen 2015) making this approach obsolete, since we use it for its efficiency. Namely, many-body calculations applying the GW approximation and Bethe–Salpeter equation give good agreement for optical properties, but their computational costs is great comparing to DFT + RPA. Our computationally inexpensive approach gives qualitatively satisfying description. The hexagonal cell parameter c was set to be very large (10–12 Å) in order to simulate vacuum and two-dimensional system and avoid an interaction due to periodicity. The plane wave kinetic energy cutoff of 70 Ry was used and the uniform k-point grid was composed of 4096 points in the first Brillouin zone. In TMDCs van der Waals interaction (Lu et al. 2017) have an important effect on the electronic structure, and in case of multilayer, structures were relaxed to their minimum position, with van der Waals interaction included to obtain proper interlayer distance (using Grimme scheme Grimme 2006). In case of monolayer, there was no need for inclusion of it. Dielectric function $\epsilon(\omega)$ was calculated, in the range 1–20 eV, within the framework of the RPA (Brener 1975) based on DFT ground-state calculations, starting from eigenvectors and eigenvalues, implemented in Quantum Espresso (QE) code as epsilon.x post-processing utility. Matrix elements were accounted only for interband transitions. RPA does not include the nonlocal part of the pseudo-potential and it is not able to include in the calculation the non-local field and excitonic effects. We are interested in the study of the optical properties of this two materials using DFT as a computational inexpensive method for the qualitative description. In QE implementation of the RPA, frequency dependence is computed from an explicit summation of dipole matrix elements and transition energies. Similar theoretical methods were already used to describe the bulk TMDCs (Molina-Sanchez et al. 2015, 2013).

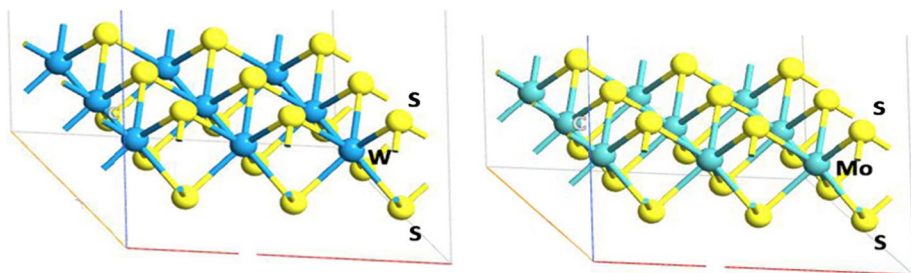


Fig. 1 Structure of monolayer of WS₂ and MoS₂

3 Synthesis of MoS₂ and WS₂ dispersions

Liquid Phase Exfoliation (LPE) is the physico-chemical process where thin sheets of van der Waals materials, ie. MoS₂ and WS₂ are exfoliated from their corresponding bulk materials by ultrasonic treatment in liquids such as organic solvents (Fig. 2). In liquid dispersion flakes mainly range from monolayer to few-layer flakes. For the fabrication of both MoS₂ and WS₂ dispersion, we followed the protocol described in earlier papers (Matković et al. 2016; Tomašević-Ilić et al. 2016; Panajotović et al. 2016; Vujin et al. 2016). An initial concentration of powders are: MoS₂ powder (Sigma Aldrich, Product No. 69860) 24 mg/ml and WS₂ powder (Sigma Aldrich Product No.243639) was 12 mg/ml. The mixture was sonicated in a low power sonic bath (Bransonic CPXH Ultrasonic 8 Cleaning Bath) for 14 h in *N*-Methyl-2-pyrrolidone (NMP) (Sigma Aldrich-328634) for both materials. In order to prevent reaggregation and reduce the amount of unexfoliated material, the solutions were centrifuged for MoS₂ 1000 rpm for 30 min and WS₂ 15 min at 3000 rpm and second centrifuge 6000 rpm for 15 min after we decanted excess of liquid.

4 Characterization of MoS₂ and WS₂ dispersions

Large quantities of TMDC flakes were observed as few-layer layered nanosheets, confirming the high quality of the prepared LPE samples. The aggregated nanosheets are absent in these SEM images (Fig. 3), which is in favor of quality of exfoliation procedure.

The UV–visible absorption spectra of the nanosheet dispersions in NMP was measured using the UV–VIS Spectrophotometer (Perkin-Elmer Lambda 4B). The quality of the obtained TMDC nanosheets was characterized by SEM (Tescan MIRA3 field-emission gun SEM). Two typical characteristic absorption peaks of MoS₂ and WS₂ are clearly observed at the region of 600 nm (Fig. 4, which correspond to the A1 and B1 direct excitonic transitions of the TMDC originated from the energy split of valence-band and spin-orbit coupling (Zhu et al. 2011; Coleman et al. 2011). Noteworthy, the splitting between A and B excitonic peaks of WS₂ is larger than that of MoS₂ because of the much heavier mass of the W atom (Shi 2013). These two peaks indicate that the TMDC are dispersed in NMP as the 2H-phase. The Lambert-Beer law was applied to UV–VIS absorption spectra to calculate TMDCs concentration by estimating the absorbance at distinctive peak (MoS₂ at 672 nm and WS₂ at 629 nm) by using a cell length of 1 cm and the extinction coefficient of MoS₂ ($\alpha = 34.00 \text{ mL mg}^{-1} \text{ m}^{-1}$), WS₂ ($\alpha = 27.56 \text{ mL mg}^{-1} \text{ m}^{-1}$), in NMP solutions, which corresponds to previously reported values (Coleman et al. 2011). The concentration of exfoliated MoS₂ is $343 \mu\text{g ml}^{-1}$ and WS₂ is $237 \mu\text{g ml}^{-1}$.

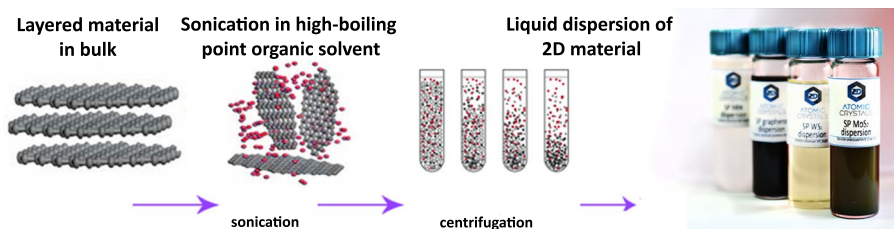


Fig. 2 Procedure of liquid phase exfoliation



Fig. 3 MoS₂ (up) and WS₂ (down) flakes on Si/SiO₂ substrate—Tescan MIRA3 field-emission gun SEM-left. Photos of MoS₂ and WS₂ dispersions-right

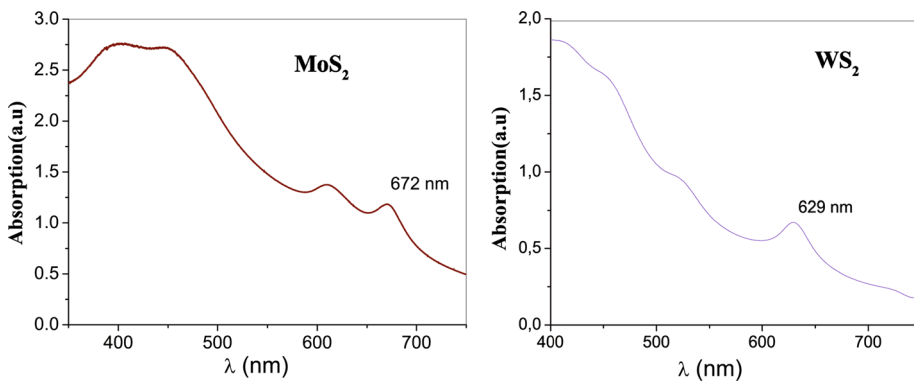


Fig. 4 UV–VIS spectra were taken using Perkin–Elmer Lambda 4B UV–VIS spectrophotometer with quartz cuvettes

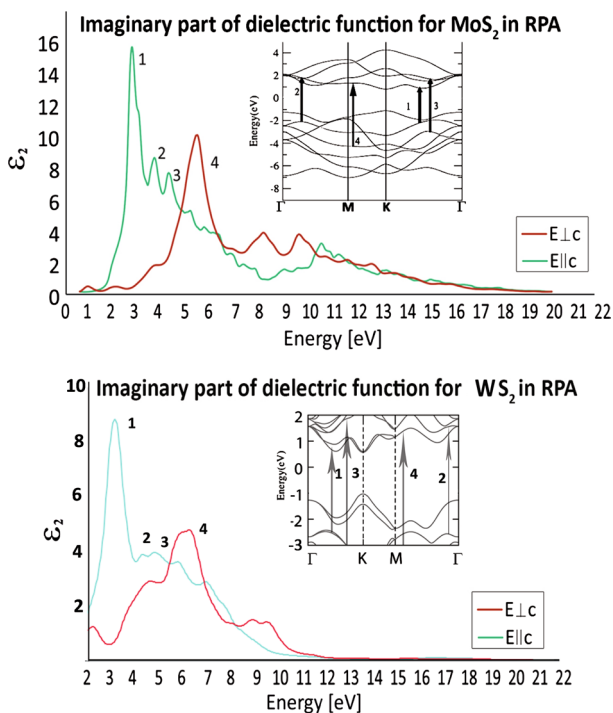
5 Results and Discussion

First we calculate the dielectric function for the MoS₂ and WS₂ monolayer (Fig. 5a). On example of MoS₂ monolayer we shall discuss dielectric function. The imaginary part of the

dielectric function for the \mathbf{E} vector perpendicular to the c axis is presented in the red color and \mathbf{E} parallel to the c axis is presented in the green on Fig. 5. Four distinct structures on Fig. 5, at 1(2.7), 2(3.7), 3(4.2) and 4(5.3 eV) can be connected to the interband transitions, marked on the inset of the electronic band structure, with 1, 2, 3 and 4 as well. All the interband transition depicted here are mainly due to the transition from the p valence bands of sulfur to the d conduction bands of the molybdenum (Kumar et al. 2012). The peak 1 is determined by the interband transitions from the valence bands I, II below the Fermi energy to the conduction bands I, II and III above the Fermi energy along ΓM and $K\Gamma$ direction. The peak 2 is due the interband transitions from the valence bands II below the Fermi energy to the conduction bands II and III above the Fermi energy along ΓM direction and near the M . The peak 3 exists due to the interband transitions from the valence bands III below the Fermi energy to the conduction bands II and III above the Fermi energy along $K\Gamma$ direction. Peak 4 is determined by the interband transitions from the valence bands IV below the Fermi energy to the conduction band I above the Fermi energy in the vicinity of the M high symmetry point. Our calculations are in agreement with the other similar DFT studies (Kumar et al. 2012) and experimental research as well (Li et al. 2014). All TMDCs have similar band structure and corresponding analysis can be applied on WS_2 monolayer. In Fig. 5 imaginary part of dielectric function of WS_2 is presented. Same as for MoS_2 , there are present four distinct peaks originating in same transitions as in MoS_2 .

Next we compare the imaginary part of the dielectric function in MoS_2 and WS_2 with experimental results. Figure 6 qualitatively compares experimental results of MoS_2 and WS_2 LPE with DFT+RPA calculations and results obtained using the Kramers–Kronig analysis (Li et al. 2014). The green line represent experimental results, UV–VIS spectra of LPE flakes. Violet lines are DFT + RPA model of MoS_2 and WS_2 . The red line is

Fig. 5 The calculated imaginary part of the dielectric function for MoS_2 and WS_2



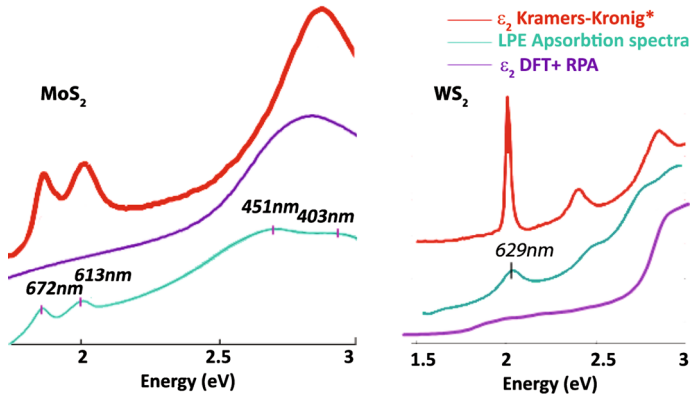
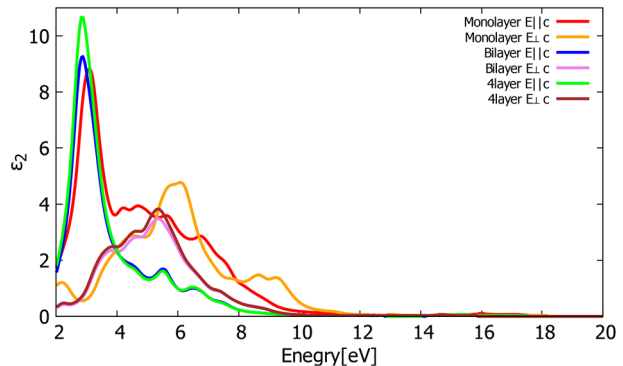


Fig. 6 The qualitative comparison of imaginary part of experimental results and theoretical calculations for MoS₂ and WS₂. Asterisks corresponds to result for the reference Li et al. (2014)

Fig. 7 The calculated imaginary part of the dielectric function for few layers of WS₂



imaginary part of the dielectric function obtained using Kramers–Kronig analysis from the reference Li et al. (2014). Due to the nature of approximation, excitonic effects are not clearly visible in DFT+RPA calculation and characteristic A and B peaks are not present. However both for MoS₂ and WS₂ peaks at around 400 nm (which originate in electronic transitions) are well described.

After analysis of monolayer we proceeded with calculations of few layer structures to observe changes in the imaginary part of dielectric function with increase of number of layers. We compared monolayer with bilayer and 4-layer WS₂, Fig. 7 and conclude its thickness-dependent nature. It can be noticed that thicker structures have higher ϵ_2 in the low energy area. This regular change shows a good agreement with the variation tendency of the density of WS₂ films, as demonstrated in the XRD analysis in ref (Li et al. 2017). Being aware of this effect, a referent model for various thicknesses of TMDCs sheets (ie. number of layers) could be made using DFT-based approach. It is planned to be used as a guide in comparison with UV–VIS spectrophotometry measurement for rapid assessment of thickness of nanoflakes in dispersion.

6 Conclusion

In this paper we studied optical properties i.e. the dielectric function of the monolayer MoS₂ and WS₂ as a monolayer TMDCs, using DFT based techniques. Many effects present due to the excitonic effects demand detail and advanced approach based addition of GW approximation and Bethe–Salpeter equation (but computationally significantly more expensive, time-demanding and resource-consuming), in this kind of the calculations they have been completely neglected. Thickness-dependent nature of MoS₂ and WS₂ dielectric function was revealed. However, we can conclude that DFT+RPA techniques can be used for quick analysis of the optical properties of these and similar 2D materials, and they provide the reliable and computationally non-expensive solution for the suitable qualitative description.

Acknowledgements This work is supported by the Serbian MPNTR through Project OI 171005 and by Qatar National Research Foundation through Projects NPRP 7-665-1-125. DFT calculations are performed using computational resources at Johannes Kepler University, Linz, Austria.


References

- Baughner, B.W.H., et al.: Optoelectronic devices based on electrically tunable p-n diodes in a monolayer dichalcogenide. *Nat. Nano* **9**(4), 262–267 (2014)
- Brener, N.E.: Random-phase-approximation dielectric function for diamond, with local field effects included. *Phys. Rev. B* **12**(4), 1487–1492 (1975)
- Britnell, L., et al.: Strong light-matter interactions in heterostructures of atomically thin films. *Science* **340**(6138), 1311–1314 (2013)
- Butler, S.Z., et al.: Challenges, and opportunities in two-dimensional materials beyond graphene. *ACS Nano* **7**(4), 2898–2926 (2013)
- Coleman, J.N., et al.: Two-dimensional nanosheets produced by liquid exfoliation of layered materials. *Science* **331**(6017), 568–571 (2011)
- Ghader, D., et al.: The electronic band structures and optical absorption spectra for incommensurate twisted few-layers graphene. [arXiv:1504.01347v1](https://arxiv.org/abs/1504.01347v1) (2015)
- Giannozzi, P., et al.: QUANTUM ESPRESSO: a modular and open-source software project for quantum simulations of materials. *J. Phys. Condens. Matter* **21**, 395502 (2009). <http://www.quantum-espresso.org>
- Grimme, S.: Semiempirical GGA-type density functional constructed with a longrange dispersion correction. *J. Comp. Chem.* **27**(15), 1787–1799 (2006)
- He, X.: Strain engineering in monolayer WS₂, MoS₂, and the WS₂/MoS₂ heterostructure. *Apl. Phys. Lett.* **109**(17), 173105 (2016)
- Huang, G.Q.: Dynamical stability and superconductivity of Li-intercalated bilayer MoS₂: A first-principles prediction. *Phys. Rev. B* **93**(10), 104511 (2016)
- Koppens, F.H.L., et al.: Photodetectors based on graphene, other two-dimensional materials and hybrid systems. *Nat. Nano* **9**, 780–793 (2014)
- Krack, M.: Pseudopotentials for H to Kr optimized for gradient-corrected exchange-correlation functionals. *Theor. Chem. Acc.* **114**(1–3), 145–152 (2005)
- Kumar, A., et al.: A first principle comparative study of electronic and optical properties of 1HMoS₂ and 2HMoS₂. *Mat. Chem. Phys.* **135**, 755–761 (2012)
- Li, Y., et al.: Measurement of the optical dielectric function of monolayer transition-metal dichalcogenides: MoS₂, MoSe₂, WS₂, and WSe₂. *Phys. Rev. B* **90**(20), 205422 (2014)
- Li, W., et al.: Broadband optical properties of large-area monolayer CVD molybdenum disulfide. *Phys. Rev. B* **90**(19), 195434 (2014)
- Li, Da-Hai, et al.: Dielectric functions and critical points of crystalline WS₂ ultrathin films with tunable thickness. *Phys. Chem. Chem. Phys.* **19**, 12022 (2017)

- Liu, G.-B., et al.: Three-band tight-binding model for monolayers of group-VIB transition metal dichalcogenides. *Phys. Rev. B* **88**(8), 085433 (2013)
- Liu, H.-L., et al.: Optical properties of monolayer transition metal dichalcogenides probed by spectroscopic ellipsometry. *Appl. Phys. Lett.* **105**, 20 (2014)
- Lu, N., et al.: Twisted MX₂/MoS₂ heterobilayers: effect of van der Waals interaction on the electronic structure. *Nanoscale* **9**, 19131–19138 (2017)
- Mak, K.F., et al.: Tightly bound trions in monolayer MoS₂. *Nat. Mater.* **12**(3), 207–211 (2013)
- Matković, A., et al.: Enhanced sheet conductivity of LangmuirBlodgett assembled graphene thin films by chemical doping. *2D Mater.* **3**(1), 015002 (2016)
- Molina-Sanchez, A., et al.: Effect of spin-orbit interaction on the optical spectra of single-layer, double-layer, and bulk MoS₂. *Phys. Rev. B* **88**(4), 045412 (2013)
- Molina-Sanchez, A., et al.: Vibrational and optical properties of MoS₂: from monolayer to bulk. *Surf. Sci. Rep.* **70**(4), 554–586 (2015)
- Panajotović, R., et al.: Modifications of Lipid/2D-Material Heterostructures by SEM, Book of Abstracts, SPIG 2016, 182–185 (2016)
- Pešić, J., et al.: Ab-initio study of the optical properties of the Li-intercalated graphene and MoS₂. *Opt Quant Electron* **48**, 368 (2016)
- Pospischil, A., et al.: Solar-energy conversion and light emission in an atomic monolayer p-n diode. *Nat. Nano* **9**(4), 257–261 (2014)
- Rasmussen, F.A.: Computational 2D materials database: electronic structure of transition-metal dichalcogenides and oxides. *J. Phys. Chem. C* **119**, 13169–13183 (2015)
- Ross, J., et al.: Electrically tunable excitonic light-emitting diodes based on monolayer WSe₂ p-n junctions. *Nat. Nano* **9**(4), 268–272 (2014)
- Shanavas, K.V., et al.: Effective tight-binding model for MX₂ under electric and magnetic fields. *Phys. Rev. B* **91**(23), 235145 (2015)
- Shi, H.: Quasiparticle band structures and optical properties of strained monolayer MoS₂ and WS₂. *Phys. Rev. B* **87**(15), 155304 (2013)
- Szczesniak, D., et al.: Complex band structures of transition metal dichalcogenide monolayers with spin-orbit coupling effects. *J. Phys. Condens. Matter* **28**(35), 355301 (2016)
- Szczesniak, R.: Metallization and superconductivity in Ca-intercalated bilayer MoS₂. *J. Phys. Chem. Solids* **111**, 254–257 (2017)
- Szczesniak, R., Durajski, A.P., Jarosik, M.W.: Strong-coupling superconductivity induced by calcium intercalation in bilayer transition-metal dichalcogenides. *Front. Phys.* **13**(2), 137401 (2018)
- Tomašević-Ilić, T., et al.: Transparent and conductive films from liquid phase exfoliated graphene. *Opt. Quant. Electron.* **48**, 319 (2016)
- Tompkins, H.G., McGahan, W.A.: *Spectroscopic ellipsometry and reflectometry: a users guide*. Wiley, New York (1999)
- Vujin, J., et al.: Physico-Chemical Characterization Of Lipid-2d-Materials Self-Assembly For Biosensors, Book of Abstracts RAD 2016, 58 (2016)
- Wang, Q.H., et al.: Electronics and optoelectronics of two-dimensional transition metal dichalcogenides. *Nat. Nano* **7**, 699–712 (2012)
- Xu, X., et al.: Spin and pseudospins in layered transition metal dichalcogenides. *Nat. Phys.* **10**, 343–350 (2014)
- Zhang, J.-J.: Strain-enhanced superconductivity of MoX₂(X=S or Se) bilayers with Na intercalation. *Phys. Rev. B* **93**(15), 155430 (2016)
- Zhu, Z.Y., Cheng, Y.C., Schwingenschlogl, U.: Giant spin-orbit-induced spin splitting in two-dimensional transition-metal dichalcogenide semiconductors. *Phys. Rev. B* **84**(15), 153402 (2011)



Differentiation of stem cells from apical papilla into neural lineage using graphene dispersion and single walled carbon nanotubes³

Jelena Simonovic¹, Bosko Toljic¹, Nadja Nikolic¹, Jasna Vujin², Radmila Panajotovic², Rados Gajic², Elena Bekyarova^{3,4}, Amelia Cataldi⁵, Vladimir Parpura⁶, Jelena Milasin¹ 

¹Department of Human Genetics, Faculty of Dental Medicine, University of Belgrade, 11000 Belgrade, Serbia

²Graphene Laboratory, Center for Solid State and New Materials, Institute of Physics, University of Belgrade, 11000 Belgrade, Serbia

³Departments of Chemistry and Chemical Engineering and Center for Nanoscale Science and Engineering, University of California, Riverside, California 92521, United States

⁴Carbon Solutions, Inc., Riverside, California 92507, United States

⁵Department of Pharmacy, Università 'G. d'Annunzio', Via dei Vestini, I-66100 Chieti, Italy

⁶Department of Neurobiology, University of Alabama, Birmingham, Alabama 35294, United States

This article has been accepted for publication and undergone full peer review but has not been through the copyediting, typesetting, pagination and proofreading process which may lead to differences between this version and the Version of Record. Please cite this article as an 'Accepted Article', doi: 10.1002/jbm.a.36461

SCAP differentiation into neural lineage using graphene dispersion and carbon nanotubes

ABSTRACT

Stem cell-based therapies are considered a promising treatment modality for many medical conditions. Several types of stem cells with variable differentiation potentials have been isolated from dental tissues, among them stem cells from apical papilla (SCAP). In parallel, new classes of biocompatible nanomaterials have also been developed, including graphene and carbon nanotube-based materials. The aim of the study was to assess whether graphene dispersion (GD) and water-soluble single walled carbon nanotubes (ws-SWCNT), may enhance SCAPs capacity to undergo neural differentiation. SCAPs cultivated in neuroinductive medium supplemented with GD and ws-SWCNT, separately and in combination, were subjected to neural marker analysis by real-time PCR (NF-M, ngn-2, β III-tubulin, MAP2) and immunocytochemistry (NeuN and β III-tubulin). GD, ws-SWCNT, and their combination, had neuro-stimulatory effects on SCAPs, as judged by the production of neural markers. Compared to cells grown in nanomaterial free medium, cells with GD showed higher production of B3T, cells with ws-SWCNT had higher production of ngn-2 and NF-M, while the combination of nanomaterials gave similar levels of both B3T and NF-M as the neuroinductive medium alone, but with the finest neuron-like morphology. In conclusion, GD and ws-SWCNT seem to enhance neural differentiation of stem cells from apical papilla.

Keywords: stem cells, apical papilla, neural induction, graphene dispersion, carbon nanotubes

SCAP differentiation into neural lineage using graphene dispersion and carbon nanotubes

INTRODUCTION

Stem cells (SCs), thanks to their ability to undergo differentiation into various cell types and great capacity for self-renewal, have a prominent role in regeneration of damaged tissues and/or organs. They could also bring under control some illnesses such as Alzheimer's disease, amyotrophic lateral sclerosis, Parkinson's disease and diabetes (1, 2).

Stem cells can be derived from embryonic tissues (embryonic stem cells, ESCs), various postnatal tissues (adult stem cells, ASCs), as well as by cell reprogramming (inducible pluripotent stem cells, iPSCs). ASCs of mesodermal origin are referred to as mesenchymal SCs (MSCs) and under permissive environment they show a remarkable capacity to differentiate into various cell lineages (3, 4). Owing to this differentiation potency, to immunosuppressive activity and high self-renewal capacity, MSCs are considered to be extremely valuable for clinical use.

Many dental tissues represent niches of MSCs and are becoming increasingly attractive in basic research and applicative regeneration studies due to their easy accessibility and absence of additional health risks for the donor. Apical papilla is a soft tissue at the apex of a not fully formed tooth, containing more than 95% of MSCs (stem cells from apical papilla or SCAP). Originating from neural crest, they express some early neural markers even without neural induction. They can be transformed into different cell types of neural lineage, therefore making them suitable for potential therapeutic applications in neurodegenerative diseases. Further exploration of their biological behavior is fundamental (5-9).

A growing number of nanomaterial-based scaffolds are being tested for their use in tissue engineering. Single wall carbon nanotubes (SWCNTs) are proposed as a promising material for neuro-regeneration, owing to their unique properties and biocompatibility (10-12), SWCNTs can

SCAP differentiation into neural lineage using graphene dispersion and carbon nanotubes

be added in neuronal cell cultures as strata or as colloidal aqueous solutions (CITs)(13, 14); the latter ws-SWCNTs are shown to enhance neurite outgrowth in neural cultures, or when applied on spinal cord injuries (9).

Graphene based nanomaterials (GBN), are also becoming increasingly popular in bioengineering, due to their biophysical properties along with their biocompatibility (15-18). Graphene improves cell adhesion during the differentiation process and promotes differentiation towards neurons more than towards glial cells. All reported data suggest that GBNs, and among them more specifically graphene oxide, may represent a superior nanostructured scaffold for neural differentiation and neuro-regeneration (19-23). While graphene oxide application in various stem cell differentiation settings has been widely studied, another potentially interesting GBN, the exfoliated liquid graphite in the form of colloidal dispersion of two-dimensional flakes (GD), has been rather ignored, though its biocompatibility and nontoxicity, along with cell proliferation support, have been demonstrated (24-28).

The aim of the present study was to explore SCAP potential to undergo neural differentiation in the presence of two types of nanomaterials (ws-SWCNT and GD), separately and in combination, i.e. to evaluate the neuro-stimulatory effects of the two nanomaterials, by means of cell morphology, immunocytochemistry and real-time gene expression analyses.

MATERIALS AND METHODS

The study protocol complied with the Fortaleza (Brazil) Revision of the Helsinki Declaration and was approved by the Ethical Committee of the School of Dental Medicine, University of Belgrade. Immature, impacted third lower molars were extracted from teenage patients at the

SCAP differentiation into neural lineage using graphene dispersion and carbon nanotubes

Clinic for Oral Surgery (Figure 1), School of Dental Medicine, University of Belgrade, Serbia after signing the informed consents by patient's parents.

Preparation of graphene dispersion

For the fabrication of graphene dispersion (GD) the method of liquid phase exfoliation (LPE) has been used as a promising route for high-quality and large-scale production of 2D materials. We followed the protocol described in earlier papers (29, 30). An initial concentration of graphite powder (Sigma Aldrich-332461) in N-Methyl-2-pyrrolidone (NMP) (Sigma Aldrich-328634) was 18 mg/ml. The mixture was sonicated in a low power sonic bath (Bransonic CPXH Ultrasonic 8 Cleaning Bath) for 14 hours. In order to prevent re-aggregation and reduce the amount of unexfoliated graphite, the solution was centrifuged for 60 min at 3000 rpm. The next step was decantation that was carried out by pipetting off the top half of the dispersion. In the end, the concentration of the grey liquid consisting of graphene sheets dispersed in solution, was 320 $\mu\text{g/ml}$. The Lambert–Beer law was applied to UV/VIS absorption spectra to calculate graphene concentration by estimating the absorbance at 660 nm. The cell's length was 1 cm and the extinction coefficient of graphene ($\alpha = 24.60 \text{ mL mg}^{-1} \text{ m}^{-1}$), in NMP solutions was taken from literature (31). Absorption spectra were measured using the UV/VIS Spectrophotometer (Perkin-Elmer Lambda 4B).

Preparation of water-soluble SWCNT functionalized with poly-m-aminobenzene sulphonic acid

The functionalization of SWCNTs, to render their water solubility, was done as described previously (10) (also See Supplemental Information for further details). In brief, commercially available purified SWCNT-COOH material (P3-SWCNT, Carbon Solutions, Inc., Riverside, CA) was reacted with oxalyl chloride in order to make an acyl chloride intermediate (SWCNT-

SCAP differentiation into neural lineage using graphene dispersion and carbon nanotubes

COCl). P3-SWNT material (1 g) was dispersed in 1 L of dry DMF by ultrasonication for 2 h and high-shear mixing for 1 h to give a homogeneous suspension. Oxalyl chloride (20 mL) was added drop-wise to the SWCNT-COOH solution at 0°C under argon. The reaction mixture was stirred at 0°C for 2 h, at room temperature for 2 h, and heated overnight at 70°C to remove the excess oxalyl chloride (boiling point 63°C). The functionalization of the resulting SWCNT-COCl intermediate was done by the addition of poly-m-aminobenzene sulphonic acid (PABS, 5 g) to form the corresponding graft copolymer (SWCNT-PABS), by allowing the components to interreact at 120°C for 5 days. Afterwards, the mixture was filtered through a membrane (pore size 0.22 µm), repeatedly rinsed with 95% ethanol and then with distilled water to remove any excess of PABS. The resulting final product (SWCNT-PABS) was collected on a membrane, dried under vacuum overnight, and then reconstituted in distilled water in 2.0 mg/mL stock solutions. SWCNT-PABS has a composition of 35 weight percent (wt%) SWCNTs and 65 wt% PABS.

Isolation and cultivation of stem cells from apical papilla (SCAP)

Atraumatically extracted teeth were transferred to the laboratory in Dulbecco's Modified Eagle Medium (DMEM) containing 20% of Mesenchymal Stem Cells qualified Fetal Bovine Serum (MSC-FBS) and 1% of antibiotic-antimycotic solution (Thermo Fisher Scientific, USA). The samples were processed within 30 minutes after the extraction. Stem cells from apical papilla were isolated according to growth explant method previously described by Kerkis et Caplan, under sterile conditions(32). Briefly, teeth were extensively rinsed with Dulbecco's Phosphate Buffered Saline (DPBS, Thermo Fisher Scientific, USA) and apical papilla was gently scrapped from the root apex using sterile surgical blade. Soft tissue was minced into small pieces, and transferred into T-25 flasks containing cell culture growth medium (DMEM supplemented with

SCAP differentiation into neural lineage using graphene dispersion and carbon nanotubes

10% MSC-FBS and 1% antibiotic-antimycotic solution). Cells were then cultured under standard conditions (37 °C, 95% air-5% CO₂ atmosphere, 95% humidity) and the culture medium was changed every 2-3 days. Subconfluent, cells were detached from the plastic surface of tissue flask with recombinant cell-dissociation enzyme (TrypLE™ Express Enzyme, Thermo Fisher Scientific, USA) according to manufacturer's protocol, and seeded into new flasks. All subsequent experiments were performed with cells from the fourth (P4) and the fifth (P5) passage.

Cell differentiation capacity

In order to confirm multipotency of SCAP, cells from the fourth passage (P4) were subjected to osteogenic, adipogenic and chondrogenic differentiation. Osteogenic potential of SCAP was determined after 28 days of cell culturing in osteogenic medium (StemPro™ Osteogenesis Differentiation Kit, Thermo Fisher Scientific, USA) according to manufacturers' recommendations. Cells were seeded in six-well plates at density of 5×10^3 cells/cm² and culturing medium was changed every 2-3 days. Adipogenic stimulation also lasted 28 days in appropriate media (StemPro™ Adipogenesis Differentiation Kit, Thermo Fisher Scientific, USA) and seeding density of 1×10^4 cells/cm² on the six well plates. For the chondrogenesis, cells were seeded in a form of micromass at total number of 1.5×10^6 and grown on six-well plates in commercially available media (StemPro™ Chondrogenesis Differentiation Kit, Thermo Fisher Scientific, USA) for 21 days. Cells cultured in standard growth medium were used as a negative control. Differentiation into the three lineages was assessed by histological staining. Prior to staining procedures, cells were fixed with 4% paraformaldehyde (PFA) for 30 minutes at room temperature and after that washed twice with DPBS. Alizarin Red S staining was used for determination of calcification nodule formations of the extracellular matrix in cultures grown in

SCAP differentiation into neural lineage using graphene dispersion and carbon nanotubes

osteogenic medium. Two percent Alizarin Red S (Centrohem, Serbia) solution, at pH 4.2, was added to the wells. After 30 minutes of incubation, dye was removed and cells were rinsed twice with distilled water. Oil Red O staining was used for visualizing intracellular lipid vacuoles upon adipogenic differentiation. Cells were incubated for 15 minutes in 0.5% Oil Red O solution (Sigma Aldrich, Germany) and the excess of dye was removed by gentle rinsing with DPBS. Chondrogenesis was confirmed by 0.1% solution Safranin O (Centrohem, Serbia) positive staining. Alizarin Red S, Oil Red O and Safranin O stained areas were observed under inverted microscope (Primovert, Zeiss, Germany), and photographed.

Flow cytometry and immunophenotyping

Flow cytometry analyses were performed in order to assess the expression of specific mesenchymal markers in SCAP from the 5th passage (P5). The markers used for these analyses were: fluorescein-isothiocyanate (FITC) labeled mouse monoclonal antibodies against CD90, CD105, CD34 and phycoerythrin (PE) labeled mouse monoclonal antibodies against CD73 and CD45 (all antibodies were purchased from Exbio, Czech Republic). Cells were harvested with TrypLE™ Express solution, washed with DPBS supplemented with 10% FBS, and finally counted on automated cell counter (Countess™, Invitrogen, USA). One million of cells were resuspended in 1 ml of 10% FBS solution in DPBS, and incubated with adequate antibodies for 45 minutes in the refrigerator. After incubation, cells were fixed with 4% paraformaldehyde for 20 minutes and finally rinsed twice with DPBS. Cells were analyzed on tabletop flow cytometer (Partec, Munster, Germany) and results were processed by software (Sysmex Partec, Goerlitz, Germany).

SCAP differentiation into neural lineage using graphene dispersion and carbon nanotubes

Neurodifferentiation

For 24 hours cells were grown in standard culture medium. After that, over the next 4 hours SCAP were incubated in neural preinduction medium, DMEM with 100 mM beta-mercaptoethanol. Differentiation of SCAP was continued in neural induction medium containing recombinant human basic fibroblast growth factor (bFGF, Thermo Fisher Scientific, USA), neural growth factor (NGF, Thermo Fisher Scientific, USA), and B27 supplement (Thermo Fisher Scientific, USA) in DMEM, according to previously reported protocol(33). To evaluate potential stimulatory effects of carbon nanomaterials on neural differentiation of SCAP, four protocols were applied: neural induction medium without nanomaterials (protocol A); neural induction medium and 10 μ l (of 2 mg/mL) of SWCNT-PABS (protocol B); neural induction medium and 10 μ l (of 18 mg/ml) of GD prepared solution (protocol C); neural induction medium supplemented with 10 μ l SWCNT-PABS and 10 μ l GD (protocol D), changed with freshly made medium every 2-3 days.

Light microscopy

Cell morphology was monitored under inverted microscope (Primovert, Zeiss, Germany) and photographed. Between days 5 and 7 of neurogenic culture, the cells showed a transition from fibroblast-like to neuron-like cell bodies with long processes, suggesting that the stem cells differentiated into neurons/neuron-like cells. At that point they were subjected to qPCR and immunocytochemistry analysis.

RNA isolation and gene expression analyses by real time PCR (qPCR)

For the gene expression analyses 1.25×10^5 cells were seeded in T-25 tissue culture flask. After neurogenic stimulation, total RNA was extracted using guanidinium thiocyanate-phenol-

SCAP differentiation into neural lineage using graphene dispersion and carbon nanotubes

chloroform extraction procedure with commercially available reagent (TRIzol™ Reagent, Thermo Fisher Scientific, USA) according to recommendations. RNA purity and concentration were assessed using microvolume spectrophotometer (BioSpec Nano, Shimadzu, Japan). One microgram of total RNA was reversely transcribed to cDNA using RevertAid First Strand cDNA Synthesis Kit (Thermo Fisher Scientific, USA) and oligo (dT)₁₈ primers. cDNA was subsequently used for Real-Time Polymerase Chain Reaction (qPCR) analyses on a Line Gene-K Fluorescence Real-time PCR Detection System (BIOER Technology, Shanghai, China). PCR reaction mix (25 μl) contained 12.5 μl of real-time PCR master mix (Maxima SYBR Green/ROX qPCR Master Mix, Thermo Fisher Scientific, USA), 1 μl of forward and reverse primer (final concentration 200 nM), 2 μl of cDNA and PCR-grade water. Each run had initial denaturation at 95°C for 10 minutes, followed by 40 cycles of denaturation (95°C, 15 s), annealing (55°C, 30 s) and elongation (72°C, 30 s). Data acquisition was performed in each elongation step. Specificity of PCR products was checked by melting curve analyses and the relative gene expression level was assessed using the comparative $2^{\Delta\Delta C_t}$ method (34). All reactions were carried out in duplicate. The relative expression levels of mRNA for neural markers for each sample were calculated as the ratio between the expression of the gene of interest and the expression of the selected endogenous control, glyceraldehyde 3-phosphate dehydrogenase (GAPDH). List of primers used in qPCR are given in Table 1.

Immunocytochemistry

For the immunocytochemical analyses cells were seeded onto 25 mm diameter round glass coverslips at density of 5×10^3 cells/cm² and subjected to neurodifferentiation protocol as described above. **On the 7th day** of neural induction, cells were rinsed three times in DPBS, fixed with 4% PFA solution for 20 minutes, rinsed three times with DPBS and incubated at room

SCAP differentiation into neural lineage using graphene dispersion and carbon nanotubes

temperature for 45 minutes in blocking and permeabilization buffer (10% Bovine Serum Albumin and 0.1% Triton X-100 in DPBS). For immunofluorescent detection of neuronal and glial cell marker expression, cells were incubated with following primary antibodies: rabbit anti- β III-tubulin (B3T, 1:400, Cell Signaling, USA), rabbit anti-neuronal nuclei (NeuN, 1:250, Millipore, Germany) and mouse anti-glial fibrillary acidic protein (GFAP, 1:400, Millipore, Germany). Primary antibodies were incubated at 4°C overnight and subsequently washed three times with DPBS. Cell samples were incubated with secondary antibodies - donkey anti-mouse Alexa Fluor 488 (1:200, Invitrogen, USA), donkey anti-rabbit Alexa Fluor 555 (1:200, Invitrogen, USA) and donkey anti-rabbit Alexa Fluor 657 (1:200, Invitrogen, USA) for 2 hours in dark at room temperature. Cells were washed three times in DPBS and stained with 4-, 6-diamidino- 2-phenylindole (1:4000, DAPI, Molecular Probes, USA) for 10 minutes in dark at room temperature. After washing in DPBS cell samples were mounted with Mowiol medium (Sigma Aldrich) on microscope slides. Immunofluorescence microscopy images were obtained by confocal laser-scanning microscope (LSM 510, Carl Zeiss GmbH, Jena, Germany) equipped with Ar 488 and HeNe 543 and 633 laser lines. Micrographs were analyzed using Fiji-Image J software (NIH, USA).

RESULTS

Osteogenic, chondrogenic and adipogenic differentiation of stem cells from apical papilla demonstrated their multipotency

Osteogenic, adipogenic and chondrogenic differentiation of SCAP were verified by appropriate histological stains. Positive staining of calcification nodule formations with Alizarin Red S was

SCAP differentiation into neural lineage using graphene dispersion and carbon nanotubes

indicative of osteogenic differentiation, accumulation of Oil Red O in intracellular lipid vacuoles of adipogenic differentiation, whereas Safranin O binding to proteoglycans was a proof of chondrogenic differentiation of SCAP (Figure 2). Cells of the control group remained unstained.

Immunophenotyping revealed expression of mesenchymal stem cell markers

Flow-cytometry analyses were performed on P5 (fifth passage) stem cell from apical papilla. Flow-cytometry revealed the expression of mesenchymal stem cell markers CD73, CD90 and CD105 (99%, 91.3% and 96%, respectively), and the absence of hematopoietic markers CD34 (0.34%) and CD45 (0.01%) (Figure 3).

Neuron like morphology was demonstrated by light microscopy

Cell morphology was observed every day, and photographed on the seventh day. Protocol A cells presented short cell projections and poor neural like morphology, similarly to cells grown under protocol B conditions. Cells in protocol C cultures had long slender projections with triangular cell bodies. Under protocol D conditions, cells also achieved a good neuron like morphology (Figure 4).

Neural markers MAP2, ngn-2, β III-tubulin, NF-M and NeuN were expressed in SCAP after neuroinduction

Pilot experiments performed in different time points (data not shown) suggested that the 7th day of neuroinduction was optimal for expression analysis. The relative expression of five neural markers (microtubule-associated protein 2 (MAP2), neurofilament medium (NF-M), neurogenin-2 (ngn-2), β III-tubulin and glial fibrillary acidic protein (GFAP)). is given in Figure 5. The predominant markers in all cell cultures were β III-tubulin and NF-M, but their ratios were different. In the presence of SWCNT-PABS the expression of NF-M was higher than the

SCAP differentiation into neural lineage using graphene dispersion and carbon nanotubes

expression of β III-tubulin while in the presence of GD it was the opposite. In cultures without nanomaterials as well as in cultures with both nanomaterials a balanced expression of NF-M and β III-tubulin was found. Cells grown in neural induction medium only, showed higher expression of MAP2 and GFAP compared to other protocols.

The markers were expressed at their proper (expected) cellular localization. As registered under light microscopy, a fine neuron-like morphology was observed in cells cultivated under protocol D, i.e. in the presence of both nanomaterials (Fig. 6A), and a robust immunoreactivity for markers β III-tubulin and NeuN was recorded (Fig. 6B and 6C, respectively). A similar morphology was obtained under protocol C although the expression of β III-tubulin was higher in cells cultivated with GD only, than with the two nanomaterials, a finding in agreement with real-time analysis (Fig.7). The expression of astroglial cell marker GFAP was observed only in cells grown in neural induction medium without nanomaterials (data not shown).

DISCUSSION

Since they originate from neural crest, dental tissue SCs have been extensively studied as a possible approach for replacing lost cells in CNS diseases or injuries (9). MSCs derived from apical papilla are becoming an increasingly attractive stem cell source because they belong to a developing, easily accessible tissue, which would be otherwise discarded as biological waste, with cells possessing high proliferation rate, plasticity and differentiation capacity (6).

Graphene, a crystalline allotrope of carbon with two-dimensional properties, may be synthesized and functionalized in various ways, and loaded with different molecules of interest. Graphene based nanomaterials have proved to be promising tools in different fields of nanomedicine, owing to their unique structure, chemical stability, exceptional mechanical properties, good

SCAP differentiation into neural lineage using graphene dispersion and carbon nanotubes

biocompatibility and bactericidal potential (35). These single-atomic layered sheet materials have also the ability to adsorb growth factors and exhibit unprecedented electrical properties, which is of particular importance when used as cell scaffolds (19, 36). Their use as support for stem cell differentiation has lately been an area of intensive studies. It has been reported that both CNTs and graphene can stimulate neural stem cells differentiation, neuronal and oligodendrocyte growth, and the formation of active synaptic contacts in cell culture. But despite some similarities, they have different impact on cells (23). According to available literature, stem cells subjected to neural differentiation on substrates filmed with graphene exhibited better neural morphology and higher expression of neural markers, while SWCNT seemed to promote both glial and neuronal differentiation (37-39).

It must be emphasized that experiments on graphene dispersion (GD) utilization in stem cell differentiation are completely inexistent. One study only has previously shown GD biocompatibility and another has demonstrated good PC12 attachment and proliferation (27, 28). Moreover, there are no studies exploring the combined use of CNT and GD as materials that hold potential to synergistically stimulate stem cell neuro-differentiation and more specifically SCAP neuro-differentiation.

In the present study, it was demonstrated that GD may exert stimulatory effects on dental stem cell neuro-differentiation. Namely, cells cultivated with GD, compared to other protocols, exhibited the highest level of β III-tubulin, a microtubule protein expressed during neurogenesis and involved in axon guidance. The level of MAP2, a mature neuron marker, was also higher in cells grown with GD than in cells grown according to the other two protocols with nanomaterials. The level of *ngn-2*, a transcription factor inhibitor of glial cell development, was

SCAP differentiation into neural lineage using graphene dispersion and carbon nanotubes

low, and yet gliogenesis seemed suppressed as judged by the lack of expression of GFAP, a glial cell marker, a phenomenon that might be attributed to GD.

SCAPs grown with SWCNT-PABS showed better neural differentiation when compared to cells grown without the addition of nanomaterial, a result which is in accordance with previously reported data (39). Levels of *ngn-2*, β III-tubulin and NF-M, a neuronal cytoskeleton element found at high concentration in axons, were higher in cells grown with SWCNT-PABS than in the basic neuroinductive medium.

The combination of the two nanomaterials resulted in a seemingly well-adjusted ratio of NF-M and β III-tubulin levels, accompanied with a robust expression of NeuN. This treatment ensured the most compelling cell morphology with clear neuron shaped body and long processes.

The predisposition of SCAPs to differentiate toward neural lineages, as well as the neuroinductive properties of GD and SWCNT, should warrant further studies of dental stem cells in conjunction with these nanomaterials, with the aim of finding a superior solution for autologous neuroregenerative therapy.

Acknowledgments: This work was supported by grant n^o 175075 of the Ministry of Education, Science and Technological Development of Serbia.

We express our deepest gratitude to dr Djordje Miljkovic from the Institute of Biological Research for the flow-cytometry analyses.

The authors declare no potential conflict of interest.

SCAP differentiation into neural lineage using graphene dispersion and carbon nanotubes

LITERATURE

1. Volkman R, Offen D. Concise Review: Mesenchymal Stem Cells in Neurodegenerative Diseases. *Stem Cells*. 2017;35(8):1867-80.
2. Pan XH, Huang X, Ruan GP, Pang RQ, Chen Q, Wang JX, et al. Umbilical cord mesenchymal stem cells are able to undergo differentiation into functional islet-like cells in type 2 diabetic tree shrews. *Mol Cell Probes*. 2017;34:1-12.
3. Le Blanc K, Pittenger M. Mesenchymal stem cells: progress toward promise. *Cytotherapy*. 2005;7(1):36-45.
4. Pittenger MF, Mackay AM, Beck SC, Jaiswal RK, Douglas R, Mosca JD, et al. Multilineage potential of adult human mesenchymal stem cells. *Science*. 1999;284(5411):143-7.
5. Sonoyama W, Liu Y, Yamaza T, Tuan RS, Wang S, Shi S, et al. Characterization of the apical papilla and its residing stem cells from human immature permanent teeth: a pilot study. *J Endod*. 2008;34(2):166-71.
6. Huang GT, Sonoyama W, Liu Y, Liu H, Wang S, Shi S. The hidden treasure in apical papilla: the potential role in pulp/dentin regeneration and bioroot engineering. *J Endod*. 2008;34(6):645-51.
7. Egusa H, Sonoyama W, Nishimura M, Atsuta I, Akiyama K. Stem cells in dentistry--part I: stem cell sources. *J Prosthodont Res*. 2012;56(3):151-65.
8. Ibarretxe G, Crende O, Aurrekoetxea M, García-Murga V, Etxaniz J, Unda F. Neural crest stem cells from dental tissues: a new hope for dental and neural regeneration. *Stem Cells Int*. 2012;2012:103503.
9. Xiao L, Tsutsui T. Human dental mesenchymal stem cells and neural regeneration. *Hum Cell*. 2013;26(3):91-6.
10. Gottipati MK, Kalinina I, Bekyarova E, Haddon RC, Parpura V. Chemically functionalized water-soluble single-walled carbon nanotubes modulate morpho-functional characteristics of astrocytes. *Nano Lett*. 2012;12(9):4742-7.
11. Lee W, Parpura V. Chapter 6 - Carbon nanotubes as substrates/scaffolds for neural cell growth. *Prog Brain Res*. 2009;180:110-25.
12. Lee HJ, Park J, Yoon OJ, Kim HW, Lee DY, Kim DH, et al. Amine-modified single-walled carbon nanotubes protect neurons from injury in a rat stroke model. *Nat Nanotechnol*. 2011;6(2):121-5.
13. Hu H, Ni Y, Montana V, Haddon RC, Parpura V. Chemically Functionalized Carbon Nanotubes as Substrates for Neuronal Growth. *Nano Lett*. 2004;4(3):507-11.
14. Ni Y, Hu H, Malarkey EB, Zhao B, Montana V, Haddon RC, et al. Chemically functionalized water soluble single-walled carbon nanotubes modulate neurite outgrowth. *J Nanosci Nanotechnol*. 2005;5(10):1707-12.
15. Wang Y, Li Z, Wang J, Li J, Lin Y. Graphene and graphene oxide: biofunctionalization and applications in biotechnology. *Trends Biotechnol*. 2011;29(5):205-12.
16. Lee WC, Lim CH, Shi H, Tang LA, Wang Y, Lim CT, et al. Origin of enhanced stem cell growth and differentiation on graphene and graphene oxide. *ACS Nano*. 2011;5(9):7334-41.
17. La WG, Park S, Yoon HH, Jeong GJ, Lee TJ, Bhang SH, et al. Delivery of a therapeutic protein for bone regeneration from a substrate coated with graphene oxide. *Small*. 2013;9(23):4051-60.

SCAP differentiation into neural lineage using graphene dispersion and carbon nanotubes

18. Lee YJ, Seo TH, Lee S, Jang W, Kim MJ, Sung JS. Neuronal differentiation of human mesenchymal stem cells in response to the domain size of graphene substrates. *Journal of Biomedical Materials Research Part A*. 2017.
19. Bressan E, Ferroni L, Gardin C, Sbricoli L, Gobbato L, Ludovichetti FS, et al. Graphene based scaffolds effects on stem cells commitment. *J Transl Med*. 2014;12:296.
20. Park SY, Park J, Sim SH, Sung MG, Kim KS, Hong BH, et al. Enhanced differentiation of human neural stem cells into neurons on graphene. *Adv Mater*. 2011;23(36):H263-7.
21. Wang Y, Lee WC, Manga KK, Ang PK, Lu J, Liu YP, et al. Fluorinated graphene for promoting neuro-induction of stem cells. *Adv Mater*. 2012;24(31):4285-90.
22. Tang M, Song Q, Li N, Jiang Z, Huang R, Cheng G. Enhancement of electrical signaling in neural networks on graphene films. *Biomaterials*. 2013;34(27):6402-11.
23. Hong SW, Lee JH, Kang SH, Hwang EY, Hwang YS, Lee MH, et al. Enhanced neural cell adhesion and neurite outgrowth on graphene-based biomimetic substrates. *Biomed Res Int*. 2014;2014:212149.
24. Nair M, Nancy D, Krishnan AG, Anjusree GS, Vadukumpully S, Nair SV. Graphene oxide nanoflakes incorporated gelatin-hydroxyapatite scaffolds enhance osteogenic differentiation of human mesenchymal stem cells. *Nanotechnology*. 2015;26(16):161001.
25. Park J, Park S, Ryu S, Bhang SH, Kim J, Yoon JK, et al. Graphene-regulated cardiomyogenic differentiation process of mesenchymal stem cells by enhancing the expression of extracellular matrix proteins and cell signaling molecules. *Adv Healthc Mater*. 2014;3(2):176-81.
26. Chaudhuri B, Bhadra D, Moroni L, Pramanik K. Myoblast differentiation of human mesenchymal stem cells on graphene oxide and electrospun graphene oxide-polymer composite fibrous meshes: importance of graphene oxide conductivity and dielectric constant on their biocompatibility. *Biofabrication*. 2015;7(1):015009.
27. Ayán-Varela M, Villar-Rodil S, Paredes JI, Munuera JM, Pagán A, Lozano-Pérez AA, et al. Investigating the Dispersion Behavior in Solvents, Biocompatibility, and Use as Support for Highly Efficient Metal Catalysts of Exfoliated Graphitic Carbon Nitride. *ACS Appl Mater Interfaces*. 2015;7(43):24032-45.
28. Gopinathan J, Quigley AF, Bhattacharyya A, Padhye R, Kapsa RM, Nayak R, et al. Preparation, characterisation, and in vitro evaluation of electrically conducting poly(ϵ -caprolactone)-based nanocomposite scaffolds using PC12 cells. *J Biomed Mater Res A*. 2016;104(4):853-65.
29. Haar S, El Gemayel M, Shin Y, Melinte G, Squillaci MA, Ersen O, et al. Enhancing the Liquid-Phase Exfoliation of Graphene in Organic Solvents upon Addition of n-Octylbenzene. *Sci Rep*. 2015;5:16684.
30. Matković A, Milošević I, Milićević M, Tomašević-Ilić T, Pešić J, Musić M, et al. Enhanced sheet conductivity of Langmuir–Blodgett assembled graphene thin films by chemical doping. *2D Materials*. 2016;3(1):015002.
31. Hernandez Y, Nicolosi V, Lotya M, Blighe FM, Sun Z, De S, et al. High-yield production of graphene by liquid-phase exfoliation of graphite. *Nat Nanotechnol*. 2008;3(9):563-8.
32. Kerkis I, Caplan AI. Stem cells in dental pulp of deciduous teeth. *Tissue Eng Part B Rev*. 2012;18(2):129-38.
33. Osathanon T, Sawangmake C, Nowwarote N, Pavasant P. Neurogenic differentiation of human dental pulp stem cells using different induction protocols. *Oral Dis*. 2014;20(4):352-8.

SCAP differentiation into neural lineage using graphene dispersion and carbon nanotubes

34. Livak KJ, Schmittgen TD. Analysis of relative gene expression data using real-time quantitative PCR and the 2(-Delta Delta C(T)) Method. *Methods*. 2001;25(4):402-8.
35. Zhu Y, Murali S, Cai W, Li X, Suk JW, Potts JR, et al. Graphene and graphene oxide: synthesis, properties, and applications. *Advanced materials*. 2010;22(35):3906-24.
36. Neto AHC, Guinea F, Peres NMR, Novoselov KS, Geim AK. The electronic properties of graphene. *Reviews of modern physics*. 2009;81(1):109.
37. Lee J-R, Ryu S, Kim S, Kim B-S. Behaviors of stem cells on carbon nanotube. *Biomaterials Research*. 2015;19:3.
38. Solanki A, Chueng STD, Yin PT, Kappera R, Chhowalla M, Lee KB. Axonal Alignment and Enhanced Neuronal Differentiation of Neural Stem Cells on Graphene-Nanoparticle Hybrid Structures. *Advanced Materials*. 2013;25(38):5477-82.
39. Yang D, Li T, Xu M, Gao F, Yang J, Yang Z, et al. Graphene oxide promotes the differentiation of mouse embryonic stem cells to dopamine neurons. *Nanomedicine*. 2014;9(16):2445-55.

Accepted Article

SCAP differentiation into neural lineage using graphene dispersion and carbon nanotubes

FIGURE LEGENDS

Figure 1. (A) Patients' panoramic X ray with non-erupted developing third molar; (B) extracted third molar with apical papilla.

Figure 2. Multipotency confirmation by Alizarin Red S staining for osteodifferentiation, Safranin O staining for chondrodifferentiation and Oil Red O staining for adipodifferentiation.

Figure 3. The presence of mesenchymal markers CD73, CD90 and CD105, and the absence of hematopoietic markers CD34 and CD45 were assessed by flow-cytometry, on P5 cells.

Figure 4. Cell morphology after seven days: (A) protocol without nanomaterials; (B) protocol with SWCNT-PABS; (C) protocol with GD; (D) protocol with the combination of nanomaterials.

Magnification 200 \times .

Figure 5. Real-time PCR analysis of neural marker expression after 7 days in cultures with neural induction medium (protocol A), neural induction medium and SWCNT-PABS (protocol B), neural induction medium and GD (protocol C), neural induction medium and SWCNT-PABS + GD (protocol D).

Figure 6. (A) The combination of SWCNT-PABS and GD resulted in a good neuron-like morphology (β III-tubulin in red, nuclei in blue-DAPI); (B) strong immunostaining of β III-tubulin (red) and (C) NeuN (turquoise).

Figure 7. (A) β III-tubulin expression was higher in cells cultivated with GD than with GD and SWCNT-PABS (B). The difference was statistically significant (C).

Table 1. Sequences of primers used for quantitative PCR

Gene	Sequence of primers (5'→3')	Accession number
NF-M	F: TGGGAAATGGCTCGTCATTT R: CTTCATGGAAACGGCCAA	NG_008388.1
ngn-2	F: CCTGGAAACCATCTCACTTCA R: TACCCAAAGCCAAGAAATGC	NM_024019.2
GFAP	F: GCCTCAAGGACGAGATGG R: TCGCCCTCTAGCAGCTTC	NM_002055.3
B III-tubulin	F: GCCAAGTTCTGGAAGTCA R: GCCTCGTTGTAGTAGACGC	NM_006086.2
MAP2	F: AACCCTTTGAGAACACGACA R: TCTTTCCGTTTCATCTGCCA	NM_002374.3
GAPDH	F: TCATGACCACAGTCCATGCCATCA R: CCCTGTTGCTGTAGCCAAATTCGT	BC083511

Abbreviations: NF-M - neurofilament medium; ngn-2 – neurogenin-2; GFAP - glial fibrillary acidic protein; MAP2 - microtubule-associated protein 2; GAPDH - glyceraldehyde 3-phosphate dehydrogenase.

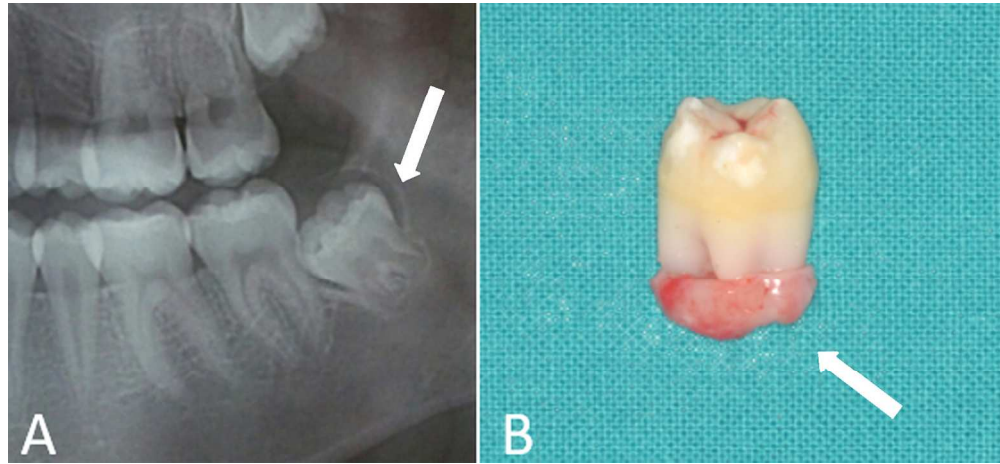
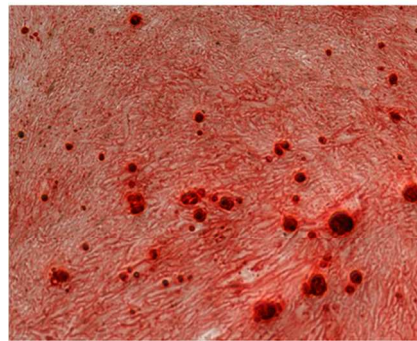


Figure 1. (A) Patients' panoramic X ray with non-erupted developing third molar; (B) extracted third molar with apical papilla.

152x69mm (300 x 300 DPI)

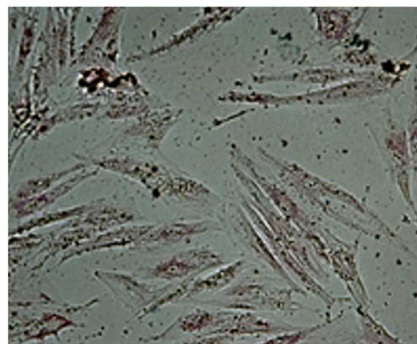
Accepted



OSTEODIFFERENTIATION



CHONDRODIFFERENTIATION



ADIPODIFFERENTIATION

Figure 2. Multipotency confirmation by Alizarin Red S staining for osteodifferentiation, Safranin O staining for chondrodifferentiation and Oil Red O staining for adipodifferentiation.

67x182mm (300 x 300 DPI)

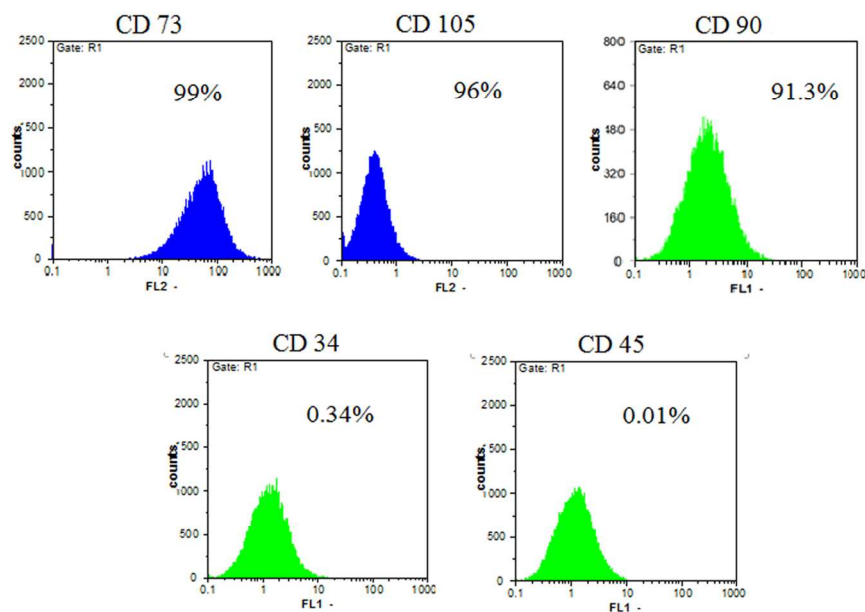


Figure 3. The presence of mesenchymal markers CD73, CD90 and CD105, and the absence of hematopoietic markers CD34 and CD45 were assessed by flow-cytometry, on P5 cells.

135x86mm (300 x 300 DPI)

Accepte

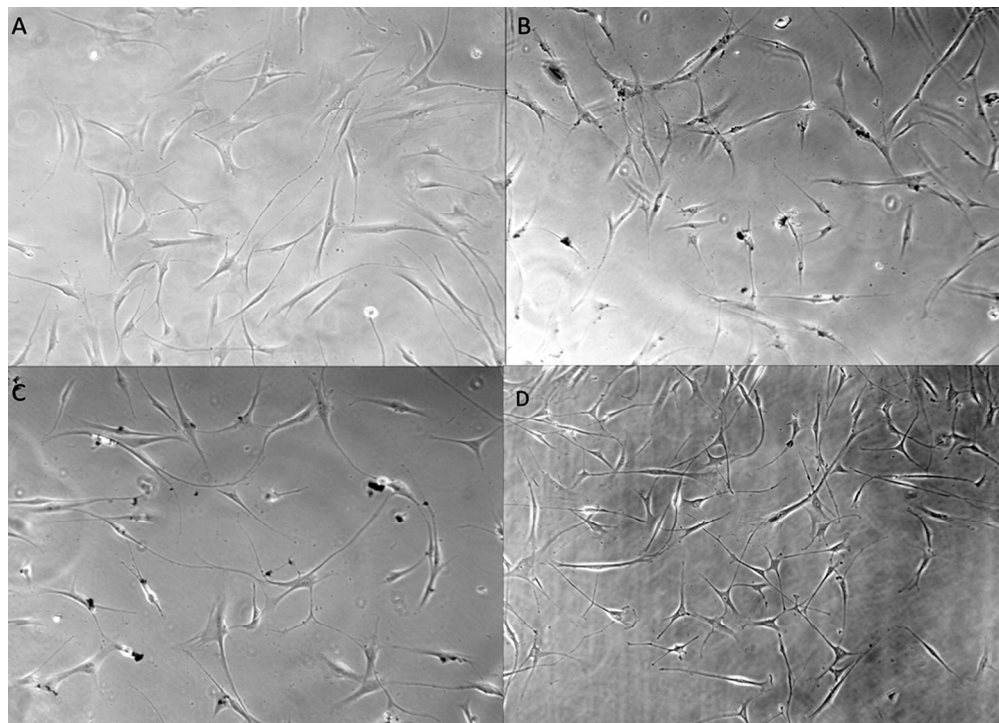


Figure 4. Cell morphology after seven days: (A) protocol without nanomaterials; (B) protocol with SWCNT-PABS; (C) protocol with GD; (D) protocol with the combination of nanomaterials. Magnification 200 \times .

127x91mm (300 x 300 DPI)

Accept

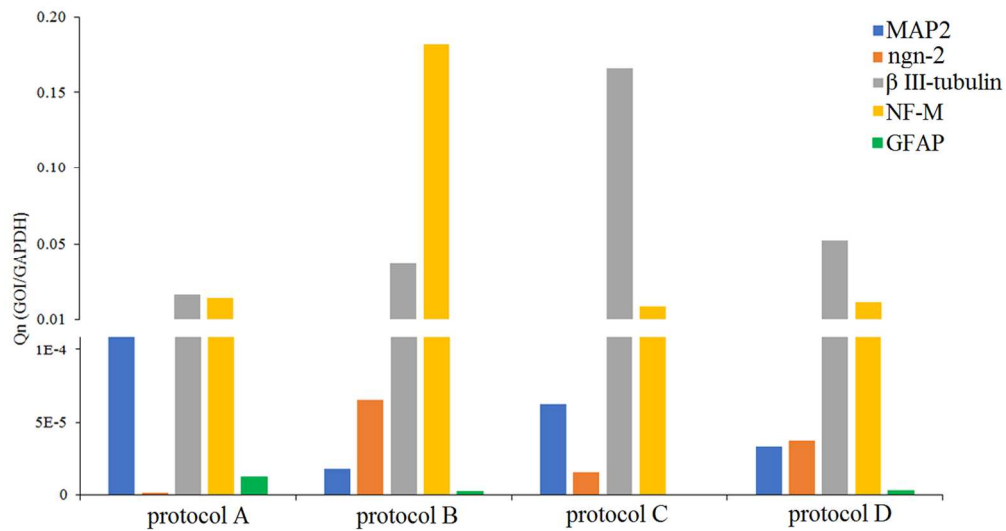


Figure 5. Real-time PCR analysis of neural marker expression after 7 days in cultures with neural induction medium (protocol A), neural induction medium and SWCNT-PABS (protocol B), neural induction medium and GD (protocol C), neural induction medium and SWCNT-PABS + GD (protocol D).

135x73mm (300 x 300 DPI)

Accepted

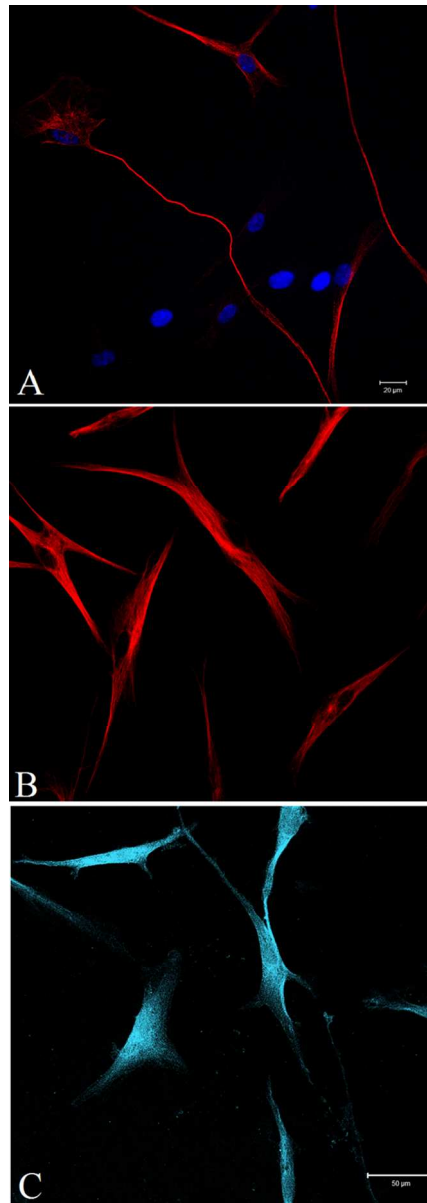


Figure 6. (A) The combination of SWCNT-PABS and GD resulted in a good neuron-like morphology (β III-tubulin in red, nuclei in blue-DAPI); (B) strong immunostaining of β III-tubulin (red) and (C) NeuN (turquoise).

53x152mm (300 x 300 DPI)

A

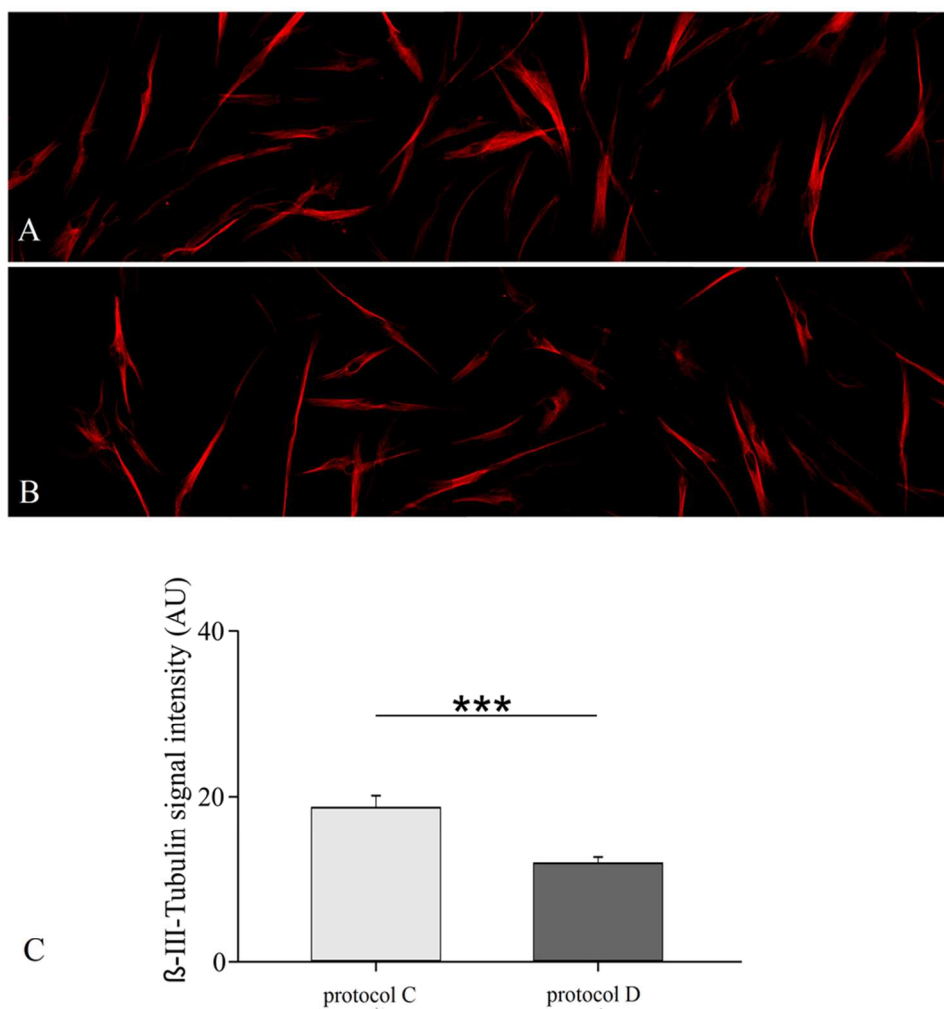


Figure 7. (A) β III-tubulin expression was higher in cells cultivated with GD than with GD and SWCNT-PABS (B). The difference was statistically significant (C).

101x108mm (300 x 300 DPI)

Acc

Direct Probing of Water Adsorption on Liquid-Phase Exfoliated WS₂ Films Formed by the Langmuir–Schaefer Technique

Jasna Vujin, Weixin Huang, Jovan Ciganović, Sylwia Ptasinska, and Radmila Panajotović*



Cite This: *Langmuir* 2023, 39, 8055–8064



Read Online

ACCESS |



Metrics & More

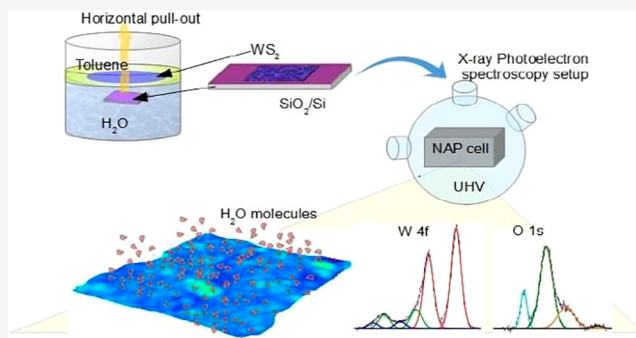


Article Recommendations



Supporting Information

ABSTRACT: Tungsten disulfide, a transition metal dichalcogenide, has numerous applications as active components in gas- and chemical-sensing devices, photovoltaic sources, photocatalyst substrates, etc. In such devices, the presence of water in the sensing environment is a factor whose role has not been well-understood. To address this problem, the *in situ* probing of H₂O molecule adsorption on WS₂ films supported on solid substrates has been performed in a near-ambient pressure X-ray photoelectron spectroscopy (NAP-XPS) setup. Instead, on the individual nanoflakes or spray-coated samples, the measurements were performed on highly transparent, homogeneous, thin films of WS₂ nanosheets self-assembled at the interface of two immiscible liquids, water and toluene, transferred onto a solid substrate by the Langmuir–Schaefer technique. This experiment shows that edge defects in nanoflakes, tungsten dangling bond ensuing the exfoliation in the liquid phase, represent active sites for the WO₃, WO_{3-x}, and WO₃·*n*H₂O formation under ambient conditions. These oxides interact with water molecules when the WS₂ films are exposed to water vapor in the NAP-XPS reaction cell. However, water molecules do not influence the W–S chemical bond, thus indicating the physisorption of H₂O molecules at the WS₂ film surface.



INTRODUCTION

Ambient humidity is an important factor in material research, especially in devices involving very thin layers of two-dimensional (2D) materials.^{1,2} When working under ambient conditions, the information about the influence of adsorbed water molecules on the surface of 2D materials represents essential information before understanding the interaction between any other adsorbed molecules and the 2D-material. If devices based on 2D-materials are designed to detect different types of analytes, their high sensitivity to humidity could cause significant issues and discrepancies during the measurements, concerning the consistency and stability of the electrical signal or their chemical response to the presence of the analyte. Hence, an insight into the variations in surface sensitivity of 2D-material thin films to ambient humidity is necessary. During the interaction with water molecules, the electronic properties of 2D-materials, such as resistance or charge carrier concentration, are easily modulated, implying that these materials can also be used as promising components of humidity sensors.^{3–5}

Tungsten disulfide (WS₂), the prominent member of the 2D transition metal dichalcogenide (TMD) material family, has attracted considerable attention regarding its potential application in the field of sensors as a result of its high surface-to-volume ratio, chemically active edges, and good electrical properties.⁶ The ultrahigh surface sensitivity to the

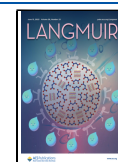
surrounding environment allows for the modification of the WS₂ surface, forming active biointerfaces convenient for biomedical applications.^{7–9} 2D WS₂ represents a very suitable platform for a sensor not only for biomolecules (proteins, DNA, and liposomes) and biological cells but also for various gas molecules, such as CO, H₂S, NH₃, NO₂, and H₂.^{10–13} WS₂ has also shown exceptional water-sensing properties with a prompt response and recovery time and good repeatability and stability that opened the possibility to use it as a humidity sensor for environmental monitoring or in healthcare applications as real-time dynamic monitoring of human breath.^{14,15}

In recent reports, it has been shown that the properties of WS₂ humidity-sensing devices depend on the defects present on the WS₂ nanosheets.^{14–18} Greater sensitivity to humidity can be a consequence of the existence of the low-coordination kinks, step edges, and dangling bonds at the edges of the WS₂ nanosheets. All of these types of defects have a significant role

Received: January 12, 2023

Revised: May 13, 2023

Published: June 2, 2023



in the humidity-sensing behavior because they represent potential active sites available for the adsorption/desorption of H₂O molecules. In the experiment of Jha et al.,¹⁷ it was reported that treatment of suspended WS₂ nanosheets with ultraviolet (UV) light improved linearity of the sensor at the expense of its response to humidity. They suggested that this effect might be due to the decreased amount of oxygen species after the UV light treatment, which, according to the Grotthuss mechanism,¹⁹ serves as a chemisorption site for water molecules. They also suggested that the existence of oxygenized sites on the WS₂ nanosheets is a consequence of the exfoliation protocol, which included acetone ketyl free radicals acting as a reducing agent. However, the direct evidence of the oxygen species in such samples and the mechanism of H₂O adsorption on WS₂ nanosheets are still missing.

The presence of humidity in ambient conditions is particularly important for the stability of the operation of gas sensors, which presents a significant limitation to their practical use.²⁰ In field-effect transistor (FET) gas sensors based on multilayer mechanically exfoliated WS₂ nanoflakes, Huo et al.¹⁶ found that the drain current and photosensitivity of the device are higher in vacuum than in ambient air. Their density functional theory (DFT) calculations showed that O₂ and H₂O molecules from air can be physically adsorbed on the surface of WS₂ nanoflakes and withdraw electrons from it, thus reducing its conductivity. As a consequence, the response of the FET sensor to reducing gases (NH₃) may be good but not so to O₂, for example. Therefore, to design efficient, stable, and reliable gas sensors based on the WS₂ nanoflakes, it is necessary to understand the mechanism of water adsorption on its surface.

Considering different methods of 2D-material production,^{14–16} liquid-phase exfoliation (LPE) stood out as a simple, inexpensive, and highly effective technique for obtaining a high yield of mono- and few-layer nanoflakes with the inherent (edges) types of defects.^{21–23} To use the full potential of LPE-processed WS₂ nanosheets for sensing applications, thin films need to be fabricated with a high degree of order and continuity and a uniform surface. Conventional few-step deposition methods of WS₂ dispersion (and other 2D-materials), such as drop-casting¹⁷ and spray and spin coating,^{24–26} suffer from non-uniformity, agglomeration of nanoflakes arising during solvent evaporation, lack of reproducibility, and lack of control over the thickness of the films, which all affect the quality of the sensor response. Langmuir–Blodgett (LB) and Langmuir–Schaefer (LS) interface assemblies were recognized as promising methods for overcoming existing drawbacks,^{27–29} especially in the case of self-assembled thin films of LPE graphene at the interface between two phases, liquid/gas or liquid/liquid.^{27,30–32} In particular, liquid/liquid interfaces provide a suitable opportunity for the formation of uniform films with better confinement of TMD nanosheets. Few reports exist of TMD assembly at the liquid/liquid interface,^{25,33,34} among them only one concerning the WS₂ nanosheet-based film.³⁵ Clark et al.³⁵ have demonstrated that continuous and closed-packed thin films can be obtained through the spontaneous creation of liquid/liquid assembly of TMDs (WS₂, MoS₂, and ReS₂), mixing the TMD nanosheet dispersion and octadecene by manual shaking. To avoid additional processing steps of film assembling and uncontrollable use of TMD dispersion, Nelson et al.²⁵ have proposed another approach, which is followed by direct injection of the MoS₂ dispersion to the preformed liquid/liquid interface. However, no such attempt for

producing the WS₂ film from nanoflakes has been made thus far, on octadecene or any other solvent on top of water.

In this work, we characterized the liquid-phase exfoliated WS₂ films obtained at the interface of two immiscible liquids, water and toluene, for the first time. The thin WS₂ films supported on the solid substrate by the LS technique were then exposed to pure water vapor in near ambient conditions for the direct, *in situ* measurement of water molecule adsorption on their surface formed of closely packed WS₂ nanoflakes. Various characterization techniques were employed to investigate the properties of the LPE-LS WS₂ films: optical spectroscopy methods [ultraviolet–visible (UV–vis) and Raman spectroscopy], near-ambient pressure X-ray photoelectron spectroscopy (NAP-XPS), as well as microscopy techniques [scanning electron microscopy (SEM) and atomic force microscopy (AFM)]. We demonstrated that films formed using the LS technique from LPE WS₂ dispersion have overlapping and edge-to-edge contact of WS₂ nanoflakes, providing a uniform large-area thin film. Notably, these films exhibit defects at the edges of overlapping nanoflakes that provide a dense grid of active sites for molecular adsorption. This simple and inexpensive protocol produces much more compact and highly uniform, thin WS₂ films that can be deposited onto various substrates compared to those previously reported.^{12,17,18,33}

We demonstrated that the heating in air or vacuum does not change the structure of such films, which allows them to be used in sensing devices at a high temperature without degradation. The NAP-XPS experimental data show that the water molecules adsorb predominantly on tungsten oxide sites, which originate from the exfoliation and film synthesis in ambient conditions, on and between the nanoflakes forming the film.

EXPERIMENTAL SECTION

Exfoliation and Characterization of WS₂ Dispersions. For liquid-phase exfoliation of WS₂ and preparation of dispersion, we followed the protocol described in an earlier paper.³⁶ We used tungsten(IV) sulfide powder (243639, Sigma-Aldrich) and *N*-methyl-2-pyrrolidone (NMP, biotechnology grade, ≥99.7%, 494496, Sigma-Aldrich) as a solvent. To optimize the exfoliation conditions for the highest yield of WS₂ nanoflakes in solution, the initial WS₂ powder concentration and sonication time were tuned. Four different initial concentrations of WS₂ dispersion were prepared: 6, 12, 18, and 24 mg mL⁻¹. All dispersions were sonicated in a low-power ultrasonic bath (Branson CPHX ultrasonic cleaning bath) for 14 h at room temperature (*T* = 23 °C) and humidity of 25–30%. To prevent aggregation and reduce the presence of non-exfoliated materials, the WS₂ dispersion was cascade-centrifuged: after the first 15 min cycle at 3000 rpm, the solution was decanted and the supernatant was centrifuged at 6000 rpm for another 15 min. The optical characterization of WS₂ dispersion was performed using UV–vis spectroscopy (see section 1 of the Supporting Information). On the basis of the results, the dispersion with 12 mg mL⁻¹ of initial WS₂ concentration was chosen for further study.

Fabrication and Deposition of LPE LS WS₂ Films. The liquid-phase exfoliated WS₂ films were prepared at the water/toluene interface by the LS method. In a 15 mL beaker filled with 9 mL of deionized water (18 MΩ cm⁻¹), the substrate was immersed horizontally. The liquid interface was formed by adding 1 mL of toluene (≥99.7%, Sigma-Aldrich). The 0.3 mL of WS₂ dispersion was continuously cast down the inside wall of the beaker using the pipet. Passing through toluene, WS₂ nanoflakes gradually self-organized into a close-packed thin film at the water/toluene interface. After the WS₂ film was created, most toluene was gently removed with a syringe. The WS₂ films were then transferred onto substrates (SiO₂/Si, Au-

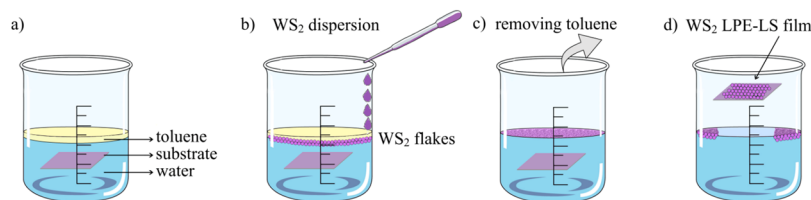


Figure 1. Schematic representation of the steps during the LPE-LS WS₂ film assembly by the LS method: (a) formation of the water/toluene interface, where the target substrate was previously horizontally immersed in the water, (b) introduction of LPE WS₂ dispersion down the inner wall of the beaker, where WS₂ nanoflakes pass through the toluene and are self-organized at the interface between liquids, (c) removing toluene, (d) thin WS₂ film transferring on a solid substrate by pulling through the interface.

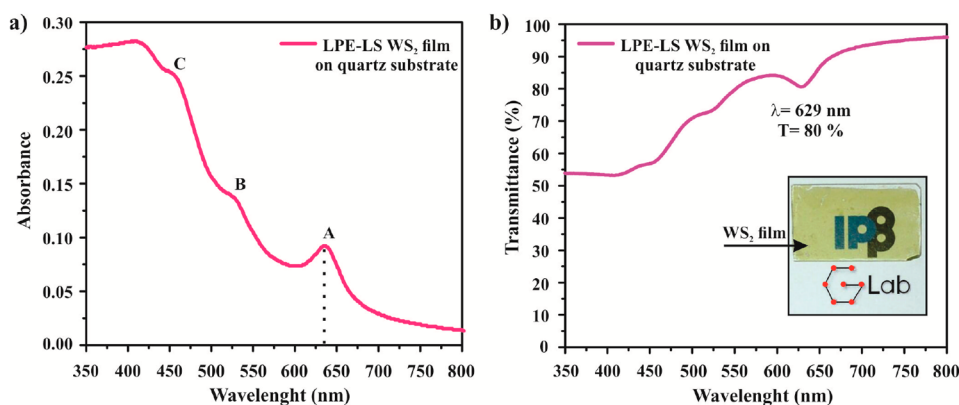


Figure 2. (a) Absorption and (b) transmission spectra for the thin LPE LS WS₂ film in the range from 350 to 800 nm. The inset in panel b illustrates the transparency and clarity of a single layer of the WS₂ film on the quartz substrate (1 × 2 cm) deposited by the LS method.

coated Si wafer, and quartz) using the homemade LS device. Further, they were left to dry for 30 min in ambient conditions. To ensure the removal of the residual solvent, the WS₂ films were annealed in a tube furnace in air for 20 min at a temperature of 120 °C.

Characterization of LPE LS WS₂ Films. The optical properties of LPE-LS WS₂ films on quartz were investigated using a UV–vis spectrophotometer (Beckman Coulter DU 720 UV–vis spectrophotometer). No more than 1% variation in the mean value existed over the entire film area, indicating LPE-LS WS₂ film uniformity on the scale of several square centimeters. Information about the morphology of WS₂ films was obtained using optical microscopy with a magnification of 400 times, and SEM (Tescan MIRA3 field-emission gun). All SEM images were taken at 20 kV. The topography of thin LPE-LS WS₂ films was characterized using a NTEGRA Prima atomic force microscope in non-contact mode. The thickness of the obtained LPE-LS WS₂ film was measured by non-contact optical profilometer ZYGO New View 7100. The gold-coated silicon wafer was chosen as a substrate as a result of its better light interference compared to the SiO₂/Si wafer. The thickness of the WS₂ film was estimated on the basis of five height profiles of film–substrate edges. The LPE-LS WS₂ film–substrate edge was made by a diamond pen. Raman spectra were measured with the Micro-Raman Tri Vista 557 triple spectrometer at room temperature ($T = 23$ °C) and humidity of 25%. To avoid the damage caused by heating, the power of the Nd:YAG laser ($\lambda = 532$ nm) was kept below 2 mW. The approximate size of the laser spot on the sample was 2 μ m. An objective lens microscope with 50 \times magnifications was used. The measurements were performed on six different positions on the surface of each WS₂ film sample using an acquisition time of 300 s. The spectrum range was 200–3800 cm^{-1} . The measurements could not be performed below 200 cm^{-1} , considering the configuration of the experimental setup. XPS measurements have been performed at the custom-built NAP-XPS setup in the Notre Dame Radiation Laboratory (NDRL). The setup contained a reaction cell with a volume of ~ 15 cm^3 , which could sustain water vapor pressure up to 20 mbar.³⁷ Photoelectrons from the samples were collected and detected by the SPECS PHOIBOS 150 hemispherical analyzer, which was differentially pumped. The

base pressure of the system was of the order of 10^{-9} – 10^{-10} mbar. The samples made of thin LPE-LS WS₂ films deposited on SiO₂/Si wafers were loaded first into the UHV chamber of the NAP-XPS setup and then introduced into the reaction cell. The pass energy of the analyzer was 20 eV for all high-resolution spectra. The energy of the spectrometer was calibrated to the gold standard sample. Considering the morphology of the thin films, we expected the presence of adventitious carbon (from air) in the form of CO or CO₂ species trapped on the surface and between the flakes in the film. To remove these and all other possible residual impurities (toluene and NMP), the LPE-LS WS₂ film was annealed at a temperature of 300 °C. After confirmation of the integrity and composition of the samples, pure water vapor was introduced into the reaction cell, within the pressure range corresponding to an approximately relative humidity (RH) between 4 and 22%.³⁸

RESULTS AND DISCUSSION

The process of formation and controlled deposition of the WS₂ film is schematically illustrated in Figure 1. The continuous insertion of a small amount of WS₂ dispersion at the interface between two immiscible liquids, water and toluene, induces the self-assembly of WS₂ nanoflakes. The interfacial tension of the water/air system is approximately equal to the surface tension of water (~ 73 mN/m at room temperature),³⁹ while the presence of toluene reduces it to 37.1 mN/m.⁴⁰ Driven by an overall reduction of the interfacial surface energy, WS₂ nanosheets form a large area of a densely packed thin film.

The successful formation of the WS₂ film at the liquid/liquid interface can be a consequence of the long-range dipolar repulsion of the particles as well as their attractive interaction.^{41,42} The difference in dielectric constants of phases that create the interface, polar (water) and nonpolar (air and oil) substances, can create an asymmetric distribution of particles charging and the formation of the dipole moment.⁴¹ The repulsive dipole–dipole interactions are responsible for

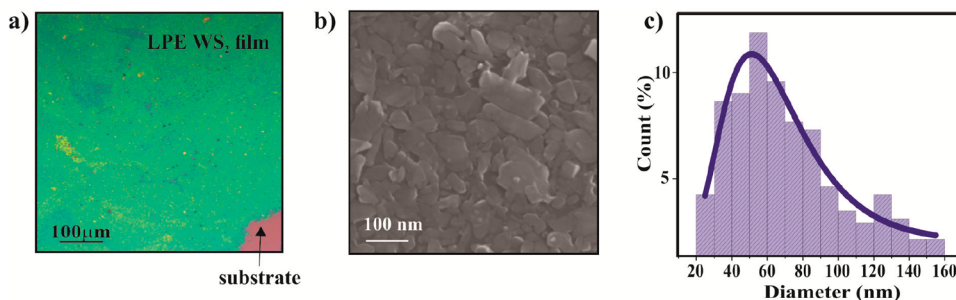


Figure 3. Images of the WS₂ film deposited on the SiO₂/Si substrate obtained by (a) optical microscopy, (b) SEM, and (c) histograms of the lateral size obtained from five 3 × 3 μm² SEM images (~1500 flakes). The distributions of the flake diameter have been fitted with a log-normal curve.

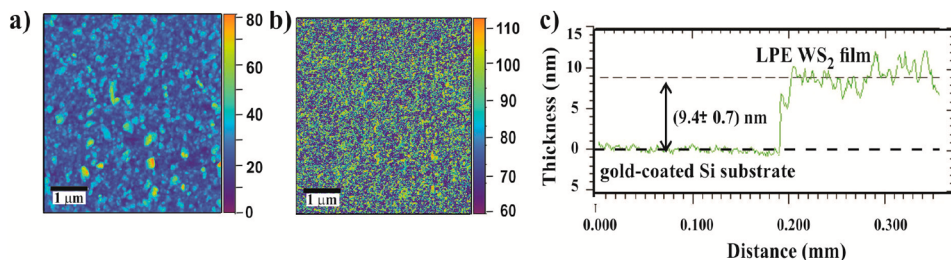


Figure 4. (a) AFM topographic image of the LPE-LS WS₂ film on the SiO₂/Si substrate (image includes a false color bar) of 5 × 5 μm², (b) phase image of the LPE-LS WS₂ thin film from the same area (image includes a false color bar) showing more contrast around the edges of the nanoflakes, and (c) height profile of the LPE-LS WS₂ film/Au-coated Si substrate performed by the optical profilometer (measurement started from the gold-coated Si substrate).

the ordering of the particles adsorbed at liquid interfaces.⁴¹ Still, Nikolaides et al.⁴² have shown that the dipolar electric field of particles causes electrical stress, inducing distortion of the liquid–liquid interface shape that results in the appearance of interparticle capillary attraction having a significant role in the stability of the particles at the liquid/liquid interface.⁴² However, because the WS₂ nanoflakes can be described as rather flat-shaped than spherical, their stability and arrangement at the interface of two liquids may be more adequately explained by the free energy of their attachment/detachment over various contact angles at the interface of liquids.^{30,43} Using an analysis developed by Binks and Horozov,⁴³ it has been shown that the attachment of the graphene and MoS₂ nanosheets at the liquid–liquid interface will be extremely energetically favorable if the energy of the detachment is maximized and the interfacial energy is minimized.^{25,30} During the self-assembly, the highest stability of liquid-phase exfoliated WS₂ nanoflakes at the water/toluene interface is likely achieved by their parallel orientation to the interface. This spontaneous arrangement through the edge to edge contact of nanosheets and their overlapping enables the reduction of the interfacial area of liquids and the formation of tightly packed WS₂ films.^{33,35} For further analysis and characterization, the LPE WS₂ films were deposited on solid substrates using the LS technique.

UV–Vis Characterization of LPE LS WS₂ Films. The optical characterization of LPE LS WS₂ films is represented in Figure 2. The absorption spectrum (Figure 2a) is characterized by three exciton peaks (A, ~629 nm; B, ~526 nm; and C, ~455 nm), confirming the 2H-semiconducting crystal structure of liquid-phase exfoliated WS₂ nanoflakes.⁴⁴ The average transparency for a single deposition of WS₂ film was 80 ± 1% at the wavelength of 629 nm (Figure 2b).

Morphology Characterization of LPE LS WS₂ Films. The morphology of LPE-LS WS₂ films is shown in Figure 3.

The optical contrast between the SiO₂/Si substrate [$d(\text{SiO}_2) \approx 300$ nm] and the film indicates complete coverage of the substrate and homogeneity of the film on the centimeter length scale (Figure 3a). In Figure 3b, the image taken by SEM provides more detailed information about the film structure. It can be noticed that the WS₂ nanoflakes collected by LS assembly form a well-packed array throughout their edge-to-edge contact. The overlapping of nanoflakes is also observed. The SEM image indicates that the water/toluene assembly technique can be used to obtain wrinkle-free WS₂ films with excellent nanosheet packing and uniformity, which cannot be achieved in a single-step spin-coating or drop-casting method.^{12,34} This is in line with previous reports on the advantages of the LB and LS techniques of liquid-phase exfoliated 2D-materials compared to conventional deposition methods, such as drop casting, spray or spin coating, and vacuum filtration.^{25,27,28,33–35} For example, the self-organization of graphene nanoflakes²⁷ at the interface enables their better mutual contact, in contrast to drop-casting, spin-coating, and vacuum-filtered techniques, where the presence of a large amount of NMP and its low volatility lead to the aggregation of graphene as a result of a longer drying time of the film. This impedes the control of the film thickness, which then affects both the transparency and the electrical properties of the film. The films produced through liquid/liquid assembly and transferred onto the substrate by LB/LS methods exhibit not only more uniform thickness but also a compact spatial arrangement, with the nanosheets aligned over a much larger area than can be achieved by spin or spray coating.³³ Similar conclusions apply to the MoS₂ thin films, where Neilson et al.²⁵ directly compare the characteristics of the LS MoS₂ film transferred from the liquid/liquid interface onto a solid substrate, with the MoS₂ film obtained by spray and spin deposition methods. On the basis of the measurement of the

flake diameter, the average lateral size of the WS₂ nanoflakes was estimated to be in the range of 60 ± 20 nm (Figure 3c).

In addition to the optical and electron microscopy, we performed the AFM topography scans of LPE-LS WS₂ films transferred on SiO₂/Si (panels a and b of Figure 4). The topography of thin LPE WS₂ films (Figure 4a) shows the existence of WS₂ nanosheets with different thicknesses and excellent surface coverage by layered overlapping WS₂ nanoflakes. The phase image (Figure 4b), which presents the phase shift in the cantilever oscillations, reflecting the combined material properties, such as stiffness, adhesion, viscosity, and dissipation, indicates good LPE-LS WS₂ film homogeneity and shows a better contrast around the nanoflake edges.

Optical profilometry measurements of the LPE-LS WS₂ film are shown in Figure 4c. On the basis of the height profiles of the film/substrate edge (Figure 4c), the thickness of the WS₂ films is estimated as 9.4 ± 0.7 nm.

Raman Spectroscopy of LPE LS WS₂ Films. For further characterization of the LPE-LS WS₂ thin film, Raman spectroscopy has been applied to verify the exfoliation of bulk WS₂ into few-layer WS₂ nanosheets. Figure 5 represents the Raman spectra of WS₂ thin films and their bulk as a reference.

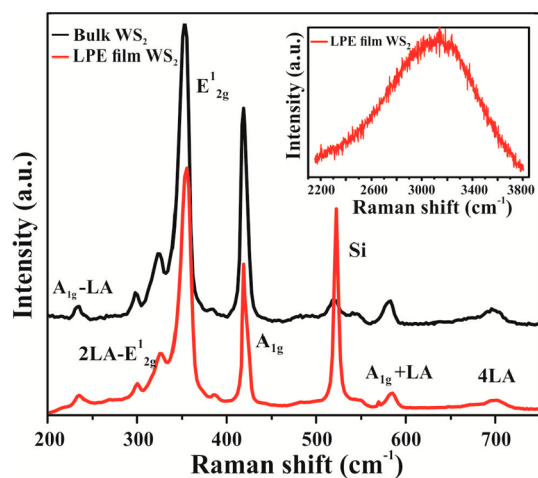


Figure 5. Raman spectra of WS₂ bulk materials and WS₂ thin films deposited on the SiO₂/Si wafer, with (inset) fluorescence in the Raman spectrum of the WS₂ thin film.

Because the laser wavelength ($\lambda = 532$ nm) corresponds to the exciton energy of WS₂ (the peak B at the absorption spectrum, Figure 2), the resulting spectra represent resonant Raman spectra.⁴⁵ Besides two characteristic Raman active first-order optical modes A_{1g}(Γ) and E_{12g}(Γ), the resonant Raman spectrum involves the longitudinal acoustic phonons at the M point of the Brillouin zone [LA(M)], overtones [2LA(M) and 4LA(M), second and fourth harmonics], and combination modes (A_{1g} - LA, 2LA - 2E_{12g}, and A_{1g} + LA).^{45,46} Under the resonance condition, the E_{12g}(Γ) mode overlaps with the 2LA(M) mode.⁴⁶ LA(M) is positioned below 200 cm⁻¹ (precisely at 176 cm⁻¹ in the experiment of Berkdemir et al.⁴⁶) and cannot be seen in spectra considering the range of our experimental setup, but the other vibrational bands are present in both spectra of thin-film WS₂ and the WS₂ bulk (Figure 5). It indicates that, during the exfoliation process, there was no interaction between the WS₂ nanosheets and the

solvent molecules (NMP), which would lead to changes in the chemical composition of the material. In comparison to the Raman spectrum of the WS₂ bulk material, there are no significant changes in the Raman shift of the vibration modes: A_{1g} - LA (234 cm⁻¹), 2LA - 2E_{12g} (299 cm⁻¹), A_{1g} + LA (582 cm⁻¹), and 4LA (698 cm⁻¹). In the Raman spectra of the LPE LS WS₂ film, A_{1g}(Γ) (418 cm⁻¹) and E_{12g}(Γ) [+2LA(M)] (354 cm⁻¹) are red- and blue-shifted (for 2 cm⁻¹) compared to the WS₂ bulk, which is expected when the number of WS₂ layers is decreasing.⁴⁷ Changes in the electronic structure, formation of the direct energy gap, which is the characteristic of exfoliated WS₂, was confirmed by the presence of fluorescence in the Raman spectrum of the LPE-LS WS₂ thin film (inset spectrum in Figure 5).⁴⁸ The Raman spectra recorded in the range from 800 to 2200 cm⁻¹ showed no vibrational modes (presented in section 3 of the Supporting Information).

The characterization of the LPE-LS WS₂ films produced at the toluene/water interface and transferred on solid substrates showed a high level of reproducibility in their physical and chemical properties. The transmittance, Raman spectra, and compactness of the films did not differ significantly between different samples (see sections 2–4 of the Supporting Information).

Effects of Water Molecules on the Surface of LPE-LS WS₂ Films.

To obtain insight into the chemical composition and binding characteristics of the LPE-LS WS₂ films when they are exposed to water vapor, XPS analysis was performed. All represented core level photoemission spectra (W 4f, S 2p, O 1s, and C 1s) have been analyzed with a Gauss (30%)–Lorentz (70%) function defined in Casa XPS as GL (30) after a Shirley-type background subtraction. The C 1s peak at 284.8 eV was used for calibration of the binding energy scale. Panels a–c of Figure 6 depict the deconvoluted XPS spectra of the pristine LPE-LS WS₂ film. The W 4f core level spectrum (Figure 6a) is deconvoluted into six components: three W 4f doublet (W 4f_{7/2} and W 4f_{5/2}). The doublet peaks arising as a result of spin–orbit splitting correspond to W⁴⁺ at 32.5 and 34.6 eV, W⁵⁺ at 35.5 and 37.8 eV, and W⁶⁺ at 36.7 and 38.7 eV binding energy. The XPS spectrum of sulfur is fitted into doublet S 2p_{3/2} and S 2p_{1/2} at 161.9 and 163.1 eV (Figure 6b). The two peaks of the S²⁻ and W⁴⁺ oxidation states are attributed, according to the literature, to the pure 2H-WS₂ phase.^{49,50} Recent studies have reported that WS₂ films show poor stability and the tendency for spontaneous oxidation in the air environment at room or higher temperatures.^{51–53} These results imply that, dependent upon the operating temperature range, WS₂ can be partially or totally converted into different forms: tungsten oxide (WO₃), non-stoichiometric tungsten oxide (WO_{3-x}), hydroxide and/or hydrate tungsten oxide (WO₃·nH₂O).^{12,50,53,54} Considering the conditions of LPE-LS WS₂ film preparation (self-assembly of nanoflakes at the toluene/water interface and the annealing of films in air at 120 °C) and the value of the binding energies of W⁵⁺ and W⁶⁺, the presence of these oxidation products in the LPE-LS WS₂ films can be expected. To complete the analysis, XPS of the O 1s core level was also performed in this study (Figure 6c). The broad O 1s spectrum observed in the range of 529–537 eV is deconvoluted into four components. The position of the peaks in the deconvoluted spectrum is tentative as a result of the large width of the O 1s peak and the overlapping of possible oxygen species with close values of binding energy. The assignment of these four peaks is based on

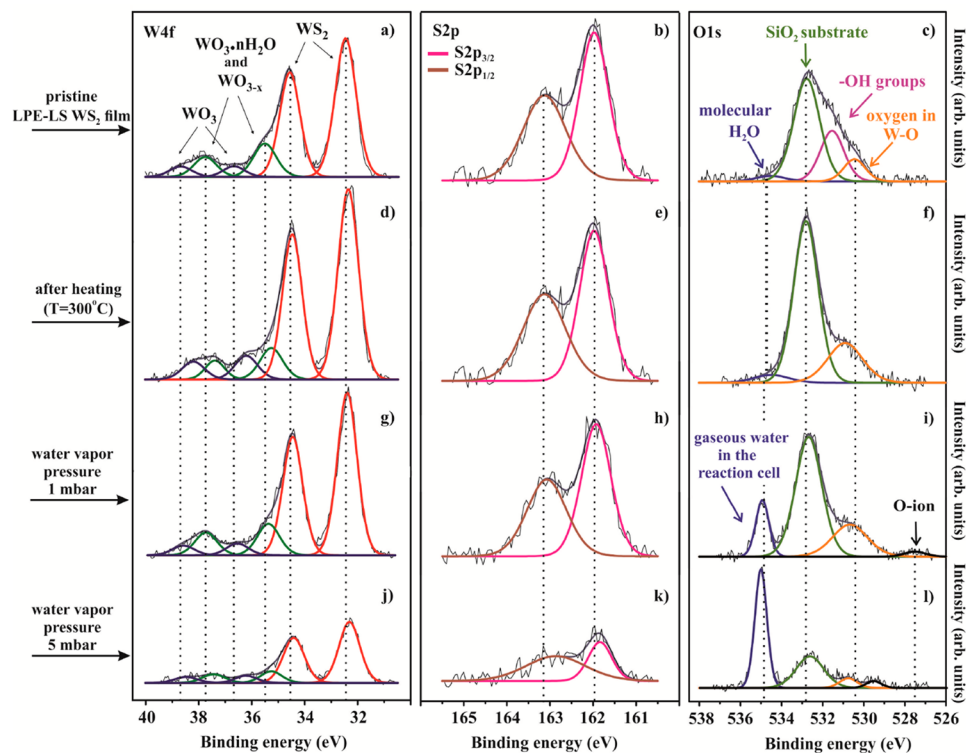


Figure 6. XPS W 4f, S 2p, and O 1s spectra of the LPE LS WS₂ film deposited on the SiO₂/Si substrate: (a–c) pristine, (d–f) after heating at $T = 300$ °C in vacuum, (g–i) exposure to 1 mbar water vapor, and (j–l) exposure to 5 mbar water vapor. The first column presents the W 4f spectrum with the three doublets attributed to WS₂ (red), WO_{3-x} and WO_{3·nH₂O} (dark green), and WO₃ (dark blue). The second column shows a doublet of sulfur, S 2p_{3/2} (pink) and S 2p_{1/2} (brown). The third column represents the O 1s spectrum deconvoluted into components assigned to molecular H₂O from the water/toluene interface and gaseous water in the reaction cell (dark blue), SiO₂ (olive green), –OH groups (purple), and oxygen in W–O_x (orange), with oxygen ions as nucleophilic oxygen (black line). The envelope curve for all spectra is marked as a dark gray line.

the literature and protocol for the creation and transfer of WS₂ films on solid substrates. The peak located at the lowest binding energy (530.3 eV) corresponds to oxygen ions (O²⁻), confirming the formation of W–O bonds.⁵⁵ The existence of the hydroxyl group (–OH), assigned to the peak at 531.5 eV, indicates the hydration of tungsten/tungsten oxide.⁵⁶ The formation of the oxidation products consisting of oxide/hydroxide compounds of W and hydrate of WO₃ can be due to the presence of WS₂ film defects, as recently reported⁵⁷ that the liquid-phase exfoliation coupled with the LB technique produces self-assembled films with a high density of nanoflake edge defects. The edge defects of LPE-LS WS₂ nanoflakes/films, like tungsten dangling bonds, behave as active sites for the interaction with O₂, humidity from the atmosphere, and water present as a component of liquid/liquid interfaces.

The origin of the major peak in the O 1s spectrum, positioned at 532.8 eV, can be ascribed to the SiO₂ substrate and adsorption of O₂ molecules from the atmosphere.^{58,59} In the previously reported studies^{60,61} and database,³⁸ the peak presented at the highest binding energy in the O 1s spectrum is usually related to the chemisorbed/physisorbed H₂O molecules on the film surface. Thus, the highest binding energy peak (at 534.9 eV) in the observed spectrum refers to the adsorption of water molecules. These water molecules can be adsorbed on the WS₂ film surface or intercalated through its structure and trapped between the nanoflakes during the film formation.

As described earlier (Experimental Section), a small amount of NMP from the WS₂ dispersion is present during the self-assembly of WS₂ nanoflakes. This compound together with

toluene may be detected in LPE-LS WS₂ films in the form of adventitious carbon. To assess the presence of carbon contamination from these solvents and other sources, including the interaction cell (adventitious carbon), we also recorded the high-resolution spectrum of C 1s (Figure S2 of the Supporting Information). Considering that, after the heating of LPE-LS WS₂ films at 120 °C in air, there was still residual water and solvents in the film (Figure 6c), the samples were additionally annealed in vacuum at 300 °C.

The XPS spectra of W 4f, S 2p, and O 1s for the post-annealed LPE-LS WS₂ film are shown in panels d–f of Figure 6. The position of the characteristic peaks (W 4f and S 2p) for pure 2H-WS₂ remained unchanged after heating of LPE-LS WS₂ films in high vacuum, suggesting that annealing does not affect the W–S chemical bonds (panels d and e of Figure 6). The S atoms are still bound exclusively to W without revealing additional chemical states or introducing new defects. However, it is worth noting that the binding energy of other peaks attributable to W with higher oxidation states in the W spectrum (Figure 6d) is downshifted for 0.5 eV. The significant chemical shift that refers to increasing of the binding energy for 0.6 eV is also remarked for the oxide ions O²⁻ (Figure 6f). The obtained results imply that changes in the W 4f and O 1s core level spectrum are probably caused by losing an oxygen atom in WO₃ during heat treatment of LPE LS WS₂ films in vacuum.⁶² The creation of oxygen vacancies, as point defects, is usually accompanied by the reduction of W⁶⁺ to W⁵⁺ and the generation of WO_{3-x} compounds.⁶² Released lattice oxygen atoms can leave the film and be evacuated from the chamber, but also their migration to filling the previously formed surface

oxygen vacancy defects, oxidation of WO_{3-x} cannot be excluded. Furthermore, in the O 1s spectrum of post-annealed LPE-LS WS_2 films (Figure 6f), the OH peak entirely disappears, as evidence of film dehydration. The other two peaks ascribed to SiO_2 (at 532.8 eV) and H_2O (at 534.9 eV) molecules did not undergo any changes in terms of the chemical shift. The presence of the peak at 534.9 eV suggests that a complete desorption of water molecules from the LPE-LS WS_2 films did not occur. Considering the porous structure of the WS_2 films, it is likely that a certain amount of H_2O remains trapped within the film, with some of it also being chemisorbed and forming bridges between the nanoflakes.

After the sample WS_2 film was cooled to the room temperature, it was exposed to 1 and 5 mbar pressure of water vapor, which corresponds approximately to RH between 4 and 22% (panels g–l of Figure 6). The high-resolution XPS spectra show that the peak position of W 4f and S 2p doublets for pure 2H- WS_2 stay unchanged in both cases (panels g, h, j, and k of Figures 6). The existence of water molecules clearly does not influence the chemical bond of W–S, suggesting that the H_2O molecules are physisorbed onto the surface of the LPE-LS WS_2 films. After the increase of water vapor pressure in the chamber, multilayers of H_2O are formed through hydrogen bonds (Figure 6l). The chemical shift of the peak positioned at 534.9 eV as well as the peak corresponding to SiO_2 (at 532.7 eV) was not observed (panels i and l of Figure 6), which indicates that introduced water did not have access to the silicon wafer substrate; i.e., the homogeneous, full coverage of the WS_2 film on the surface has not been disrupted. The suppressed intensity and broadening of all peaks, except the peak at 534.9 eV (panels g–l of Figure 6), is due to the smaller number of photoelectrons reaching the detector in the presence of the water multilayer on the surface and free gaseous water molecules in the reaction cell.

The charge transfer in tungsten oxides, at 1 mbar, is evidenced by the shift (0.3 eV) of W^{5+} and W^{6+} peak positions toward the higher binding energy (Figure 6g) compared to those at the post-heating LPE-LS WS_2 films (Figure 6d). Also, the position of the peak corresponding to O^{2-} (Figure 6l) has undergone an alteration and downshift for 0.3 eV. The obtained results indicate the oxidation of W^{5+} to W^{6+} . Once the water vapor molecules come into contact with the surface of LPE-LS WS_2 films, the oxygen atoms will fill the previously formed point defects, oxygen vacancies in non-stoichiometric WO_{3-x} forming WO_3 , which is the opposite of the reduction of these compounds that occurs at post-annealed LPE-LS WS_2 .⁶² During the chemical bonding of oxygen with its adjacent tungsten atom, the transfer of electrons from W to the O atom has occurred and the electronic density near the tungsten atom decreases. In that case, the Coulomb interaction between the nucleus and the remaining electrons in the W atom becomes stronger. Thus, the binding energy of W peaks will be shifted to higher values, and for the O^{2-} peak, the binding energy will be shifted to lower values. In the O 1s spectrum shown in Figure 6i, the new peak has appeared at 527.5 eV and can be tentatively ascribed to the creation of hydrate tungsten oxide ($\text{WO}_3 \cdot n\text{H}_2\text{O}$)⁶³ or nucleophilic (atomic) oxygen.⁶⁴

The introduction of water vapor at 5 mbar leads to W^{5+} and W^{6+} peak shift from 0.3 eV to lower binding energies (Figure 6j) and the large chemical shift by more than 2 eV of the O 1s peak, previously at 527.5 eV, to higher binding energies (Figure 6l). Such a shift has been previously observed in the

adsorption of oxygen on Ag(110) and Ag(111) surfaces,⁶⁴ where atomic oxygen trapped in defects or different adsorption sites can have different ionic states and, therefore, different charges. In the case of the porous WS_2 film, the edge-rich structure offers a wide range of adsorption sites for oxygen, which can then be more weakly (ionic-like states) or more strongly (covalent bonds) bound to tungsten in the film. In the case of more covalently bound but not yet electrophilic, O 1s will still be lower than that which corresponds to WO_x but significantly higher than that in the nucleophilic form. An additional possibility for the appearance and binding energy shift of this O 1s peak could be that the chemical changes of the LPE-LS WS_2 film are caused by the formation of additional hydrides of tungsten oxides through the interaction of water molecules with defects (WO_3 , and WO_{3-x}).⁶³ Considering the structure of our WS_2 films, it is plausible that both mechanisms are taking place during the exposure of LPE-LS WS_2 films to H_2O in a vacuum.

CONCLUSION

In this work, we presented the study of the water adsorption effect on WS_2 thin films obtained using the new toluene/water interfacial self-assembly technique from the liquid-phase exfoliated 2D material. In the first part, we characterized LPE-LS WS_2 films using various spectroscopic and microscopic techniques (UV–vis, Raman spectroscopy, SEM, and AFM). The toluene/water interfacial self-assembly technique and LS film deposition method provide a strong confinement of the WS_2 flakes. Using a small volume of the WS_2 dispersion allows the facile and rapid formation of theoretically unlimited large-area, highly transparent, and thin films of few-layer WS_2 nanosheets.

Chemical properties of the LPE-LS WS_2 films and their interaction with water molecules under near-ambient water vapor pressures reveal that defects in the WS_2 flakes play a major role in the chemical interaction of the water and LPE-LS WS_2 film surface. The presence of WO_3 , WO_{3-x} , and hydrated tungsten oxide, in the freshly prepared LPE-LS WS_2 films, can be explained by the existence of the edge defects from tungsten dangling bonds that arose during the liquid-phase exfoliation of the WS_2 material. The temperature treatment of the LPE-LS WS_2 films in vacuum, performed before their exposure to water vapor, to remove the residual solvent, had a partial effect on their dehydration. This implies that the trapping of the H_2O molecules in the film structure and their chemisorptions represents the first stage of the water– WS_2 film interaction and an unavoidable event during the exposition of the film to the liquid water at the moment of its formation at the interface. Besides the expected significant physisorption of H_2O at the surface of LPE-LS WS_2 films, during their exposure to H_2O gas at 1 and 5 mbar, oxygen-activated sites, such as WO_3 and WO_{3-x} , are the central places for the interaction with the water molecules from the gas phase. Except for the oxidation of W^{5+} , adsorption of intact and dissociated H_2O molecules is responsible for the formation of hydrated tungsten oxides.

The investigation of the interaction of water molecules with the surface of the thin 2D semiconductor WS_2 film is an imperative for fine tuning the sensing properties, regardless of the sensing target, because the presence of water in ambient conditions is unavoidable. Therefore, the characterization of molecular interactions between water molecules and the WS_2 film and the identification of specific chemical and physical bonds under near-ambient conditions are essential for further

use in sensing applications. These new data may be especially useful for improving the accuracy and responsiveness of various gas sensor devices operating in various environmental conditions, such as low or high humidity and high temperatures, or improving the sensitivity of biochemical sensors that usually deal with analytes in aqueous solution.

■ ASSOCIATED CONTENT

SI Supporting Information

The Supporting Information is available free of charge at <https://pubs.acs.org/doi/10.1021/acs.langmuir.3c00107>.

UV–vis spectroscopy used to determine the concentration of WS₂ dispersions, detailed AFM images of the LPE LS WS₂ film on a silicone substrate, Raman spectra recorded in the spectral range between 800 and 2200 cm⁻¹, transmittance for five thin LPE LS WS₂ films recorded in the range of 350–800 nm, and X-ray photoelectron spectra of the carbon C 1s state in the LPE LS WS₂ films deposited on the SiO₂/Si wafer (PDF)

■ AUTHOR INFORMATION

Corresponding Author

Radmila Panajotović – Institute of Physics Belgrade, University of Belgrade, 11080 Belgrade, Serbia; orcid.org/0000-0002-2174-0062; Email: radmila@ipb.ac.rs

Authors

Jasna Vujin – Institute of Physics Belgrade, University of Belgrade, 11080 Belgrade, Serbia

Weixin Huang – Radiation Laboratory, University of Notre Dame, Notre Dame, Indiana 46556, United States

Jovan Ciganović – Department for Physical Chemistry, Institute of Nuclear Sciences Vinča, University of Belgrade, 11351 Belgrade, Serbia

Sylwia Ptasińska – Radiation Laboratory and Department for Physics and Astronomy, University of Notre Dame, Notre Dame, Indiana 46556, United States; orcid.org/0000-0002-7550-8189

Complete contact information is available at: <https://pubs.acs.org/10.1021/acs.langmuir.3c00107>

Notes

The authors declare no competing financial interest.

■ ACKNOWLEDGMENTS

The authors acknowledge the funding provided by the Institute of Physics Belgrade, Institute of Nuclear Sciences Vinča (Grant 451-03-68/2022-14/200017), through the grant by the Ministry of Education, Science, and Technological Development of the Republic of Serbia. Weixin Huang and Sylwia Ptasińska acknowledge the U.S. Department of Energy, Office of Science, Office of Basic Energy Sciences, under Award DE-FC02-04ER15533 (NDRL 5372).

■ REFERENCES

- (1) Davis, R. E.; McGregor, G. R.; Enfield, K. B. Humidity: A Review and Primer on Atmospheric Moisture and Human Health. *Environ. Res.* **2016**, *144*, 106–116.
- (2) Sharma, A. K.; Kaur, B.; Popescu, V. A. On the Role of Different 2D Materials/Heterostructures in Fiber-Optic SPR Humidity Sensor in Visible Spectral Region. *Opt. Mater.* **2020**, *102*, 109824.
- (3) Melios, C.; Giusca, C. E.; Panchal, V.; Kazakova, O. Water on Graphene: Review of Recent Progress. *2D Mater.* **2018**, *5* (2), 022001.
- (4) He, P.; Brent, J. R.; Ding, H.; Yang, J.; Lewis, D. J.; O'Brien, P.; Derby, B. Fully Printed High Performance Humidity Sensors Based on Two-Dimensional Materials. *Nanoscale* **2018**, *10* (12), 5599–5606.
- (5) Zhao, J.; Li, N.; Yu, H.; Wei, Z.; Liao, M.; Chen, P.; Wang, S.; Shi, D.; Sun, Q.; Zhang, G. Highly Sensitive MoS₂ Humidity Sensors Array for Noncontact Sensation. *Adv. Mater.* **2017**, *29* (34), 1702076.
- (6) Chhowalla, M.; Shin, H. S.; Eda, G.; Li, L.-J.; Loh, K. P.; Zhang, H. The Chemistry of Two-Dimensional Layered Transition Metal Dichalcogenide Nanosheets. *Nat. Chem.* **2013**, *5* (4), 263–275.
- (7) Li, A.; Zhang, J.; Qiu, J.; Zhao, Z.; Wang, C.; Zhao, C.; Liu, H. A Novel Aptameric Biosensor Based on the Self-Assembled DNA–WS₂ Nanosheet Architecture. *Talanta* **2017**, *163*, 78–84.
- (8) Convertino, D.; Mishra, N.; Marchetti, L.; Calvello, M.; Viegi, A.; Cattaneo, A.; Fabbri, F.; Coletti, C. Effect of Chemical Vapor Deposition WS₂ on Viability and Differentiation of SH-SY5Y Cells. *Front. Neurosci.* **2020**, *14*, 592502.
- (9) Yi, H.; Zhou, X.; Zhou, C.; Yang, Q.; Jia, N. Liquid Exfoliated Biocompatible WS₂ @BSA Nanosheets with Enhanced Theranostic Capacity. *Biomater. Sci.* **2021**, *9* (1), 148–156.
- (10) Asres, G. A.; Baldoví, J. J.; Dombovari, A.; Järvinen, T.; Lorite, G. S.; Mohl, M.; Shchukarev, A.; Pérez Paz, A.; Xian, L.; Mikkola, J.-P.; Spetz, A. L.; Jantunen, H.; Rubio, Á.; Kordás, K. Ultrasensitive H₂S Gas Sensors Based on P-Type WS₂ Hybrid Materials. *Nano Res.* **2018**, *11* (8), 4215–4224.
- (11) Järvinen, T.; Lorite, G. S.; Peräntie, J.; Toth, G.; Saarakkala, S.; Virtanen, V. K.; Kordas, K. WS₂ and MoS₂ Thin Film Gas Sensors with High Response to NH₃ in Air at Low Temperature. *Nanotechnology* **2019**, *30* (40), 405501.
- (12) Paolucci, V.; Emamjomeh, S. M.; Nardone, M.; Ottaviano, L.; Cantalini, C. Two-Step Exfoliation of WS₂ for NO₂, H₂ and Humidity Sensing Applications. *Nanomaterials* **2019**, *9* (10), 1363.
- (13) Kuru, C.; Choi, D.; Kargar, A.; Liu, C. H.; Yavuz, S.; Choi, C.; Jin, S.; Bandaru, P. R. High-Performance Flexible Hydrogen Sensor Made of WS₂ Nanosheet–Pd Nanoparticle Composite Film. *Nanotechnology* **2016**, *27* (19), 195501.
- (14) Pawbake, A. S.; Waykar, R. G.; Late, D. J.; Jadkar, S. R. Highly Transparent Wafer-Scale Synthesis of Crystalline WS₂ Nanoparticle Thin Film for Photodetector and Humidity-Sensing Applications. *ACS Appl. Mater. Interfaces* **2016**, *8* (5), 3359–3365.
- (15) Guo, H.; Lan, C.; Zhou, Z.; Sun, P.; Wei, D.; Li, C. Transparent, Flexible, and Stretchable WS₂ Based Humidity Sensors for Electronic Skin. *Nanoscale* **2017**, *9* (19), 6246–6253.
- (16) Huo, N.; Yang, S.; Wei, Z.; Li, S.-S.; Xia, J.-B.; Li, J. Photoresponsive and Gas Sensing Field-Effect Transistors Based on Multilayer WS₂ Nanoflakes. *Sci. Rep.* **2014**, *4* (1), 5209.
- (17) Jha, R. K.; Guha, P. K. Liquid Exfoliated Pristine WS₂ Nanosheets for Ultrasensitive and Highly Stable Chemiresistive Humidity Sensors. *Nanotechnology* **2016**, *27* (47), 475503.
- (18) Leonardi, S. G.; Wlodarski, W.; Li, Y.; Donato, N.; Sofer, Z.; Pumera, M.; Neri, G. A Highly Sensitive Room Temperature Humidity Sensor Based on 2D-WS₂ Nanosheets. *FlatChem* **2018**, *9*, 21–26.
- (19) Chen, Z.; Lu, C. Humidity Sensors: A Review of Materials and Mechanisms. *Sens. Lett.* **2005**, *3* (4), 274–295.
- (20) Mao, S.; Chang, J.; Pu, H.; Lu, G.; He, Q.; Zhang, H.; Chen, J. Two-Dimensional Nanomaterial-Based Field-Effect Transistors for Chemical and Biological Sensing. *Chem. Soc. Rev.* **2017**, *46* (22), 6872–6904.
- (21) Coleman, J. N.; Lotya, M.; O'Neill, A.; Bergin, S. D.; King, P. J.; Khan, U.; Young, K.; Gaucher, A.; De, S.; Smith, R. J.; Shvets, I. V.; Arora, S. K.; Stanton, G.; Kim, H.-Y.; Lee, K.; Kim, G. T.; Duesberg, G. S.; Hallam, T.; Boland, J. J.; Wang, J. J.; Donegan, J. F.; Grunlan, J. C.; Moriarty, G.; Shmeliov, A.; Nicholls, R. J.; Perkins, J. M.; Grievson, E. M.; Theuwissen, K.; McComb, D. W.; Nellist, P. D.

- Nicolosi, V. Two-Dimensional Nanosheets Produced by Liquid Exfoliation of Layered Materials. *Science* **2011**, *331* (6017), 568–571.
- (22) Backes, C.; Higgins, T. M.; Kelly, A.; Boland, C.; Harvey, A.; Hanlon, D.; Coleman, J. N. Guidelines for Exfoliation, Characterization and Processing of Layered Materials Produced by Liquid Exfoliation. *Chem. Mater.* **2017**, *29* (1), 243–255.
- (23) Yao, Y.; Lin, Z.; Li, Z.; Song, X.; Moon, K.-S.; Wong, C. Large-Scale Production of Two-Dimensional Nanosheets. *J. Mater. Chem.* **2012**, *22* (27), 13494.
- (24) Kymakis, E.; Stratakis, E.; Stylianakis, M. M.; Koudoumas, E.; Fotakis, C. Spin Coated Graphene Films as the Transparent Electrode in Organic Photovoltaic Devices. *Thin Solid Films* **2011**, *520* (4), 1238–1241.
- (25) Neilson, J.; Avery, M. P.; Derby, B. Tiled Monolayer Films of 2D Molybdenum Disulfide Nanoflakes Assembled at Liquid/Liquid Interfaces. *ACS Appl. Mater. Interfaces* **2020**, *12* (22), 25125–25134.
- (26) Zeng, X.; Hirwa, H.; Metel, S.; Nicolosi, V.; Wagner, V. Solution Processed Thin Film Transistor from Liquid Phase Exfoliated MoS₂ Flakes. *Solid-State Electron.* **2018**, *141*, 58–64.
- (27) Kim, H.; Mattevi, C.; Kim, H. J.; Mittal, A.; Mkhoyan, K. A.; Riman, R. E.; Chhowalla, M. Optoelectronic Properties of Graphene Thin Films Deposited by a Langmuir–Blodgett Assembly. *Nanoscale* **2013**, *5* (24), 12365.
- (28) Kaur, H.; Yadav, S.; Srivastava, A. K.; Singh, N.; Schneider, J. J.; Sinha, O. P.; Agrawal, V. V.; Srivastava, R. Large Area Fabrication of Semiconducting Phosphorene by Langmuir–Blodgett Assembly. *Sci. Rep.* **2016**, *6* (1), 34095.
- (29) Andrić, S.; Tomašević-Ilić, T.; Bošković, M. V.; Sarajlić, M.; Vasiljević-Radović, D.; Smiljanić, M. M.; Spasenović, M. Ultrafast Humidity Sensor Based on Liquid Phase Exfoliated Graphene. *Nanotechnology* **2021**, *32* (2), 025505.
- (30) Biswas, S.; Drzal, L. T. A Novel Approach to Create a Highly Ordered Monolayer Film of Graphene Nanosheets at the Liquid–Liquid Interface. *Nano Lett.* **2009**, *9* (1), 167–172.
- (31) Woltonist, S. J.; Oyer, A. J.; Carrillo, J.-M. Y.; Dobrynin, A. V.; Adamson, D. H. Conductive Thin Films of Pristine Graphene by Solvent Interface Trapping. *ACS Nano* **2013**, *7* (8), 7062–7066.
- (32) Salvatierra, R. V.; Souza, V. H. R.; Matos, C. F.; Oliveira, M. M.; Zarbin, A. J. G. Graphene Chemically Synthesized from Benzene at Liquid–Liquid Interfaces. *Carbon* **2015**, *93*, 924–932.
- (33) Yu, X.; Prévot, M. S.; Guijarro, N.; Sivula, K. Self-Assembled 2D WSe₂ Thin Films for Photoelectrochemical Hydrogen Production. *Nat. Commun.* **2015**, *6* (1), 7596.
- (34) Adilbekova, B.; Lin, Y.; Yengel, E.; Faber, H.; Harrison, G.; Firdaus, Y.; El-Labban, A.; Anjum, D. H.; Tung, V.; Anthopoulos, T. D. Liquid Phase Exfoliation of MoS₂ and WS₂ in Aqueous Ammonia and Their Application in Highly Efficient Organic Solar Cells. *J. Mater. Chem. C* **2020**, *8* (15), 5259–5264.
- (35) Clark, R. M.; Berean, K. J.; Carey, B. J.; Pillai, N.; Daeneke, T.; Cole, I. S.; Latham, K.; Kalantar-zadeh, K. Patterned Films from Exfoliated Two-Dimensional Transition Metal Dichalcogenides Assembled at a Liquid–Liquid Interface. *J. Mater. Chem. C* **2017**, *5* (28), 6937–6944.
- (36) Pešić, J.; Vujan, J.; Tomašević-Ilić, T.; Spasenović, M.; Gajić, R. DFT Study of Optical Properties of MoS₂ and WS₂ Compared to Spectroscopic Results on Liquid Phase Exfoliated Nanoflakes. *Opt. Quantum Electron.* **2018**, *50* (7), 291.
- (37) Zhang, X.; Ptasinska, S. Dissociative Adsorption of Water on an H₂O/GaAs(100) Interface: In Situ near-Ambient Pressure XPS Studies. *J. Phys. Chem. C* **2014**, *118* (8), 4259–4266.
- (38) National Institute of Standards and Technology (NIST). NIST X-ray Photoelectron Spectroscopy Database, NIST Standard Reference Database Number 20; NIST: Gaithersburg MD, 2000; DOI: 10.18434/T4T88K, <https://srdata.nist.gov/xps/citation.aspx>.
- (39) Vargaftik, N. B.; Volkov, B. N.; Voljak, L. D. International Tables of the Surface Tension of Water. *J. Phys. Chem. Ref. Data* **1983**, *12*, 817–820.
- (40) Saien, J.; Akbari, S. Interfacial Tension of Toluene + Water + Sodium Dodecyl Sulfate from (20 to 50) °C and pH between 4 and 9. *J. Chem. Eng. Data* **2006**, *51* (5), 1832–1835.
- (41) Pieranski, P. Two-Dimensional Interfacial Colloidal Crystals. *Phys. Rev. Lett.* **1980**, *45* (7), 569–572.
- (42) Nikolaides, M. G.; Bausch, A. R.; Hsu, M. F.; Dinsmore, A. D.; Brenner, M. P.; Gay, C.; Weitz, D. A. Electric-Field-Induced Capillary Attraction between like-Charged Particles at Liquid Interfaces. *Nature* **2002**, *420* (6913), 299–301.
- (43) Binks, B. P.; Horozov, T. S. Colloidal Particles at Liquid Interfaces: An Introduction. *Colloidal Particles at Liquid Interfaces*; Cambridge University Press: Cambridge, U.K., 2006; Chapter 1, pp 1–74, DOI: 10.1017/CBO9780511536670.002.
- (44) Pagona, G.; Bittencourt, C.; Arenal, R.; Tagmatarchis, N. Exfoliated Semiconducting Pure 2H-MoS₂ and 2H-WS₂ Assisted by Chlorosulfonic Acid. *Chem. Commun.* **2015**, *51* (65), 12950–12953.
- (45) Zhao, W.; Ghorannevis, Z.; Amara, K. K.; Pang, J. R.; Toh, M.; Zhang, X.; Kloc, C.; Tan, P. H.; Eda, G. Lattice Dynamics in Mono- and Few-Layer Sheets of WS₂ and WSe₂. *Nanoscale* **2013**, *5* (20), 9677.
- (46) Berkdemir, A.; Gutiérrez, H. R.; Botello-Méndez, A. R.; Perea-López, N.; Elías, A. L.; Chia, C.-I.; Wang, B.; Crespi, V. H.; López-Urías, F.; Charlier, J.-C.; Terrones, H.; Terrones, M. Identification of Individual and Few Layers of WS₂ Using Raman Spectroscopy. *Sci. Rep.* **2013**, *3* (1), 1755.
- (47) Lee, C.; Yan, H.; Brus, L. E.; Heinz, T. F.; Hone, J.; Ryu, S. Anomalous Lattice Vibrations of Single- and Few-Layer MoS₂. *ACS Nano* **2010**, *4* (5), 2695–2700.
- (48) Qiao, S.; Yang, H.; Bai, Z.; Peng, G.; Zhang, X. Identifying the Number of WS₂ Layers via Raman and Photoluminescence Spectrum. *Proceedings of the 2017 5th International Conference on Mechatronics, Materials, Chemistry and Computer Engineering (ICMMCCCE 2017)*; Chongqing, China, July 24–25, 2017; DOI: 10.2991/icmmccce-17.2017.247.
- (49) Kosmala, T.; Palczynski, P.; Amati, M.; Gregoratti, L.; Sezen, H.; Mattevi, C.; Agnoli, S.; Granozzi, G. Strain Induced Phase Transition of WS₂ by Local Dewetting of Au/Mica Film upon Annealing. *Surfaces* **2021**, *4* (1), 1–8.
- (50) Zhou, P.; Xu, Q.; Li, H.; Wang, Y.; Yan, B.; Zhou, Y.; Chen, J.; Zhang, J.; Wang, K. Fabrication of Two-Dimensional Lateral Heterostructures of WS₂/WO₃·H₂O through Selective Oxidation of Monolayer WS₂. *Angew. Chem., Int. Ed.* **2015**, *54* (50), 15226–15230.
- (51) Gao, J.; Li, B.; Tan, J.; Chow, P.; Lu, T.-M.; Koratkar, N. Aging of Transition Metal Dichalcogenide Monolayers. *ACS Nano* **2016**, *10* (2), 2628–2635.
- (52) Rong, Y.; He, K.; Pacios, M.; Robertson, A. W.; Bhaskaran, H.; Warner, J. H. Controlled Preferential Oxidation of Grain Boundaries in Monolayer Tungsten Disulfide for Direct Optical Imaging. *ACS Nano* **2015**, *9* (4), 3695–3703.
- (53) Perrozzi, F.; Emamjomeh, S. M.; Paolucci, V.; Taglieri, G.; Ottaviano, L.; Cantalini, C. Thermal Stability of WS₂ Flakes and Gas Sensing Properties of WS₂/WO₃ Composite to H₂, NH₃ and NO₂. *Sens. Actuators, B* **2017**, *243* (2), 812–822.
- (54) Liu, Q.; Wang, F.; Lin, H.; Xie, Y.; Tong, N.; Lin, J.; Zhang, X.; Zhang, Z.; Wang, X. Surface Oxygen Vacancy and Defect Engineering of WO₃ for Improved Visible Light Photocatalytic Performance. *Catal. Sci. Technol.* **2018**, *8* (17), 4399–4406.
- (55) Dupin, J.-C.; Gonbeau, D.; Vinatier, P.; Levasseur, A. Systematic XPS Studies of Metal Oxides, Hydroxides and Peroxides. *Phys. Chem. Chem. Phys.* **2000**, *2* (6), 1319–1324.
- (56) Warren, A.; Nylund, A.; Olefjord, I. Oxidation of Tungsten and Tungsten Carbide in Dry and Humid Atmospheres. *Int. J. Refract. Met. Hard Mater.* **1996**, *14* (5–6), 345–353.
- (57) Tomašević-Ilić, T.; Jovanović, Đ.; Popov, I.; Fandan, R.; Pedrós, J.; Spasenović, M.; Gajić, R. Reducing Sheet Resistance of Self-Assembled Transparent Graphene Films by Defect Patching and Doping with UV/Ozone Treatment. *Appl. Surf. Sci.* **2018**, *458*, 446–453.

(58) Chow, P. K.; Singh, E.; Viana, B. C.; Gao, J.; Luo, J.; Li, J.; Lin, Z.; Elías, A. L.; Shi, Y.; Wang, Z.; Terrones, M.; Koratkar, N. Wetting of Mono and Few-Layered WS₂ and MoS₂ Films Supported on Si/SiO₂ Substrates. *ACS Nano* **2015**, *9* (3), 3023–3031.

(59) Huang, G.; Liu, H.; Wang, S.; Yang, X.; Liu, B.; Chen, H.; Xu, M. Hierarchical Architecture of WS₂ Nanosheets on Graphene Frameworks with Enhanced Electrochemical Properties for Lithium Storage and Hydrogen Evolution. *J. Mater. Chem. A* **2015**, *3* (47), 24128–24138.

(60) Han, G.-F.; Li, F.; Zou, W.; Karamad, M.; Jeon, J.-P.; Kim, S.-W.; Kim, S.-J.; Bu, Y.; Fu, Z.; Lu, Y.; Siahrostami, S.; Baek, J.-B. Building and Identifying Highly Active Oxygenated Groups in Carbon Materials for Oxygen Reduction to H₂O₂. *Nat. Commun.* **2020**, *11* (1), 2209.

(61) Kerber, S. J.; Bruckner, J. J.; Wozniak, K.; Seal, S.; Hardcastle, S.; Barr, T. L. The Nature of Hydrogen in X-ray Photoelectron Spectroscopy: General Patterns from Hydroxides to Hydrogen Bonding. *J. Vac. Sci. Technol., A* **1996**, *14* (3), 1314–1320.

(62) Universitaria, C.; Jardines, C.; Manuel, D. S. Structural Properties of WO₃ Dependent of the Annealing Temperature Deposited by Hot-Filament Metal Oxide Deposition. *Rev. Mex. Fis.* **2012**, *58* (6), 504–509.

(63) Albanese, E.; Di Valentin, C.; Pacchioni, G. H₂O Adsorption on WO₃ and WO_{3-x} (001) Surfaces. *ACS Appl. Mater. Interfaces* **2017**, *9* (27), 23212–23221.

(64) Jones, T. E.; Rocha, T. C. R.; Knop-Gericke, A.; Stampfl, C.; Schlögl, R.; Piccinin, S. Insights into the Electronic Structure of the Oxygen Species Active in Alkene Epoxidation on Silver. *ACS Catal.* **2015**, *5* (10), 5846–5850.

Recommended by ACS

Room-Temperature NO₂ Sensing of CVD-Modified WS₂-WSe₂ Heterojunctions

Abderrahim Moumen, Elisabetta Comini, *et al.*

MAY 04, 2023
ACS APPLIED NANO MATERIALS

READ 

WS₂ and WS₂-ZnO Chemiresistive Gas Sensors: The Role of Analyte Charge Asymmetry and Molecular Size

Farman Ullah, Kevin Musselman, *et al.*

MARCH 16, 2023
ACS SENSORS

READ 

Layer-Dependent NO₂-Sensing Performance in MoS₂ for Room-Temperature Monitoring

Meng Qi, Jianbo Wang, *et al.*

MAY 23, 2023
ACS APPLIED NANO MATERIALS

READ 

Drastic Gas Sensing Selectivity in 2-Dimensional MoS₂ Nanoflakes by Noble Metal Decoration

Taehoon Kim, Ho Won Jang, *et al.*

FEBRUARY 24, 2023
ACS NANO

READ 

Get More Suggestions >

SCIENTIFIC REPORTS



OPEN

Probing charge transfer between molecular semiconductors and graphene

Aleksandar Matković¹, Markus Kratzer¹, Benjamin Kaufmann¹, Jasna Vujan², Radoš Gajić² & Christian Teichert¹ 

Received: 5 June 2017

Accepted: 24 July 2017

Published online: 25 August 2017

The unique density of states and exceptionally low electrical noise allow graphene-based field effect devices to be utilized as extremely sensitive potentiometers for probing charge transfer with adsorbed species. On the other hand, molecular level alignment at the interface with electrodes can strongly influence the performance of organic-based devices. For this reason, interfacial band engineering is crucial for potential applications of graphene/organic semiconductor heterostructures. Here, we demonstrate charge transfer between graphene and two molecular semiconductors, parahexaphenyl and buckminsterfullerene C₆₀. Through *in-situ* measurements, we directly probe the charge transfer as the interfacial dipoles are formed. It is found that the adsorbed molecules do not affect electron scattering rates in graphene, indicating that charge transfer is the main mechanism governing the level alignment. From the amount of transferred charge and the molecular coverage of the grown films, the amount of charge transferred per adsorbed molecule is estimated, indicating very weak interaction.

Graphene has a significant potential to be used as a new transparent conductive electrode material in flexible and wearable electronics, optoelectronics, and energy applications^{1,2}. In addition to high transparency, high mechanical strength, flexibility, thermal as well as chemical stability, and ease of functionalization, there are also crucial advantages of graphene as an electrode material in organic electronics. These are mainly based on the favorable band alignment with many organic semiconductors and on their impeccable growth morphologies on graphene, which relies on the van der Waals (vdW) nature of the interface³. As a consequence, these heterostructures exhibit low injection barriers, high charge extraction and injection efficiencies with electronic decoupling and preservation of the intrinsic functionality of the molecular crystals at the interface^{4–19}. Hence, graphene is employed as a carrier injection layer between organic semiconductors and metallic contacts⁴ and as vdW electrode^{5–7}. Efficient charge separation in graphene/organic semiconductors photo-transistors¹⁵ as well as organic light emitting diodes^{20–23} have been demonstrated. Moreover, heterointerfaces between organic semiconductors and other two-dimensional (2D) materials – like hexagonal boron nitride and MoS₂ – have been realized, enhancing existing and enabling new functionalities in organic electronics based devices^{7,13,18,24,25}.

Interfacial band engineering—through charge transfer and band alignment—is crucial for potential applications of graphene-organic semiconductor heterostructures. Doping of graphene by charge transfer with organic molecular layers has been investigated using Kelvin probe force microscopy and electrical measurements of graphene field effect devices^{9,10}. Using a gated graphene field-effect device enables precise control of graphene's Fermi level position²⁶, which affects charge transport through the interface^{14,23}. This allows even tuning the molecular orbitals at the interface²⁷. Furthermore, *in-situ* sheet resistance measurements combined with ultraviolet photoelectron spectroscopy have been used to investigate charge transfer between graphene and Cs₂CO₃ in an organic matrix²², where the formation of a large interface dipole and n-type doping of graphene were observed. In general, materials with a work function (Φ) substantially lower than that of graphene are needed to achieve n-type doping, as was also demonstrated by deposition of potassium and ZnO^{23,28}. Recently, interfaces between graphene and metal oxides have been investigated as effective hole-injection layers in organic light emitting diodes^{20,21}, exhibiting p-type doping of graphene through charge transfer and formation of an interfacial dipole.

¹Institute of Physics, Montanuniversität Leoben, Franz Josef Strasse 18, 8700, Leoben, Austria. ²Graphene Laboratory of Center for Solid State Physics and New Materials, Institute of Physics, University of Belgrade, Pregrevica 118, 11080, Belgrade, Serbia. Correspondence and requests for materials should be addressed to C.T. (email: teichert@unileoben.ac.at)

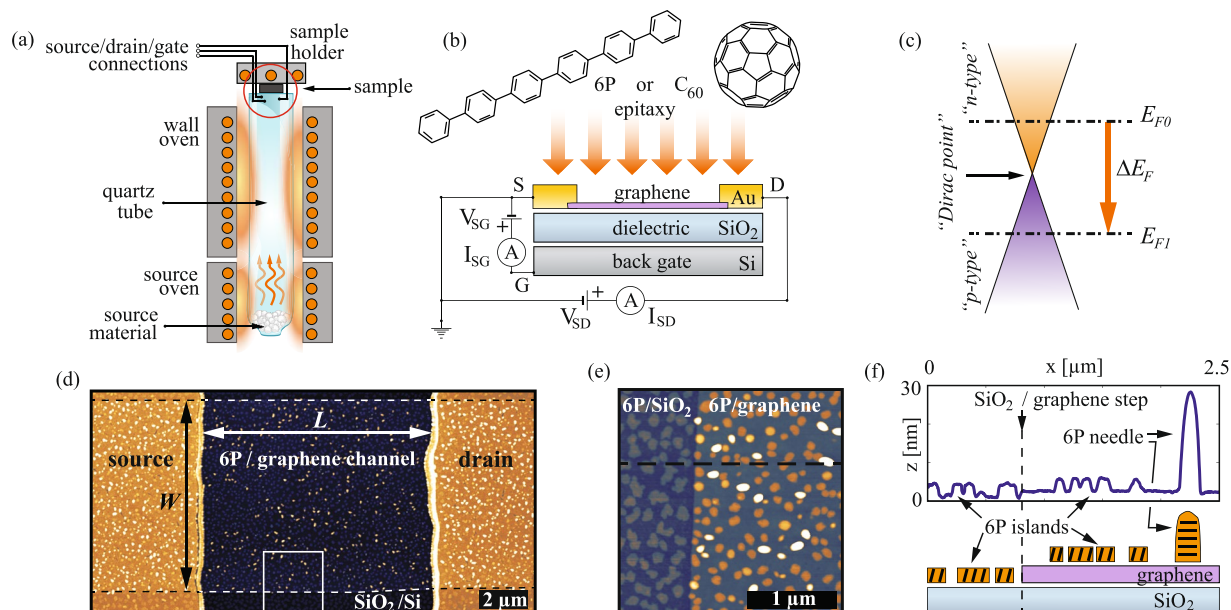


Figure 1. Experimental setup: (a) layout of the HWE setup. The scheme of the sample (marked by an orange circle) is enlarged in (b) showing upside-down the graphene FET with the *in-situ* DC electrical characterization scheme. (c) Graphene's dispersion relation. E_{F0} and E_{F1} indicate the position of the Fermi level (with respect to the Dirac point) before and after epitaxy, while ΔE_F indicates the shift of graphene's Fermi level. (d) AFM topography image of one of the devices used in the study after the deposition of a sub-monolayer of 6P (z scale 50 nm). Dashed lines in (d) highlight the rims of the graphene flake. L and W mark channel length and width. (e) Area exhibiting a step-edge between graphene and SiO_2 , indicated in (d) by a square and rotated by 90° with respect to (d) (z scale 25 nm). (f) A height cross section along the dashed line in (e) is shown (top), with a corresponding layout of the structure (bottom).

Owing to the unique density of states of graphene²⁶ and the exceptionally low electrical noise²⁹, field effect devices can be utilized as extremely sensitive potentiometers for probing charge transfer between graphene and adsorbed species. This was used even to detect individual adsorption/desorption events of gas molecules as NO_2 on micrometer-scale devices³⁰. Moreover, *in-situ* electrical characterization was employed to reveal the relation between SiO_2 and the effective p-type doping of graphene under ambient conditions³¹, showing the necessity of both, water and oxygen in this process.

Nonetheless, the high sensitivity of graphene devices goes along with a lack of selectivity. The effects of marginal remnants, arising from the device preparation (degassing, annealing, purging, exposure to ambient conditions) often mask the charge transfer effect that is actually under investigation. For this reason, *in-situ* electrical characterization is needed which strictly avoids further sample treatment and exposure to ambient atmosphere, especially in the cases when charge transfer is expected to be small. Yet, a study of charge transfer between molecular crystals and graphene by *in-situ* electrical measurements with simultaneous capability of tuning graphene's Fermi level position and type of majority carriers is greatly lacking.

In this study, we examine charge transfer between graphene and two molecular crystals: para-hexaphenyl (6P)^{32,33}, a wide HOMO-LUMO gap, intrinsic organic semiconductor with well matching Φ to graphene^{34,35}; and buckminsterfullerene C_{60} , an n-type semiconductor with Φ over 1 eV larger than that of graphene^{36,37}. The organic thin films (0.5–10.0 monolayers (ML)) have been prepared using a hot wall epitaxy (HWE) setup³⁸ equipped with electrical contacts to the sample in order to enable *in-situ* electrical characterization. As substrates, field effect transistors (FETs) with an exfoliated graphene channel have been used.

We study *in-situ* the effect that deposited molecular crystals have on the transfer curves of graphene FETs, and thus probe the formation of the interfacial dipole. The setup allows us to control graphene's Fermi level position prior (and during) the growth experiments. The estimated charge transfer per adsorbed molecule deduced from the graphene's Fermi level shift and the molecular coverage indicate a very weak interaction. Furthermore, the same setup has been used for desorption experiments with 6P, showing that the charge transfer process is completely reversible upon 6P desorption.

Results and Discussion

Introducing the setup. The custom-built HWE chamber used in this study has three electrical contacts attached to the sample holder, which allow to probe and tune electrical properties of the samples prior and during the growth. A layout of the growth chamber is illustrated in Fig. 1a. A schematic representation of a graphene FET is shown in Fig. 1b, also indicating the connections for the *in-situ* electrical measurement setup. Graphene films exhibit trace amounts of photoresist contaminations from FET fabrication³⁹. These residues were observed

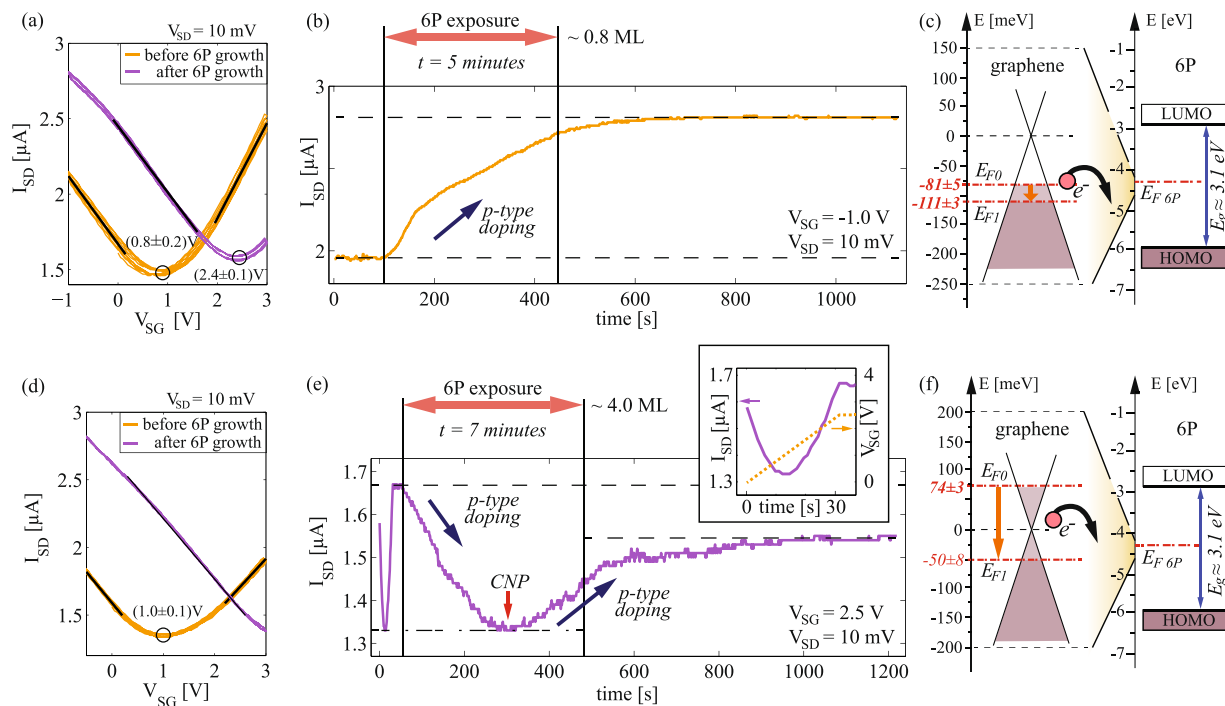


Figure 2. 6P growth experiments: (a) Transfer curves (five subsequent forward and backward V_{SG} sweeps) of a graphene field-effect device directly before and after deposition of ~ 0.8 ML of 6P. (b) I_{SD} as a function of time during the deposition, starting from p-type graphene. (c) Band diagrams of graphene (left) and 6P (right) prior to interaction. (d–f) Analogue results for another device, on which the growth was started from n-type graphene and ~ 4 ML of 6P were grown. Inset of (e) shows an initial V_{SG} ramp (and corresponding I_{SD}) used to bias the device prior to growth.

to have similar impact on the morphology of the grown films as in the case of wet-transferred chemical vapor deposited graphene⁴⁰.

From the transfer curves of graphene FETs ($I_{SD}(V_{SG})$) it is possible to recalculate the position of graphene's Fermi level, both prior and after the growth (E_{F0} and E_{F1}) as illustrated in Fig. 1c (see supplementary information for more details). The charge neutrality point (CNP) of graphene was found not to be exactly at $V_{SG} = 0$ V prior to the growth experiments. This has been attributed to the unintentional doping that results mainly from the trapped interfacial layer between graphene and SiO_2 , exposure to ambient water vapor, and lithography residues, thus giving a different CNP value for each sample^{31,39}. For this reason, performing *in-situ* measurements of the charge transfer during the growth is essential to eliminate all other contributions (degassing, annealing, and exposure to ambient) which would affect the transfer curves of graphene in a similar way (see supplementary information for the details on the pre-treatment of graphene FETs). Figure 1d shows an atomic force microscopy (AFM) overview topography image of one of the devices covered with ~ 0.8 ML of 6P. A magnified region of the channel rim is shown in Fig. 1e. The height cross-section of Fig. 1e and the scheme of the structure are presented in Fig. 1f.

6P growth experiments. Figure 2a shows transfer curves of a graphene FET measured at 2×10^{-6} mbar (300 K) in the growth chamber, directly prior and after the growth of ~ 0.8 ML of 6P. The device was slightly p-doped with a CNP at $V_{CNP} = (0.8 \pm 0.2)$ V, giving $E_F = -(56 \pm 8)$ meV. The Fermi level was kept below the neutrality point ($E_{F0} = -(81 \pm 5)$ meV), within the linear part of the transfer curve by setting $V_{SG} = -1$ V during the growth experiments. The *in-situ* measurements of I_{SD} during the growth (Fig. 2b) reveal that upon exposure of the device surface to 6P I_{SD} immediately starts to increase. Considering that graphene was initially p-type, an increase in the current indicates further p-doping by the adsorbed molecules. Schematic representations of the band diagrams of graphene and 6P are shown in Fig. 2c, indicating the estimated positions of the graphene's Fermi level prior and after the growth. The different scale (a factor of 20) for the energy axis between graphene and 6P is used to make graphene's Fermi level shift visible.

Solid lines in Fig. 2a represent linear fits used to estimate the field-effect mobilities⁴¹. Devices used in this study had field-effect electron and hole mobilities in the range of $3000\text{--}6000 \text{ cm}^2 \text{ V}^{-1} \text{ s}^{-1}$, which is in a good agreement with the data reported for exfoliated graphene on SiO_2 ³⁰. Interestingly, the main difference between the transfer curves prior and after the deposition of 6P is a parallel shift. Only minor changes in the minimal value of I_{SD} and in the field-effect mobilities (slopes of the curves) were detected in all growth experiments. This fact unambiguously proves that the deposited thin layers of the molecular crystals did not affect scattering rates in graphene. Thus, the doping mechanism is mainly based on charge transfer between graphene and the adsorbed molecules.

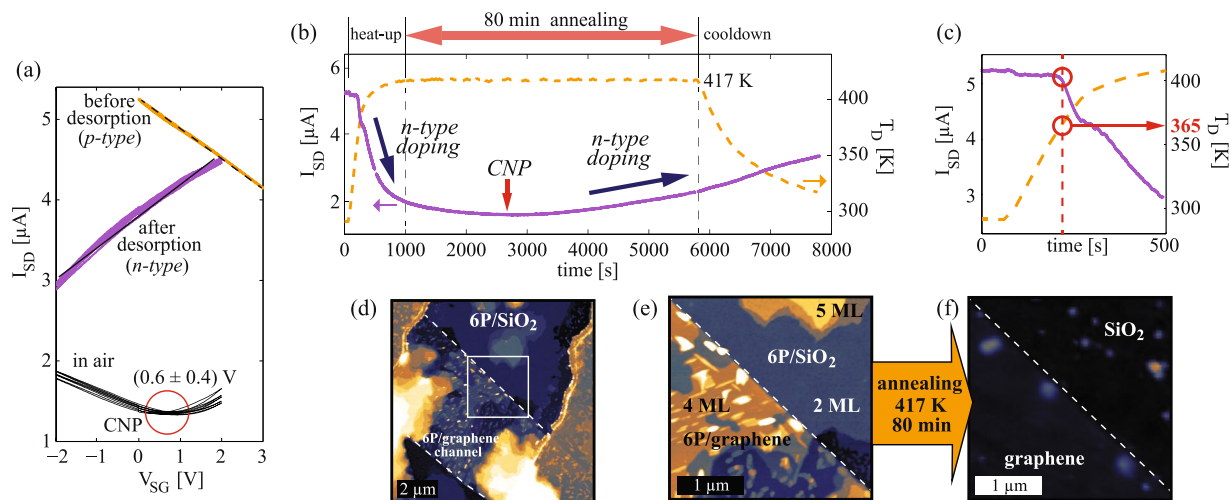


Figure 3. 6P desorption experiment: (a) Set of transfer curves of a device initially covered with ~ 4 ML of 6P (Fig. 2(d–f)), in high vacuum before and after desorption of 6P, and in air after desorption of 6P. (b) Current through the device during annealing (solid line) and the corresponding T_D (dashed line). (c) Enlarged initial 500 s of (b) showing the desorption temperature for the 6P thin film on graphene. (d) AFM topography of the device prior to desorption experiment, z scale 60 nm. (e,f) Enlarged AFM images of a graphene/SiO₂ edge (marked by a square in (d)) before and after annealing (z scale 30 nm).

Figure 2d–f shows analogue results to those presented in Fig. 2a–c, obtained from another device on which the growth was started from n-type graphene and ~ 4 ML of 6P were grown. As shown in Fig. 2d (orange curves), the device was unintentionally p-doped prior to the growth experiments, with CNP at $V_{SG} = (1.0 \pm 0.1)$ V. In order to ensure that graphene's Fermi level is above the CNP at the beginning of the growth experiment, a constant voltage $V_{SG} = 2.5$ V was applied during the growth, thus giving the initial position of the Fermi level of $E_{F0} = (74 \pm 3)$ meV. The inset in Fig. 2e highlights the first 40 seconds of the diagram, during which V_{SG} was ramped from 0 V to 2.5 V prior to 6P deposition. As the gate voltage increases, the I_{SD} curve changes from p-type graphene-through CNP–to n-type graphene. Then, the device was exposed to 6P vapor and the current immediately decreased. Since the experiment started from initially n-type graphene, a decrease in current (at constant V_{SG}) indicates again p-type doping by the adsorbed molecules. Interestingly, the minimal value in current which was reached during the growth experiment matches exactly the minimal value reached by sweeping V_{SG} . This indicates that adsorbed molecules lower the Fermi level of graphene from n-type–through the neutrality point and into p-type–where further p-type doping is seen as an increase in the current. This was confirmed by measuring transfer curves after the growth (Fig. 2d). The fact that the electrostatic gating and 6P deposition yield the exact same minimal value of I_{SD} further supports that charge transfer doping at the 6P/graphene interface is the main mechanism through which the adsorbed molecules affect the electrical properties of the device.

6P desorption experiment. The reversibility of the charge transfer process was demonstrated by desorption experiments, for the case of 6P. The experiments were carried out in the same HWE chamber, where previously grown 6P films were annealed (at 415–425 K) in high vacuum for an extended period of time, hence releasing the molecules from the surface of the graphene FETs. The same *in-situ* electrical characterization has been carried out as for the growth experiments, with the slight difference that the transfer curves after annealing were only measured once the sample has reached again 300 K.

In Fig. 3, we present the data obtained from the desorption experiment of the device shown in Fig. 2d–f. Between the growth and desorption experiments, the morphology of the 6P film was characterized by AFM under ambient conditions, thus inevitably exposing the graphene/6P interface to water vapor, enhancing p-type doping of graphene³¹. For comparison, we provide in Fig. 3a transfer curves of the device before and after desorption of ~ 4 ML of 6P, as well as in ambient air after the desorption. Annealing in high vacuum was carried out by heating the sample up to 417 K for 80 minutes, followed by a slow cool-down to room temperature. During annealing of the device, I_{SD} was measured and correlated to sample temperature T_D , as shown in Fig. 3b. Since the graphene was initially p-doped, a reduction of I_{SD} indicates n-type doping demonstrating the reversibility of the charge transfer mechanism. The minimal value of the current reached by annealing was slightly higher than for the case of electrostatic gating (Figs 2d and 3a), since in this case the sample was at $T_D = 417$ K, which certainly affects both, the scattering rates in graphene and the serial resistance. After cool-down, transfer curves were again measured, showing n-type behavior (Fig. 3a). The field-effect mobilities of graphene were not significantly affected by the annealing and desorption of the molecules.

Figure 3c shows the magnified heat-up step of the annealing process (the first 500 s of Fig. 3b). Initially, as the device heats up, almost no change in the current is detected. This is the case until T_D reaches (365 ± 5) K, then, a rapid reduction in the current sets in, which is attributed to 6P desorption. This might be useful to determine

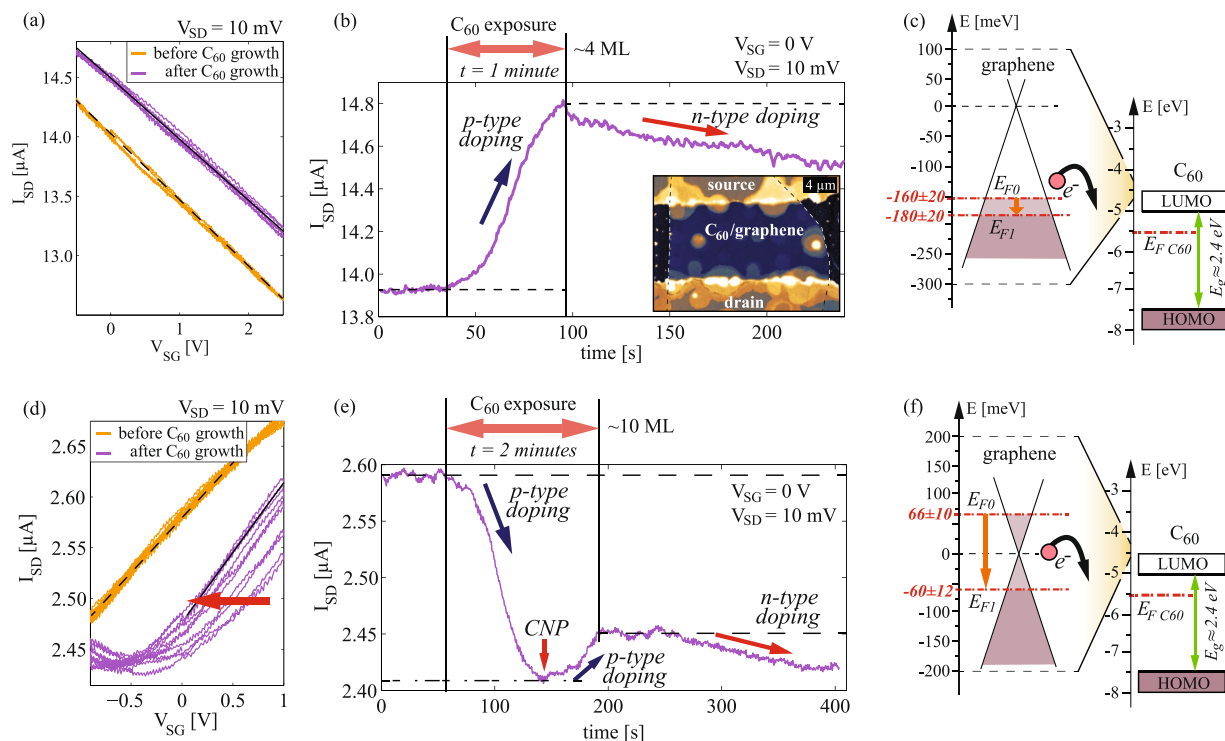


Figure 4. C₆₀ growth experiments: (a) Transfer curves (five subsequent forward and backward V_{SG} sweeps) of a graphene field-effect device immediately before and after deposition of ~4 ML of C₆₀ and (b) I_{SD} as a function of time during the deposition starting from p-type graphene. The inset in (b) shows the AFM topography of the sample after the growth. (c) Band diagrams of graphene (left) and C₆₀ (right) prior to interaction. The energy scales between graphene and C₆₀ have a factor of 20 difference. (d–f) Analogue results for another device, on which the growth was started from n-type graphene, and ~10 ML of C₆₀ were grown. An arrow in (d) indicates the direction of the shifting of the subsequently measured transfer curves.

the desorption temperature of organic semiconductors from graphene. However, both molecular rearrangement prior to desorption and the heating rate could affect the desorption temperature⁴².

AFM was used to monitor the amount of material removed from the surface by annealing. An overview of the device prior to thermal desorption is presented in Fig. 3d. Figure 3e–f compares AFM images of an area at the channel edge (indicated by the white square in Fig. 3d) before and after annealing. The same z scale for both images is used to highlight that the majority (over 95%) of the material was successfully removed by annealing for only 80 minutes. Extended annealing times or higher annealing temperatures would entirely remove the 6P, however, this could also affect the serial resistance of the thin gold electrodes and was therefore avoided.

C₆₀ growth experiments. Using the same method as for 6P, charge transfer at the interface between graphene and C₆₀ was also investigated. Figure 4 provides results from the *in-situ* electrical measurements during the growth of C₆₀. Data for two devices are presented in the same manner as for 6P (Fig. 2). Figure 4a shows transfer curves of an intrinsically p-doped device prior to growth, V_{CNP} = (7.0 ± 1.5) V. Due to strong initial intrinsic p-doping of the sample, the CNP could not be reached within the accessible range of V_{SG} (without risking electrostatic breakdown of the SiO₂). The position of the CNP was estimated considering the value observed in air prior to degassing and annealing of the device. Hence, there is a larger uncertainty of the exact initial position of the Fermi level (E_{F0} = -(160 ± 20) meV). However, this does not affect the shift of the transfer curves and the amount of transferred charge introduced by the adsorbed molecules, which can still be estimated from Fig. 4a. During the growth, I_{SD} was recorded as a function of time (Fig. 4b). Starting from p-type graphene, an increase in current upon exposure to C₆₀ indicates further p-doping. The inset in Fig. 4b is an AFM topography image of the device with ~4 ML of C₆₀. In Fig. 4c, a scheme of the graphene and C₆₀ band structures is presented with different energy scales for graphene and C₆₀ visualizing the graphene's Fermi level shift.

In analogy to Fig. 4a–c, data of another device (initially slightly n-doped) is shown in Fig. 4d–f with ~10 ML of C₆₀ grown. Steady p-type doping of graphene with C₆₀ exposure was also observed in this case leading to a lowering of graphene's Fermi level from the n-type- through the neutrality point- into the p-type regime. This can be well observed by following the *in-situ* measurements of I_{SD} in Fig. 4e.

Interestingly, in the case of C₆₀, I_{SD} did not saturate at a certain value immediately after the growth, as it was the case for 6P. Yet, after C₆₀ deposition I_{SD} kept changing, indicating n-type doping of graphene (see Fig. 4b,e). The value for I_{SD} saturated just several minutes after the growth has been stopped. An unstable level of doping was also observed in the transfer curves after the growth (shown in Fig. 4d). There, successive transfer curves are shifted to

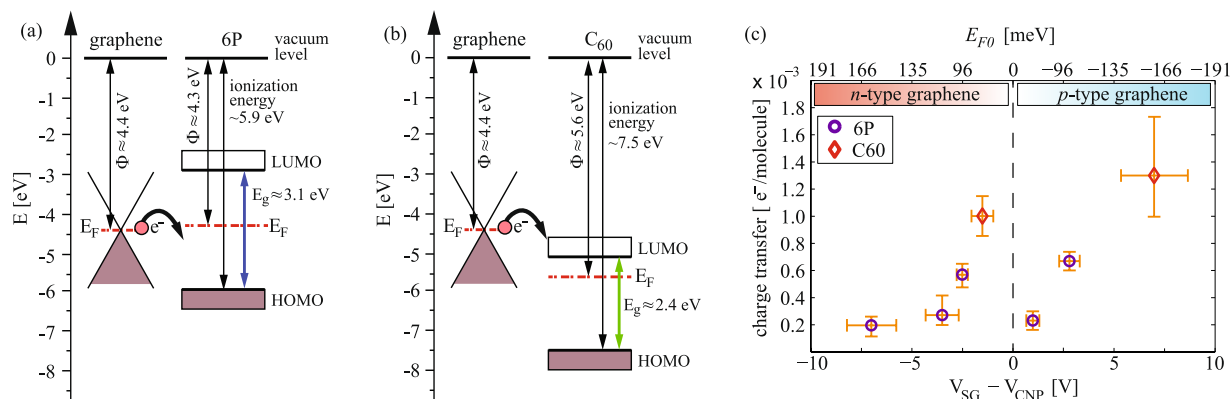


Figure 5. Band diagrams and charge transfer: **(a,b)** band diagrams prior to establishing the equilibrium (equal vacuum levels) for graphene/6P and graphene/ C_{60} , respectively. **(c)** Charge transfer per molecule as a function of the position of CNP prior to the growth, for all the devices used in this study. Circles represent the data for 6P/graphene and diamonds for C_{60} /graphene interfaces.

lower voltages as indicated by the arrow. Again, the lateral shift of the transfer curves indicates that the underlying process is mainly based on the charge transfer. The direction of the shift (marked by a red arrow in Fig. 4d) reveals that electrons were transferred back to graphene, introducing n-type doping. The observed doping instability in graphene after C_{60} exposure is most likely caused by interaction with the remaining oxygen in the HWE growth chamber. Diffusion of oxygen into C_{60} films was previously shown to affect the interfacial dipole formed between C_{60} and highly oriented pyrolytic graphite³⁷ and to deteriorate electrical conductivity of C_{60} based devices⁴³.

Band diagrams and charge transfer. Transfer of electrons from graphene—and consequent p-type doping of graphene by both 6P and C_{60} —is self-evident when the difference between the Φ of graphene (≈ 4.4 eV)⁴⁴ and the ionization energy of the molecular crystals is considered. In both cases, the Fermi level in graphene is expected to be at least 1 eV above the highest occupied molecular orbitals. Figure 5a,b shows band diagrams for graphene/6P and graphene/ C_{60} prior to interaction (considering equal vacuum levels). The data for the ionization energies, Φ , and band gaps of 6P and C_{60} were taken from ultraviolet photoelectron spectroscopy (UPS) of bulk molecular crystals and thin films deposited on highly oriented pyrolytic graphite^{35–37,45}. As the interface is formed, electrons are transferred from graphene into the growing molecular crystals. Considering the low density of states of both, 6P and C_{60} , and the small amount of material in the grown films (less than 10 nm), Fermi level alignment in the ordinary sense (bulk interfaces) is most likely not possible and would require significantly thicker films³⁷.

Since the shift of the CNP is known, it is possible to estimate the number of transferred electrons from graphene. The detailed morphology of the grown films revealed by AFM (see supplementary information) together with the most probable crystal phases of both 6P and C_{60} (Baker structure and face centered cubic, respectively), allow an estimation of the number of deposited molecules. From these two values, the average charge transfer per adsorbed molecule can be calculated. A compilation of the estimated charge transfer per adsorbed molecule as function of the CNP position (initial Fermi level position) is provided in Fig. 5c. Error bars in the x axis indicate the uncertainty of the initial CNP position, while error bars in the y axis mainly originate from the uncertainty of the total volume of the molecular crystals grown on the device surfaces (measured by AFM). The obtained charge transfer per adsorbed 6P molecule was found to be $\sim 4.7 \times 10^{-4}$ electrons/6P, and for the case of C_{60} somewhat higher values of $\sim 1.1 \times 10^{-3}$ electrons/ C_{60} were deduced. No significant change of the charge transfer was observed within the available range of the applied gate voltage (initial position of graphene's Fermi level), and the observed differences between individual devices are likely related to sample-to-sample variations.

Similar results were obtained for the charge transfer at the graphene/pentacene interface measured by UPS⁶ and for the graphene/ C_{60} interface measured by scanning tunneling spectroscopy and transport characteristics^{11,46}, revealing weak interaction and small charge transfer from graphene. Vertical heterostructures using a graphene/ C_{60} interface have shown slight downshifts of graphene's Fermi level upon C_{60} deposition¹⁴. In addition, charge transfers between epitaxial graphene and gold, antimony, and bismuth have somewhat larger values⁴⁷, in the order of $2\text{--}10 \times 10^{-3}$ electrons taken from graphene per adsorbed metal atom. Very recently, molecules (as acetone and toluene) trapped at the interface between graphene and SiO_2 , and the influence of arrangement of C_{60} on graphene and the role of the supporting substrate on the charge transfer have been investigated^{48,49}, in both cases exhibiting charge transfer in the order of $\sim 10^{-3}$ electrons per molecule.

The fact that over thousand molecules are needed to extract only one electron from graphene raises the question of the nature of the charge transfer mechanism. The charge transfer could either be fractional or integer^{50,51}. Fractional charge transfer has been reported for molecules adsorbed on clean metal surfaces, usually through weak chemisorption or covalent bonding^{50–52} resulting in an excess charge homogeneously distributed among the molecules, yielding an effective fractional charge per each molecule. As an alternative scenario, the integer charge transfer was reported for weakly interacting interfaces like passivated metal surfaces^{50,51}. In this case, electrons tunnel from the metal and are localized only on some molecules, while the others remain electrically neutral. In

this study, fractional charge transfer is less likely due to the vdW nature of the interface. Moreover, measurements of the source-drain current during the growth did not show significant changes between the first and several subsequent layers, for the case when multi-layers are grown. This observation further indicates that the charge transfer mechanism is more likely an integer than a fractional one.

Conclusions

In summary, a weak electronic interaction through charge transfer between graphene and molecular semiconductors (6P and C₆₀) was observed. As the interface forms, less than 10⁻³ electrons per molecule are taken from graphene, consequently lowering graphene's Fermi level and introducing p-type doping of graphene. This result was found not to be dependent on the initial type of the majority carriers in graphene (initially p- or n-type), confirming that band alignment is more important than the type of doping when considering interfacial band engineering with graphene. Moreover, the fact that the adsorbed molecules have mainly affected the ambipolar transfer curves of graphene field-effect devices through lateral shifts unambiguously proves that the scattering rates in graphene were not affected by the adsorbed molecules. This confirms that the interaction occurs principally through charge transfer and formation of an interfacial dipole, with further indications that integer charge transfer occurs in these systems.

Methods

Fabrication of graphene field effect devices. Graphene flakes were prepared by micromechanical exfoliation of kish graphite. Flakes were deposited on highly doped Si substrates (less than 0.01 Ω cm), serving as a back-gate electrode (G), with (80 ± 2) nm thin layer of dry thermal SiO₂, which acts as a gate dielectric and enhances optical contrast of the flakes. Single-layer graphene flakes were selected by optical microscopy and were checked for any contaminations, wrinkles, and cracks by AFM, prior to the deposition of the electrodes. Source (S) and drain (D) top contacts were made by positive mask UV photolithography, with a (20–30) nm thick gold layer. Channel length was ~10 μm, and width (W) was (5–30) μm (depending on the shape of the flakes).

In order to have stable transfer characteristics of the devices and to ensure reproducibility of the data, all samples were left to degas in high vacuum (≈1 × 10⁻⁶ mbar) for 12 hours, followed by annealing in high vacuum prior to the growth of molecular crystals. More details on the pre-treatment of the graphene FETs is given in the supporting information, where 6P crystallites are also grown at elevated T_D (365 K) in order to accent the impact of the surface contaminations on the growth of the molecules.

Electrical measurements and field-effect mobility estimates. Electrical measurements were carried out within an HWE chamber, using a Keithley 2636 A SYSTEM SourceMeter. Voltages between S and D (V_{SD}) and S and G (V_{SG}) were applied, and the currents between S and D (I_{SD}) and S and G (I_{SG}) were measured. To avoid electrostatic breakdown of the SiO₂, I_{SG} was monitored and set not to exceed 1 nA. All transfer curves I_{SD}(V_{SG}) were measured at room temperature in either high vacuum or ambient atmosphere. Five subsequent transfer curves were measured each time to ensure reproducibility, with ΔV_{SG} = 0.01 V and time steps of 200 ms. For *in-situ* measurements of I_{SD}, the time step was set to 500 ms. The sample temperature (T_D) was kept constant at (300 ± 2) K in order to exclude other potential contributions to the charge transfer process. The position of the Fermi level in graphene was calculated considering a parallel plate capacitor between graphene and SiO₂ and taking the Fermi velocity of electrons in graphene as 10⁶ m/s (see supplementary information for more details). Field effect mobilities were extracted considering the diffusive regime of charge transport (L = 10 μm). ΔI_{SD}/ΔV_{SG} was obtained from the linear parts of the transfer curves. Serial resistances (R_S) of the devices (mainly arising from thin Au pads) were measured for each device batch by Kelvin probe force microscopy measurements of the voltage drop between S and D. R_S was found to be between 20% and 30% of the total device resistivity. It is worth to mention that only the absolute values for the field-effect mobilities are affected by R_S.

Hot wall epitaxy setup. Thin films of molecular semiconductors were grown using a home-built HWE setup with electrical connections to the sample holder that allow *in-situ* electrical measurements. The growth was carried out in high vacuum (base pressure of 1 × 10⁻⁶ mbar) with fix source (T_S) and wall (T_W) temperatures, for 6P T_S = 508 K, T_W = 518 K, and for C₆₀ T_S = 623 K, T_W = 638 K.

AFM measurements and molecular semiconductors film morphologies. The morphology of the samples was investigated employing an Asylum Research MFP-3D AFM system operating under ambient conditions. Olympus AC160TS probes were used with typical force constants of 20–80 N/m and tip curvature radii of 5–7 nm. AFM topography images of the samples were processed using the open source software Gwyddion (version 2.38). The thickness of the molecular crystals was estimated considering the total volume on the device active area and presented as an equivalent in complete monolayers (ML) of the bulk structure (in the case of 6P considering up-right standing molecules that form island-like crystallites) of the molecular crystals, since an ideal layer-by-layer growth was not observed. In the considered ranges of the growth temperatures, only the monoclinic β-phase of 6P crystallites is expected (the Baker structure) and the fcc structure of C₆₀. The morphology of C₆₀ films indicated layered growth (step edge height of ~0.8 nm), while 6P films were found to consist of both, islands of up-right standing molecules (~2.6 nm) and needles with flat-laying molecules (taller than 10 nm).

Data availability statement. The datasets generated during and/or analysed during the current study that are not included in this published article (and its supplementary information files) are available from the corresponding author on reasonable request.

References

- Ferrari, A. C. *et al.* Science and technology roadmap for graphene, related two-dimensional crystals, and hybrid systems. *Nanoscale* **7**, 4598–4810 (2014).
- Bonaccorso, F. *et al.* Graphene, related two-dimensional crystals, and hybrid systems for energy conversion and storage. *Science* **347**, 1246501 (2015).
- Koma, A. Van der Waals epitaxy for highly lattice-mismatched systems. *J. Cryst. Growth* **201**, 236–241 (1999).
- Di, C. *et al.* Patterned graphene as source/drain electrodes for bottom-contact organic field-effect transistors. *Adv. Mater.* **20**, 3289–3293 (2008).
- Pang, S., Tsao, H. N., Feng, X. & Müllen, K. Patterned graphene electrodes from solution-processed graphite oxide films for organic field-effect transistors. *Adv. Mater.* **21**, 3488–3491 (2009).
- Lee, W. H. *et al.* Surface-directed molecular assembly of pentacene on monolayer graphene for high-performance organic transistors. *J. Am. Chem. Soc.* **133**, 4447–4454 (2011).
- Lee, C.-H. *et al.* Epitaxial growth of molecular crystals on van der Waals substrates for high-performance organic electronics. *Adv. Mater.* **26**, 2812–2817 (2014).
- Wang, X., Xu, J.-B., Wang, C., Du, J. & Xie, W. High-Performance Graphene Devices on SiO₂/Si Substrate Modified by Highly Ordered Self-Assembled Monolayers. *Adv. Mater.* **23**, 2464–2468 (2011).
- Wang, X., Xu, J.-B., Xie, W. & Du, J. Quantitative analysis of graphene doping by organic molecular charge transfer. *J. Phys. Chem. C* **115**, 7596–7602 (2011).
- Ha, T.-J., Akinwande, D. & Dodabalapur, A. Hybrid graphene/organic semiconductor field-effect transistors. *Appl. Phys. Lett.* **101**, 033309 (2012).
- Cho, J. *et al.* Structural and electronic decoupling of C₆₀ from epitaxial graphene on SiC. *Nano Lett.* **12**, 3018–3024 (2012).
- Lee, G.-H. *et al.* Heterostructures based on inorganic and organic van der Waals systems. *APL Mater.* **2**, 092511 (2014).
- He, D. *et al.* Two-dimensional quasi-freestanding molecular crystals for high-performance organic field-effect transistors. *Nat. Commun.* **5**, 5162 (2014).
- Kim, K. *et al.* Structural and electrical investigation of C₆₀-graphene vertical heterostructures. *ACS Nano* **9**, 5922–5928 (2015).
- Liu, X. *et al.* Epitaxial Ultrathin Organic Crystals on Graphene for High-Efficiency Phototransistors. *Adv. Mater.* **28**, 5200–5205 (2016).
- Wu, B. *et al.* Precise, self-limited epitaxy of ultrathin organic semiconductors and heterojunctions tailored by van der Waals interactions. *Nano Lett.* **16**, 3754–3759 (2016).
- Xu, Y. *et al.* Contacts Between Two- and Three-Dimensional Materials: Ohmic, Schottky and pn Heterojunctions. *ACS Nano* **10**, 4895–4919 (2016).
- Matkovic', A. *et al.* Epitaxy of highly ordered organic semiconductor crystallite networks supported by hexagonal boron nitride. *Sci. Rep.* **6**, 38519 (2016).
- Kratzer, M. & Teichert, C. Thin film growth of aromatic rod-like molecules on graphene. *Nanotechnology* **27**, 292001–292001 (2016).
- Kuruwila, A. *et al.* Organic light emitting diodes with environmentally and thermally stable doped graphene electrodes. *J. Mat. Chem. C* **2**, 6940–6945 (2014).
- Meyer, J. *et al.* Metal oxide induced charge transfer doping and band alignment of graphene electrodes for efficient organic light emitting diodes. *Sci. Rep.* **4**, 5380 (2014).
- Sanders, S. *et al.* Engineering high charge transfer n-doping of graphene electrodes and its application to organic electronics. *Nanoscale* **7**, 13135–13142 (2015).
- Han, K. S. *et al.* A non-destructive n-doping method for graphene with precise control of electronic properties via atomic layer deposition. *Nanoscale* **8**, 5000–5005 (2016).
- Zhang, Y. *et al.* Probing carrier transport and structure-property relationship of highly ordered organic semiconductors at the two-dimensional limit. *Phys. Rev. Lett.* **116**, 016602 (2016).
- Jariwala, D. *et al.* Hybrid, gate-tunable, van der Waals pn heterojunctions from pentacene and MoS₂. *Nano Lett.* **16**, 497–503 (2016).
- Novoselov, K. S. *et al.* Electric field effect in atomically thin carbon films. *Science* **306**, 666–669 (2004).
- Wickenburg, S. *et al.* Tuning charge and correlation effects for a single molecule on a graphene device. *Nat. Commun.* **7**, 13553 (2016).
- Chen, J.-H. *et al.* Tuning charge and correlation effects for a single molecule on a graphene device. *Nat. Phys.* **4**, 377–381 (2008).
- Balandin, A. A. Low-frequency 1/f noise in graphene devices. *Nat. Nanotechnol.* **8**, 549–555 (2013).
- Schedin, F. *et al.* Detection of individual gas molecules adsorbed on graphene. *Nat. Mat.* **6**, 652–655 (2007).
- Levesque, P. L. *et al.* Probing charge transfer at surfaces using graphene transistors. *Nano Lett.* **11**, 132–137 (2010).
- Simbrunner, C. Epitaxial growth of sexi-thiophene and para-hexaphenyl and its implications for the fabrication of self-assembled lasing nano-fibres. *Semicond. Sci. Tech.* **28**, 053001 (2013).
- Hlawacek, G. & Teichert, C. Nucleation and growth of thin films of rod-like conjugated molecules. *J. Phys.-Condens. Mat.* **25**, 143202 (2013).
- Grem, G. *et al.* Stable poly (para-phenylene)s and their application in organic light emitting devices. *Synthetic Met.* **71**, 2193–2194 (1995).
- Schwabegger, G. *et al.* Interface Properties of Organic para-Hexaphenyl/ α -Sexithiophene Heterostructures Deposited on Highly Oriented Pyrolytic Graphite. *Langmuir* **29**, 14444–14450 (2013).
- Yoo, R. K., Ruscic, B. & Berkowitz, J. Vacuum ultraviolet photoionization mass spectrometric study of C₆₀. *J. Chem. Phys.* **96**, 911–918 (1992).
- Tanaka, Y., Kanai, K., Ouchi, Y. & Seki, K. Oxygen effect on the interfacial electronic structure of C₆₀ film studied by ultraviolet photoelectron spectroscopy. *Chem. Phys. Lett.* **441**, 63–67 (2007).
- Lopez-Otero, A. Hot wall epitaxy. *Thin Solid Films* **49**, 3–57 (1978).
- Dan, Y., Lu, Y., Kybert, N. J., Luo, Z. & Johnson, A. T. C. Intrinsic response of graphene vapor sensors. *Nano Lett.* **9**, 1472–1475 (2009).
- Kratzer, M. *et al.* Effects of polymethylmethacrylate-transfer residues on the growth of organic semiconductor molecules on chemical vapor deposited graphene. *Appl. Phys. Lett.* **106**, 103101 (2015).
- Liang, X., Fu, Z. & Chou, S. Y. Graphene transistors fabricated via transfer-printing in device active-areas on large wafer. *Nano Lett.* **7**, 3840–3844 (2007).
- Winkler, A. Initial stages of organic film growth characterized by thermal desorption spectroscopy. *Surf. Sci.* **643**, 124–137 (2016).
- Tapponnier, A., Biaggio, I. & Günter, P. Ultrapure C₆₀ field-effect transistors and the effects of oxygen exposure. *Appl. Phys. Lett.* **86**, 112114 (2005).
- Yu, Y.-J. *et al.* Tuning the graphene work function by electric field effect. *Nano Lett.* **9**, 3430–3434 (2009).
- Zhong, J. Q. *et al.* Molecular-scale investigation of C₆₀/p-sexiphenyl organic heterojunction interface. *J. Chem. Phys.* **134**, 154706 (2011).
- Wang, R. *et al.* Charge Transfer and Current Fluctuations in Single Layer Graphene Transistors Modified by Self-Assembled C₆₀ Adlayers. *Small* **9**, 2420–2426 (2013).
- Gierz, I., Riedl, C., Starke, U., Ast, C. & Kern, K. Atomic hole doping of graphene. *Nano Lett.* **8**, 4603–4607 (2008).
- Srivastava, P. K., Yadav, P., Rani, V. & Ghosh, S. Atomic hole doping of graphene. *ACS Appl. Mater. Interfaces* **9**, 5375–5381 (2017).

49. Ojeda-Aristizabal, C. *et al.* Molecular Arrangement and Charge Transfer in C₆₀/Graphene Heterostructures. *ACS Nano* **11**, 4686–4693 (2017).
50. Braun, S., Salaneck, W. & Fahlman, M. Energy-level alignment at organic/metal and organic/organic interfaces. *Adv. Mater.* **21**, 1450–1472 (2009).
51. Hofmann, O. T., Rinke, P., Scheffler, M. & Heimel, G. Integer versus fractional charge transfer at metal (/insulator)/organic interfaces: Cu (/NaCl)/TCNE. *ACS Nano* **9**, 5391–5404 (2015).
52. Savu, S.-A. *et al.* Fingerprint of fractional charge transfer at the metal/organic interface. *J. Phys. Chem. C* **119**, 12538–12544 (2015).

Acknowledgements

This work has been supported by Austrian Science Fund (FWF Der Wissenschaftsfonds) through project I1788-N20 and by Austrian Academic Exchange Service through the project SRB 09/2016. J.V. and R.G. acknowledge support from Serbian MPNTR through projects ON171005 and 451-03-01039/2015-09/40. The authors are grateful to Prof. E. Zojer (TU Graz, Austria) for fruitful discussions.

Author Contributions

A.M. and J.V. prepared graphene flakes and fabricated FETs. A.M. and B.K. made the *in-situ* electrical measurements setup for the hot wall epitaxy system. A.M. deposited molecular semiconductors, did electrical and AFM measurements, and with M.K. and C.T. did data interpretation. R.G. provided facilities and know-how for the fabrication and characterization of graphene FETs. C.T. evoked and oversaw the study. A.M., M.K. and C.T. wrote the manuscript. All authors discussed the results and reviewed the manuscript.

Additional Information

Supplementary information accompanies this paper at doi:[10.1038/s41598-017-09419-3](https://doi.org/10.1038/s41598-017-09419-3)

Competing Interests: The authors declare that they have no competing interests.

Publisher's note: Springer Nature remains neutral with regard to jurisdictional claims in published maps and institutional affiliations.



Open Access This article is licensed under a Creative Commons Attribution 4.0 International License, which permits use, sharing, adaptation, distribution and reproduction in any medium or format, as long as you give appropriate credit to the original author(s) and the source, provide a link to the Creative Commons license, and indicate if changes were made. The images or other third party material in this article are included in the article's Creative Commons license, unless indicated otherwise in a credit line to the material. If material is not included in the article's Creative Commons license and your intended use is not permitted by statutory regulation or exceeds the permitted use, you will need to obtain permission directly from the copyright holder. To view a copy of this license, visit <http://creativecommons.org/licenses/by/4.0/>.

© The Author(s) 2017



Article

The Effect of Liquid-Phase Exfoliated Graphene Film on Neurodifferentiation of Stem Cells from Apical Papilla

Jelena Simonovic¹, Bosko Toljic¹ , Milos Lazarevic¹ , Maja Milosevic Markovic¹, Mina Peric², Jasna Vujin³, Radmila Panajotovic³ and Jelena Milasin^{1,*}

¹ School of Dental Medicine, University of Belgrade, 11000 Belgrade, Serbia

² Center for Laser Microscopy, Faculty of Biology, University of Belgrade, 11000 Belgrade, Serbia

³ Graphene Laboratory, Center for Solid State Physics and New Materials, Institute of Physics, University of Belgrade, 11000 Belgrade, Serbia

* Correspondence: jelena.milasin@stomf.bg.ac.rs

Abstract: Background: Dental stem cells, which originate from the neural crest, due to their easy accessibility might be good candidates in neuro-regenerative procedures, along with graphene-based nanomaterials shown to promote neurogenesis *in vitro*. We aimed to explore the potential of liquid-phase exfoliated graphene (LPEG) film to stimulate the neuro-differentiation of stem cells from apical papilla (SCAP). Methods: The experimental procedure was structured as follows: (1) fabrication of graphene film; (2) isolation, cultivation and SCAP stemness characterization by flowcytometry, multilineage differentiation (osteo, chondro and adipo) and quantitative PCR (qPCR); (3) SCAP neuro-induction by cultivation on polyethylene terephthalate (PET) coated with graphene film; (4) evaluation of neural differentiation by means of several microscopy techniques (light, confocal, atomic force and scanning electron microscopy), followed by neural marker gene expression analysis using qPCR. Results: SCAP demonstrated exceptional stemness, as judged by mesenchymal markers' expression (CD73, CD90 and CD105), and by multilineage differentiation capacity (osteo, chondro and adipo-differentiation). Neuro-induction of SCAP grown on PET coated with graphene film resulted in neuron-like cellular phenotype observed under different microscopes. This was corroborated by the high gene expression of all examined key neuronal markers (Ngn2, NF-M, Nestin, MAP2, MASH1). Conclusions: The ability of SCAPs to differentiate toward neural lineages was markedly enhanced by graphene film.

Keywords: graphene; dental stem cells; stem cells from apical papilla; neurogenic differentiation



Citation: Simonovic, J.; Toljic, B.; Lazarevic, M.; Markovic, M.M.; Peric, M.; Vujin, J.; Panajotovic, R.; Milasin, J. The Effect of Liquid-Phase Exfoliated Graphene Film on Neurodifferentiation of Stem Cells from Apical Papilla. *Nanomaterials* **2022**, *12*, 3116. <https://doi.org/10.3390/nano12183116>

Academic Editors: Jinfeng Zhang, Minhuan Lan and Huiqing Peng

Received: 3 August 2022

Accepted: 5 September 2022

Published: 8 September 2022

Publisher's Note: MDPI stays neutral with regard to jurisdictional claims in published maps and institutional affiliations.



Copyright: © 2022 by the authors. Licensee MDPI, Basel, Switzerland. This article is an open access article distributed under the terms and conditions of the Creative Commons Attribution (CC BY) license (<https://creativecommons.org/licenses/by/4.0/>).

1. Introduction

Regenerative medicine aims at replacing damaged human cells, tissues or organs and restoring their normal architecture and functions [1]. Stem cells (SCs) emerged as a promising tool in regenerative therapies due to their ability to differentiate into numerous cell lineages, high self-renewal capacity and immunosuppressive activity. A variety of new materials and new devices, enhancing cell migration, proliferation, and differentiation, have been developed as well [2,3].

Since SC research has dramatically evolved over the past years, it is possible now to isolate SCs from almost any tissue [4–7]. Yet, in many instances, the most appropriate and matching source of stem cells for a given regenerative therapy remains to be identified.

Dental SCs share a similar origin as neuronal stem cells, as they originate from the neural crest, and due to their accessibility and absence of ethical issues, they might be a good candidate for neuro-regeneration. Apical papilla is a soft tissue at the apex of a not fully formed tooth, containing more than 95% of mesenchymal SCs (stem cells from apical papilla, SCAP) [8,9]. SCAP express some early neural markers even without neural induction and can be transformed into different cell types belonging to neural lineage [10],

making them suitable for potential therapeutic applications in different clinical settings necessitating neuro-repair. SCAP differentiation potential has been extensively tested, but mainly in experiments of osteogenesis and odontogenesis. Only a few studies have dealt with the use of SCAP in neurodifferentiation. For instance, it was shown that fibrin gels [11] and hypoxia [12] stimulate SCAP neurogenesis.

Graphene, an allotrope of carbon, owing to its physico-chemical and biological properties, is also becoming increasingly popular in bioengineering [13–17]. Graphene and graphene-based nanomaterials (GBN), especially graphene oxide, improve cell adhesion during proliferation and differentiation and, due to their electrical conductivity, have the ability to promote the process of differentiation towards neural cells [18–26]. Furthermore, a colloidal dispersion of graphene demonstrated excellent biocompatibility, nontoxicity and remarkable support for cell proliferation [27–31].

As already stated, in numerous studies focusing on tissue engineering, graphene-based materials have been used in conjunction with different dental stem cells, such as dental pulp stem cells, periodontal ligament stem cells and dental follicle stem cells (reviewed by Guazzo et al. [32]). However, differentiation experiments involving graphene derivatives and stem cells from apical papilla are extremely scarce.

Given the lack of studies on SCAP biological behavior when in contact with graphene film, we sought to explore, by means of different microscopy techniques and real-time gene expression analyses, the potential of liquid-phase exfoliated graphene (LPEG) film to induce and stimulate the neuro-differentiation of SCAP.

2. Materials and Methods

The experimental procedure was structured into four phases: phase 1—fabrication of graphene film; phase 2— isolation, cultivation and characterization of stem cells derived from apical papilla; phase 3—seeding stem cells on graphene film and PET; phase 4—evaluation of neural differentiation (Figure 1).

2.1. Fabrication of Graphene Film

2.1.1. Preparation of Graphene Dispersion

The graphene dispersion utilized in this study was prepared by the liquid-phase exfoliation method (LPE) [33]. Following the procedure described in our previous work [34], the mixture was made by adding the graphite powder (Sigma Aldrich-332461) in N-Methyl-2-pyrrolidone (NMP, Sigma Aldrich-328634). The initial concentration was 18 mg/mL. The solution was exposed to ultrasound (Sonic bath, Branson CPXH, Emerson, St. Louis, MO, USA) for 14 h and immediately after the sonication, the graphene dispersion was centrifuged for 60 min at 3000 rpm. The resulting graphene dispersion collected as the top 80% of the supernatant was characterized by UV-VIS spectroscopy (Beckman Coulter DU 720 UV/VIS Spectrophotometer, Brea, CA, USA) [33]. The concentration of LPE graphene dispersion was calculated by Lambert–Beer law [33] and it was 355 $\mu\text{g mL}^{-1}$ (Figure 2).

2.1.2. Liquid-Phase Exfoliated Graphene Film Fabrication

Langmuir–Blodgett technique was applied to transfer graphene thin films from the liquid–gas interface to the solid support substrate [33]. Adding a small amount of liquid-phase exfoliation (LPE) graphene dispersion into the water–air interface, the graphene nanosheets were self-organized into a close-packed film [33]. The thin and transparent film was intently scooped onto the polyethylene terephthalate (PET) substrate. After deposition, the LPE graphene film was left to dry for 20 min in ambient conditions. For the optical characterization of the liquid-phase exfoliated graphene (LPEG) films, UV-VIS spectroscopy (Beckman Coulter DU 720 UV/VIS Spectrophotometer, Brea, CA, USA) was used. The transparence of 80% was estimated for the obtained LPEG film. The transparence of the obtained LPEG film at 550 nm was estimated at 80%, which is consistent with the previously reported study [35].

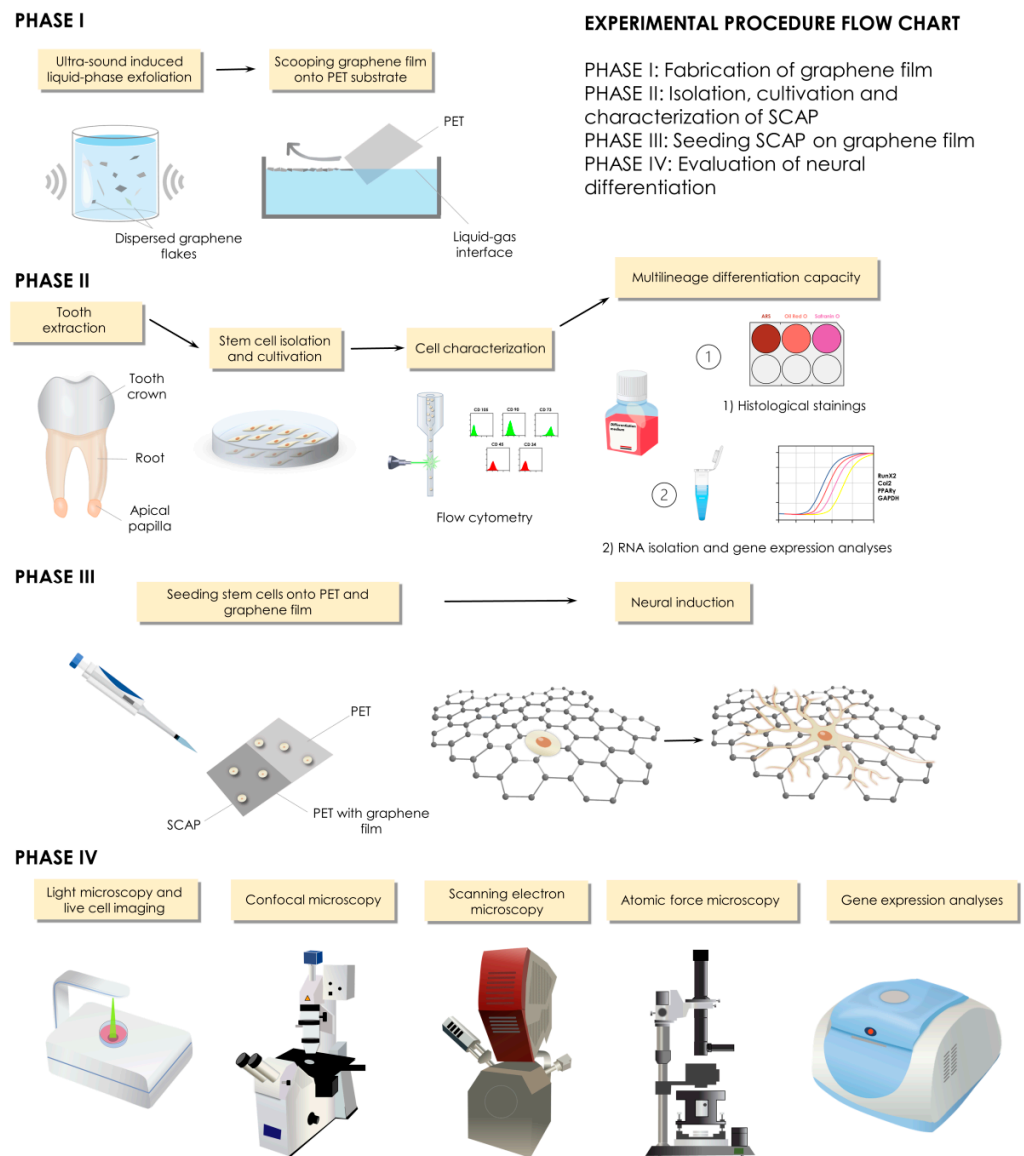


Figure 1. Study design and experimental procedures.

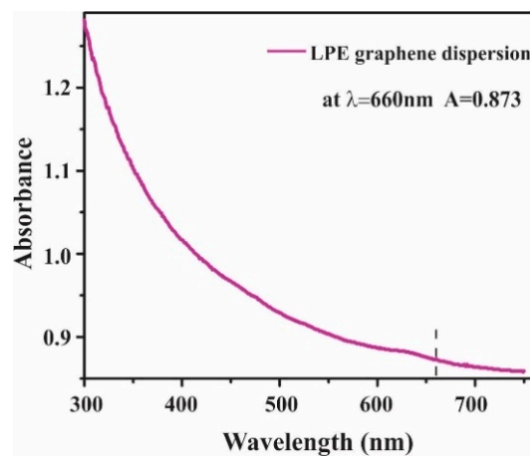


Figure 2. UV-VIS absorption spectrum of LPE graphene dispersion.

2.2. Graphene Film Characterization

2.2.1. Raman Spectroscopy of Graphene Film

Raman spectroscopy, as a noninvasive technique, has been used to provide essential information in the characterization of graphene-based materials [18,19]. Raman spectra were collected with the Micro-Raman Tri Vista 557 triple spectrometer using Nd:YAG laser ($\lambda = 532$ nm) and kept the power below 20 mW to avoid chemical damage of the film induced by the laser heating. The measurements were performed at room temperature and the acquisition time for spectra was 240 s.

2.2.2. Scanning Electron Microscopy (SEM) of Graphene Film

The morphology of the LBA graphene films was characterized with scanning electron microscopy (SEM). SEM images were obtained by Tescan MIRA3 field emission gun SEM working at 20 kV acceleration (Tescan), and SiO₂/Si wafer was used as a substrate.

2.2.3. Atomic Force Microscopy (AFM) of Graphene Film

Graphene film was characterized on an atomic force microscope (AFM), NTEGRA Spectra (NT-MDT). An NT MDT gold-plated tip with a nominal radius of about 30 nm was used. Scans were performed in ambient conditions, RH: 40–50%, t: 23–26 °C in semi-contact mode, with a scan frequency of 0.5 Hz and with 512 × 512 dots in the scan (10 × 10 μm surface). AFM image analysis has been performed using Gwyddion open source software package ver. 2.60 (Prague, Czech Republic). Thickness has been estimated at the edge of the film using profile function and statistical function in the software.

2.3. Cell Cultures

The study was approved by the Ethical Committee of the School of Dental Medicine, University of Belgrade (No 36/19). Immature, impacted third lower molar was extracted from a teenage patient at the Clinic for Oral Surgery (Figure 3), School of Dental Medicine, University of Belgrade, after signing the informed consents by patient's parents. Stem cells from apical papilla were isolated as previously described [34]. Briefly, extracted tooth was rinsed with Dulbecco's Phosphate-Buffered Saline (DPBS, Thermo Fisher Scientific, Waltham, MA, USA), and apical papilla was separated from the root apex and transferred into T-25 flasks after mincing. The tissues were grown in cell complete medium (DMEM supplemented with 10% fetal bovine serum and 1% antibiotic-antimycotic solution). Cells were cultured under standard conditions (37 °C, 95% air–5% CO₂ atmosphere, 95% humidity) and growth medium was changed every third day. All following experiments were carried out with the cells from the fourth and fifth passage.

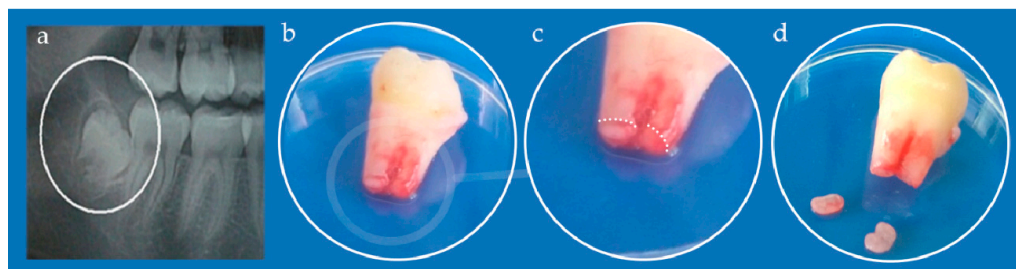


Figure 3. (a) Orthopantomogram of right mandibular impacted third molar (encircled); (b) Extracted tooth; (c) Detail from (b) white dotted line depicts border between apical papilla (lower parts) and tooth root (upper part); (d) Kidney-shaped apical papilla tissues separated from the tooth.

2.4. SCAP Characterization

2.4.1. Flow Cytometry

Flow cytometry analyses were performed in order to assess the expression of specific mesenchymal markers of SCAP. The markers used for these analyses were: fluorescein-

isothiocyanate-labeled mouse monoclonal antibodies against CD90, CD105, and CD34; phycoerythrin-labeled mouse monoclonal antibodies against CD73 and CD45 (all antibodies were purchased from Exbio, Vestec, Czech Republic). Cells were harvested with TrypLE™ Express solution, washed with DPBS supplemented with 10% FBS, and finally counted on automated cell counter Countess™ (Invitrogen, Waltham, MA, USA). One million of the cells were resuspended in 1 mL of 10% FBS solution in DPBS and incubated with adequate antibodies for 45 min in the refrigerator. After incubation, cells were fixed with 4% paraformaldehyde (PFA) for 20 min and finally rinsed 2 times with DPBS. Cells were analyzed on a tabletop flow cytometer (Partec, Munster, Germany) and results were processed by software (FloMax 2.82, Partec, Munster, Germany).

2.4.2. Multilineage Differentiation Capacity

To evaluate the stemness characteristics of SCAP, their potential of differentiation into multiple lineages (osteo-, chondro- and adipo-) was tested. Cells were seeded onto 6-well plates either on PET alone or on PET coated with LPEG film, at density of $5 \times 10^3/\text{cm}^2$, and grown in the respective differentiation medium, which was changed every 2 days. After the required differentiation period of time elapsed, cells from one well were used for RNA isolation for gene expression analysis.

Osteo-Differentiation

After 28 days of culturing in osteo-differentiation medium (StemPro™ Osteogenesis Differentiation Kit, Thermo Fisher Scientific, Waltham, MA, USA) according to manufacturers' recommendations, cells were subjected to histological staining method using Alizarin Red S, as previously described [34]. Briefly, after rinsing with DPBS and fixating with 4% PFA for 30 min, cells were stained with 2% Alizarin Red S (Centrom, Belgrade, Serbia) solution, at pH 4.2. After 30 min of incubation, dye was removed, and cells were rinsed twice with distilled water. Stained cultures were observed using inverted light microscopy (Primovert, Zeiss, Oberkochen, Germany) and photographed.

Chondro-Differentiation

For the chondro-induction, cells were seeded in a form of micromass at total number of 1.5×10^6 and grown on 6-well plates in commercially available chondrogenesis media (StemPro™ Chondrogenesis Differentiation Kit, Thermo Fisher Scientific, Waltham, MA, USA) for 21 days. Chondrogenesis was confirmed by 0.1% solution Safranin O (Centrom, Belgrade, Serbia) positive staining. Stained cells were observed using inverted light microscopy and photographed.

Adipo-Differentiation

Adipogenic stimulation lasted 28 days in commercially available adipogenesis media (StemPro™ Adipogenesis Differentiation Kit, Thermo Fisher Scientific, Waltham, MA, USA) at seeding density of 1×10^4 cells/cm² onto 6-well plates. In order to confirm adipodifferentiation, Oil Red O (Centrom, Belgrade, Serbia) staining was used to visualize intracellular lipid accumulation as lipid vacuoles. Stained cells were observed using inverted light microscopy and photographed.

2.5. LPEG Neuro-Induction

To induce neurogenic differentiation, cells (1.5×10^5) were seeded onto T-25 tissue culture flasks in standard culture medium. After 24 h, neural pre-induction medium and DMEM with 100 mM beta-mercaptoethanol were added, and cells were incubated for 4 h. Then, cell differentiation was continued in a neural induction medium containing recombinant human basic fibroblast growth factor, neural growth factor, and B27 supplement (all from Thermo Fisher Scientific, Waltham, MA, USA) in DMEM either on PET alone or on PET coated with LPEG film. After 7 days of cultivation, cell morphology was observed under inverted microscope. Control cells were incubated in standard culture medium.

2.6. Cell Morphology Analysis Following LPEG Neuro-Induction

2.6.1. Light Microscopy

Cell morphology was observed under inverted microscope (Primover, Zeiss, Oberkochen, Germany) and photographed. Between days 3 and 7 of neurogenic culture, the cells showed a transition from fibroblast-like to neuron-like cell bodies with long processes, suggesting that the stem cells differentiated into neurons/neuron-like cells. At that point they were subjected to RNA isolation, gene expression and immunocytochemistry analysis. In addition, the growth and morphology of the cells during 5 days of LPEG neuro-induction was recorded with CytoSMART Lux 2 camera (CytoSmart Technologies BV, Eindhoven, The Netherlands).

2.6.2. Confocal Microscopy

For the immunocytochemical analyses, cells were seeded onto 25 mm diameter round glass coverslips at density of $5 \times 10^3/\text{cm}^2$ and subjected to neuro-differentiation protocol as described. On the 7th day of neural induction, cells were rinsed 3 times in DPBS, fixed with 4% PFA solution for 20 min, rinsed three times with DPBS and incubated at room temperature for 45 min in blocking and permeabilization buffer (10% Bovine serum albumin and 0.1% Triton X-100 in DPBS). For immunofluorescent detection of neuronal cell marker expression, cells were incubated with the following primary antibodies: rabbit anti- β III-tubulin (B3T, 1:400, Cell Signaling, Danvers, MA, USA), rabbit anti-MAP2 (MAP 1:400, Millipore, Germany) and rabbit anti-neuronal nuclei (NeuN, 1:250, Millipore, Taufkirchen, Germany). Primary antibodies were incubated at 4 °C overnight and subsequently washed 3 times with DPBS. Cell samples were incubated with secondary antibodies—donkey anti-mouse Alexa Fluor 488 (1:200, Invitrogen, Waltham, MA, USA), donkey anti-rabbit Alexa Fluor 555 (1:200, Invitrogen, Waltham, MA, USA) and donkey anti-rabbit Alexa Fluor 657 (1:200, Invitrogen, Waltham, MA, USA) for 2 h in dark at room temperature. Cells were washed 3 times in DPBS and stained with 4-, 6- diamidino- 2-phenylindole (1:4000, DAPI, Molecular Probes, Eugene, OR, USA) for 10 min in dark at room temperature. After washing in DPBS cell samples were mounted with Mowiol(Sigma Aldrich, St. Louis, MO, USA) on microscope slides. Immunofluorescence microscopy images were obtained by confocal laser-scanning microscope (LSM 510, Carl Zeiss GmbH, Jena, Germany) equipped with Ar 488 and HeNe 543 and 633 laser lines. Micrographs were analyzed using Fiji-Image J softwarever 1.46 (NIH, Bethesda, MD, USA).

2.6.3. AFM of Neuron-like Cells

For the purposes of atomic force microscopy, cells had to be seeded on SiO₂ slides coated with a 2 × 2 cm graphene monolayer at a concentration of 200 cells in 10 μL of complete growth medium. The slides were placed in the wells of the 6-well plate. One hour after seeding, 740 μL of complete medium was added to the cells. After 24 h from seeding, neuro-differentiation was performed by the protocol described above.

Seven days after neuro-induction, the medium was aspirated from the well, and the plates were washed twice with DPBS, then the cells were fixed with 4% PFA solution for 20 min. Any excess fixation solution was removed by rinsing twice more with DPBS.

The morphology of the obtained cells after LPEG neuro-differentiation was characterized by microscopy on an atomic force microscope, using the same device and experimental conditions as for the graphene film characterization.

2.6.4. SEM of Neuron-like Cells

After neuro-induction, cell morphology was observed by SEM using a high-resolution electron microscope, MIRA3 FEG-SEM (Tescan, Brno—Kohoutovice, Czech Republic), at a voltage acceleration of 20 kV. Cell fixation using the increasing concentrations of ethanol was done as previously described [36]. In preparation, the sample surface was coated with an ultrathin layer of gold using an SC7620 mini atomizer (Quorum Technologies, Laughton, East Sussex, UK) to prevent the accumulation of static field electricity.

2.7. RNA Isolation and Gene Expression

The expression of different markers was assessed by real-time PCR (qPCR) analysis. RNA was isolated using TRIzol Reagent (Thermo Fisher Scientific, Waltham, MA, USA), according to manufacturers' recommendation. Subsequent reverse transcription from 1 µg of total RNA was performed using RevertAid First Strand cDNA Synthesis Kit (Thermo Fisher Scientific, Waltham, MA, USA) in order to obtain cDNA for qPCR analysis. The list of specific primers is given in Table 1. The results obtained from each qPCR run were threshold cycle (Ct) values. The relative expression level was assessed using the $\Delta\Delta C_t$ method [37]. The relative mRNA expression levels for each sample were calculated as the ratio between the expression of the gene of interest and the expression of the housekeeping gene (GAPDH).

Table 1. Primers with corresponding sequences used in the study.

Primer Name		Sequences (5'→3')
Runx2	Forward	ACAAACAACCACAGAACCACAAGT
	Reverse	GTCTCGGTGGCTGGTAGTGA
Col2	Forward	TTCAGCTATGGAGATGACAATC
	Reverse	AGAGTCCTAGAGTGACTGAG
PPARG	Forward	GCTGTGCAGGAGATCACAGA
	Reverse	GGCTCCATAAAGTCACCAA
Ngn2	Forward	CCTGGAAACCATCTCACTTCA
	Reverse	TACCCAAAGCCAAGAAATGC
NF-M	Forward	TGGGAAATGGCTCGTCATTT
	Reverse	CTTCATGGAAACGGCCAA
Nestin	Forward	AACAGCGACGGAGGTCTCTA
	Reverse	TTCTCTTGTCGCCGAGACTT
MAP2	Forward	AACCCTTTGAGAACACGACA
	Reverse	TCTTTCCGTTTCATCTGCCA
MASH1	Forward	CCAGTTGTACTTCAGCACC
	Reverse	TGCCACTTTGAGTTTGGAC
GAPDH	Forward	TCATGACCACAGTCCATGCCATCA
	Reverse	CCCTGTTGCTGTAGCCAAATTCGT

2.8. Statistical Analysis

GraphPad Prism ver. 9 was used for the analyses (GraphPad Software, Inc., San Diego, CA, USA). After examination of the distribution normality by Kolmogorov–Smirnov normality test, independent sample T tests were performed. The values are presented as mean \pm SD. Statistical significance was set at $p < 0.05$. The experiments were performed in triplicate, repeated at least two times.

3. Results

3.1. Graphene Film Characterization

3.1.1. Raman Spectroscopy of Graphene Film

Raman spectroscopy has been applied to verify the exfoliation of the pristine graphite powder, as bulk material, into few-layer graphene nanosheets. Figure 4 represents the Raman spectra of LPEG thin films and pristine graphite powder as a reference.

D (~1352) and G (~1582) peaks are noted in the same position at both Raman spectra. The changes of shape and Raman shift of 2D peak at Raman spectra of graphene film are evident. A well-defined and sharp shape of the 2D peak, as well as a considerable shift to lower wavenumbers (by 12 cm^{-1}) compared to graphite, are characteristics of a few-layer graphene nanoflakes [24]. D' peak (~1618 cm^{-1}), visible as the shoulder of G peak in the graphene film, together with D peak, confirms the presence of defects and some amount of

disorder in the graphene lattice. The combinations of the main peaks can be also observed: $D + D'$ ($\sim 2939 \text{ cm}^{-1}$) and $D + D''$ ($\sim 2452 \text{ cm}^{-1}$), where the D'' peak is known as a weak defect induced one phonon process.

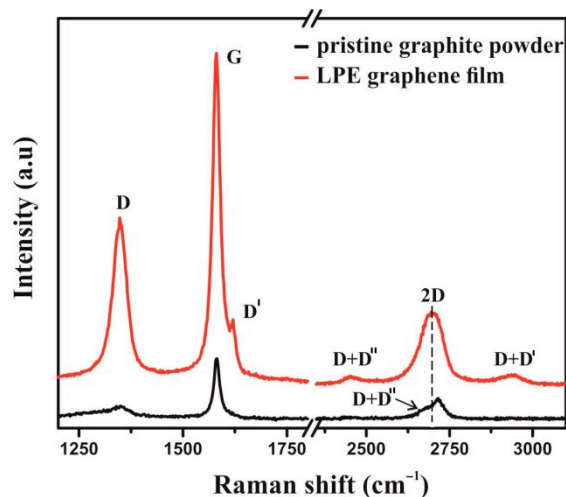


Figure 4. Raman spectrum of LPE graphene film (red line) and pristine graphite powder (black line).

3.1.2. SEM Characterization of Graphene Film

Information about the morphology and film structure was obtained by SEM (Figure 5). The overlapping of the graphene nanosheets and the formation of a closed packed film can be noticed in Figure 5a. Based on the measurement of lateral size, the average diameter of graphene nanosheets was estimated to be in the range of $125 \pm 10 \text{ nm}$ (Figure 5b).

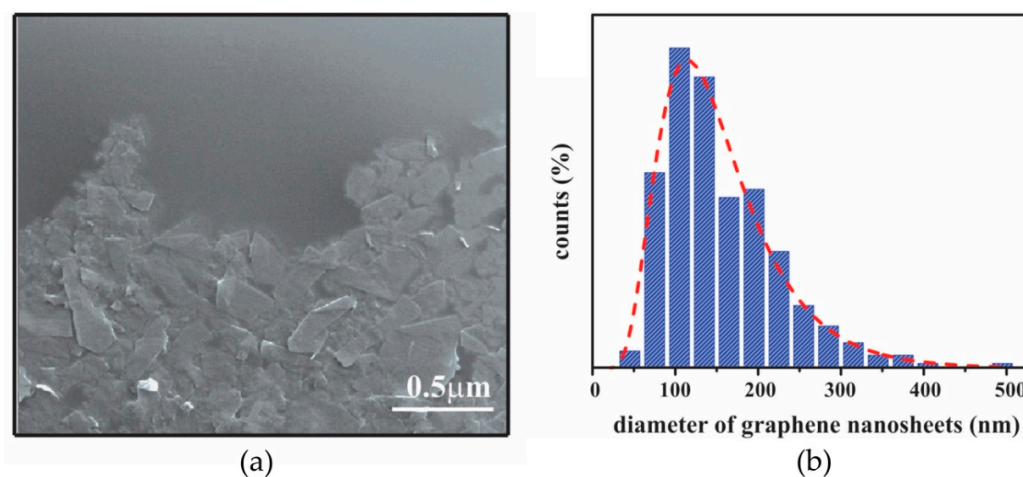


Figure 5. (a) SEM image of graphene film; (b) Histograms of lateral size of graphene nanosheets obtained from six $3 \times 3 \mu\text{m}^2$ SEM images (~ 1800 flakes); The red dashed line represents a log-normal fit.

3.1.3. AFM Characterization of Graphene Film

AFM scans of graphene film along with their characteristics are given in Figure 6. Both 2D (a) and 3D (b) images are shown for a scan area of $20 \times 20 \mu\text{m}$ (512×512 lines), as well as for a scan area of $5 \times 5 \mu\text{m}$ —2D image (c), 3D image (d) and phase image (e). Height distribution for the area of $20 \times 20 \mu\text{m}$ and average height profile across the film are given in Figure 6f,g, respectively.

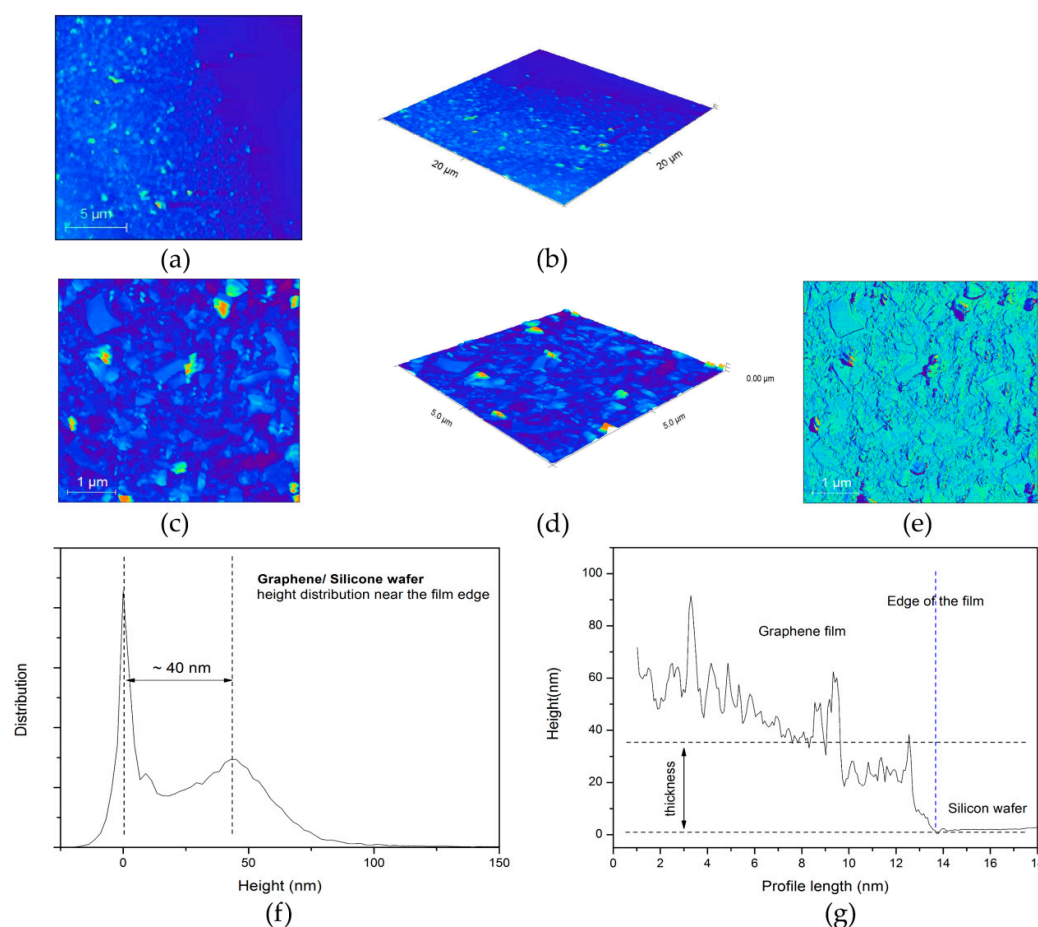


Figure 6. Graphene film near the edge. (a) 2D and (b) 3D image of the scan area $20 \times 20 \mu\text{m}$; (c) 2D, (d) 3D and (e) phase image of the scan area $5 \times 5 \mu\text{m}$; Thickness of graphene film. (f) Height distribution near the edge of the film measured for the area $20 \times 20 \mu\text{m}$ and (g) average height profile across the edge of the film.

3.2. SCAP Characterization

3.2.1. Flow Cytometry Analysis

Flowcytometry analyses were performed on P5 (fifth passage) stem cell from apical papilla. Flowcytometry revealed the expression of mesenchymal stem cell markers CD73, CD90 and CD105 (99%, 91.3% and 96%, respectively), and the absence of hematopoietic markers CD34 (0.34%) and CD45 (0.01%).

3.2.2. Multilineage Differentiation Capacity

Alizarin Red S staining of mineralized nodules around cells confirmed osteogenic differentiation (Figure 7a); the presence of Safranin O clusters of proteoglycans characteristic for cartilage cells confirmed chondro-differentiation (Figure 7b); the presence of Oil Red O staining was indicative of intracellular lipid accumulation (Figure 7c). In the control group (non-induced cells) there were no stained cells (Figure 7d).

3.2.3. Gene Expression Analysis of Multilineage Differentiation

Real-time PCR analysis of gene expression confirmed successful SCAP differentiation, both when cells were grown on graphene film and when they were grown on PET only (control), thus confirming SCAP stemness. Differentiated cells grown on graphene film showed several times higher expression of Runx2—marker of bone tissue (9.59-fold increase), Col2—marker of cartilage tissue (62.90-fold increase) and PPARG—marker of

adipose tissue (17.48-fold increase) compared to the control group (Figure 8), pointing to the positive effect of graphene in terms of its multilineage induction capacity.

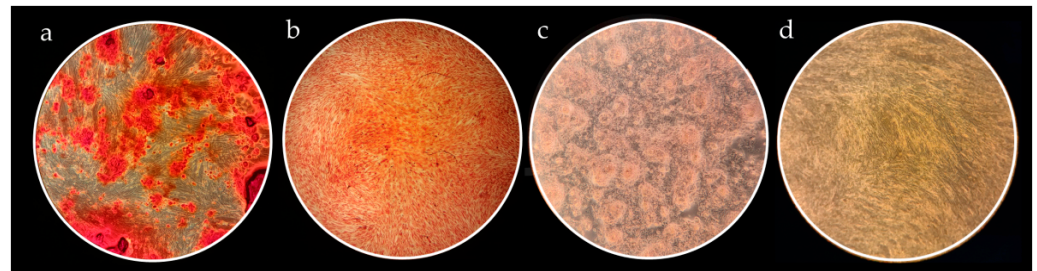


Figure 7. Histological evaluation of SCAP multilineage differentiation capacity. All micrographs were taken at 40× magnification. (a) Alizarin Red S staining of calcium deposits showing osteogenic potential of SCAP; (b) Safranin O staining of proteoglycan aggregates evidencing successful SCAP chondrogenic potential; (c) Oil Red O positive staining of intracellular lipid droplets as a sign of SCAP adipogenic differentiation; (d) Representative image of unstained controls.

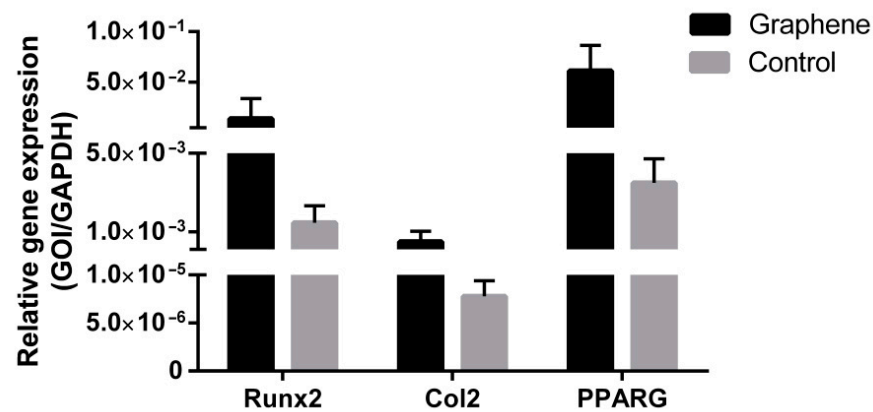


Figure 8. Gene expression evaluation of SCAP osteogenic (Runx2), chondrogenic (Col2) and adipogenic (PPARG) differentiation potential.

3.3. LPEG Neuro-Induction of SCAP

3.3.1. Light Microscopy

After 3–5 days of neuro-induction, cells grown on LPEG film reshaped into polygonal structures with long, slender cytoplasmic processes that were mainly in contact with adjacent cells. Representative light microscopy images of those neuron-like cells are given in Figure 9a–c. While SCAPs on LPEG film gradually changed their morphology into multipolar cells, similar to neurons, cells grown on PET showed minor changes in cell shape (Figure 9d). The growth and morphology of cells during LPEG film neuro-induction were recorded with a CytoSMART Lux 2 camera (CytoSmart Technologies BV, Eindhoven, the Netherlands). A graphical representation of the time-dependent extension of cytoplasmic processes (in μm) is shown in Figure 9e, along with 6 h time frames that were extracted from the video (Figure 9f). The real-time recording of cell morphology changes can be also viewed (Video S1).

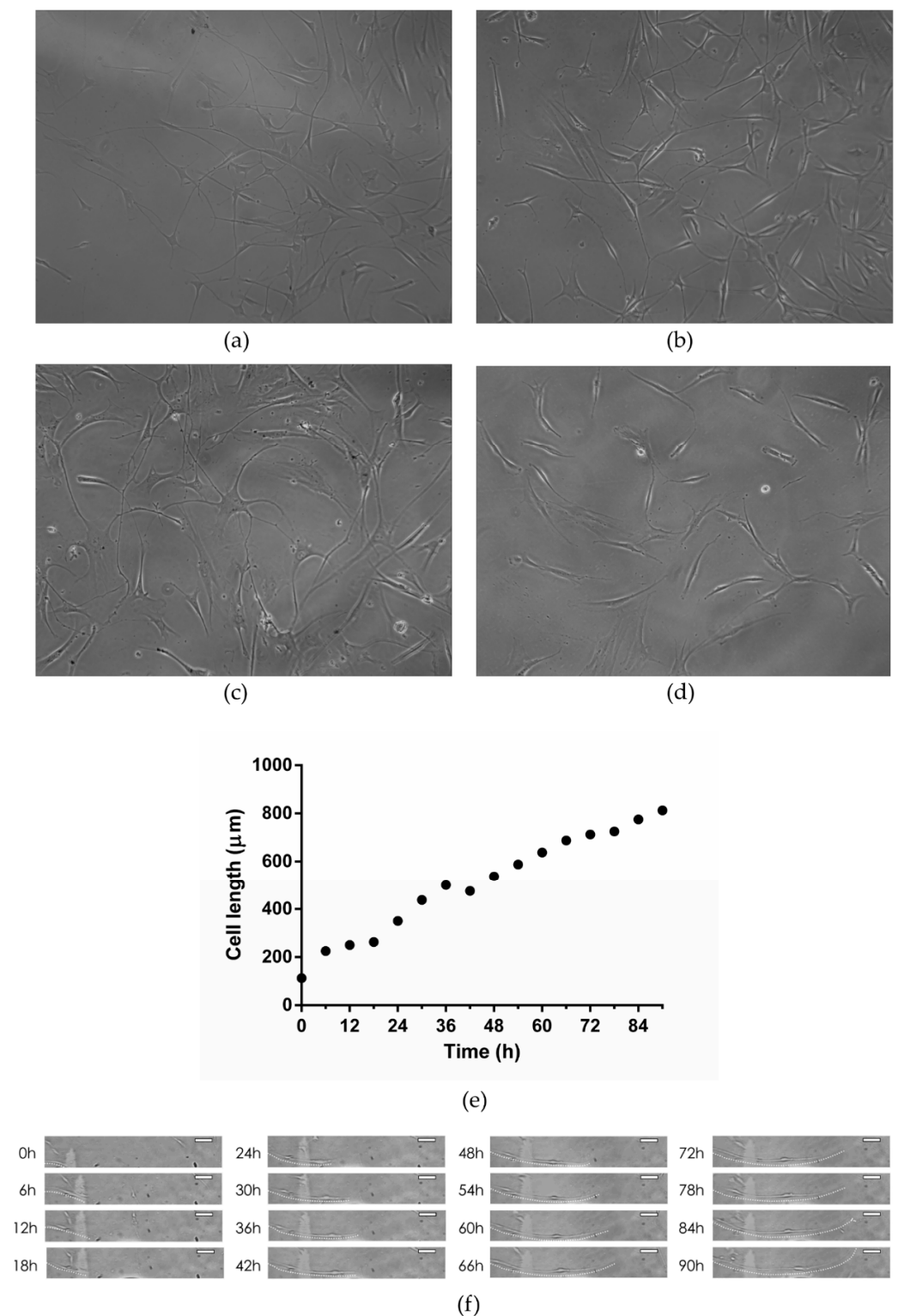


Figure 9. (a–c) Representative light micrographs of SCAP grown on graphene film; (d) Representative light micrograph of SCAP grown on PET; (e) Time-dependent changes in major axis length of SCAP grown on graphene film; (f) Time-lapse light micrographs of SCAP grown on graphene film (dotted white line represents cell extension pathway; white scale bar represents $100\ \mu\text{m}$).

3.3.2. Confocal Microscopy

Confocal microscopy showed the increased expression of three major neural cell markers (NeuN, MAP2 and β -3 tubulin) in SCAPs grown on graphene, compared to cells grown on PET alone (control) (Figure 10).

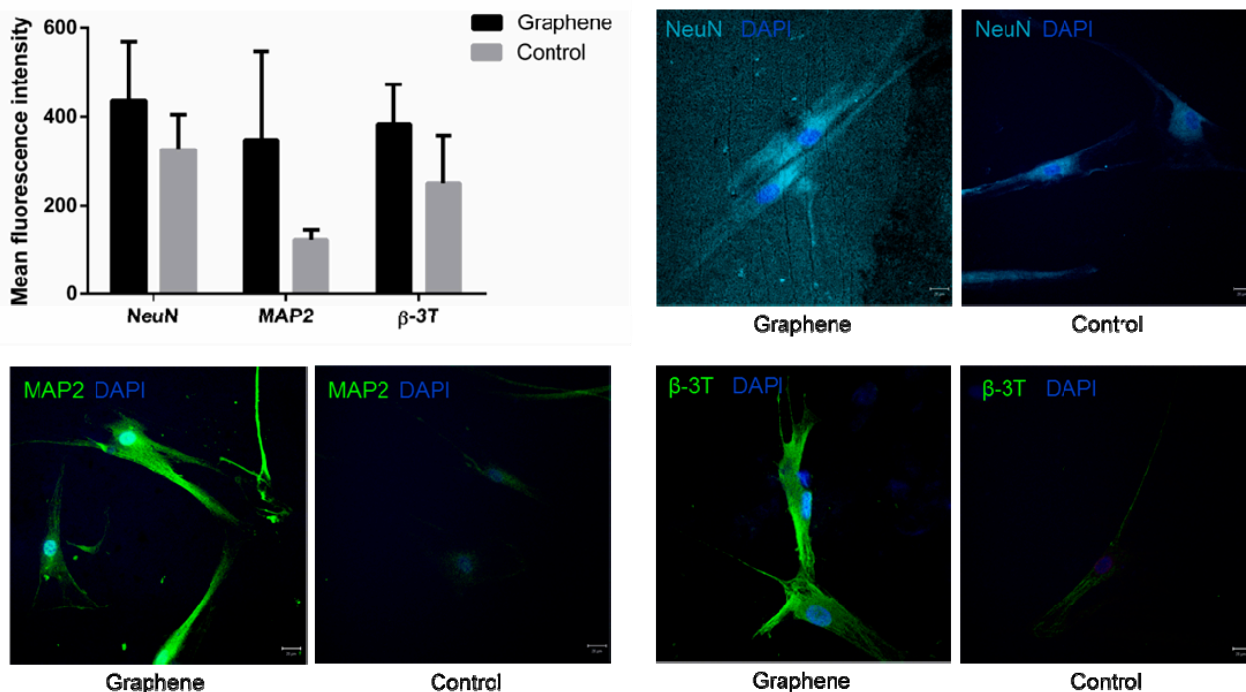


Figure 10. Mean fluorescence intensities and laser confocal micrographs of SCAP immunolabeled for neuronal markers NeuN, MAP2 and β -3-tubulin (nuclei are labeled with DAPI).

3.3.3. AFM of Neuron-like Cells

Atomic force microscopy (AFM) revealed subtle surface topography and morphological differences between stem cells grown on graphene film compared to those placed over PET. SCAP grown on graphene were polygonal in shape (Figure 11a,b) with multiple long-distance, slender cytoplasmic projections emerging from cell body (Figure 11c,d) compared to the less complex cell morphology of SCAP grown on PET (Figure 11e,f). Note that AFM height panel also revealed numerous globular protrusions on the surface of the cell bodies, which were more present on SCAP grown on graphene.

3.3.4. SEM of Neuron-like Cells

Scanning electron microscopy (SEM) of SCAP grown on graphene film depicted a triangular cell body with long, slender projections (Figure 12a). The endings of these projections were in close proximity or direct contact with cytoplasmic projections of surrounding cells forming a connected cell population (Figure 12b).

3.3.5. Gene Expression Analysis after LPEG Neuro-Induction

Gene expression analysis of key neural differentiation markers of SCAP grown on LPEG film and control material is presented in Figure 13. All examined markers showed higher expression in cells grown on graphene film compared to those on non-coated PET (control).

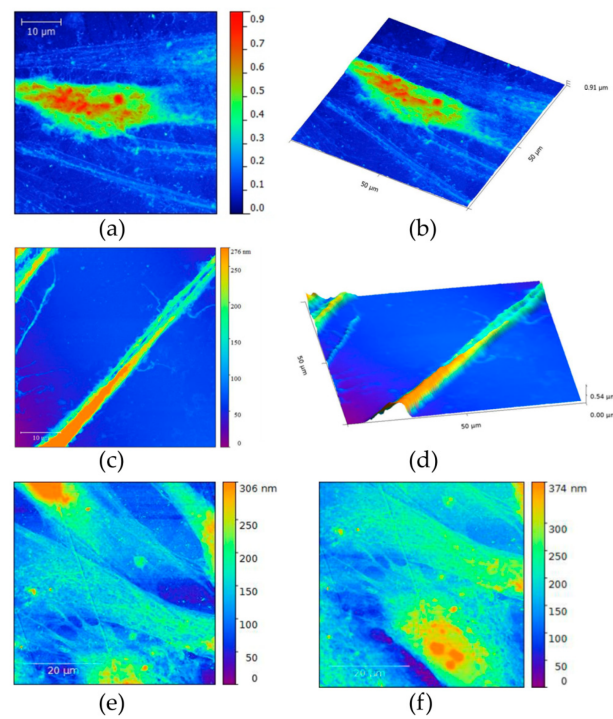


Figure 11. (a,b) Atomic force micrographs of SCAP grown on graphene film; (c,d) Long, slender projections of SCAP cell membrane covering graphene film; (e,f) AFMs of control SCAP grown on PET (control).

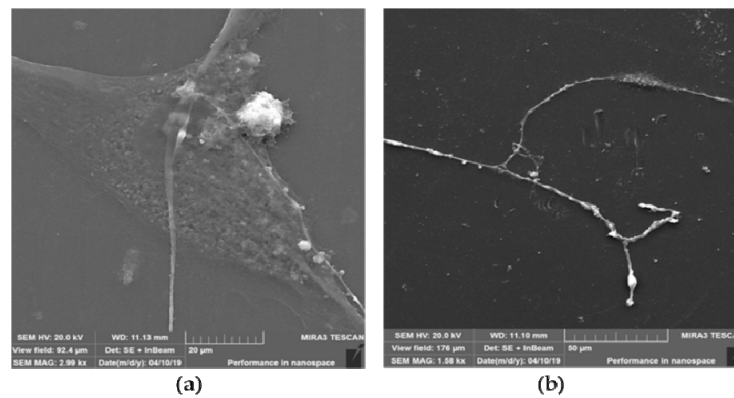


Figure 12. SEM of SCAP grown on graphene film. (a) Triangular cell body with arising long-distance membrane projections; (b) Slender cell projections synapsing with adjacent cell.

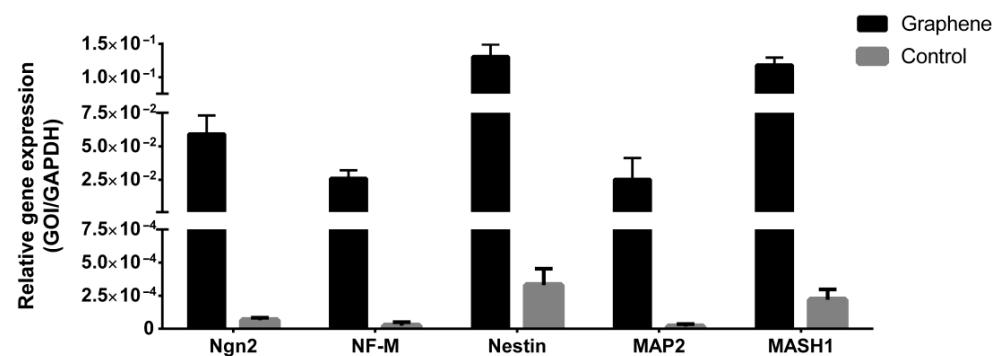


Figure 13. Gene expression analyses of neuronal markers of SCAP grown on graphene film and PET (control).

4. Discussion

Many dental tissues are precious niches of mesenchymal stem cells that are becoming increasingly appealing in regenerative medicine due to their easy accessibility and lack of health risks for the donor. They are especially attractive for the field of neuro-regeneration given that they originate from the neural crest and possess the capacity of differentiation into diverse neural cell types. Apical papilla, the soft tissue at the apex of a not fully formed tooth, contains a very high percentage of MSCs characterized by great plasticity, proliferation rate and differentiation ability. Previous studies, based on immunophenotyping, gene expression analyses, and patch clamping, have reported that SCAP grown under neural inductive conditions could give rise to a variety of neural cell phenotypes, from neuroprogenitors to mature neurons [10,34].

The number of novel materials used as cell carriers/scaffolds, tested for tissue engineering application, is constantly increasing, especially in the field of neuro-repair and regeneration. Great emphasis has been put on carbon nanostructured scaffolds that may display suitable characteristics for neural differentiation [13,34,38,39]. Graphene nanomaterials are carbon crystal allotropes with a two-dimensional structure and, according to data from the literature, have proven to be an excellent nanomaterial for neurodifferentiation due to their unique organization, chemical stability, exceptional mechanical properties, bactericidal potential, and biocompatibility [40,41]. This monoatomic layer of carbon shows the ability to absorb growth factors and exhibits electrical conductivity, which is of particular interest for the field of neuroscience. For instance, Lee et al. have convincingly demonstrated, on a neuroblastoma cell line, that graphene substrate enhanced neurite outgrowth, both in terms of length and number [42]. Rodrigues-Losada et al. also showed that different graphene materials (graphene oxide and reduced derivatives) promoted the differentiation, proliferation and maturation of dopaminergic neurons [43]. Importantly, graphene-based materials also exert stimulating effect on cell differentiation towards neurons rather than glial cells [44]. In neural regeneration, the induction of stem cell differentiation in favor of neurons against glial cells is highly desirable, making graphene-based nanomaterials a promising agent in neuroregenerative therapies. In addition to graphene oxide, the most studied graphene nanomaterial, there are other forms of graphene that are non-toxic and biocompatible, such as fully reduced or partially reduced graphene oxide, in the form of powder or film, but their positive effects in terms of neurodifferentiation have not yet been sufficiently investigated. This is the case with liquid-phase exfoliated graphene (LPEG) film that was the subject of this research. In the present study, Raman spectroscopy has been applied to verify the exfoliation of the pristine graphite powder, as bulk material, into graphene nanosheets. Indeed, the obtained closed packed film was made of few-layer graphene nanoflakes, as seen on SEM. The changes of shape and Raman shift of the 2D peak at Raman spectra of graphene film are evident. A well-defined and sharp shape of the 2D peak as well as a considerable shift to lower wave number compared to graphite are characteristics of few-layer graphene nanoflakes [45]. Edge defects, as the dominant type of defect in graphene film, are the result of the cavitation process at the liquid phase exfoliated technique [46]. Generally, the Raman spectra as well as the average diameter of the nanosheets and their height were in agreement with some previous reports [47].

In the present study, the mandatory characterization of SCAP cultures has shown a highly predominant presence of cells displaying mesenchymal stem cell markers (between 91 and 99% of cells in the culture expressed a given mesenchymal marker). Concomitantly, a negligible percentage of cells expressed hematopoietic stem cell markers (only 0.01% and 0.34% of cells expressed CD45 and CD34, respectively), as determined by flowcytometry, pointing to the fact that cell cultures contained principally MSCs. Similarly, stemness characterization by means of multiple lineages induction showed a successful osteo-, chondro- and adipo-differentiation of SCAPs. The specific osteo-, chondro- and adipo cellular phenotypes, assessed by appropriate staining procedures, were also confirmed by high mRNA levels of selected markers (Runx2, Col2 and PPARG, for osteo-, chondro- and adipo-differentiation, respectively). These findings are in general agreement with some

previous reports [48–50]. Interestingly, the three examined processes of differentiation also appeared to be enhanced in the presence of graphene (especially chondrogenesis) but more markers specific for osteo-, chondro- and adipo- lineages should be evaluated in order to confirm that positive effect of graphene film. This is in line with some previous studies. Namely, it was found that graphene derivatives exhibit great stimulatory effects on adipogenesis and osteogenesis [19,51–53], pointing to the possibility of their use in composite tissue cultures when more than one cell type is needed. This is of utmost importance in regenerative medicine and dentistry when huge defects require complex reconstructions. The classical example is the surgical removal of a portion of maxilla or mandible in cases of oral cancer, resulting in massive bone, muscle and nerve defects, which necessitate multiple tissues' replacement.

Regarding neurogenesis, the present study showed for the first time that LPEG films can have strong stimulatory effects on SCAPs' induction towards neural lineage. Namely, cells cultured in neurodifferentiation medium on graphene film demonstrated increased levels of all neural markers (studied either by confocal microscopy or by quantitative PCR), compared to cells grown in neurodifferentiation medium only. The levels of *ngn-2*, an inhibitor of glial cell transcription factor, were very high, indicative of LPEG capacity to suppress gliogenesis, thus favoring neurogenesis [54]. Gene expression of Nestin, a marker of neuroepithelial and radial cells, was, as well, increased in cells grown on graphene film compared to those seeded over the non-coated substrate. This protein has a crucial role in assembling and disassembling intermediate filaments and thus maintains the structure and regulates the growth of developing neural cells [55]. Similarly, a higher expression of Mash-1, a marker of intermediate progenitors, was also noted. Mash-1, as one of the early markers that determine cellular fate, is involved in the differentiation of neuroblasts, as well as in cell protection mechanisms that prevent cell damage and apoptosis. β III-tubulin, a neuronal microtubule protein that is particularly expressed during neurogenesis and is thought to be responsible for axon growth, was upregulated in the presence of graphene. The level of MAP2, a cytoskeletal element essential for the binding and stabilization of neuronal microtubules with major impact on neuronal development, was also higher in cells grown on graphene film [56]. Another neural marker of mature neurons that has never been found in glial cells—NeuN—was more expressed in SCAP stimulated by LPEG compared to the control condition. This marker was detected, both in the cell nucleus and perinuclear cytoplasm. Unlike the nuclear form, which binds to DNA and most probably has an important role in the regulation of neurogenesis, the role of the cytoplasmatic variant is still unclear. It is assumed that, together with Synapsin I, cytoplasmatic NeuN regulates the mobility of synaptic vesicles and release of neurotransmitters, thus playing a potential role in synaptogenesis and establishing neural circuits [57]. The last examined, final stage marker of neural development, along with MAP2 and NeuN, was Neurofilament Medium (NF-M) and, again, its expression was higher in cells grown on graphene. In agreement with our findings, which showed positive effects of graphene film on neurogenesis, a previous study that examined several types of graphene material established that the morphology of the film and the species of graphene influenced the behavior of neurons, but generally film species exhibited higher biocompatibility than powder materials [43]. Our results support the central concept of graphene substrates' beneficial effects on the neural induction of several types of mesenchymal stem cells [58].

Future studies testing the neuroinductive capacity of graphene should use films with different physico-chemical characteristics along with other stem cells of dental origin, such as pulp or follicle cells, combined with different culture media. In addition, markers' quantification at the protein level should rely on ELISA or Westernblot analyses as more precise than immunofluorescence quantification, thus overcoming some limitations of this study.

5. Conclusions

The predisposition of SCAPs to differentiate toward neural lineages, as well as the neuroinductive properties of graphene film, should warrant further studies of dental stem cells in conjunction with this nanomaterial, with the aim of finding an optimal solution for autologous neuroregenerative therapy.

Supplementary Materials: The following supporting information can be downloaded at: <https://www.mdpi.com/article/10.3390/nano12183116/s1>, Video S1: Time-dependent changes in morphology of SCAP grown on LPEG film.

Author Contributions: Conceptualization, J.S. and J.M.; methodology, J.S., R.P. and J.M.; validation, J.M.; formal analysis, J.S., B.T., M.L. and M.M.M.; investigation, J.S., B.T., M.L., M.M.M., M.P. and J.V.; resources, R.P. and J.M.; data curation, J.S., M.P. and J.V.; writing—original draft preparation, J.S.; writing—review and editing, M.L., M.M.M. and J.M.; visualization, B.T. and M.L.; supervision, J.M.; project administration, J.M.; funding acquisition, J.M. All authors have read and agreed to the published version of the manuscript.

Funding: This research was supported by the Ministry of Education, Science and Technological Development of the Republic of Serbia grant number 451-03-9/2021-14/200129 and by the Science Fund of the Republic of Serbia, #GRANT No 7750038, ORAL CANCER—NEW APPROACHES IN PREVENTION, CONTROL AND POST-OPERATIVE REGENERATION—AN IN VIVO STUDY—ORCA-PCR.

Institutional Review Board Statement: The study was conducted in accordance with the Declaration of Helsinki, and approved by the Ethics Committee of the School of Dental Medicine, University of Belgrade (No 36/19, 19.04.2016).

Informed Consent Statement: Informed consent was obtained from all subjects involved in the study.

Data Availability Statement: Not applicable.

Acknowledgments: We extend our appreciation to Djordje Miljkovic from the Institute of Biological Research Sinisa Stankovic, University of Belgrade, for the flowcytometry analyses.

Conflicts of Interest: The authors declare no conflict of interest. The funders had no role in the design of the study; in the collection, analyses, or interpretation of data; in the writing of the manuscript; or in the decision to publish the results.

References

1. Mitrečić, D.; Hribljan, V.; Jagečić, D.; Isaković, J.; Lamberto, F.; Horánszky, A.; Zana, M.; Foldes, G.; Zavan, B.; Pivoriūnas, A.; et al. Regenerative Neurology and Regenerative Cardiology: Shared Hurdles and Achievements. *Int. J. Mol. Sci.* **2022**, *23*, 855. [[CrossRef](#)]
2. Liu, A.; Long, Y.; Li, J.; Gu, L.; Karim, A.; Wang, X.; Gibson, A.L.F. Accelerated complete human skin architecture restoration after wounding by nanogenerator-driven electrostimulation. *J. Nanobiotechnol.* **2021**, *19*, 280. [[CrossRef](#)] [[PubMed](#)]
3. Long, Y.; Wei, H.; Li, J.; Yao, G.; Yu, B.; Ni, D.; Gibson, A.L.; Lan, X.; Jiang, Y.; Cai, W.; et al. Effective Wound Healing Enabled by Discrete Alternative Electric Fields from Wearable Nanogenerators. *ACS Nano* **2018**, *12*, 12533–12540. [[CrossRef](#)] [[PubMed](#)]
4. Vishwakarma, A.; Sharpe, P.; Shi, S.; Ramalingam, M. (Eds.) *Stem Cell Biology and Tissue Engineering in Dental Sciences*; Elsevier: Amsterdam, The Netherlands, 2014.
5. Egusa, H.; Iida, K.; Kobayashi, M.; Lin, T.Y.; Zhu, M.; Zuk, P.A.; Wang, C.J.; Thakor, D.K.; Hedrick, M.H.; Nishimura, I. Downregulation of extracellular matrix-related gene clusters during osteogenic differentiation of human bone marrow- and adipose tissue-derived stromal cells. *Tissue Eng.* **2007**, *13*, 2589–2600. [[CrossRef](#)] [[PubMed](#)]
6. Ding, D.C.; Shyu, W.C.; Lin, S.Z. Mesenchymal stem cells. *Cell Transplant.* **2011**, *20*, 5–14. [[CrossRef](#)]
7. Fernandes, K.J.; McKenzie, I.A.; Mill, P.; Smith, K.M.; Akhavan, M.; Barnabé-Heider, F.; Biernaskie, J.; Juneak, A.; Kobayashi, N.R.; Toma, J.G.; et al. A dermal niche for multipotent adult skin-derived precursor cells. *Nat. Cell Biol.* **2004**, *6*, 1082–1093. [[CrossRef](#)]
8. Sonoyama, W.; Liu, Y.; Fang, D.; Yamaza, T.; Seo, B.M.; Zhang, C.; Liu, H.; Gronthos, S.; Wang, C.Y.; Wang, S.; et al. Mesenchymal stem cell-mediated functional tooth regeneration in swine. *PLoS ONE* **2006**, *1*, e79. [[CrossRef](#)]
9. Huang, G.T.; Sonoyama, W.; Liu, Y.; Liu, H.; Wang, S.; Shi, S. The hidden treasure in apical papilla: The potential role in pulp/dentin regeneration and bioroot engineering. *J. Endod.* **2008**, *34*, 645–651. [[CrossRef](#)]
10. Abe, S.; Yamaguchi, S.; Amagasa, T. Multilineage Cells from Apical Pulp of Human Tooth with Immature Apex. *Oral. Sci. Int.* **2007**, *4*, 45–48. [[CrossRef](#)]

11. Germain, L.; De Berdt, P.; Vanacker, J.; Leprince, J.; Diogenes, A.; Jacobs, D.; Vandermeulen, G.; Bouzin, C.; Pr eat, V.; Dupont-Gillain, C.; et al. Fibrin hydrogels to deliver dental stem cells of the apical papilla for regenerative medicine. *Regen. Med.* **2015**, *10*, 153–167. [[CrossRef](#)]
12. Vanacker, J.; Viswanath, A.; De Berdt, P.; Everard, A.; Cani, P.D.; Bouzin, C.; Feron, O.; Diogenes, A.; Leprince, J.G.; des Rieux, A. Hypoxia modulates the differentiation potential of stem cells of the apical papilla. *J. Endod.* **2014**, *40*, 1410–1418. [[CrossRef](#)] [[PubMed](#)]
13. Wang, Y.; Li, Z.; Wang, J.; Li, J.; Lin, Y. Graphene and graphene oxide: Biofunctionalization and applications in biotechnology. *Trends Biotechnol.* **2011**, *29*, 205–212. [[CrossRef](#)] [[PubMed](#)]
14. Lee, W.C.; Lim, C.H.; Shi, H.; Tang, L.A.; Wang, Y.; Lim, C.T.; Loh, K.P. Origin of enhanced stem cell growth and differentiation on graphene and graphene oxide. *ACS Nano* **2011**, *5*, 7334–7341. [[CrossRef](#)] [[PubMed](#)]
15. La, W.G.; Park, S.; Yoon, H.H.; Jeong, G.J.; Lee, T.J.; Bhang, S.H.; Han, J.Y.; Char, K.; Kim, B.S. Delivery of a therapeutic protein for bone regeneration from a substrate coated with graphene oxide. *Small* **2013**, *9*, 4051–4060. [[CrossRef](#)] [[PubMed](#)]
16. Lee, Y.J.; Seo, T.H.; Lee, S.; Jang, W.; Kim, M.J.; Sung, J.S. Neuronal differentiation of human mesenchymal stem cells in response to the domain size of graphene substrates. *J. Biomed. Mater. Res. A* **2018**, *106*, 43–51. [[CrossRef](#)]
17. Mousavi, S.M.; Yousefi, K.; Hashemi, S.A.; Afsa, M.; Bahrani, S.; Gholami, A.; Ghahramani, Y.; Alizadeh, A.; Chiang, W.H. Renewable Carbon Nanomaterials: Novel Resources for Dental Tissue Engineering. *Nanomaterials* **2021**, *11*, 2800. [[CrossRef](#)]
18. Bressan, E.; Ferroni, L.; Gardin, C.; Sbricoli, L.; Gobbato, L.; Ludovichetti, F.S.; Tocco, I.; Carraro, A.; Piattelli, A.; Zavan, B. Graphene based scaffolds effects on stem cells commitment. *J. Transl. Med.* **2014**, *12*, 296. [[CrossRef](#)] [[PubMed](#)]
19. Park, S.Y.; Park, J.; Sim, S.H.; Sung, M.G.; Kim, K.S.; Hong, B.H.; Hong, S. Enhanced differentiation of human neural stem cells into neurons on graphene. *Adv. Mater.* **2011**, *23*, 263–267. [[CrossRef](#)]
20. Wang, Y.; Lee, W.C.; Manga, K.K.; Ang, P.K.; Lu, J.; Liu, Y.P.; Lim, C.T.; Loh, K.P. Fluorinated graphene for promoting neuro-induction of stem cells. *Adv. Mater.* **2012**, *24*, 4285–4290. [[CrossRef](#)]
21. Tang, M.; Song, Q.; Li, N.; Jiang, Z.; Huang, R.; Cheng, G. Enhancement of electrical signaling in neural networks on graphene films. *Biomaterials* **2013**, *34*, 6402–6411. [[CrossRef](#)]
22. Hong, S.W.; Lee, J.H.; Kang, S.H.; Hwang, E.Y.; Hwang, Y.S.; Lee, M.H.; Han, D.W.; Park, J.C. Enhanced neural cell adhesion and neurite outgrowth on graphene-based biomimetic substrates. *Biomed. Res. Int.* **2014**, *2014*, 212149. [[CrossRef](#)] [[PubMed](#)]
23. Bellet, P.; Gasparotto, M.; Pressi, S.; Fortunato, A.; Scapin, G.; Mba, M.; Menna, E.; Filippini, F. Graphene-Based Scaffolds for Regenerative Medicine. *Nanomaterials* **2021**, *11*, 404. [[CrossRef](#)] [[PubMed](#)]
24. Zare, P.; Aleemardani, M.; Seifalian, A.; Bagher, Z.; Seifalian, A.M. Graphene Oxide: Opportunities and Challenges in Biomedicine. *Nanomaterials* **2021**, *11*, 1083. [[CrossRef](#)] [[PubMed](#)]
25. Sanchez, V.C.; Jachak, A.; Hurt, R.H.; Kane, A.B. Biological interactions of graphene-family nanomaterials: An interdisciplinary review. *Chem. Res. Toxicol.* **2012**, *25*, 15–34. [[CrossRef](#)] [[PubMed](#)]
26. Kempainen, J.M.; Hollister, S.J. Tailoring the mechanical properties of 3D-designed poly (glycerol sebacate) scaffolds for cartilage applications. *J. Biomed. Mater. Res. A* **2010**, *94*, 9–18. [[CrossRef](#)]
27. Nair, M.; Nancy, D.; Krishnan, A.G.; Anjusree, G.S.; Vadukumpully, S.; Nair, S.V. Graphene oxide nanoflakes incorporated gelatin-hydroxyapatite scaffolds enhance osteogenic differentiation of human mesenchymal stem cells. *Nanotechnology* **2015**, *26*, 161001. [[CrossRef](#)]
28. Lee, T.J.; Park, S.; Bhang, S.H.; Yoon, J.K.; Jo, I.; Jeong, G.J.; Hong, B.H.; Kim, B.S. Graphene enhances the cardiomyogenic differentiation of human embryonic stem cells. *Biochem. Biophys. Res. Commun.* **2014**, *452*, 174–180. [[CrossRef](#)]
29. Chaudhuri, B.; Bhadra, D.; Moroni, L.; Pramanik, K. Myoblast differentiation of human mesenchymal stem cells on graphene oxide and electrospun graphene oxide-polymer composite fibrous meshes: Importance of graphene oxide conductivity and dielectric constant on their biocompatibility. *Biofabrication* **2015**, *7*, 015009. [[CrossRef](#)]
30. Ay an-Varela, M.; Villar-Rodil, S.; Paredes, J.I.; Munuera, J.M.; Pag an, A.; Lozano-P erez, A.A.; Cenis, J.L.; Mart inez-Alonso, A.; Tasc on, J.M. Investigating the Dispersion Behavior in Solvents, Biocompatibility, and Use as Support for Highly Efficient Metal Catalysts of Exfoliated Graphitic Carbon Nitride. *ACS Appl. Mater. Interfaces* **2015**, *7*, 24032–24045. [[CrossRef](#)]
31. Gopinathan, J.; Quigley, A.F.; Bhattacharyya, A.; Padhye, R.; Kapsa, R.M.; Nayak, R.; Shanks, R.A.; Houshyar, S. Preparation, characterisation, and in vitro evaluation of electrically conducting poly(ϵ -caprolactone)-based nanocomposite scaffolds using PC12 cells. *J. Biomed. Mater. Res. A* **2016**, *104*, 853–865. [[CrossRef](#)]
32. Guazzo, R.; Gardin, C.; Bellin, G.; Sbricoli, L.; Ferroni, L.; Ludovichetti, F.S.; Piattelli, A.; Antoniac, I.; Bressan, E.; Zavan, B. Graphene-Based Nanomaterials for Tissue Engineering in the Dental Field. *Nanomaterials* **2018**, *8*, 349. [[CrossRef](#)]
33. Matkovi c, A.; Milo evi c, I.; Mili evi c, M.; Toma evi c-Ili c, T.; Pe i c, J.; Musi c, M.; Spasenovi c, M.; Jovanovi c, D.; Vasi c, B.; Deeks, C.; et al. Enhanced sheet conductivity of Langmuir–Blodgett assembled graphene thin films by chemical doping. *2D Mater.* **2016**, *3*, 015002. [[CrossRef](#)]
34. Simonovic, J.; Toljic, B.; Nikolic, N.; Peric, M.; Vujan, J.; Panajotovic, R.; Gajic, R.; Bekyarova, E.; Cataldi, A.; Parpura, V.; et al. Differentiation of stem cells from apical papilla into neural lineage using graphene dispersion and single walled carbon nanotubes. *J. Biomed. Mater. Res. A* **2018**, *106*, 2653–2661. [[CrossRef](#)] [[PubMed](#)]
35. Milo evi c, I.R.; Vasi c, B.; Matkovi c, A.; Vujan, J.; A krabi c, S.; Kratzer, M.; Griesser, T.; Teichert, C.; Gaji c, R. Single-step fabrication and work function engineering of Langmuir–Blodgett assembled few-layer graphene films with Li and Au salts. *Sci. Rep.* **2020**, *10*, 8476. [[CrossRef](#)] [[PubMed](#)]

36. Shehadat, S.A.; Gorduysus, M.O.; Hamid, S.S.A.; Abdullah, N.A.; Samsudin, A.R.; Ahmad, A. Optimization of scanning electron microscope technique for amniotic membrane investigation: A preliminary study. *Eur. J. Dent.* **2018**, *12*, 574–578. [[CrossRef](#)]
37. Livak, K.J.; Schmittgen, T.D. Analysis of relative gene expression data using real-time quantitative PCR and the 2(-Delta Delta C(T)) Method. *Methods* **2001**, *25*, 402–408. [[CrossRef](#)]
38. Han, F.; Ma, X.; Zhai, Y.; Cui, L.; Yang, L.; Zhu, Z.; Hao, Y.; Cheng, G. Strategy for Designing a Cell Scaffold to Enable Wireless Electrical Stimulation for Enhanced Neuronal Differentiation of Stem Cells. *Adv. Healthc. Mater.* **2021**, *10*, 2100027. [[CrossRef](#)]
39. Madanagopal, T.T.; Tai, Y.K.; Lim, S.H.; Fong, C.H.; Cao, T.; Rosa, V.; Franco-Obregón, A. Pulsed electromagnetic fields synergize with graphene to enhance dental pulp stem cell-derived neurogenesis by selectively targeting TRPC1 channels. *Eur. Cells Mater.* **2021**, *41*, 216–232. [[CrossRef](#)]
40. Zhang, Q.; Zhang, Z.; Yin, J. Free-Standing Buckle-Delaminated 2D Organic Nanosheets with Enhanced Mechanical Properties and Multifunctionality. *Adv. Mater. Interfaces* **2019**, *6*, 1900561. [[CrossRef](#)]
41. Hung, H.S.; Kung, M.L.; Chen, F.C.; Ke, Y.C.; Shen, C.C.; Yang, Y.C.; Tang, C.M.; Yeh, C.A.; Hsieh, H.H.; Hsu, S.H. Nanogold-Carried Graphene Oxide: Anti-Inflammation and Increased Differentiation Capacity of Mesenchymal Stem Cells. *Nanomaterials* **2021**, *11*, 2046. [[CrossRef](#)]
42. Lee, J.S.; Lipatov, A.; Ha, L.; Shekhirev, M.; Andalib, M.N.; Sinitiskii, A.; Lim, J.Y. Graphene substrate for inducing neurite outgrowth. *Biochem. Biophys. Res. Commun.* **2015**, *460*, 267–273. [[CrossRef](#)] [[PubMed](#)]
43. Rodriguez-Losada, N.; Wendelbob, R.; Ocaña, M.C.; Casares, A.D.; Guzman de Villoria, R.; Aguirre Gomez, J.A.; Arraez, M.A.; Gonzalez-Alegre, P.; Medina, M.A.; Arenas, E.; et al. Graphene Oxide and Reduced Derivatives, as Powder or Film Scaffolds, Differentially Promote Dopaminergic Neuron Differentiation and Survival. *Front. Neurosci.* **2020**, *14*, 570409. [[CrossRef](#)] [[PubMed](#)]
44. Chen, L.; Wang, W.; Lin, Z.; Lu, Y.; Chen, H.; Li, B.; Li, Z.; Xia, H.; Li, L.; Zhang, T. Conducting molybdenum sulfide/graphene oxide/polyvinyl alcohol nanocomposite hydrogel for repairing spinal cord injury. *J. Nanobiotechnol.* **2022**, *20*, 210. [[CrossRef](#)] [[PubMed](#)]
45. Ferrari, A.C.; Meyer, J.C.; Scardaci, V.; Casiraghi, C.; Lazzeri, M.; Mauri, F.; Piscanec, S.; Jiang, D.; Novoselov, K.S.; Roth, S.; et al. Raman spectrum of graphene and graphene layers. *Phys. Rev. Lett.* **2006**, *97*, 187401. [[CrossRef](#)] [[PubMed](#)]
46. Bracamonte, M.V.; Lacconi, G.I.; Urreta, S.E.; Torres, L.E.F.F. On the Nature of Defects in Liquid-phase Exfoliated Graphene. *J. Phys. Chem. C* **2014**, *118*, 15455–15459. [[CrossRef](#)]
47. Amaro-Gahete, J.; Benítez, A.; Otero, R.; Esquivel, D.; Jiménez-Sanchidrián, C.; Morales, J.; Caballero, Á.; Romero-Salguero, F.J. A Comparative Study of Particle Size Distribution of Graphene Nanosheets Synthesized by an Ultrasound-Assisted Method. *Nanomaterials* **2019**, *9*, 152. [[CrossRef](#)]
48. Qu, G.; Li, Y.; Chen, L.; Chen, Q.; Zou, D.; Yang, C.; Zhou, Q. Comparison of Osteogenic Differentiation Potential of Human Dental-Derived Stem Cells Isolated from Dental Pulp, Periodontal Ligament, Dental Follicle, and Alveolar Bone. *Stem. Cells Int.* **2021**, *2021*, 6631905. [[CrossRef](#)]
49. Son, Y.B.; Kang, Y.H.; Lee, H.J.; Jang, S.J.; Bharti, D.; Lee, S.L.; Jeon, B.G.; Park, B.W.; Rho, G.J. Evaluation of odonto/osteogenic differentiation potential from different regions derived dental tissue stem cells and effect of 17β-estradiol on efficiency. *BMC Oral. Health.* **2021**, *21*, 15. [[CrossRef](#)]
50. Petrescu, N.B.; Jurj, A.; Sorițău, O.; Lucaciu, O.P.; Dirzu, N.; Raduly, L.; Berindan-Neagoe, I.; Cenariu, M.; Boșca, B.A.; Campian, R.S.; et al. Cannabidiol and Vitamin D3 Impact on Osteogenic Differentiation of Human Dental Mesenchymal Stem Cells. *Medicina* **2020**, *56*, 607. [[CrossRef](#)]
51. Nayak, T.R.; Andersen, H.; Makam, V.S.; Khaw, C.; Bae, S.; Xu, X.; Ee, P.L.; Ahn, J.H.; Hong, B.H.; Pastorin, G.; et al. Graphene for controlled and accelerated osteogenic differentiation of human mesenchymal stem cells. *ACS Nano* **2011**, *5*, 4670–4678. [[CrossRef](#)]
52. Kim, J.; Choi, K.S.; Kim, Y.; Lim, K.T.; Seonwoo, H.; Park, Y.; Kim, D.H.; Choung, P.H.; Cho, C.S.; Kim, S.Y.; et al. Bioactive effects of graphene oxide cell culture substratum on structure and function of human adipose-derived stem cells. *J. Biomed. Mater. Res. A* **2013**, *101*, 3520–3530. [[CrossRef](#)] [[PubMed](#)]
53. Di Carlo, R.; Zara, S.; Ventrella, A.; Siani, G.; Da Ros, T.; Iezzi, G.; Cataldi, A.; Fontana, A. Covalent Decoration of Cortical Membranes with Graphene Oxide as a Substrate for Dental Pulp Stem Cells. *Nanomaterials* **2019**, *9*, 604. [[CrossRef](#)] [[PubMed](#)]
54. Heng, B.C.; Jiang, S.; Yi, B.; Gong, T.; Lim, L.W.; Zhang, C. Small molecules enhance neurogenic differentiation of dental-derived adult stem cells. *Arch. Oral. Biol.* **2019**, *102*, 26–38. [[CrossRef](#)] [[PubMed](#)]
55. Park, D.; Xiang, A.P.; Mao, F.F.; Zhang, L.; Di, C.G.; Liu, X.M.; Shao, Y.; Ma, B.F.; Lee, J.H.; Ha, K.S.; et al. Nestin is required for the proper self-renewal of neural stem cells. *Stem Cells* **2010**, *28*, 2162–2171. [[CrossRef](#)] [[PubMed](#)]
56. Hochuli, A.H.D.; Senegaglia, A.C.; Selenko, A.H.; Fracaro, L.; Brofman, P.R.S. Dental Pulp from Human Exfoliated Deciduous Teeth-derived Stromal Cells Demonstrated Neuronal Potential: In Vivo and In Vitro Studies. *Curr. Stem. Cell Res. Ther.* **2021**, *16*, 495–506. [[CrossRef](#)]
57. Kim, K.S.; Zhao, Y.; Jang, H.; Lee, S.Y.; Kim, J.M.; Kim, K.S.; Ahn, J.H.; Kim, P.; Choi, J.Y.; Hong, B.H. Large-scale pattern growth of graphene films for stretchable transparent electrodes. *Nature* **2009**, *457*, 706–710. [[CrossRef](#)]
58. Reddy, S.; He, L.; Ramakrishana, S.; Luo, H. Graphene nanomaterials for regulating stem cell fate in neurogenesis and their biocompatibility. *Curr. Opin. Biomed. Eng.* **2019**, *10*, 69–78. [[CrossRef](#)]

Transparent and conductive films from liquid phase exfoliated graphene

Tijana Tomašević-Ilić¹ · Jelena Pešić¹ · Ivana Milošević¹ ·
Jasna Vujin¹ · Aleksandar Matković¹ · Marko Spasenović¹ ·
Radoš Gajić¹

Received: 5 November 2015 / Accepted: 6 May 2016
© Springer Science+Business Media New York 2016

Abstract We describe transparent and conductive films of liquid-phase exfoliated graphene deposited with the Langmuir–Blodgett (LB) method. Graphene sheets (GS) were exfoliated from graphite by ultrasonic treatment in N-Methyl-2-pyrrolidone (NMP) and N, N-dimethylacetamide (DMA) solvents. For comparison, graphene sheets were also exfoliated in a water solution of surfactants. We confirm a higher exfoliation rate for surfactant-based processing compared to NMP and DMA. Furthermore, we demonstrate that our films exfoliated in NMP and DMA, deposited with LB and annealed have a higher optical transmittance and lower sheet resistance compared to films obtained with vacuum filtration, which is a necessary step for GS exfoliated in water solutions. The structural, optical and electrical properties of graphene layers were characterized with scanning electron microscopy, atomic force microscopy, UV/VIS spectrophotometry and sheet resistance measurements. Our facile and reproducible method results in high-quality transparent conductive films with potential applications in flexible and printed electronics and coating technology.

Keywords Graphene · LPE · Langmuir–Blodgett assembly

1 Introduction

Transparent conductors are an essential part of many optical devices. Many of the thin metallic or metal oxide films used as transparent conductors (Granqvist 2007) exhibit nonuniform absorption across the visible spectrum (Phillips et al. 1994), or they are

This article is part of the Topical Collection on Advances in the Science of Light.

Guest Edited by Jelena Radovanovic, Milutin Stepic, Mikhail Sumetsky, Mauro Pereira and Dragan Indjin.

✉ Tijana Tomašević-Ilić
ttijana@ipb.ac.rs

¹ Center for Solid State Physics and New Materials, Institute of Physics, University of Belgrade, Pregrevica 118, 11080 Belgrade, Serbia

chemically unstable, or both (Scott et al. 1996; Schlatmann et al. 1996). The experimental discovery of graphene (Novoselov et al. 2004) brought a new alternative to this field. Graphene is a material with high optical transparency, large carrier mobility, good chemical stability, and mechanical strength, making it an excellent choice for transparent electrodes in various optoelectronic devices (Blake et al. 2008).

Although graphene is a natural choice for transparent conductive films (Bonaccorso et al. 2010), the feasibility of its mass production is essential for applications. In order to produce large quantities of graphene Blake et al. (Blake et al. 2008) and Hernandez et al. (2008) developed a method of graphene production using solvent assisted exfoliation (or liquid phase exfoliation, LPE) of bulk graphite, which is simpler and less costly than chemical vapor deposition and returns a higher yield than mechanical exfoliation (Novoselov et al. 2004, 2005). LPE allows the possibility to scale up the synthesis of graphene making it economically available in a large amount, presenting a promising route for large-scale production (Paton et al. 2014).

Numerous research efforts followed up to increase the concentration and quality of the graphene flakes produced. One of the most promising synthesis routes for LPE graphene is non-covalent exfoliation using solvents that have surface energy values comparable to that of graphite (Hernandez et al. 2008). Typically ultrasound assists the separation of graphene flakes from graphite powder in solvent. Exfoliation conditions such as the initial concentration of graphite powder, sonication time (Khan et al. 2010), solvent type (O'Neill et al. 2011; Bourlinos et al. 2009; Hernandez et al. 2010; Lotya et al. 2009; Guardia et al. 2011), and possible filtration (Khan et al. 2011) were tuned in order to optimize the yield and quality of graphene dispersions. These graphene dispersions can be used to form films by various methods, for example spray coating (Blake et al. 2008), vacuum filtration (Hernandez et al. 2008; Lotya et al. 2009) or Langmuir–Blodgett assembly (LBA) (Cote 2009; Kim et al. 2013; Li et al. 2008).

In this study, graphene sheets (GS) were exfoliated from graphite by ultrasonic treatment in organic solvents with high boiling points, N-Methyl-2-pyrrolidone (NMP), N,N-dimethylacetamide (DMA), and for comparison, in a water solution of surfactant, sodium dodecylbenzenesulfonate (SDBS) and Pluronic P-123 (P-123). The graphene dispersions from NMP and DMA were used to form films by controlled deposition of few-layer graphene using the Langmuir–Blodgett (LB) method on a water–air interface. We confirm a higher exfoliation rate for surfactant-based processing, but demonstrate that our films exfoliated in organic solvents with high boiling points and deposited with LB have a higher optical transmittance and lower sheet resistance compared to films obtained with vacuum filtration, which is a necessary step for GS exfoliated in water solutions. The structural, optical and electrical properties of graphene layers were characterized with scanning electron microscopy, atomic force microscopy, UV/VIS spectrophotometry and sheet resistance measurements.

2 Experimental procedure

All chemicals used were purchased from Sigma Aldrich: graphite powder (product number 332461), N-Methyl-2-pyrrolidone (product number 328634), N,N-dimethylacetamide (product number 38840), sodium dodecylbenzenesulfonate (product number 289957) and Pluronic P-123 (product number 435467). The particular graphite powder product was chosen for its large initial flake size, which should result in the largest possible graphene

flakes after exfoliation. Stock solutions of SDBS and P-123 of different concentrations were prepared in deionized water (resistivity 18 M Ω) by stirring overnight. A range of graphene dispersions were prepared. A typical sample was prepared by dispersing graphite in the desired solvent using from 30 min to 14 h of sonication in a low power sonic bath. The resulting dispersion was centrifuged for 60 min at 3000 rpm in order to reduce the amount of unexfoliated graphite.

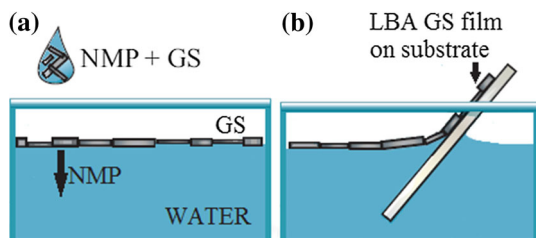
The graphene sheets exfoliated from graphite by ultrasonic treatment in NMP were used to form films at a water–air interface. Beakers filled with deionized water, 10 mL volume, were used for film formation. A 1.5–2 vol% of GS + NMP was added to the interface with a continuous flow rate of 5–10 mL/s (Fig. 1a). This set of parameters provides enough surface pressure for the film to be close-packed. After the film is formed, it is slowly scooped onto the targeted substrate (Fig. 1b), as shown in our previous work (Matković et al. 2016). PET and SiO₂/Si were used as substrates. As it has been shown that annealing decreases sheet resistance due to solvent evaporation (Hernandez et al. 2008; Lotya et al. 2009), some of these deposited films were annealed. Annealing was carried out in a tube furnace at 250 °C in an argon atmosphere for 2 h.

For optical characterization, UV–VIS spectra were taken using a SUPER SCAN Varian spectrophotometer with quartz cuvettes. The resistance of each sample was measured in a two-point probe configuration, and the sheet resistance was obtained by including the sample geometry factors. AFM measurements were taken with an atomic force microscope, NTEGRA Spectra, in tapping mode. SiO₂/Si was chosen as a substrate for AFM due to its low surface roughness. The lateral profile of graphene flakes was analyzed with a Tescan MIRA3 field-emission gun SEM.

3 Results and discussion

We optimized for high graphene concentration and large flake size, tuning exfoliation conditions such as initial graphite concentration, sonication time and solvent type. The Lambert–Beer law was applied to UV–VIS absorption spectra to find graphene concentration. The concentration was estimated from the absorbance at 660 nm by using the extinction coefficient of graphene ($\alpha = 13.90 \text{ mL mg}^{-1} \text{ m}^{-1}$) previously determined in surfactant/water solutions (Hernandez et al. 2008; Lotya et al. 2009; Guardia et al. 2011) and ($\alpha = 24.60 \text{ mL mg}^{-1} \text{ m}^{-1}$) in NMP and DMA solutions (Hernandez et al. 2008). Figure 2a depicts a higher final concentration for surfactant-based processing for all initial concentrations of graphite powder, from 0.5 to 18 mg mL⁻¹. The most commonly used deposition technique for LPE GS is vacuum filtration. This is a necessary step for GS exfoliated in water solutions. For GS films formed by evaporation of a high boiling point

Fig. 1 Schematic representations of **a** LBA GS film formation, **b** scooping of the film onto a targeted substrate



solvent, one of the biggest problems is that graphene flakes aggregate during evaporation (O'Neill et al. 2011) hindering fine control over the film thickness (Hernandez et al. 2008). This can be avoided by depositing with LB, which allows reliable and reproducible thickness control and prevents further agglomeration of graphene flakes during drying (Kim et al. 2013). We chose the dispersion in NMP with the highest graphene concentration (Fig. 2b) for experiments on LB films.

A single LB deposition resulted in films with an average thickness 3.3 nm, as measured with AFM, indicating an average GS thickness of 10 layers (Fig. 3).

Figure 4 shows optical transmittance versus sheet resistance for varying number of LB depositions on PET, compared to graphene film obtained with vacuum filtration of GS exfoliated from the same graphite precursor using the same experimental procedure (Hernandez et al. 2008; Lotya et al. 2009) before and after annealing. The highest transparency for a single LB film deposition prior to annealing was found to be about 83 %, which is between 20 and 40 % higher than the transmittance that can be accomplished with vacuum-filtration. The sheet resistance of one LB film deposition is between 70 and 250 k Ω /sq, 2–5 times lower than sheet resistance achieved with vacuum filtration without annealing. Increasing the graphene film thickness with additional LB depositions led to consistent increases in conductivity, but a decrease in transparency. Our graphene films for three LB depositions prior to annealing have comparable sheet resistance but higher optical transmittance compared to vacuum-filtered films after annealing.

The electrical conductivity is affected by the size and connectivity of the flakes as well as the thickness of the films. Our average GS diameter was is 120 nm, as measured with SEM (Fig. 5). SEM also revealed the presence of pinholes between flakes for a single LB deposition, which probably results in parasitic sheet resistance (Fig. 5a). In order to remove the residual solvent between the overlapping flakes, which may affect transport, we employed thermal annealing. Annealing does not repair the holes and other irreversible defects (Fig. 5b), but it can remove residual solvents, improving the coupling between graphene flakes and hence decreasing sheet resistance. For a single LB deposition, annealing reduced sheet resistance by about six times, without considerably decreasing transparency (Fig. 4). The sheet resistance of a singly deposited film after annealing was found to be between 10 and 20 k Ω /sq, a significant improvement over other published data. After annealing we performed a second LB deposition and achieved sheet resistance of

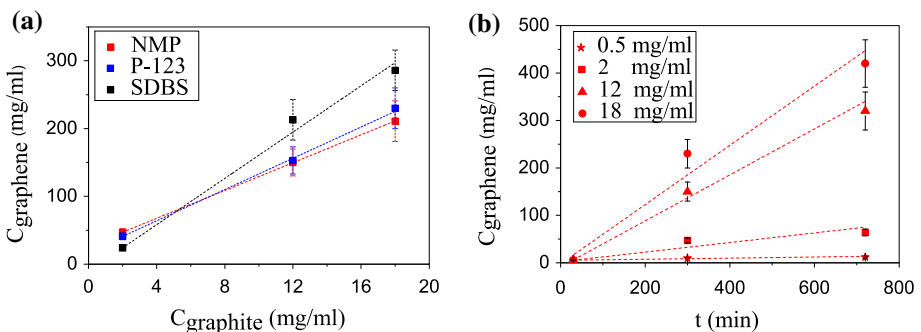


Fig. 2 Concentration of dispersed graphene: **a** in different solutions for different initial graphite concentration and sonication time of 5 h, **b** in NMP for different sonication time and different initial graphite concentration

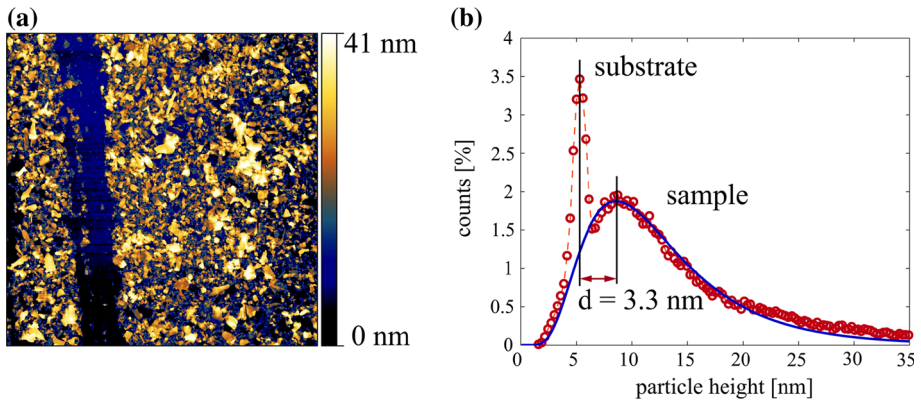


Fig. 3 **a** AFM image of a LB graphene film on a SiO_2/Si substrate, **b** an LB GS film/substrate height histogram fitted with a log-normal curve

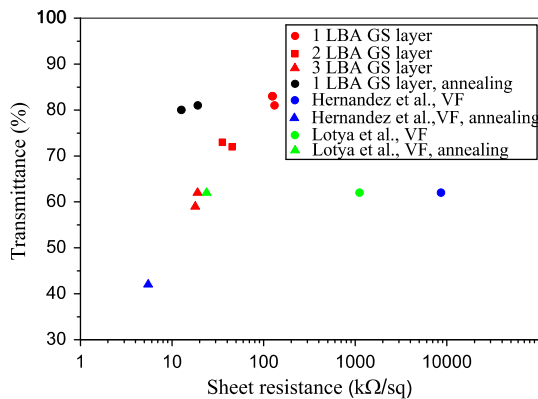


Fig. 4 Optical transmittance versus sheet resistance for varying number of LB deposition of graphene sheets on PET exfoliated in NMP before (*red*) and after annealing (*black*), compared to graphene films obtained with vacuum filtration in the same solvent (*blue*) (Hernandez et al. 2008) and graphene films obtained with vacuum filtration in surfactant/water solutions (*green*) (Lotya et al. 2009) before and after annealing. (Color figure online)

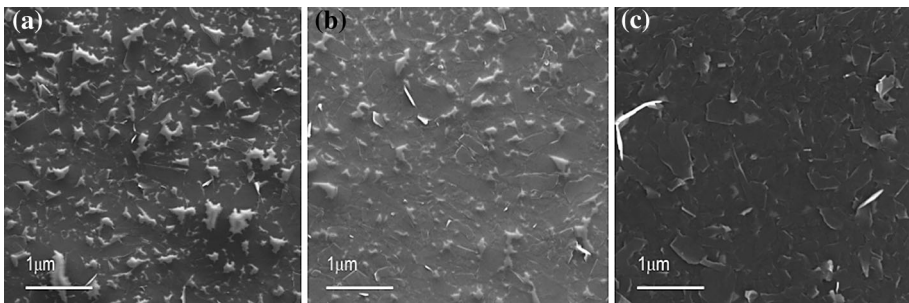


Fig. 5 SEM images of: **a** singly deposited LB film on a glass substrate, **b** the same film after annealing, **c** two LB depositions with an annealing step in between

3 k Ω /sq and a transparency of more than 70 %. Decreased resistance is the result of reduced density of pinholes (Fig. 5c) as well as increased film thickness.

4 Conclusion

In summary, we have shown that Langmuir–Blodgett assembly of multi-layer graphene sheets produced from liquid phase exfoliation of graphite powder in solvents can be used to fabricate transparent and conductive films. The sheet resistance of deposited LBA GS layers was found to be between 15 and 250 k Ω /sq, with transmittance between 60 and 85 %, depending on the number of deposited LBA graphene layers. The conductivity of these LBA films can be further increased by about six times with annealing, without considerably decreasing transparency. Optoelectronic properties of these films are much better compared to graphene films obtained with vacuum filtration of GS exfoliated with the same experimental procedure, which is the most commonly used deposition technique for LPE GS. Ours is a facile, reproducible and low-cost technique for transparent conductive films with potential applications in coating technology.

Acknowledgments This work was funded by the Serbian MPNTR through Projects OI 171005 and Innovation Project 451-03-2802-IP/1/167 and by Qatar National Research Foundation through Projects NPRP 7-665-1-125. The authors would like to express their gratitude to S. Novkovic for technical support with annealing.

References

- Blake, P., et al.: Graphene-based liquid crystal device. *Nano Lett.* **8**, 1704–1708 (2008)
- Bonaccorso, F., et al.: Graphene photonics and optoelectronics. *Nat. Photonics* **4**, 611–622 (2010)
- Bourlinos, A.B., et al.: Liquid-phase exfoliation of graphite towards solubilized graphenes. *Small* **5**, 1841–1845 (2009)
- Cote, L.J.: Langmuir–Blodgett assembly of graphite oxide single layers. *J. Am. Chem. Soc.* **131**, 1043–1049 (2009)
- Granqvist, C.G.: Transparent conductors as solar energy materials: a panoramic review. *Sol. Energy Mater. Sol. Cells* **91**, 1529–1598 (2007)
- Guardia, L., et al.: High-throughput production of pristine graphene in an aqueous dispersion assisted by non-ionic surfactants. *Carbon* **49**, 1653–1662 (2011)
- Hernandez, Y., et al.: High-yield production of graphene by liquid-phase exfoliation of graphite. *Nat. Nanotechnol.* **3**, 563–568 (2008)
- Hernandez, Y., et al.: Measurement of multicomponent solubility parameters for graphene facilitates solvent discovery. *Langmuir* **26**, 3208–3213 (2010)
- Khan, U., et al.: High-concentration solvent exfoliation of graphene. *Small* **6**, 864–871 (2010)
- Khan, U., et al.: Solvent-exfoliated graphene at extremely high concentration. *Langmuir* **27**, 9077–9082 (2011)
- Kim, H.K., et al.: Optoelectronic properties of graphene thin films deposited by a Langmuir–Blodgett assembly. *Nanoscale* **5**, 12365–12374 (2013)
- Li, X., et al.: Highly conducting graphene sheets and Langmuir–Blodgett films. *Nat. Nanotechnol.* **3**, 538–542 (2008)
- Lotya, M., et al.: Liquid phase production of graphene by exfoliation of graphite in surfactant/water solutions. *J. Am. Chem. Soc.* **131**, 3611–3620 (2009)
- Matković, A., et al.: Enhanced sheet conductivity of Langmuir-Blodgett assembled graphene thin films by chemical doping. *2D Mater.* **3**(1), 015002 (2016)
- Novoselov, K.S., et al.: Electric field effect in atomically thin carbon. *Science* **306**, 666–669 (2004)
- Novoselov, K.S., et al.: Two-dimensional atomic crystals. *Natl. Acad. Sci. U.S.A.* **102**, 10451–10453 (2005)
- O'Neill, A., et al.: Graphene dispersion and exfoliation in low boiling point solvents. *J. Phys. Chem. C* **115**, 5422–5428 (2011)

- Paton, K.R., et al.: Scalable production of large quantities of defect-free few-layer graphene by shear exfoliation in liquids. *Nat. Mater.* **13**, 624–630 (2014)
- Phillips, J.M., et al.: Transparent conducting thin films of GaInO₃. *Appl. Phys. Lett.* **65**, 115–117 (1994)
- Schlatmann, A.R., et al.: Indium contamination from the indium–tin–oxide electrode in polymer light emitting diodes. *Appl. Phys. Lett.* **69**, 1764–1766 (1996)
- Scott, J.C., et al.: Degradation and failure of MEH-PPV light-emitting diodes. *J. Appl. Phys.* **79**, 2745–2751 (1996)

PHOTONICA2015.

V International School and Conference on Photonics
& COST actions: MP1204 and BM1205
& the Second international workshop "Control of light and
matter waves propagation and localization in photonic
lattices"
www.vin.bg.ac.rs/photonica_2015

Book of Abstracts



Editors

Suzana Petrović, Goran Gligorić and Milutin Stepić

Belgrade, 2015.

Book of abstracts



PHOTONICA2015

the Fifth international school and conference on
photonics

& COST actions: MP1204 and BM1205

& the Second international workshop "Control of light and matter
waves propagation and localization in photonic lattices"

24 August – 28 August 2015

Belgrade, Serbia

Editors

Suzana Petrović, Goran Gligorić and Milutin Stepić

Vinča Institute of Nuclear Sciences, Belgrade, Serbia

Belgrade, 2015

Transparent and conductive films from liquid phase exfoliated graphene

T. Tomašević-Ilić¹, J. Pešić¹, I. Milošević¹, J. Vujin¹, A. Matković¹, M. Spasenović¹ and R. Gajić¹

¹Center for Solid State Physics and New Materials, Institute of Physics, University of Belgrade, Pregrevica 118, 11080 Belgrade, Serbia
e-mail: ttijana@ipb.ac.rs

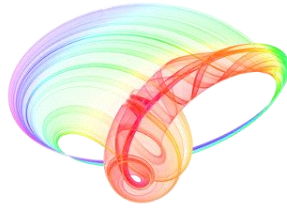
Liquid phase exfoliation of graphite presents a promising route for large-scale graphene production [1]. We describe basic advantages and disadvantages of the controlled deposition of few-layer graphene using the Langmuir-Blodgett (LB) method, which is compatible with usage in transparent conductors [2,3]. The graphene sheets (GS) were exfoliated from graphite by ultrasonic treatment in N-Methyl-2-pyrrolidone (NMP) and dimethylacetamide (DMA) solvents. For comparison, graphene sheets were also exfoliated in a water solution of surfactants. We confirm a higher exfoliation rate for surfactant-based processing compared to NMP and DMA. Furthermore, we demonstrate that our films exfoliated in NMP and DMA and deposited with LB have a higher optical transmittance compared to films obtained with vacuum filtration, which is a necessary step for GS exfoliated in water solutions [4]. The structural, optical and electrical properties of graphene layers were characterized with scanning electron microscopy, atomic force microscopy, ellipsometry, UV/VIS spectrophotometry and sheet resistance measurements. Our facile and reproducible method results in high-quality transparent conductive films with potential applications in flexible and printed electronics and coating technology.

This work is supported by the Serbian MPNTR through Projects OI 171005 and Innovation Project 451-03-2802-IP/1/167 and by Qatar National Research Foundation through Projects NPRP 7-665-1-125.

REFERENCES

- [1] K. R. Paton et al., *Nat. Mater.* 13, 624 (2014).
- [2] H. K. Kim et al., *Nanoscale* 5, 12365 (2013).
- [3] F. Bonaccorso et al., *Nat. Photon.* 4, 611 (2010).
- [4] M. Lotya et al., *J. Am. Chem. Soc.* 131, 3611 (2009).

Book of abstracts



PHOTONICA2017

The Sixth International School and Conference on Photonics

& COST actions: MP1406 and MP1402



&H2020-MSCA-RISE-2015 CARDIALLY workshop



28 August – 1 September 2017

Belgrade, Serbia

Editors

Marina Lekić and Aleksandar Krmpot

Institute of Physics Belgrade, Serbia

Belgrade, 2017

ABSTRACTS OF TUTORIAL, KEYNOTE, INVITED LECTURES,
PROGRESS REPORTS AND CONTRIBUTED PAPERS

of

The Sixth International School and Conference on Photonics
PHOTONICA2017

28 August – 1 September 2017
Belgrade Serbia

Editors

Marina Lekić and Aleksandar Krmpot

Technical assistance

Marko Nikolić and Danica Pavlović

Publisher

Institute of Physics Belgrade
Pregrevica 118
11080 Belgrade, Serbia

Printed by

Serbian Academy of Sciences and Arts

Number of copies

300

ISBN 978-86-82441-46-5

Ab-initio study of optical properties of MoS₂ and WS₂ compared to spectroscopic results of liquid phase exfoliated nanoflakes

Jelena Pešić¹, Jasna Vujin¹, Tijana Tomašević-Ilić¹, Marko Spasenović¹, Radoš Gajić¹

¹Graphene Laboratory (GLAB) of the Center for Solid State Physics and New Materials,
Institute of Physics, University of Belgrade,
Pregrevica 118, Belgrade, 11080, Serbia
e-mail: yelena@ipb.ac.rs

MoS₂ and WS₂ are part of the family of transition metal dichalcogenide crystals (TMDC). TMDCs have emerged as a new class of semiconductors that display distinctive properties at a thickness of one and few layers [1-3]. They have also attracted much interest for applications in optoelectronics as detectors, photovoltaic devices and light emitters [4-8].

Spectroscopic techniques are among the most important methods for research in the field of nanoscience and nanotechnologies. Parallel with the development of experimental methods, computational science becomes a very valuable tool in pursuit for new low-dimensional materials and their characterization. Employing high-end modeling codes, it is possible to simulate from first principles more than a few spectroscopic techniques. Using approaches based on density functional theory (DFT), including density functional perturbation theory, time-dependent DFT and many-body perturbation theory, implemented in the Quantum Espresso software package [9], we study optical properties of low-dimensional materials, MoS₂ and WS₂.

We calculate the dielectric function within the framework of the random-phase approximation (RPA) [10] based on DFT ground-state calculations, starting from eigenvectors and eigenvalues all calculated with Quantum Espresso. The final goal of our theoretical work is a comparison to corresponding experimental data. We compare our computational results with optical measurements on MoS₂ and WS₂ nanoflakes. MoS₂ and WS₂ were exfoliated by ultrasonic treatment in low-boiling point organic solvent [11-15] and characterized using UV/VIS spectrophotometry. We use our results for analysis of optical properties of liquid phase exfoliated MoS₂ and WS₂ nanoflakes, as a proven method for analysis of basic optical properties of 2D materials [11].

This work is supported by the Serbian MPNTR through Project OI 171005 and by Qatar National Research Foundation through Projects NPRP 7-665-1-12

REFERENCES

- [1] S. Z. Butler, et al., ACS Nano 7, 2898 (2013).
- [2] Q. H. Wang, et al., Nat Nano 7, 699 (2012).
- [3] X. Xu et al., Nat Phys 10, 343 (2014).
- [4] A. Pospischil, M. M. Furchi, and T. Mueller, Nat Nano 9, 257 (2014).
- [5] B. W. H. Baugher, et al., Nat Nano 9, 262 (2014).
- [6] L. Britnell, et al., Science 340, 1311 (2013).
- [7] F. H. L. Koppens, et al., Nat Nano 9, 780 (2014).
- [8] J. Ross, Nat Nanotechnol. 4, 268 (2014).
- [9] P. Giannozzi et al., J. Phys.:Condens. Matter 21 395502 (2009) <http://www.quantum-espresso.org>
- [10] Brener, N.E., Phys. Rev. B 12, 1487, (1975).
- [11] A. Matković et al., 2D Mater. 3(1), 015002 (2016).
- [12] T. Tomašević-Ilić, et al. Opt Quant Electron 48: 319, (2016).
- [13] T. Tomašević-Ilić et al., submitted (2017).
- [14] R. Panajotović et al. Book of Abstracts, SPIG 2016, 182-185, (2016).
- [15] J. Vujin et al. Book of Abstracts RAD 2016, (2016).
- [16] J. Pešić et al. , Opt Quant Electron, 48:368 (2016).

7-11th October 2019
Belgrade, Serbia



<http://www.sfkm.ac.rs/>

The 20th Symposium on Condensed Matter Physics

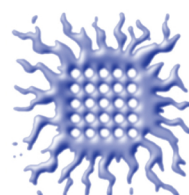
BOOK OF ABSTRACTS



University of Belgrade,
Faculty of Physics



Institute of Physics Belgrade



Vinca Institute
of Nuclear Sciences



Serbian Academy
of Sciences and Arts



Ministry of Education, Science and
Technological Development,
Republic of Serbia

Conference Chair

Cedomir Petrovic, *Brookhaven National Laboratory, USA*

Željko Šljivančanin, *Vinča Institute of Nuclear Sciences Serbia*

Organizing Committee

Jelena Pešić, *Institute of Physics Belgrade*

Andrijana Šolajić, *Institute of Physics Belgrade*

Petar Mali, *Faculty of Sciences, University of Novi Sad*

Jelena Pajović, *Faculty of Physics, University of Belgrade, Serbia*

Srđan Stavrčić, *Vinča Institute of Nuclear Sciences*

Svetislav Mijatović, *Faculty of Physics, University of Belgrade, Serbia*

Božidar Nikolić, *Faculty of Physics, University of Belgrade, Serbia – chair*

Organized by

Institute of Physics Belgrade

Faculty of Physics, University of Belgrade

Vinča Institute of Nuclear Sciences

Serbian Academy of Sciences and Arts

Program Committee

Ivan Božović, *Brookhaven National Laboratory, USA*

Vladimir Dobrosavljević, *Florida State University, USA*

Milan Damnjanović, *Faculty of Physics, University of Belgrade, Serbia*

Vladimir Djoković, *Vinča Institute, University of Belgrade, Serbia*

Gyula Eres, *Oak Ridge National Laboratory, USA*

Laszló Forró, *Ecole Polytechnique Fédérale de Lausanne, Switzerland*

Radoš Gajić, *Institute of Physics Belgrade, University of Belgrade, Serbia*

Igor Herbut, *Simon Fraser University, Canada*

Zoran Ikonić, *University of Leeds, UK*

Ivanka Milošević, *Faculty of Physics, University of Belgrade, Serbia*

Branislav Nikolić, *University of Delaware, USA*

Cedomir Petrovic, *Brookhaven National Laboratory, USA*

Dragana Popović, *National High Magnetic Field Laboratory USA*

Zoran S. Popović, *Vinča Institute, University of Belgrade, Serbia*

Zoran V. Popović, *Institute of Physics, University of Belgrade, Serbia*

Zoran Radović, *Faculty of Physics, University of Belgrade, Serbia*

Miljko Satarić, *Faculty of Technical Sciences, University of Novi Sad, Serbia*

Vojislav Stamenković, *Argonne National Laboratory, USA*

Željko Šljivančanin, *Vinča Institute, University of Belgrade, Serbia*

Bosiljka Tadić, *Jožef Štefan Institute, Slovenia*

Milan Tadić, *School of Electrical Engineering, University of Belgrade, Serbia*

Darko Tanasković, *Institute of Physics, University of Belgrade, Serbia*

Liquid-phase Exfoliation of Graphene and Chemical Doping of Langmuir-Blodgett Assembled Graphene Films

Ivana R. Milošević^a, Borislav Vasić^a, Aleksandar Matković^b, Jasna Vujin^a
and Radoš Gajić^a

^aLaboratory for Graphene, Other 2D Materials and Ordered Nanostructures of Center for Solid State Physics and New Materials, Institute of Physics, University of Belgrade, Serbia

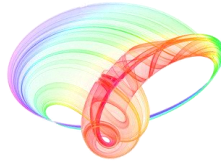
^bInstitute of Physics, Montanuniversität Leoben, Austria

Abstract. In current optoelectronic devices transparent conductive (TC) electrodes are widely used [1]. Graphene films as new TC material can be used to overcome shortcomings of the existed TC electrodes especially using graphene films as an active electrode. They offer advantages such as higher transparency over a broad range of light wavelengths, higher flexibility, excellent electrical conductivity and chemical stability. Using graphene films as an active electrode, band-structure alignment at the interface can be achieved with an appropriate work function (WF). Therefore, appropriate WF can enhance the charge injection and improve device performances. Chemical doping is an effective method for tuning of the WF by charge transfer between the graphene sheet films and dopants [2, 3]. Liquid-phase exfoliation (LPE) via sonication was the method for the preparation of graphene sheet (GS) dispersion. The films were self-assembled from LPE few-layer GS dispersion by Langmuir-Blodgett (LBA) technique at the water-air interface. Chemical doping of the films was performed in two ways. In the first approach, chemical doping with nitric acid is introduced after the film was formed. Fivefold improvement of sheet conductivity was achieved, with no change in transparency [4]. In the second approach, chemical doping of the film was happening at the moment of its formation. To achieve doping, metal standard solutions were introduced instead of water. Au based salts increase the WF of the films (p-doping), while Li based salts decrease it (n-doping). A span of 0.7 eV in both directions was obtained. Formation of the graphene films and both procedures of their chemical doping are very simple, low-cost and extend their potential use in low-cost optoelectronic applications as well as using them as an active electrode.

REFERENCES

1. Syu, J-Y., Chen, Y-M., Xu, K-X., He, S-M., Hung, W-C., Chang, C-L. and Su, C-Y., *RSC Adv.* **6**, 32746-32756 (2016).
2. Park, J., Lee, W. H., Huh, S., Sim, S. H., Bin Kim, S., Cho, K., Hong, B. H. and Kim, K. S., *J. Phys. Chem. Lett.* **2**, 841-845 (2011).
3. Kwon, K. C., Choi, K. S., Kim, B. J., Lee, J. L., and Kim, S. Y., *J. Phys. Chem. C.* **118**, 8187-8193 (2014).
4. Matković, A., Milošević, I., Milićević, M., Tomašević-Ilić, T., Pešić, J., Musić, et al. *2D Mater.* **3**, 015002 (2016).

Book of abstracts



PHOTONICA2019

The Seventh International School and Conference on
Photonics, 26 August – 30 August 2019, Belgrade, Serbia

& Machine Learning with Photonics Symposium
(ML-Photonica 2019)



& ESUO Regional Workshop



& COST action CA16221



Editors: Milica Matijević, Marko Krstić and Petra Beličev

Belgrade, 2019

ABSTRACTS OF TUTORIAL, KEYNOTE, INVITED LECTURES,
PROGRESS REPORTS AND CONTRIBUTED PAPERS

of

The Seventh International School and Conference on Photonics
PHOTONICA2019, 26 August – 30 August 2019, Belgrade, Serbia

and

Machine Learning with Photonics Symposium

and

ESUO Regional Workshop

Editors

Milica Matijević, Marko Krstić and Petra Beličev

Technical Assistance

Danka Stojanović and Goran Gligorić

Publisher

Vinča Institute of Nuclear Sciences

Mike Petrovića Alasa 12-14, P.O. Box 522

11000 Belgrade, Serbia

Printed by

Serbian Academy of Sciences and Arts

Number of copies

300

ISBN 978-86-7306-153-5

Chemical doping of Langmuir-Blodgett assembled few-layer graphene films with Au and Li salts aimed for optoelectronic applications

I. R. Milošević¹, B. Vasić¹, A. Matković², J. Vujin¹, S. Aškračić³, C. Teichert² and R. Gajić¹

¹Laboratory for Graphene, other 2D materials and Ordered Nanostructures of Center for Solid State Physics and New Materials, Institute of Physics, University of Belgrade, Belgrade, Serbia

²Institute of Physics, Montanuniversität Leoben, Leoben, Austria

³Nanostructured Matter Laboratory of Center for Solid State Physics and New Materials, Institute of Physics, University of Belgrade, Belgrade, Serbia

e-mail: novovic@ipb.ac.rs

For mass production of graphene, simple and low-cost methods are needed especially in the cases where high-quality films are not crucial for the desired purposes. Thus, liquid-phase exfoliation (LPE) is a perspective way of obtaining stable dispersion of few-layer graphene sheets (GS) in the solvent [1]. A promising pathway to achieve high degree of ordering of graphene sheets prepared via LPE-process is to utilize Langmuir-Blodgett assembly (LBA) technique. Thin-films are self-assembled from LPE dispersion by LBA technique at the water-air interface. LBA method is a suitable method for production of large-scale, transparent, thin solution-processed graphene films [2, 3]. Chemical doping of graphene films allows to tune its work function (WF) and therefore gives LPE GS films the ability to serve two different roles in electronic and optoelectronic applications, both as an anode and as a cathode.

Here, we demonstrate the method for the forming and doping of LPE graphene sheet films (LPE GS) in one-step by metal standard solutions. Doping of the graphene film occurs at the moment of its formation from the LPE graphene dispersion by LBA method at the air-metal standard solution interface. n-doping is achieved by Li standard solutions (LiCl, LiNO₃, Li₂CO₃), while Au standard solution (H(AuCl₄)) leads to p-doping. WF of the film was decreased with Li based salts, while Au based salts increase the WF of the film. The maximal doping in both directions allow a significant range of around 0.7 eV for the WF modulation. The results were obtained for 0.1 mol/dm³ concentration of dopants. Roughness of the LPE GS films does not change by the doping, except that doped films contain occasional agglomerates. FT-IR measurements point out that the charge transfer process is enabled by physical adsorption of the metal salts and that the graphene basal planes stay chemically unchanged by metal doping. No significant shifts of any characteristic Raman peaks of graphene were detected after chemical doping. Calculated values of the intensity ratio between D and D' peak indicate that the edges are the dominant type of defects in the undoped and metal salt doped LPE GS films. Electrical properties of the films were significantly influenced by changing the dopant (Au or Li). A significant suppression of the field-effect mobility and the increase of the sheet resistivity were observed in the case of the Li standard solution doping of the film. This indicates that adsorbed Li anions act as scattering centers for the charges. Lithium nitrate provides the largest work function modulation (by 400 meV) and the least influence on the sheet resistance of the film. Therefore, it was selected as the best choice for n-type doping.

Since, the proposed one-step method for chemical doping of graphene films allows to tune WF in a large range, it extends the potential use of these materials in low-cost optoelectronic applications, as in low-power lighting, sensors, transparent heating, and de-icing applications.

REFERENCES

- [1] C. Backes et al., Chem. Mater. 29, 243 (2017).
- [2] Q. Zheng et al., ACS Nano. 5, 6039 (2011).
- [3] A. Matković et al., 2D Mater. 3, 015002 (2016).

**21. СИМПОЗИЈУМ ФИЗИКЕ
КОНДЕНЗОВАНЕ МАТЕРИЈЕ**
**THE 21st SYMPOSIUM ON
CONDENSED MATTER PHYSICS**

BOOK OF ABSTRACTS



Conference Chairs

Vladimir Dobrosavljević, *Florida State University, USA*

Zorica Konstantinović, *Institute of Physics Belgrade*

Željko Šljivančanin, *Vinča Institute of Nuclear Sciences*

Organizing Committee

Jelena Pešić, *Institute of Physics
Belgrade- chair*

Bojana Višić, *Institute of Physics
Belgrade*

Andrijana Šolajić, *Institute of Physics
Belgrade*

Jovan Blagojević, *Institute of Physics
Belgrade*

Ivana Milošević, *Institute of Physics
Belgrade*

Marko Orozović, *Vinča Institute of
Nuclear Sciences*

Tijana Tomašević-Ilić, *Institute of
Physics Belgrade*

Mitra Stepić, *Vinča Institute of Nuclear
Sciences*

Jelena Mitrić, *Institute of Physics
Belgrade*

Igor Popov, *Institute for
Multidisciplinary Research, Belgrade*

Program Committee

Ivan Božović, *Brookhaven National
Laboratory, USA*

Vladimir Djoković, *Vinča Institute,
University of Belgrade, Serbia*

Vladimir Dobrosavljević, *Florida State
University, USA*

Gyula Eres, *Oak Ridge National
Laboratory, USA*

Milan Damnjanović, *Faculty of
Physics, University of Belgrade, Serbia*

Laszló Forró, *University of Notre
Dame, USA*

Fe-nanoparticle-modified Langmuir-Blodgett Graphene Films for Pb(II) Water Purification

Ivana R. Milošević^a, Jasna Vujin^a, Muhammad Zubair Khan^b, Thomas Griesser^c, Christian Teichert^b and Tijana Tomašević-Ilić^a

^aInstitute of Physics Belgrade, University of Belgrade, 11080 Belgrade, Serbia

^bChair of Physics, Montanuniversität Leoben, Leoben, Austria

^cChair of Chemistry of Polymeric Materials, Montanuniversität Leoben, 8700 Leoben, Austria

Abstract. The surface of nonmagnetic Langmuir-Blodgett self-assembled (LBSA) graphene films is modified through structure engineering by chemical functionalization with Fe nanoparticles in order to induce local magnetic domains and investigate the application of such films for heavy metal water purification. We prepared and modified our films by single-step Langmuir-Blodgett procedure [1]. The influence of Fe-based magnetic nanoparticles on the structure and magnetic properties of LBSA films was examined by Raman spectroscopy, X-ray photoelectron spectroscopy (XPS), and Magnetic Force Microscopy (MFM). Raman and XPS confirmed the surface modification of the graphene films. Compared to an unmodified graphene film, which has no detectable magnetic response, MFM phase images show a strong phase shift difference compared to the substrate ($\sim 0.2^\circ$), indicating the presence of a local magnetic moment. In addition, we examined the use of magnetized LBSA graphene films for the adsorption of Pb(II) ions by immersing the films into Pb(II) solution. Results from XPS measurements depict the ability of modified films to detect and adsorb Pb(II) ions from water-based solutions. The development of a new generation of magnetic self-assembled 2D material films for heavy metal sensing and water purification that can overcome the deficiencies such as low purification efficiency, short-term stability, and high cost is of great interest for various applications in green technology.

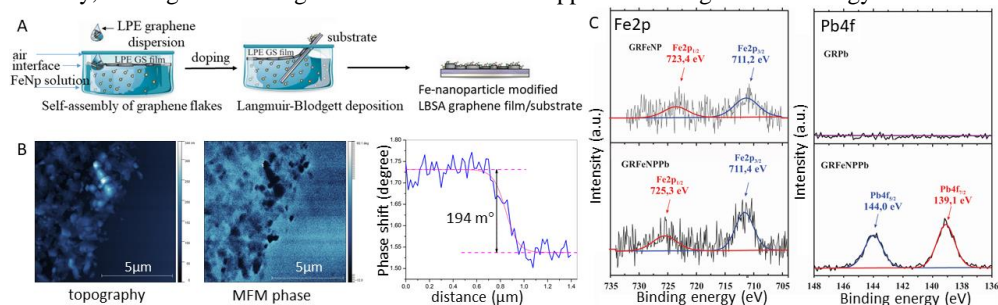


FIGURE 1. A) Fabrication of Fe-modified LBSA graphene films, B) AFM topography, MFM phase image, and representative MFM phase shift profile of Fe-modified LBSA films, C) XPS Fe2p spectra of modified films before and after interaction with Pb(II) ions, and Pb4f spectra of unmodified and modified films after interaction with Pb(II) ions.

REFERENCES

1. Milošević I. R. et al., *Sci. Rep.* **10**, 8476 (2020).



TECHNISCHE UNIVERSITÄT
CHEMNITZ

Faculty of Natural Science



ICSFS 18

International Conference on Solid Films and Surfaces

August 28 - September 02, 2016
in Chemnitz, Germany

Abstract - Book

(with space for your notes)



www.ICSFS18.de

EPITAXY OF HIGHLY ORDERED CONJUGATED ORGANIC SEMICONDUCTOR CRYSTALLITE NETWORKS ON GRAPHENE BASED DEVICES

A. Matković^a, M. Kratzer^a, J. Genser^a, B. Kaufmann^a, J. Vujin^b, B. Vasić^b, R. Gajić^b, and C. Teichert^a

^aInstitute of Physics, Montanuniversität Leoben, Franz Josef Straße 18, 8700 Leoben, Austria

^bCenter for Solid State Physics and New Materials, Institute of Physics, University of Belgrade, Pregrevica 118, 11080 Belgrade, Serbia

We focus on the hot wall epitaxial growth of sub-monolayer films of a rod-like conjugated organic semiconductor (OSC), para-hexaphenyl (C₃₆H₂₆, 6P) [1-3], on the surface of graphene based devices. For this purpose, mechanically exfoliated flakes supported by SiO₂/Si substrates are used and contacted in a back-gated two-point probe field effect device configuration.

Charge transfer and doping of graphene channel by OSCs are investigated in situ. Atomic force microscopy (AFM) is used to characterize OSC crystallite morphology (Fig.1a), and Kelvin probe force microscopy (KPFM) is used to investigate changes in the work functions of graphene and 6P crystallites with applied external electric fields (Fig.1b). Furthermore, we show how residues from the lithography and annealing steps affect morphology of the grown OSC thin films.

Van der Waals nature of the interface between OSCs and graphene allows for the growth of crystallites that are several tens of micrometers large, thus minimizing the number of OSC grain boundaries within the device channel, and allowing investigations of the intrinsic properties of the OSCs.

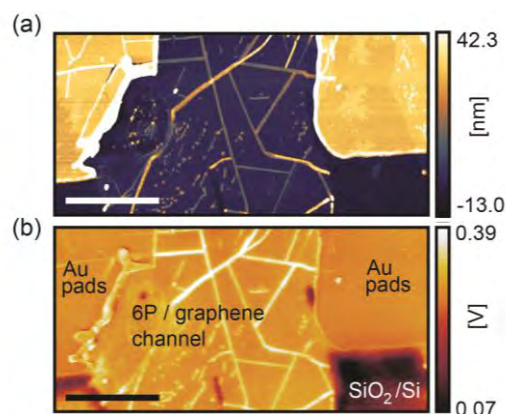


Fig.1. (a) and (b) respectively show AFM and KPFM images of the same 6P/graphene channel area, with grounded back-gate electrode (scale bars 5 μ m).

Keywords: hybrid organic/inorganic van der Waals interfaces, charge transfer OSC/graphene, KPFM of OSC crystallites.

References

- [1] M. Kratzer, S. Klima, C. Teichert, B. Vasić, A. Matković, U. Ralević, and R. Gajić, *Journal of Vacuum Science & Technology B* **31**, 4 (2013) 04D114.
- [2] M. Kratzer, S. Klima, C. Teichert, B. Vasić, A. Matković, M. Milićević, and R. Gajić, *e-Journal of Surface Science and Nanotechnology* **12**, (2014) 31-39.
- [3] M. Kratzer, B. C Bayer, P. R Kidambi, A. Matković, R. Gajić, A. Cabrero-Vilatela, R. S Weatherup, S. Hofmann, and C. Teichert, *Applied Physics Letters* **106**, 10 (2015) 103101-1 - 5.

RAD 7



**BOOK OF
ABSTRACTS**

SEVENTH
INTERNATIONAL
CONFERENCE
ON RADIATION
IN VARIOUS FIELDS
OF RESEARCH

June 10-14, 2019
Herceg Novi
Montenegro



Effects of water on thin films consisting of biomolecules and 2D-materials

Jasna Vujin¹, Weixin Huang², Sylwia Ptasinska³, Radmila Panajotovic¹

¹ Institute of Physics, Belgrade, Serbia

² Stanford University, Stanford, United States

³ University of Notre Dame, South Bend, United States

One of the hottest research topics in the field of 2D-materials is the one concerning their heterostructures with biomolecules. They can serve as scaffolds for growing cells, or bio-chemical sensors, for example. The most popular 2D-material, graphene, and transition metal dichalogenides(WS_2) in combination with various biomolecules (lipids, biopolymers, amino acid, protein...) attracted considerable attention as active components of organic electronic devices. A relatively simple and cheap method of producing thin graphene films is from the liquid phase. The ever present question of how water/humidity from air or biomolecule aqueous solution affects the properties of these heterostructures is very difficult to answer because of the complicated interplay between these components.

In our experiment, we first exposed bare graphene and WS_2 thin films to water in the controlled environment. Then we did the same experiment with the lipid layer (DPPC dipalmitoyl-sn-glycero-phosphotidilcholine), by collecting the XPS (X-ray Photo-Electron) spectra. In order to examine electrical properties of such heterostructures in ambient condition, we measured the current-voltage response after the deposition of aqueous solution of amino acids, protein and cell culture. In addition, we collected the information about the topography of our heterostructures and Raman.



FOURTH INTERNATIONAL CONFERENCE ON RADIATION
AND APPLICATIONS IN VARIOUS FIELDS OF RESEARCH

May 23 - 27, 2016 | Niš | Serbia | rad-conference.org

BOOK OF ABSTRACTS



PUBLISHER: University of Niš, Faculty of Electronic Engineering
P.O.Box 73, 18000 Niš, Serbia
www.elfak.ni.ac.rs

FOR THE PUBLISHER: Prof. Dr Dragan Mančić

EDITOR: Prof. Dr Goran Ristić

COVER DESIGN: Vladan Nikolić, PhD

TECHNICAL EDITING: Vladan Nikolić, PhD and Sasa Trenčić, MA

PROOF-READING: Saša Trenčić, MA and Mila Aleksov, MA

PRINTED BY: Sven, Niš

PRINT RUN: 50 copies

The Fourth International Conference on Radiation and Applications in Various Fields of Research (RAD 2016) was financially supported by:

- Central European Initiative (CEI)
- Ministry of Education, Science and Technological Development of the Republic of Serbia

ISBN: 978-86-6125-160-3

CIP - Каталогизacija y yубликации -
Народна библиотека Србије, Београд

539.16(048)

INTERNATIONAL Conference on Radiation and Applications
in Various Fields of Research (4th ; 2016 ; Niš)
Book of Abstracts / Fourth International Conference on Radiation and
Applications in Various Fields of Research, RAD 4, May 23-27, 2016, Niš,
Serbia ; [editor Goran Ristić]. - Niš : University, Faculty of Electronic
Engineering, 2016 (Niš : Sven). - [XL], 510 str. ; 25 cm

Tiraž 50. - Bibliografija uz svaki rad.

ISBN 978-86-6125-160-3

a) Јонизујуће зрачење - Дозиметрија - Апстракти

COBISS.SR-ID 223620620



ELECTRON-BEAM DAMAGE FROM SEM TO LIPID-(GRAPHENE, MoS₂, WS₂) HETEROSTRUCTURES

Radmila Panajotovic, Jasna Vujin, Djordje Jovanovic

Institute of Physics Belgrade, Belgrade, Serbia

Interfaces of lipids with its surroundings are important in defining the physical properties of lipid films supported as mono- bi- or multilayers on solid surfaces [1]. These assemblies are usually engineered by means of chemical or mechanical processing, which allow them to be tailored to a specific application, either as a coating of a nano-particle for drug delivery or a multilayer heterostructure for biochemical sensing. Among most convenient materials used as solid support for lipid heterostructures are the 2D-materials, such as graphene and transition-metal dichalcogenides that may be used as a mechanical scaffold or a base for an electrical biochemical sensor nano-device. As these devices may often be required to function in an environment where radiation from space, nuclear reactors, or scientific instruments may interfere with their operation, it is important to assess the potential damage that radiation causes to all the materials comprising these devices.

The imaging technique that is routinely used in scientific research, Scanning Electron Microscopy (SEM) employs an intense high-energy electron beam that is participating in elastic and inelastic collisions within the thin lipid films and the solid substrate that supports them. Recent studies of electron damage to WS₂ nanosheets [2] show that the electron beam can cause considerable morphological and structural changes in these materials. Also, a previous study [3] on the damage of low-energy electrons on DPPC monolayer films supported on silicon demonstrated that even sub-keV electrons can degrade the lipids.

In order to study an overall effect of keV-energy focused electron beams from SEM on our heterostructures consisting of DPPC, DPHyPC, sphingomyelin and cholesterol supported on graphene, MoS₂ and WS₂ thin films, we performed the AFM, KPFM, FT-IR and Raman spectroscopy measurements.

References:

1. Ann E. Oliver, Atul N. Parikh, *Biochimica et Biophysica Acta* 1798 (2010) 839–850
2. Yuqing Wang, Yi Feng, Yangming Chen, Fei Mo, Gang Qian, Dongbo Yu, Yang Wang and Xuebin Zhang, *Phys.Chem.Chem.Phys.* 17 (2015) 2678
3. R. Panajotović, S. Ptasinska, V. Lyamayev, and K. Prince, *Proceedings of the Third International Conference on Radiation and Applications in Various Fields of Research, RAD2015, June 8-12, 2015, Slovenska plaza, Budva, Montenegro*, Ed. Prof. Dr. Goran Ristić, RAD Association, Niš, Serbia, ISBN: 978-86-80300-01-6, p.27, <http://www.rad-conference.org/proceedings.php>

RAD 7



**BOOK OF
ABSTRACTS**

SEVENTH
INTERNATIONAL
CONFERENCE
ON RADIATION
IN VARIOUS FIELDS
OF RESEARCH

June 10-14, 2019
Herceg Novi
Montenegro



Application of 2D-materials in building biomolecular heterostructures

Jasna Vujin¹, Martina Gilić², Radmila Panajotović¹

¹ Laboratory for Graphene, Other 2D-Materials and Ordered Nanostructures, Institute of Physics, Belgrade, Serbia

² Laboratory for Electronic Materials, Institute of Physics, Belgrade, Serbia

A quest for non-toxic, easily produced and inexpensive materials with satisfactory chemical (inertness, resistance to degradation) and physical (mechanical robustness, flexibility) properties, that can be used in combination with biological molecules and cells, was greatly accomplished by the discovery of atomically thin 2D-materials. Their exceptional mechanical and tunable electrical properties offer an excellent base for building various types of bio-chemical sensors, growth of self-assembled bio-membranes, and scaffolds for biological tissue engineering. As the most popular of these materials, graphene has become widely used, in various forms – as nanotubes, nanoflakes, nanopaticles, etc. Others, like MoS₂ and WS₂, have gained their popularity as active elements of biochemical sensors, mostly due to their tunable (semi) conductivity after physi- or chemisorption on their surface. In both conductive (graphene) and semi-conductive (MoS₂ and WS₂) thin films of 2D-materials it is necessary to assess their surface morphology, and the chemical and physical changes in combination with water, and biological molecules, such as aminoacids, proteins, lipids, etc. In order to do this, we used several experimental methods – AFM, KPFM Raman and FT-IR spectroscopy. We used graphene and WS₂ thin films for deposition of two different amino acids – cystein, arginine – and sphynomyelin – playing an important role in neuro-signalling and in the structure of neuron's axon sheath.



FOURTH INTERNATIONAL CONFERENCE ON RADIATION
AND APPLICATIONS IN VARIOUS FIELDS OF RESEARCH

May 23 - 27, 2016 | Niš | Serbia | rad-conference.org

BOOK OF ABSTRACTS



PUBLISHER: University of Niš, Faculty of Electronic Engineering
P.O.Box 73, 18000 Niš, Serbia
www.elfak.ni.ac.rs

FOR THE PUBLISHER: Prof. Dr Dragan Mančić

EDITOR: Prof. Dr Goran Ristić

COVER DESIGN: Vladan Nikolić, PhD

TECHNICAL EDITING: Vladan Nikolić, PhD and Sasa Trenčić, MA

PROOF-READING: Saša Trenčić, MA and Mila Aleksov, MA

PRINTED BY: Sven, Niš

PRINT RUN: 50 copies

The Fourth International Conference on Radiation and Applications in Various Fields of Research (RAD 2016) was financially supported by:

- Central European Initiative (CEI)
- Ministry of Education, Science and Technological Development of the Republic of Serbia

ISBN: 978-86-6125-160-3

CIP - Каталогизacija y yублиkaciji -
Hapoyna библиотека Србије, Београд

539.16(048)

INTERNATIONAL Conference on Radiation and Applications
in Various Fields of Research (4th ; 2016 ; Niš)
Book of Abstracts / Fourth International Conference on Radiation and
Applications in Various Fields of Research, RAD 4, May 23-27, 2016, Niš,
Serbia ; [editor Goran Ristić]. - Niš : University, Faculty of Electronic
Engineering, 2016 (Niš : Sven). - [XL], 510 str. ; 25 cm

Tiraž 50. - Bibliografija uz svaki rad.

ISBN 978-86-6125-160-3

a) Јонизујуће зрачење - Дозиметрија - Апстракти

COBISS.SR-ID 223620620



PHYSICO-CHEMICAL CHARACTERIZATION OF LIPID-2D-MATERIALS SELF-ASSEMBLY FOR BIOSENSORS

Jasna Vujin, Djordje Jovanovic, Radmila Panajotovic

Institute of Physics Belgrade, Belgrade, Serbia

Solid supported phospholipid-bilayer technology [1] is one of the major avenues for development of sensors and nanodevices, especially in the fields of proteomics. Since the drug targeting is usually aimed to the cell membrane associated proteins, building a well-tailored and sensitive biosensor is of utmost value [2]. On the other hand, modern research in material science explores the possibilities of materials suitable for building small, sensitive, and robust sensors. 2D-materials, such as graphene, MoS₂, and WS₂, in combination with lipid mono- and multilayers present an excellent base for building organic field-effect transistors (oFET), whose properties are able to meet these requirements [1,3,4]. In order to accomplish a satisfactory design of such devices, it is necessary to produce thin (ideally homogenous, defect-free) films of graphene and other 2D-materials and establish their physico-chemical properties, alone and in combination with various biomolecular assemblies, such as lipids, cholesterol and biopolymers. In our study we have obtained composite thin films of these materials (from a few nm to several tens of nm) and explored the electrostatic properties, structural topography, and chemical bonds of DPPC, DPHyPC, sphingomyelin and cholesterol supported on graphene, MoS₂ and WS₂ thin films. The AFM, KPFM, FT-IR and Raman spectroscopy have been employed for that purpose.

References

1. Ann E. Oliver, Atul N. Parikh, *Biochimica et Biophysica Acta* 1798 (2010) 839–850
2. Edward T. Castellana, Paul S. Cremer, *Surface Science Reports* 61 (2006) 429–444
3. Nengjie Huo, Shengxue Yang, Zhongming Wei, Shu-Shen Li, Jian-Bai Xia and Jingbo Li, *Scientific Reports* 4 (2014) 5209
4. Jitendra N. Tiwari, Varun Vij, K. Christian Kemp, and Kwang S. Kim, *ACS Nano Article ASAP* (2015) Open access



28th Summer School and International Symposium on the Physics of Ionized Gases

Aug. 29 - Sep. 2, 2016, Belgrade, Serbia

CONTRIBUTED PAPERS

&

ABSTRACTS OF INVITED LECTURES,
TOPICAL INVITED LECTURES, PROGRESS REPORTS
AND WORKSHOP LECTURES

Editors:

Dragana Marić, Aleksandar Milosavljević,
Bratislav Obradović and Goran Poparić



University of Belgrade,
Faculty of Physics



Serbian Academy
of Sciences and Arts

**28th Summer School and International
Symposium on the Physics of Ionized
Gases**

S P I G 2016

CONTRIBUTED PAPERS

&

ABSTRACTS OF INVITED LECTURES,
TOPICAL INVITED LECTURES, PROGRESS REPORTS
AND WORKSHOP LECTURES

Editors

Dragana Marić, Aleksandar Milosavljević,
Bratislav Obradović and Goran Poparić

University of Belgrade,
Faculty of Physics

Serbian Academy
of Sciences and Arts

Belgrade, 2016

MODIFICATIONS OF LIPID/2D-MATERIAL HETEROSTRUCTURES BY SEM

Radmila Panajotović and Jasna Vujin

Institute of Physics, University of Belgrade, Pregrevica 118, 11080 Belgrade, Serbia

Abstract. The use of 2D-materials as solid support for lipids in the organic Field-Effect Transistors has been in expansion in recent years, particularly for their increased sensitivity to detecting small molecular concentrations. Molecular binding and charge transfer in these devices is governed by the chemical and electrical properties of the interface, as well as by its homogeneity and roughness. In our experiment we used the Scanning Electron Microscope (SEM) to modify the surface of thin lipid/graphene and lipid/WS₂ films. We showed that in these heterostructured film surface potential modifications can be achieved without significant morphological changes in the interface.

1. BACKGROUND

Lipid films in the form of mono-, bi- or multipliers supported on solid surfaces [1] are one of the center-points in the fields of biotechnology, organic material science and Bioelectronics. These assemblies are usually engineered through chemical or mechanical processing, which allow them to be tailored to a specific application, such as biochemical sensing. Recently, the use of 2D-materials as solid support for lipid heterostructures, particularly graphene and transition metal dichalcogenides, has been suggested, especially as a component of organic FET (Field-Effect Transistor) devices [1, 2]. In terms of sensing properties, it is crucial to these devices to possess the largest possible binding surface; hence the need for a porous substrate that will provide for this feature. To this end, thin films of graphene and other 2D-material substrates produced from liquid exfoliation seem to be good candidates because of their structure consisting of multilayered flakes with edges exposing dangling bonds. At the same time, such films allow the formation of uniform and homogenous lipid films as a stable and versatile platform for molecular binding in FET sensing devices.

Electrical properties of these heterostructures are crucial for their operation. As the pure lipid layer is likely to have high resistivity (of the order of M Ω) and is supported either on a conductive (graphene) or semiconductive (WS₂) substrate, our idea was to use the source of electrons that is routinely used in imaging, the Scanning Electron Microscope (SEM), to modify electric properties of the surface of such heterostructures. Since the SEM employs an intense high-

Citation overview

Self citations of selected authors are excluded. ✕

[Back to author details](#)

[Export](#) [Print](#)

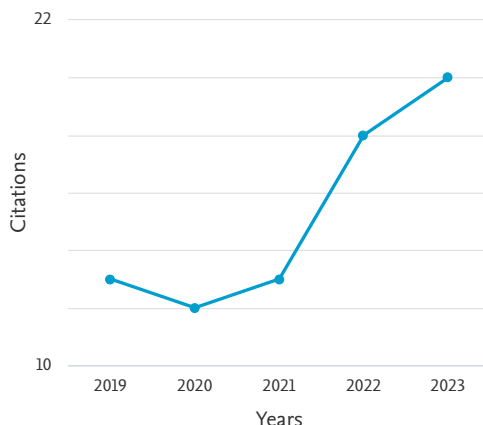
This is an overview of citations for this author.

Author *h*-index : 5 [View *h*-graph](#)

7 Cited Documents from "Vujin, Jasna" [+ Add to list](#)

Author ID:57189458411

Date range: 2019 to 2023 Exclude self citations of selected author Exclude self citations of all authors Exclude citations from books [Update](#)



Sort on: Citation count (descending)

Page [Remove](#)

Documents	Citations	<2019	2019	2020	2021	2022	2023	Subtotal	>2023	Total
	Total	7	13	12	13	18	20	76	0	83
<input type="checkbox"/> 1 Differentiation of stem cells from apical papilla into neuro...	2018	1	6	5	5	6	4	26		27
<input type="checkbox"/> 2 Probing charge transfer between molecular semiconductors and...	2017	2	6	4	3	3	4	20		22
<input type="checkbox"/> 3 Transparent and conductive films from liquid phase exfoliate...	2016	4	1	3	3	5	3	15		19
<input type="checkbox"/> 4 Single-step fabrication and work function engineering of Lan...	2020				2	1	3	6		6
<input type="checkbox"/> 5 DFT study of optical properties of MoS ₂ and WS	2018					3	2	5		5
<input type="checkbox"/> 6 The Effect of Liquid-Phase Exfoliated Graphene Film on Neuro...	2022						4	4		4
<input type="checkbox"/> 7 Direct Probing of Water Adsorption on Liquid-Phase Exfoliate...	2023							0		0

Display: 20 results per page

About Scopus

[What is Scopus](#)

[Content coverage](#)

[Scopus blog](#)

[Scopus API](#)

[Privacy matters](#)

Language

[日本語版を表示する](#)

[查看简体中文版本](#)

[查看繁體中文版本](#)

[Просмотр версии на русском языке](#)

Customer Service

[Help](#)

[Tutorials](#)

[Contact us](#)

ELSEVIER

[Terms and conditions](#) ↗ [Privacy policy](#) ↗

Copyright © Elsevier B.V. ↗ . All rights reserved. Scopus® is a registered trademark of Elsevier B.V.

We use cookies to help provide and enhance our service and tailor content. By continuing, you agree to the use of cookies ↗.



Citation Report

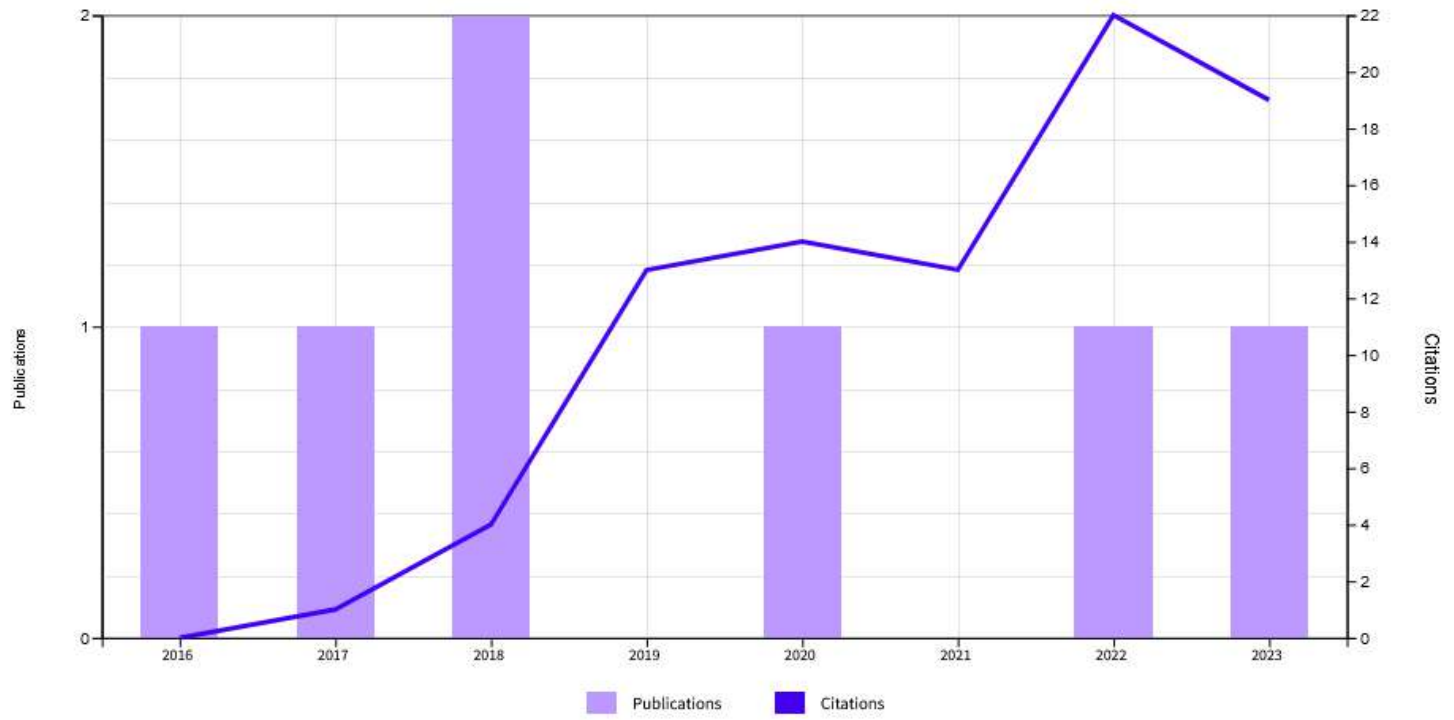
Vujin, Jasna (Author) [Analyze Results](#) [Create Alert](#)

[Export Full Report](#)

Publications 7 Total From 1995 to 2023	Citing Articles 82 Analyze Total 78 Analyze Without self-citations	Times Cited 86 Total 80 Without self-citations	12.29 Average per item	5 H-Index
---------------------------------------------------------------	-----------------------------------------------------------------------------------------------------	---------------------------------------------------------------------------------	----------------------------------	---------------------

Times Cited and Publications Over Time

[DOWNLOAD](#)



7 Publications		Sort by: Citations: highest first		< 1 of 1 >		Citations							
						< Previous year					Next year >	Average per year	Total
						2019	2020	2021	2022	2023			
Total		13	14	13	22	19	12.29	86					
1	Differentiation of stem cells from apical papilla into neural lineage using graphene dispersion and single walled carbon nanotubes Simonovic, J; Toljic, B; (-); Milasin, J Oct 2018 JOURNAL OF BIOMEDICAL MATERIALS RESEARCH PART A 106 (10) , pp.2653-2661	6	6	4	8	3	4.5	27					
2	Probing charge transfer between molecular semiconductors and graphene Matkovic, A; Kratzer, M; (-); Teichert, C Aug 25 2017 SCIENTIFIC REPORTS 7	6	5	3	3	4	3.29	23					
3	Transparent and conductive films from liquid phase exfoliated graphene Tomasevic-Illic, T; Pesic, J; (-); Galic, B Jun 2016 OPTICAL AND QUANTUM ELECTRONICS 48 (6)	1	3	3	5	3	2.25	18					
4	Single-step fabrication and work function engineering of Langmuir-Blodgett assembled few-layer graphene films with Li and Au salts Milosevic, IR; Vasic, B; (-); Galic, B May 21 2020 SCIENTIFIC REPORTS 10 (1) Enriched Cited References	0	0	3	3	2	2	8					
5	DFT study of optical properties of MoS2 and WS2 compared to spectroscopic results on liquid phase exfoliated nanoflakes Pejac, J; Wu@in, J; (-); Galic, B Jul 2018 OPTICAL AND QUANTUM ELECTRONICS 50 (7)	0	0	0	3	3	1	6					
6	The Effect of Liquid-Phase Exfoliated Graphene Film on Neurodifferentiation of Stem Cells from Apical Papilla Simonovic, J; Toljic, B; (-); Milasin, J Sep 2022 NANOMATERIALS 12 (18) Enriched Cited References	0	0	0	0	4	2	4					
Direct Probing of Water Adsorption on Liquid-Phase Exfoliated WS2 Films Formed by the Langmuir-													

1	<p>Simonovic, J; Toljic, B; L--; Milasin, J Oct 2018 JOURNAL OF BIOMEDICAL MATERIALS RESEARCH PART A 106 (10), pp.2653-2661</p>	6	6	4	8	3	4.5	27
2	<p>Probing charge transfer between molecular semiconductors and graphene Matkovic, A; Kratzer, M; L--; Teichert, C Aug 25 2017 SCIENTIFIC REPORTS 7</p>	6	5	3	3	4	3.29	23
3	<p>Transparent and conductive films from liquid phase exfoliated graphene Tomasevic-Ilic, T; Pesic, J; L--; Galic, R Jun 2016 OPTICAL AND QUANTUM ELECTRONICS 48 (6)</p>	1	3	3	5	3	2.25	18
4	<p>Single-step fabrication and work function engineering of Langmuir-Blodgett assembled few-layer graphene films with Li and Au salts Milosevic, IR; Vasic, B; L--; Galic, R May 21 2020 SCIENTIFIC REPORTS 10 (1)</p> <p>Enriched Cited References</p>	0	0	3	3	2	2	8
5	<p>DFT study of optical properties of MoS2 and WS2 compared to spectroscopic results on liquid phase exfoliated nanoflakes Pelic, J; Wjito, J; L--; Galic, R Jul 2018 OPTICAL AND QUANTUM ELECTRONICS 50 (7)</p>	0	0	0	3	3	1	6
6	<p>The Effect of Liquid-Phase Exfoliated Graphene Film on Neurodifferentiation of Stem Cells from Apical Papilla Simonovic, J; Toljic, B; L--; Milasin, J Sep 2022 NANOMATERIALS 12 (18)</p> <p>Enriched Cited References</p>	0	0	0	0	4	2	4
7	<p>Direct Probing of Water Adsorption on Liquid-Phase Exfoliated WS2 Films Formed by the Langmuir-Schaefer Technique Wujin, J; Huang, WX; L--; Panajotovic, B Jun 2 2023 Jun 2023 (Early Access) LANGMUIR 39 (23), pp.8055-8064</p> <p>Enriched Cited References</p>	0	0	0	0	0	0	0

Citation Report Publications Table

Датум: 26.09.2023.
Број: 1276

З А П И С Н И К

са јавне одбране докторске дисертације кандидата **маст физ.-хем. Јасне Вујин**, одржане 26.09.2023. године, у библиотеци Универзитет у Београду – Факултета за физичку хемију, Студентски трг 12-16 у Београду.

Комисију за одбрану именовану на седници Наставно-научног већа Факултета за физичку хемију одржаној 07.09.2023. године одлуком Наставно-научног већа Факултета број 1194 од 07.09.2023. године, чинили су:

- 1) др Немања Гаврилов, ванредни професор, Факултет за физичку хемију,
- 2) др Ана Доброта, доцент, Факултет за физичку хемију,
- 3) др Ивана Милошевић, научни сарадник, Институт за физику.

Пре отварања јавног састанка, Комисија је за председника изабрала

Др Ана Доброта, доцент

Председник Комисије је у 15:30 часова отворио састанак за јавну одбрану докторске дисертације кандидата **маст физ.-хем. Јасне Вујин**, студента докторских студија, под називом „Физичкохемијска карактеризација хетероструктура дводимензионалних материјала (графен, волфрам-дисулфид) и биолошких молекула (цистеин, 1,2 дипалмитоил-*sn*-глицеро-3-фосфохолин)“.

Пошто је председник Комисије прочитао биографске податке о кандидату и податке о његовом досадашњем раду, позвао је кандидата да изнесе резултате до којих је дошао у својој докторској дисертацији.

По завршеном излагању кандидата, чланови Комисије су поставили питања кандидату и дали критички осврт на докторску дисертацију.

Након што је кандидат **маст физ.-хем. Јасна Вујин**, студент докторских студија, одговорио на постављена питања у вези са докторском дисертацијом, Комисија се повукла ради већања.

После већања, председник Комисије је јавно саопштио једногласну одлуку Комисије, да је кандидат **маст физ.-хем. Јасна Вујин**, студент докторских студија, **о д б р а н и о** докторску дисертацију, под називом „Физичкохемијска карактеризација хетероструктура дводимензионалних материјала (графен, волфрам-дисулфид) и биолошких молекула (цистеин, 1,2 дипалмитоил-*sn*-глицеро-3-фосфохолин)“ и тиме стекао право да буде промовисан у научни степен „доктор наука - физичкохемијске науке“.

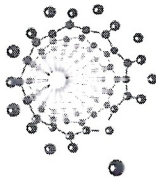
Састанак за јавну одбрану је завршен у 16.30 часова.

Комисија:

Гаврилов Немања
Милошевић Ивана

Председник Комисије:

Ана Доброта



Универзитет у Београду
Факултет за физичку хемију
Број индекса: 2014/0308
Број: Д2023Д19
Датум: 29.09.2023.

На основу члана 29. Закона о општем управном поступку („Сл. гласник РС”, бр.18/2016 и 95/2018), допуни дозволе за рад број 612-00-00730/2021-06 од 13.05.2021. године коју је издало Министарство просвете, науке и технолошког развоја Републике Србије и службене евиденције, Универзитет у Београду - Факултет за физичку хемију, издаје

У В Е Р Е Њ Е

Јасна Вујин

име једној родитеља Гордана, ЈМБГ 0708984715342, рођена 07.08.1984. године, Београд, олимпијана Звездара, Република Србија, уписана школске 2014/15. године, дана 26.09.2023. године завршила је докторске академске студије на студијском програму Физичка хемија, у трајању од три године, обима 180 (сто осамдесет) ЕСПБ бодова, са просечном оценом 9,00 (девет и 00/100).

На основу наведеног издаје јој се ово уверење о стеченом високом образовању и научном називу **доктор наука - физичкохемијске науке.**



Декан

Мирослав Кузмановић
проф. др Мирослав Кузмановић



Република Србија
Универзитет у Београду
Факултет за физичку хемију
Број индекса: 2014/0308
Датум: 29.09.2023.

На основу члана 29. Закона о општем управном поступку („Сл. гласник РС”, бр.18/2016 и 95/2018) и службене евиденције

УВЕРЕЊЕ О ПОЛОЖЕНИМ ИСПИТИМА

Јасна Вујин, име једног родитеља Гордана, ЈМБГ 0708984715342, рођена 07.08.1984. године, Београд, општина Звездара, Република Србија, уписана школске 2014/15. године, дана 26.09.2023. године завршила је докторске академске студије на студијском програму Физичка хемија, у трајању од три године, обима 180 (сто осамдесет) ЕСПБ бодова, доктор наука - физичкохемијске науке. Током студија положила је испите из следећих предмета:

Р.бр.	Шифра	Назив предмета	Оцена	ЕСПБ	Фонд часова**	Датум
1.	21ДС1002	Нове физичкохемијске методе	7 (седам)	10	I:(90+0+45)	03.06.2016.*
2.	21ДС1001	Математичке методе у физичкохемијским истраживањима	9 (девет)	10	I:(90+0+45)	24.09.2015.*
3.	21ДСЗИ19	Физичкохемијске методе у медицини и медицинским истраживањима	9 (девет)	10	II:(75+0+30)	26.12.2017.*
4.	21ДСЗИ08	Примењена фотохемија	10 (десет)	10	II:(75+0+30)	29.09.2017.*
5.	21ДСЗИ30	Графен	9 (девет)	10	II:(75+0+30)	16.01.2023.*
6.	21ДСЗИ29	Физичка хемија наноматеријала	9 (девет)	10	II:(75+0+30)	16.01.2023.*
7.	21ДС4001	Специјални курс	10 (десет)	12	IV:(0+0+180)	29.01.2019.*

* - еквивалентиран/признат испит.

** - Фонд часова је у формату (предавања+вежбе+остало).

Одрађене обавезе:

Р.бр.	Назив обавезе	ЕСПБ
1.	Израда докторске дисертације 1	10
2.	Израда докторске дисертације 2	10
3.	Израда докторске дисертације 3	10
4.	Израда докторске дисертације 4	18
5.	Израда докторске дисертације 5	25
6.	Израда докторске дисертације 6	20
7.	Научно-истраживачки рад 1	3
8.	Научно-истраживачки рад 2	3

Укупно остварено 180 ЕСПБ.

Општи успех: 9,00 (девет и 00/100), по годинама студија (8,83, 10,00, /).

Докторска дисертација под насловом: "Физичкохемијска карактеризација хетероструктура дводимензионалних материјала (графен, волфрам-дисулфид) и биолошких молекула (цистеин, 1,2 дипалмитоил-sn-глицеро-3-фосфохолин)" одбрањена је дана 26.09.2023. године.

Овлашћено лице факултета